VOLCANIC HISTORY AND ERUPTION PROCESSES OF BLUE LAKE CRATER, TONGARIRO

A thesis submitted in partial fulfilment

of the requirements for the degree

of

Master of Science

in Earth Sciences

at

The University of Waikato

by

Benjamin Clifford Simons

THE UNIVERSITY OF
WAIKATO
Te Whare Wānanga o Waikato

2014

Abstract

Blue Lake Crater (BLC) is a volcanic crater lake situated on the northern end of the Tongariro Volcanic Centre (TgVC) and is one of at least 11 vents that have been active since c. 25 ka. The stratigraphy of the proximal-to-vent deposits and associated eruption history of BLC has been poorly constrained compared to many of the other young TgVC vents. The resurgence of volcanic activity on the northern end of the TgVC in 2012 prompted research into other young northern vents to determine if any relationships exist, and whether these vents are capable of future eruptions.

The stratigraphy, geomorphological and facies characteristics have been compiled from detailed field mapping and stratigraphic logs around the BLC pyroclastic rim and the Mangahouhounui Valley. BLC is surrounded by a rim of agglutinates and pyroclastic fall deposits that drape over older Tongariro landforms. The northern rim is comprised of Rotopaunga peak (~130 m above Blue Lake) which includes a series of four thick, welded agglutinate units (the Rotopaunga Agglutinates) which are considered to pre-date BLC, overlain by a succession of scoria and spatter beds (the Rotopaunga Scorias) which are sourced, at least in part, from BLC. A discontinuous exposure of agglutinate, up to 8 m thick, mantles the western and southern rim. A ~4 m thick, ~700 m long a'a lava flow derived from BLC extends over the eastern rim into the Mangahouhounui valley. The proximal-vent-forming deposits are comprised of non to intensely welded and agglutinated spatter and scoria and have all been produced by explosive Hawaiian-and Strombolian-style fire-fountaining. These deposits do not represent the original crater-forming event however, which based on geomorphology, is suggested to have been pheatomagmatic.

Petrography, electron microprobe and x-ray fluorescence analyses were carried out on a selection of samples. The deposits are all plagioclase-dominated porphyritic pyroxene andesites and basaltic andesites, some of which contain rare olivine. A lack of phenocryst and whole rock geochemical trends through the stratigraphic sequence indicates that there is no progression or evolution of the magmas through time, and that multiple magma batches mingled prior to eruption.

The hazards associated with BLC include: phreatomagmatic pyroclastic density currents, ballistic blocks and bombs and fire-fountaining, and lahars caused either by a future eruption or from the failure of the BLC rim.

The northern vents of the TgVC (North Crater, Te Maari craters and BLC) are closely spaced and of a similar age and similar geochemical composition. BLC and Te Maari are likely to share a similar subsurface hydrothermal system and a spatial distribution of seismicity, although these alone do not imply a link in subsurface magma plumbing between the two vents.

Acknowledgements

This project would not have been possible without the invaluable assistance, support and encouragement I have received from so many people and I am honoured to have the opportunity to acknowledge and thank them in these pages.

I am indebted to my supervisor Adrian Pittari for his guidance, endless patience, constant academic and logistic support and the many hours spent editing chapters. Thanks also to Roger Briggs who contributed a great deal of advice and many stimulating discussions. Thanks to David Lowe for his tireless support with the many issues that impeded progress, and thanks to Vicki Moon and Willem de Lange for generously providing accommodation during my fieldwork. This research would not have progressed without the expertise and guidance of the Department of Earth and Ocean Sciences technical staff; Annette Rodgers, Renat Radosinsky, Ganqing Xu and Dean Barker.

Special thanks to Harry Keys from the Department of Conservation, and to the Ngati Tuwharetoa iwi, for granting permission to operate within a Rahui (restricted zone) for the duration of my fieldwork, and for allowing me to collect samples. I am also extremely grateful to Dougal Townsend, Graham Leonard and Brad Scott at Geological and Nuclear Sciences (GNS) for providing me with invaluable mapping data and advice. Thanks also to Shane Cronin from Massey University for allocating a very generous amount of his time, patience and expertise while conducting electron microprobe work.

Funding for this study was generously provided by: the University of Waikato (Master's Scholarship); the Broad Memorial Fund; the Geoscience Society of New Zealand Hastie Award; and the Project Tongariro Memorial Fund.

A very special thank you to my field assistants, fellow earth scientists and friends Matthew Norton and Jai Davies-Campbell, for the long hours spent in the field with me, carrying rocks, providing a scale in photographs, and trying not to look bored while I scratched my head and scribbled in my notebook.

I would not have survived this experience without the love, patience and understanding of my family. To my parents, thank you for your constant encouragement, support and unwavering faith in me. A final, very special thank you to my new wife Amanda for putting up with me, supporting me, and generally keeping me washed and fed. I am glad that you were able to experience field geology and see what all the fuss is about, even though I might have left out a few details about the steeper parts of the track.

Table of Contents

List of Figures

Chapter One

Chapter Two

Chapter Three

Chapter Four

Chapter Five

List of Tables

Chapter Three

Chapter Four

Chapter One

Introduction

1.1 Introduction

Te Wai-whaakata-o-te-Rangihiroa, or Blue Lake, is a volcanic crater lake at the northern end of the Tongariro Volcanic Centre (TgVC) at the southern end of the Taupo Volcanic Zone (TVZ). Blue Lake Crater (BLC) represents one of at least 11 vents that have been active on Tongariro since c.25 ka. The eruption history from this vent is poorly defined and stratigraphy of the proximal-to-vent deposits is poorly constrained compared to many of the other young TgVC vents. The August 6 and November 21, 2012 eruptions were the first on Tongariro since 1975 (Ngauruhoe) and the first eruption from the northern end of Tongariro since 1896 (Te Maari). The resurgence in volcanic activity has sparked a great deal of scientific interest (Christenson *et al.* 2013; Hurst *et al.* in-press; Prado *et al.* in-press) but it also raises concerns for the safety of the many thousands of users of the Tonagriro Alpine Track (one of the world's great walks) and for the infrastructure and population that surrounds the volcano. This has prompted research into the other young northern vents to determine if any relationships exist, and whether they are capable of future eruptions.

1.2 Aims

The aims of this thesis are;

i. to establish a detailed volcanic history of Blue Lake Crater and it's surrounding proximal-to-vent deposits, and
ii. to determine the physical eruption dynamics and emplacement processes associated with the eruptive activity of Blue Lake Crater.

1.3 Geological Setting

Blue Lake Crater is a volcanic crater lake situated at the northern end of Mt. Tongariro, an andesitic composite vent complex which is part of the Tongariro Volcanic Centre (TgVC). The TgVC sits at the southern end of the Taupo Volcanic Zone (TVZ), a Neogene volcanic arc situated within the North Island of New Zealand (Figure 1.1). The TVZ formed as a consequence of subduction-related tectonic activity. It exists as series of volcanic centres trending along a roughly NE-SW lineament. It is approximately 300 kms long (200 km's on land) and 60 kms wide (Deering *et al*. 2008). The TVZ is a rifting arc (currently rifting at a rate of 7-18 mm per year), and this has caused the continental crust below to thin considerably to ~15 km (Cole 1979; Wilson *et al.* 1995). Faulted metasediments (greywacke and argillite) form most of the immediate sub-volcanic basement (Wilson *et al.* 1995). The eruptives of the TVZ are entirely calc-alkaline, and fall within the basalt-andesite-dacite-rhyolite series (Cole 1981). A striking feature of the TVZ is that it shows near complete geographical separation of andesites from rhyolites and basalts. Over 95% of andesite occurs within the NE and SW extremities (forming composite cone volcanoes), while rhyolites and high-Al basalts are almost entirely restricted to the central segment and are related to calderas (Figure 1.2). The TVZ is the dominant region of young volcanism in New Zealand, and is one of the most highly active volcanic centres in the world. Andesitic activity began c. 2 Ma followed by voluminous rhyolitic activity c. 1.6 Ma. 90 percent of the eruptives produced by the TVZ were ejected during the late Pliocene to Quaternary (Wilson *et al.* 1995).

The TgVC is the andesite dominated centre at the southern extremity of the TVZ. It comprises four major andesitic volcanoes (Kakaramea, Pihanga, Tongariro and Ruapehu) and two small eroded centres (Mangakatote and Hauhungatahi) a satellite cone (Pukeonake) and four craters near Ohakune (Cole 1981; Donaghue *et al.* 1995). The first significant cone building episodes of the Mt. Tongariro stratocone complex occurred ~275–215 ka. A period of relative quiescence began ~65 ka until 25 ka when activity recommenced. The Tongariro complex is now comprised of over 17 overlapping vents, which collectively cover an area of roughly 60 km^2. Its highest peak is Mt. Ngauruhoe (2280 m). Ngauruhoe is

informally named separately, but is geologically considered part of Tongariro (Hobden *et al.* 1999). Most of the tephras erupted from the TgVC accumulated to the east of the vents, a result of being blown by the prevailing westerly winds. The tephras form thick sequences of bedded lapilli and ash, interbedded with local ring-plain-forming debris flow and stream flow deposits, and with distal rhyolitic tephras from the Taupo and Okataina Volcanic Centres (TVC and OVC, respectively) (Donaghue *et al.* 1995).

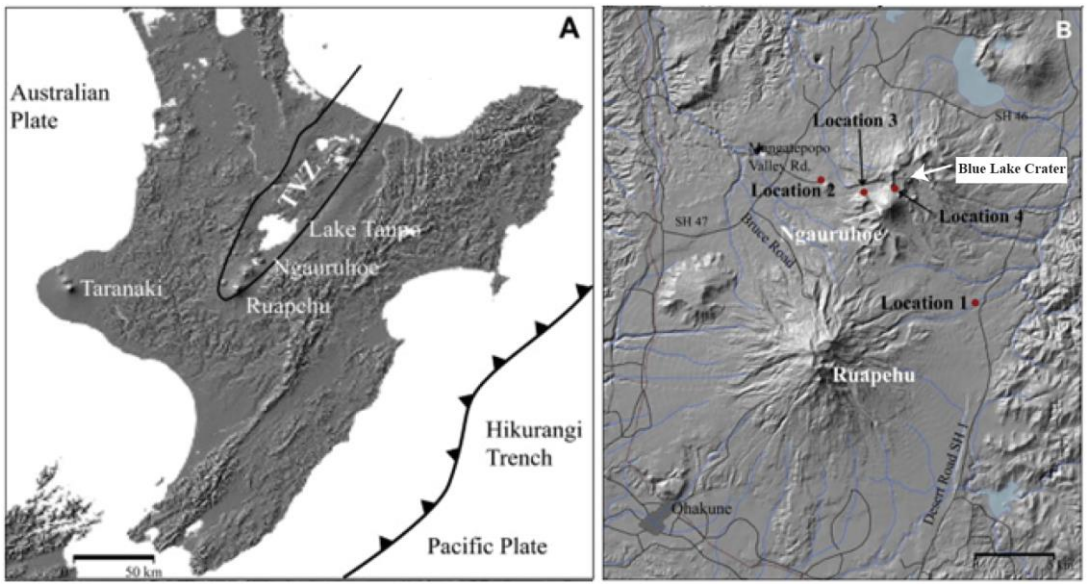

Figure 1.1. Digital Elevation Model (DEM) of the central North Island showing the boundary of the Taupo Volcanic Zone (TVZ), Ruapehu, Ngauruhoe, Taranaki and Taupo and their relationship to the top of the subduction zone (A). DEM of the Tongariro Volcanic Centre showing the main vents (B). Adapted from Möebis *et al.* (2011).

Blue Lake Crater (BLC) represents one of 11 young vents that have been active on Tongariro since ~25 Ka, (others include the recently active Te Maari craters, North Crater, Emerald Lakes, Red Crater, Tama Lakes and Pukekaikiore). The eruptives of these young (post-glacial) vents lie in a NNE-trending alignment over a major basement fracture within a graben defined by normal faults (Nairn *et al.* 1998). BLC lies at the northern end of the Tongariro complex, adjacent to North Cone at an elevation of ~1700 m. It is a wide, seemingly shallow crater lake with thin flank deposits that thicken on the northern side. Little is known about the eruptive activity of Blue Lake. The most recent eruption is thought to have occurred anywhere between ~14 - 10ka (Topping 1973; Dongahue 1995; Nairn *et al.* 1998) although this is contentious among volcanologists. It remains unclear,

however, when activity began at BLC, and exactly which eruption produced the crater that has now filled with water.

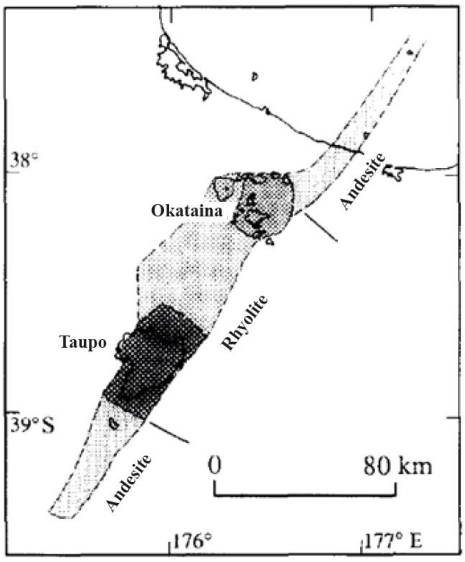

Figure 1.2. Map showing the position of TVC and geospatial distribution of magma types. Adapted from Sutton *et al.* (1995).

1.4 Previous Work

1.4.1 19th Century Literature

The first published accounts of activity at Tongariro appeared in the journal *Nature* in 1870. An account by J.D. Hooker records an eruption from Tongariro beginning in April 1869 that continued until mid-July. Explosions occurred every 5 minutes producing ash clouds, lava flows and bursts of magma jets that were witnessed as far away as Taupo (Hector 1870). This event is thought to have originated from the vents at Te Maari, and this was later confirmed by Dibble *et al.* (1985). The only description of the Te Maari craters before the eruption of 1869 exists in the form of a field notebook written by Sir James Hector who visited Te Maari on 23 November 1867. Hector called the lower crater the 'great Ngawha', and described a brown-coloured lake and a mound of white sinter about 200 ft across (Gregg 1960a, 1960b). Subsequent descriptions (i.e. post 1890) do not mention this sinter mound which suggests that is was destroyed in the eruption of 1869. In Hector's account the slopes were covered in sinter fragments but no scoria was evident.

A second Te Maari eruption was witnessed by H. Hill in 1882. The Te Maari craters also released black ash clouds at the time of the Tarawera eruption (Hill 1891). Hill (1891) described the TgVC volcanoes as 'special features both curious and suggestive to the student of volcanology'. He estimated the depths of the crater shafts by rolling boulders into them and listening for their bounces as they toppled down. Hill (1891) gave an account of the eruptions of 1892, describing a fresh vent located at the lower Te Maari crater as an 'enormous fissure'. Friedlander (1898) provided a beautifully detailed eyewitness account of another eruption at Te Maari on December 11, 1896. Friedlander was camped about an hour's distance below the Ketetahi Hot Springs when his camp was awakened by a thunderous noise. He described a gigantic pillar of ash with a 'wonderful display of many kinds of light phenomena', including incandescent boulders reflected through the steam, lightning and blue flames. He compared the eruptions to that of activity witnessed from eruptions from Vulcano (Friedlander 1898).

1.4.2 20th Century Literature

What could be called the first modern day scientific studies, began in the 1960's. Gregg (1960a, 1960b) illustrated the tectonic setting of Tongariro. He emphasized how the fault traces were aligned in the same NE-SW trending zone as the volcanic vents. Gregg included mention of articles in the NZ Herald (5, 6 and 10 September 1927) that reported an ash eruption from Tongariro. He suggested this eruption may have been from the explosion pit in North Crater, although its location has never been definitively located (Griffin 2007).

Matthews (1967) described the proximal units near Blue Lake and North Crater, describing them as welded agglomerates. He proposed this was created by lava-fountaining from a near-by crater. This agglomerate is particularly abundant on the slopes of North Crater. BLC and North Crater welded agglutinates show an assortment of mono-lithological clasts, 3-5 cm in diameter, of non-vesicular to weakly-vesicular porphyritic andesite (Matthews 1967). Accumulations are typically one of two colours, reddish or grayish. He notes that the degree of welding within the agglomerate units varies from layer to layer and from location to location. With weakly welded material, the rock surface appears knobbly and

coarse, allowing large clasts to be plucked from the outcrop. The agglomerate beds drape the topography and taper out with distance from the craters. He described the regional faults in great detail, and showed that apart from the poorly defined fault marked through Red Crater and the Emerald Lakes; faults are largely limited to the outer slopes of Tongariro.

The work done by Topping (1973, 1974) was, at the time, the most comprehensive study undertaken at the TgVC. Topping (1973)'s research of the Tongariro Subgroup (13.8 ka to present) used distal outcrops to identify source vents for the various formations and members. He used distal localities to identify and name the Mangamate Tephra Formation and its six members, including it as part of the Tongariro Subgroup. The Mangamate Tephra Formation comprises six andesitic tephras bounded unconformably by the rhyolitic Papanetu Tephra (at the base) and the Papakai Tephra Formation (at the top). The Papakai Tephra thickness distribution suggests that the major volume originated from the Ngauruhoe-Tama Lakes region and a minor amount from one of the northern Tongariro craters (Lower Te Maari, North Crater or Blue Lake). Several debris flows came down the Mangatipua Stream during deposition of Papakai Tephra, confirming activity from one of the northern vents. The volume of Papakai Tephra is about 1·5 km^3 (Topping 1973). Topping (1973) suggested that the source vent for the Poutu Lapilli Member was also possibly BLC (Figure 1.3). The Poutu Lapilli was ejected largely to the north of Tongariro. It is overlain by Papakai Tephra and conformably underlain by the Wharepu Tephra Member. It consists of finely vesicular grey lapilli and minor andesitic lava fragments. The iron-stained lapilli are bedded with little vertical change in grade-size. Topping's isopach map (Figure 1.3) for the Poutu Lapilli shows a tri-lobed distribution pattern pointing to the NW, NE and SE. The three lobe axes meet in the vicinity of Blue Lake, which Topping regarded as the most likely source. The volume of Poutu Lapilli is about 0·9 km^3. The formation was radiocarbon-dated using wood fragments preserved in peat deposits that gave a base age of 9780 ±170 yrs (Topping 1973). Topping's nomenclature remained unchallenged until 1995 when Donoghue *et al.* (1995) restructured the formations, formally naming the Pahoka Tephra, and defining it as the oldest member of the Tongariro Subgroup, chiefly because of its good regional distribution and easily identifiable characteristics (Donoghue *et al.* 1995).

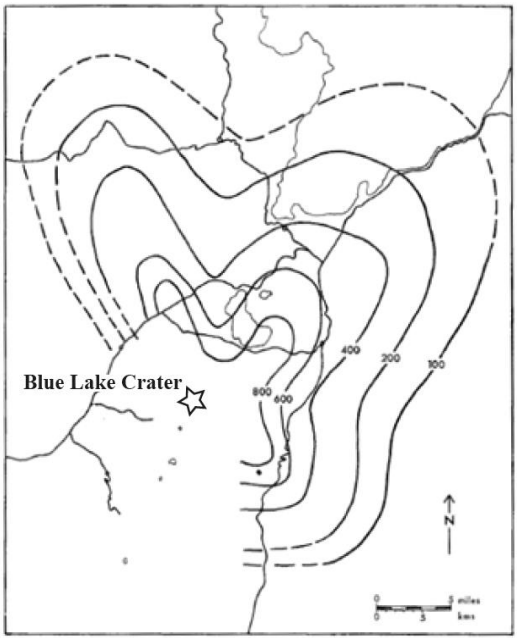

Figure 1.3. Isopach of Poutu Lapilli with Blue Lake suggested as a source. Adapted from Topping (1973).

Nairn and Self (1978) documented the atmospheric shock waves of the 1975 Ngauruhoe eruptions and investigated the pyroclastic avalanches that occurred. Cole (1978) presented the findings of his work on andesites of the TgVC. He confirmed two vent lineaments within the complex; an older NW-SE zone, and a more recent NE-SW trending zone.

Studies during the 1980s included Moore and Brock's (1981) discovery of a steam-dominated hydrothermal system below the volcano (the Ketetahi Hot Springs on the northern face of Tongariro being a surface expression of this). Hochstein (1985)'s research examined steaming ground around Te Maari and Red craters. Steaming ground (temperatures above 70°C) was also observed at the head of the central crater lava flows, which is the same elevation as the steaming ground beneath Red Crater. This is the result of an enhanced natural draught of steam which presumably moves laterally beneath the valley floor (Hochstein 1985). This steaming ground is at an elevation of 1775 m, making it the highest geothermal field in the TVZ. Cole *et al.* (1983) examined rare earth elements within the TVZ, finding that the TgVC basalts (only found on Red Crater) are low-Al, with LREE values similar to the andesites that they erupted through.

Graham *et al.* (1988) confirmed the make-up of the sedimentary sub-volcanic basement (based on buchitic metagreywacke xenoliths erupted from Ngauruhoe), as greywacke and argillite Mesozoic Torlesse basement.

Many influential studies were undertaken during the 1990s. Rogan and Blake (1994) confirmed, based upon trace element zonations in plagioclase crystals, that contamination and crystallisation has occurred in the magma system beneath Ngauruhoe. Donoghue *et al.* (1995) produced an in-depth study that revised the earlier work of Topping (1973) grouping all Tongariro eruptives into two groups; the Tongariro Subgroup and the Tukino Subgroup. Donoghue *et al.* (1995) identified a tri-lobed distribution for the Poutu Lapilli, with deposition NW, NE and SE of Mt Tongariro, suggesting a source at Blue Lake in agreement with Topping's estimate. Donaghue and Neall (1996) suggested that several of the Tongariro Subgroup tephras can be used as chronostratigraphic marker-beds. Further work by Cronin and Neall (1997) revealed that a number of lahar episodes had occurred; 15 from Ruapehu (>65 and 5ka), and five from Tongariro (>24 and 14 ka). A doctorate thesis by Hobden (1997) looked at K-Ar age determinations to understand the growth of the Tongariro complex. She was able to identify the times of rapid cone growth at Tongariro as being between 210-200 ka, 130-70 ka, and 25 ka to present. Hobden (1997) described the stratigraphy at Blue Lake, concluding that the spatter material had built up at a similar time to the one at North Crater. Further research by Hobden (1999) found that the complex plumbing system feeding Tongariro has produced numerous small (<0.1 km^3) and short lived (<1,000 yrs) magma batches.

Nairn *et al.* (1998) re-examined major pyroclastic eruptions from the TgVC since ~10 ka. They showed that multiple vents may have been active at the same time, all located within the NNE striking lineament. Increased activity in the last 10 ka was determined to be a result of accelerated rifting or extension that was occurring right across the complex. This event was not specific to Tongariro but was regional, with large rhyolitic tephras erupted from Taupo at the same time. Nairn *et al.* (1998) attempted to correlate distal tephras with their proximal equivalents. They were able to define probable source vents and proximal deposits for the Pahoka and Mangamate members, further redefining the original nomenclature of

Topping (1973) by joining the Pahoka and Mangamate into one formation, the PM Formation, to stress that they are part of the one eruptive sequence. The PM Formation consists of six named tephras and two unnamed tephras that were erupted from ~9 vents across the Tongariro massif around 10 ka (Nairn *et al.*1998). Nairn *et al.* (1998) considerably revised Topping (1973)'s vent locations by creating more complete maps that combined new proximal data with the distal material identified in earlier works. The PM2 Tephra (Te Rato Lapilli of Topping (1973) shows widespread dispersal to the NNE of the TgVC consistent with a short-duration event producing a high eruption column from a single main vent (Figure 1.4). Nairn *et al.* (1998) postulated that source may have been Half Cone, Red Crater, Blue Lake, or North Crater. The PM6 Tephra (Poutu Lapilli of Topping, 1973) was also revised (Figure 1.5). Previous isopach maps indicated at least three different wind directions, with intersection of dispersal lobes suggesting a source at BLC (Figure 1.6). Nairn *et al.* (1998) suggested that the main vent was not BLC, and that the thick welded scoria fall deposits associated with the formation of BLC are 10 ka in age.

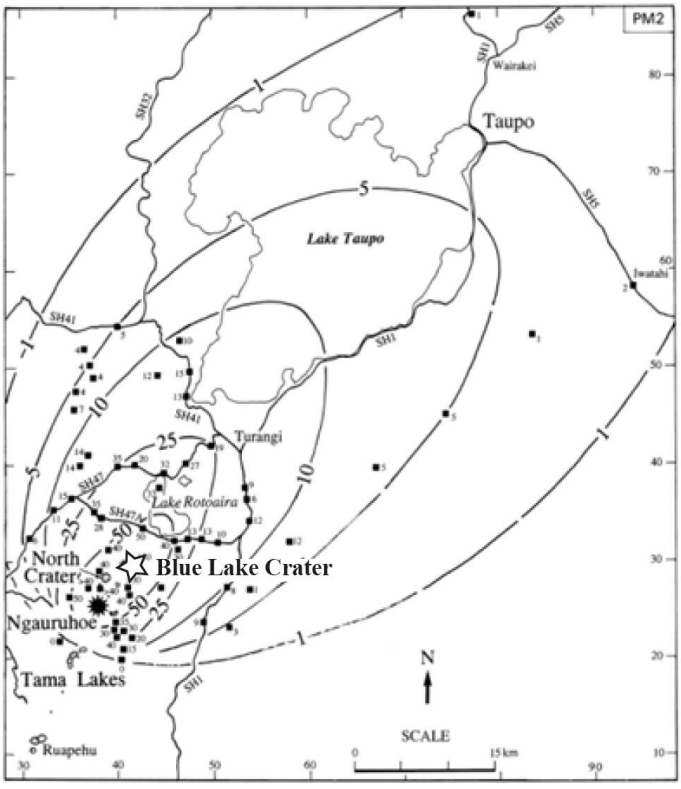

Figure 1.4. PM2 (Te Rato) tephra shows widespread dispersal to NNE of TgVC, consistent with an apparently short-duration event producing a high eruption column from a single main vent. Possible vent sites at Half Cone, Red Crater, Blue Lake, or North Crater. Adapted from Nairn *et al.*(1998).

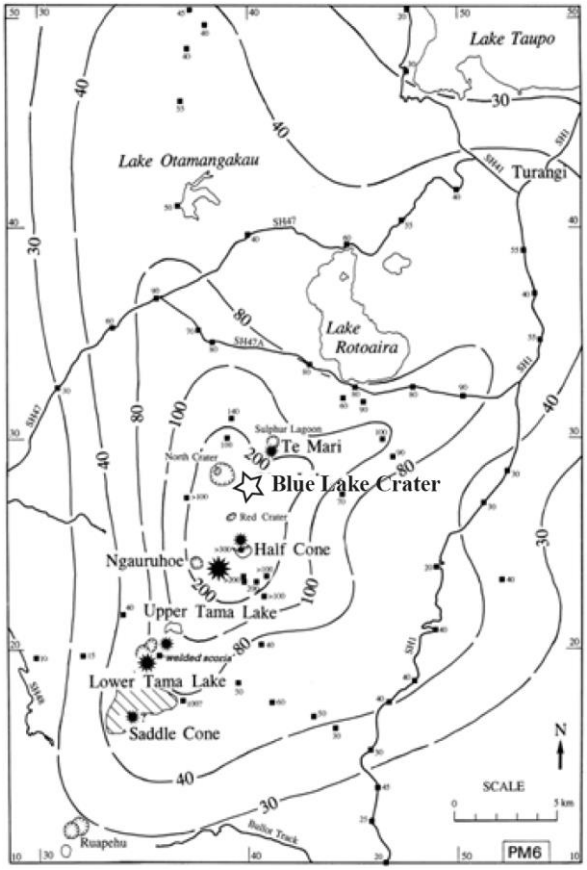

Figure 1.5. PM6 (Poutu) tephra, previous isopach maps indicated at least three different wind directions, with intersection of dispersal lobes suggesting a source at BLC. Data indicate that the main vent was not at BLC. Adapted from Nairn *et al.* (1998).

In a companion paper to Nairn *et al.* (1998) Nakagawa *et al.* (1998) examined the geochemistry of the PM eruptives. They discovered the formation can be divided into three petrological groups. The early group, PM 1 and 2, comprised of silicic andesites and dacites, including banded pumice. PM 3, the middle group, is dominated by basaltic andesite. The late group, PM 4, 5 and 6, comprises mainly basaltic andesite to andesite but the units are more basic and enriched in mafic phenocrysts. Nakagawa *et al.* (1998) also showed that crystallization of dacitic magmas was occurring at ~8 km depth, while andesite and basalt-andesite magmas crystallised at greater depths of ~>20 km.

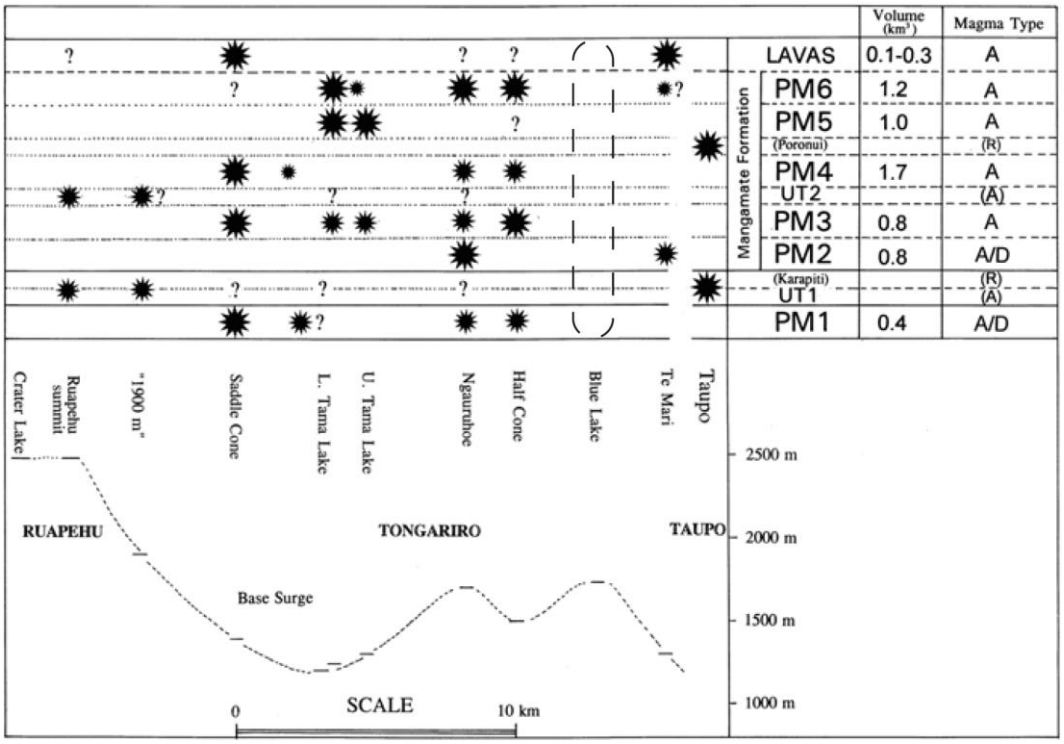

Figure 1.6. Relationships between vent locations and altitude for vents active during the PM eruption sequence. Main vents are shown by large stars, minor vents by smaller stars, uncertain vents by a question mark. Note that BLC is not assigned any PM Formation tephras. Magma types are A—andesite and basaltic andesite; D—dacite; R—rhyolite. Volumes are erupted tephra volumes calculated from isopachs. Adapted from Nairn *et al.* (1998).

1.4.3 21st Century Literature

The interest in the volcanic study of the Tongariro complex has continued into the 21st Century. Lecointre *et al.* (2002) showed that the Te Whaiau Formation located on the NW Tongariro ring plain is a massive debris flow, sourced from the area of the current summit of Tongariro. Hobden (2002) detailed the growth of the frequently active Ngauruhoe cone. The cone's history consists of numerous eruptive styles, including effusive, strombolian, vulcanian and sub-plinian. Hagerty and Benites (2003) investigated seismic activity beneath Tongariro. They found low frequency seismic events, tornillos that appeared to have similar waveforms to those recorded at Galeras volcano, Columbia, which were found to precede small to medium ash eruptions. The tornillos were first detected in June 2001 as part of routine monitoring. Further investigation showed a complex mix of seismic waves and identified a shallow epicentre below the Te Maari Craters. Rowlands *et al.* (2005) studied the tomography of Tongariro and were able to

identify pronounced sub-vertical low velocity zones extending 6–9 km depth below Tongariro (and Ruapehu) which were attributed to either remnant partial melt, hydrothermal alteration or thickened volcanic material (Rowlands *et al.* 2005).

Lowe *et al.* (2008) provided a description of the tephra marker beds from Tongariro in order to provide important fingerprint and age-model frameworks. Shane *et al.* (2008) helped to expand upon the poorly documented 26–16.6 ka interval of pyroclastic volcanism of the TgVC. This period is marked by three distal lapilli units (Rt1-3) exposed in ring-plain deposits. The Rt1-3 eruptions were from an open magmatic system consisting of one or more long-lived stagnant crystal mush zones, from which eruptions were rapidly triggered by new injections of mafic magmas from greater depths. A similar pattern of magmatic dynamics was observed in the much smaller 1995 eruptions of the neighbouring Ruapehu Volcano. Cassidy *et al.* (2009) used integrated geophysical investigation using gravity and magnetotelluric methods. Their data across the Tama Lakes saddle shows that the outcropping volcanic deposits are up to 800 m thick, underlain by Tertiary sediments (of a few 10's to a few 100 m in thickness), and in turn, lying above a basement of probable Mesozoic greywacke.

Price *et al.* (2005) investigated U-Th-Ra disequilibrium in andesitic lavas of Ngauruhoe. They found a correlation between eruption age and Nd and Pb isotopic composition. The oldest samples showed the least radiogenic isotopic ratios, indicating that Ngauruhoe U–Th disequilibrium is determined by variations in parental magmatic compositions in combination with assimilation and fractional crystallisation. Möebis *et al.* (2011) conducted a very thorough analysis and fine-scaled mapping of Holocene tephras on the ring plain of the TgVC, and used this information to document the comprehensive explosive eruption record over the last ~12 000 cal years. This provides the basis for correlating multiple tephra packages on the ring plains surrounding the TgVC, and for establishing a revised eruption frequency for each of the volcanoes. For example, new data show that Ngauruhoe began erupting about 7000 cal years ago, up to 4500 cal years earlier than previously thought (Möebis *et al.* 2011).

A number of Masters research papers have been produced by students of the University of Waikato in the last decade. Chizmar (2003) studied the nature and dynamics of explosive eruptions and associated crater formation at Tama Lakes. Bardsley (2004) described the physical volcanology of Red Crater. Basher (2005) investigated the Te Maari craters with particular emphasis of future risks. Basher (2005) noted the absence of any pyroclastic deposits, suggesting that Te Maari craters were not significantly explosive (sub-plinian). Griffin (2007) studied the products and processes of cone-building eruptions from North Crater. Krippner (2009) studied the changes in Ngauruhoe's crater summit between 1954 and 1975. Sanders (2010) investigated the properties and flow emplacement processes of the Ngauruhoe lava flows of 1954.

At the time of writing this thesis, a special issue of the Journal of Volcanological and Geothermal Research on the 2012 Te Maari eruptions was under production (unknown publishing date). Several articles were made available online early and were able to be incorporated into this research (e.g. Hurst *et al.* in press; Pardo *et al.* in press).

1.5 Thesis Outline

The remaining chapters of this thesis outline the physical, petrographic and geochemical properties of the proximal-to-vent deposits that surround BLC. Chapter 2 describes the geomorphology of BLC and the stratigraphy of the deposits. Chapter 3 describes the textural and petrographic characteristics of the proximal-to-vent deposits. Chapter 4 describes the geochemistry of the deposits and discusses the results of electron microprobe and whole rock x-ray fluorescence spectrometry. Chapter 5 discusses the origin of the BLC and establishes a history of activity. Magmatic processes of the proximal-to-vent deposits are discussed, as are eruption dynamics and post-depositional processes. A brief section on the potential hazards associated with BLC is included. Finally, the possible connections between BLC and Te Maari are discussed.

Chapter Two

Geomorphology, Stratigraphy and Facies Architecture

2.1 Introduction

This chapter describes the geomorphology, facies, and stratigraphy of Blue Lake Crater (BLC) and in particular its proximal-to-vent-forming deposits. Previous studies of the deposits (section 1.4) associated with BLC include Healy (1963) (1967), Topping (1973), Hobden (1997) and Nairn *et al.* (1998) however these have only addressed Blue Lake as a small aspect in their studies of the TgVC as a whole.

2.2 Methodology

Field work and sampling was conducted during February to May 2013 after acquiring a high impact research and collection permit from the Department of Conservation. 52 fist-sized rock samples were collected using a small geological hammer, with special care taken to preserve the natural aesthetics of the volcanic features as well as the Tongariro Alpine Crossing track. Activity was conducted with careful reverence to Blue Lake, which is held in sacred regard by the indigenous owners, the Ngati Tuwharetoa Iwi. A total of 36 site localities were visited. Stratigraphic logs were recorded at representative sites, and these form the basis for the stratigraphy of Blue Lake deposits presented in this research. Figure 2.1 shows GPS locations of sites and co-ordinate are recorded in Appendix One. One of the major aspects of this research was the construction of a geological map, which is presented in Figure 2.2. Regional unpublished map data acquired from GNS Science assisted in the development of the more detailed map of this study. GNS Science map data include preliminary results of regional mapping by G. Leonard and D. Townsend; and earlier unpublished maps across The TgVC by I. Nairn. The map produced in this study is focused on BLC eruptives and it maps individual depositional units. Wraps aerial images (2006) were used as the base map (at a scale of 1:10,000). Geological features were illustrated using Adobe Suite software and contour data was obtained from LINZ at 20 m intervals.

2.3 **Terminology**

The terminology used to describe the products and eruptive processes of BLC are based on Sumner *et al.* (2005) who classified chiefly 'hot' deposits produced by Hawaiian and Strombolian-style fire-fountaining. The key terms of Sumner *et al.* (2005) are discussed.

Spatter deposits are comprised of an accumulation of hot, fluid pyroclasts which agglutinate on landing (the resultant deposit becomes agglutinated). Clast outlines are partly or wholly retained. Spatter eruptions give rise to distinctive deposits and are the first step in complete coalescence of clasts to form lava in Hawaiian and Strombolian style fire-fountain eruptions. **Compactional welding** is the fusing together at point contacts and the subsequent compaction of particles under the influence of the overburden pressure in a still hot deposit. **Agglutination** is the flattening, sticking together, and gradual cooling of hot, fluid pyroclasts (spatter) as they land. Agglutination resembles compactional welding in that it involves strong shortening of vertical axis, and lengthening of horizontal axis of individual clasts. Agglutination differs in that the energy used during deformation is derived from the kinetic energy of the falling clast, rather than the weight of the overlying deposit. **Coalescence** is a process by which hot, fluidal spatter droplets form a homogeneous liquid in which the remnant particle outlines are destroyed. **Clastogenic lavas** are lava flows that have formed by the remobilisation of coalesced and agglutinated hot pyroclasts. They are typically fed by a lava fountaining and usually contain obvious traces of spatter fragments (Woolf and Sumner 2000). It must be noted that agglutination, coalescence, and post-depositional welding are part of a process continuum, and that deposits may transition from one facies to another quite gradually. These processes form a continuum of clast types ranging from:

i. cold brittle clasts such as scoria and spindle bombs,
ii. clasts with viscous/brittle rims and fluid interiors such as cowpat bombs,
iii. completely fluid clasts that agglutinate, splash or coalesese on landing,
iv. or clasts with a brittle core and fluid rim produced by recycling of clasts in the vent.

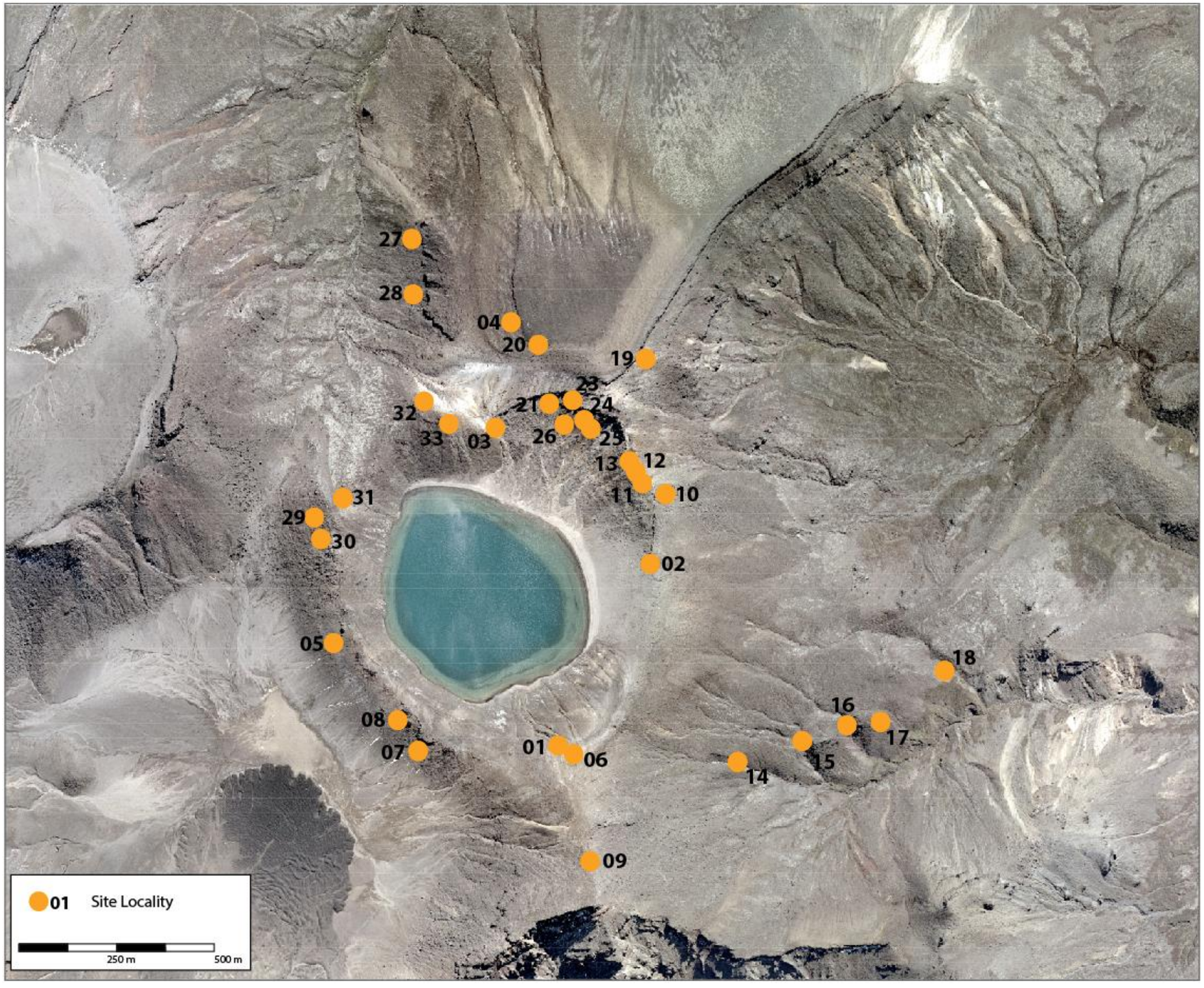

Figure 2.1. Site localities around the Blue Lake Crater study area.

Geological Map of Blue Lake Crater Study Area

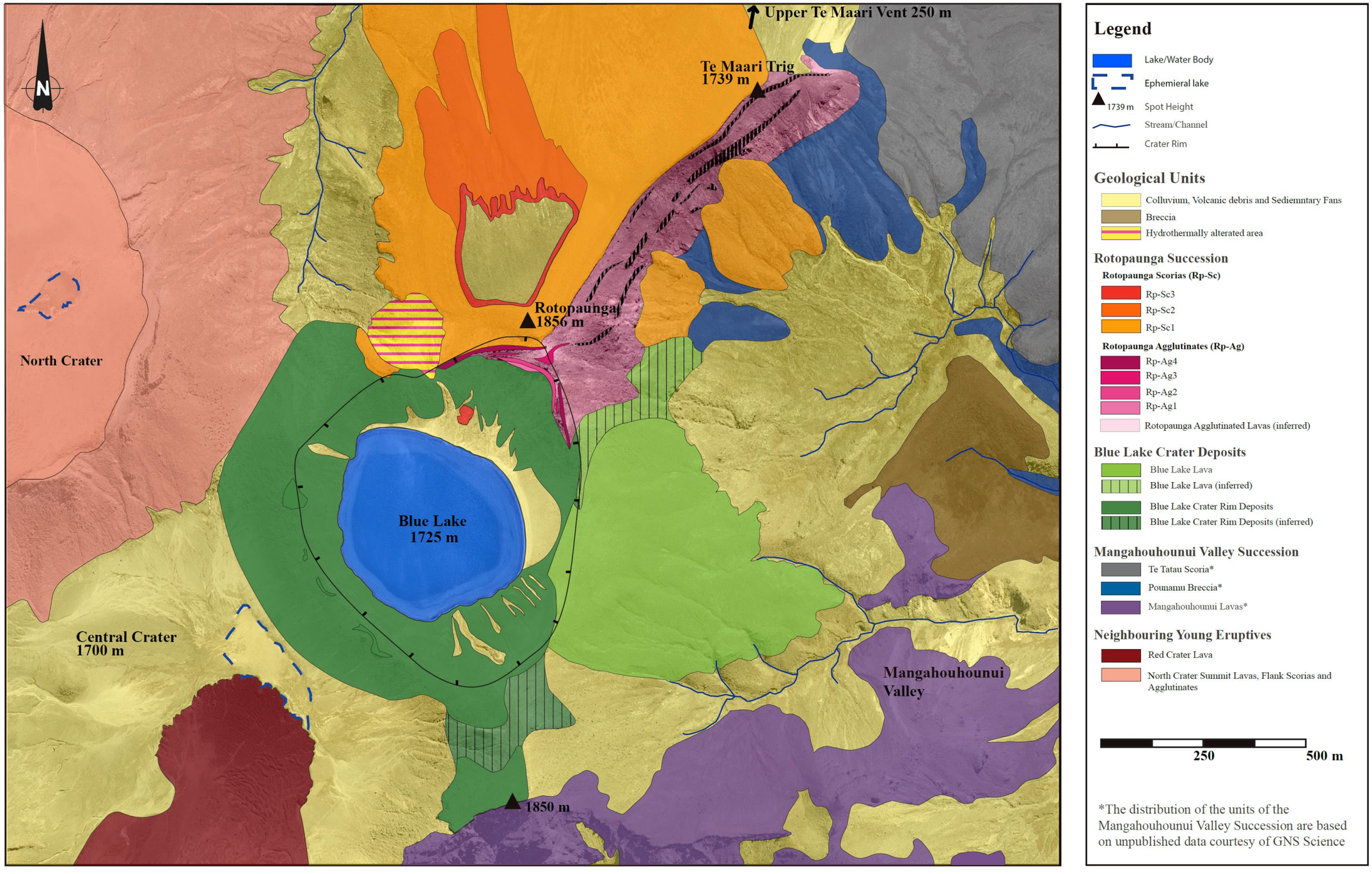

Figure 2.2. Map of the geology of the Blue Lake Crater study area.

2.4 Geomorphology of Blue Lake Crater

BLC is a small crater lake within the northern confines of the Tongariro summit complex (Figure 2.3). The crater rim is built from tephra and ranges in height drastically from 1740 m to 1856 m above sea level (a.s.l) elevation. The excavated vent is now filled with water and sediments. A small, roughly circular lake exists with a diameter of ~400 m and a depth of ~16.5 m (Hobden 1997). Blue Lake is a cold lake but is noticeably acidic (pH of 3.1-5.2) (Michaelis 1981; Hochstein 1985; Hobden 1997).

Figure 2.3. Aerial view of BLC and surrounding young vents looking south, Ngauruhoe and Ruapehu can be seen in the background. Adapted from Roscoe (undated).

To the west, BLC is adjacent to the young cone North Crater (1863 m a.s.l), (Figure 2.3, Figure 2.4, Figure 2.5) which is a large, flat-topped cone with slope angles similar to those of most stratovolcanoes ~30°. BLC and North Crater are divided from one another by a small valley running north. BLC's western rim at its highest location is 1785 m a.s.l (Figure 2.4). The western rim has an outer slope angle of 22°, with the inner slope slightly steeper at 28° (Figure 2.6).

The southwest crater rim of BLC lies above the glacially-shaped feature known as Central Crater (Figure 2.5, Figure 2.6 Figure 2.7) which sits at an almost uniformly flat 1700 m a.s.l. Several lava flows from Red Crater to the south have flowed onto Central Crater, with the toes of one flow coming within 50 m of the southwest crater rim of BLC (Figure 2.2). The southwest crater rim is ~44 m above Central Crater. Here the inner crater has a gentle 14° slope while the outer rim has a slope angle of 21° (Figure 2.7) which shallows towards the floor of Central Crater.

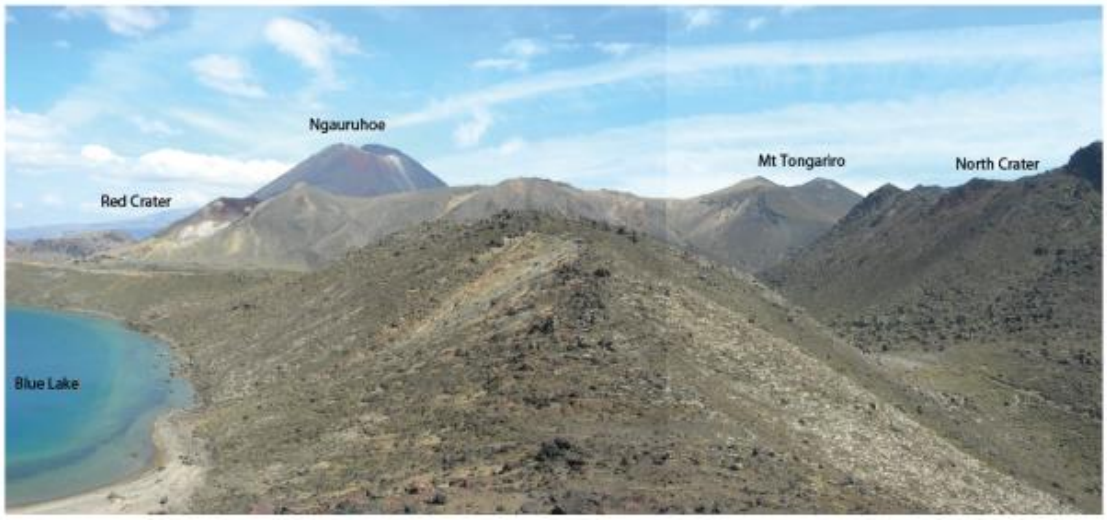

Figure 2.4. The western inner and outer rim of Blue Lake Crater looking south.

The south of BLC is dominated by what here is called the Central Crater Peak. (Figure 2.5) rising to1846 m a.s.l and forming part of the eastern wall of Central Crater. Steep cliffs drop away into the Mangahouhounui and Oterere vallies. This massif is primarily constructed of pre-glacial, volcanic edifice eroded off the northern NE Oturere composite cone, although a thin veneer of younger, welded pyroclastic deposits mantle the top (Figure 2.2).

The eastern crater rim of Blue Lake is perched at the top of the Mangahouhounui Valley (Figure 2.5) and it forms part of the valley's upper-crown. The crater rim is at its lowest here, 1740 m a.s.l (20 m above the lake) with a shallow slope angle of 13°. The outer crater wall drops away quite steeply (22°) down the Mangahouhounui Valley. A small-volume lava flow has breached the crater in this location and has travelled into the Mangahouhounui Valley.

The northern rim of BLC is dominated by the Rotopaunga massif, the highest point of the BLC rim (1856 m a.s.l, and 136 m above the lake surface). The southern-facing slopes of Rotopaunga form the inner crater wall at the base has a slope angle of 16° which steepens to 27° for the upper half (Figure 2.8). The outer flank of Rotopaunga drops away towards the ring plain, and is a part of the northern flank of the Tongariro complex. The eastern flank of Rotopaunga is capped by 20 m high bluffs that then steeply drop into the Mangahouhounui Valley. These bluffs extend from BLC northwards to the Te Maari trig (1739 m a.s.l), very close to the active Te Maari craters that lie ~1 km to the north of BLC and are ~500 m lower in elevation.

It is difficult to determine the pre-BLC topography. Most likely it was irregular, with BLC perched between the Mangahouhounui Valley and Central Crater. Te Maari Trig was also a likely feature pre-BLC activity.

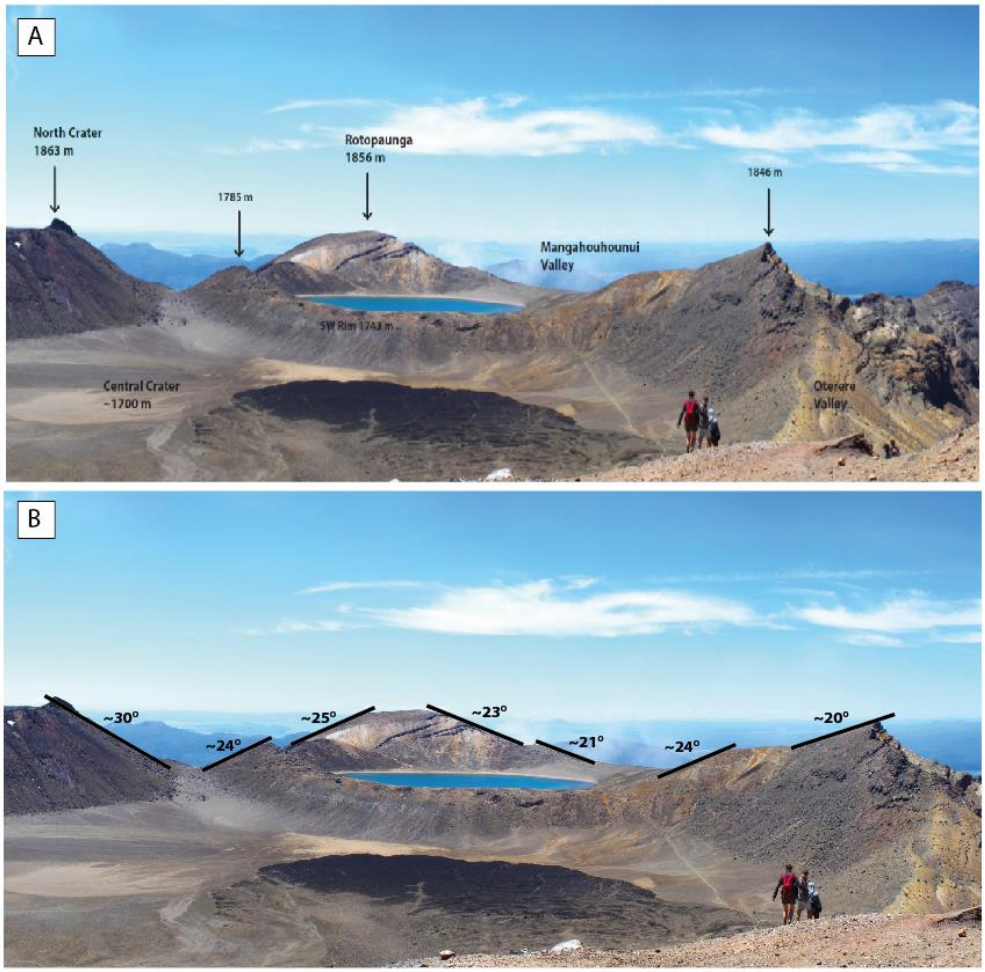

Figure 2.5. BLC study area showing major topographic controls. (A) Elevation in m a.s.l. (B) Slope angles of the major topographic features.

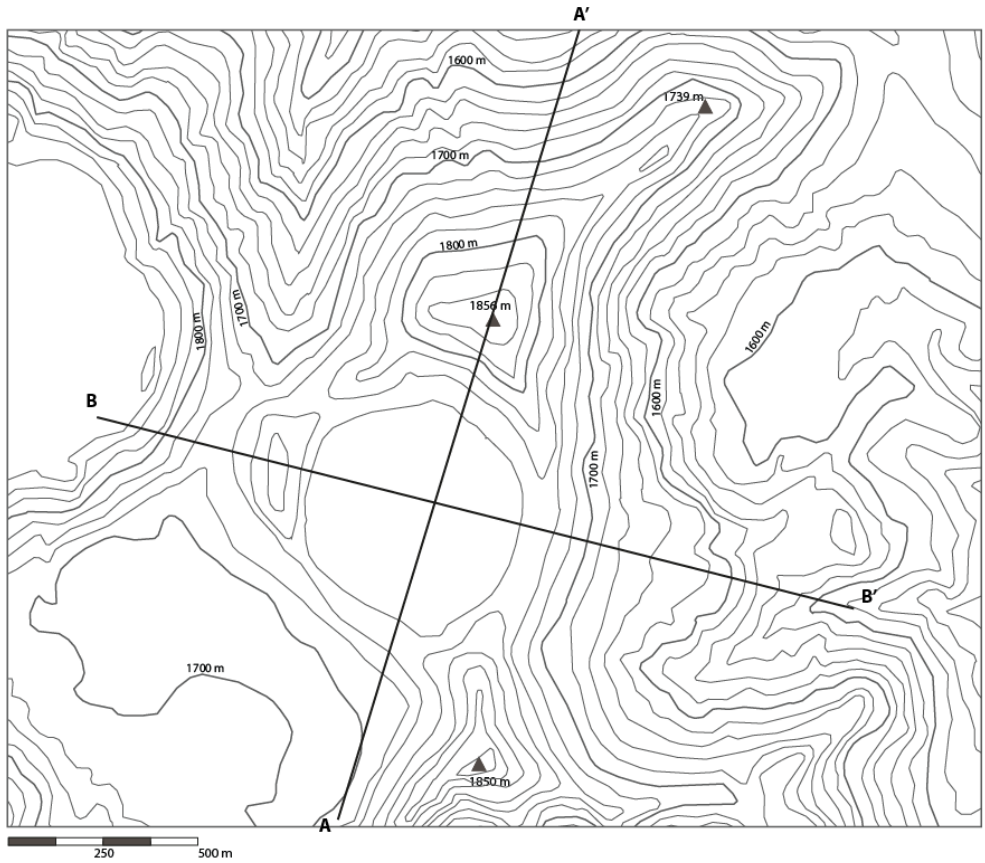

Figure 2.6. Topographic contour map of the BLC study area. Peaks are represented by triangles with spot heights. Cross sections A-A' and B-B' are used in Figures 2.7 and 2.8 below to illustrate slope profiles.

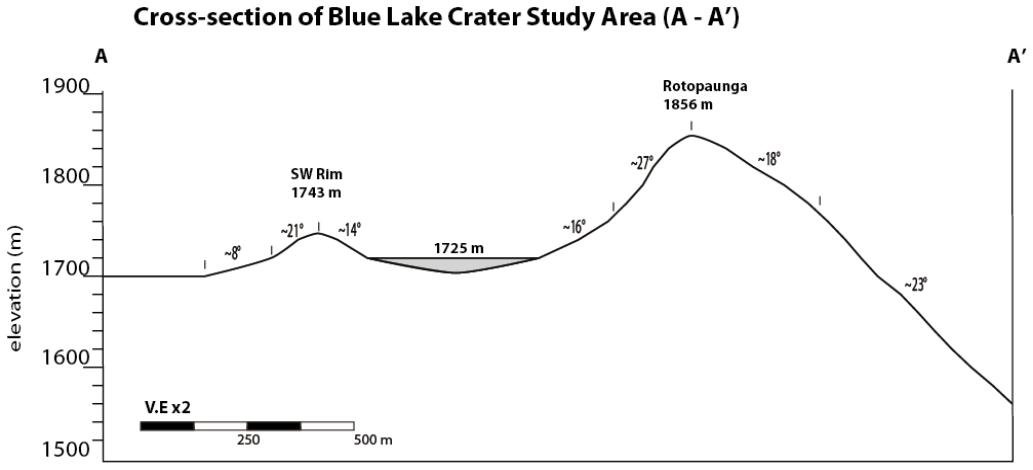

Figure 2.7. Cross section of BLC rim from A-A'. The northern rim of BLC is the highest point (Rotopaunga at 1856 m a.s.l), with the southwestern rim 113 m lower in elevation.

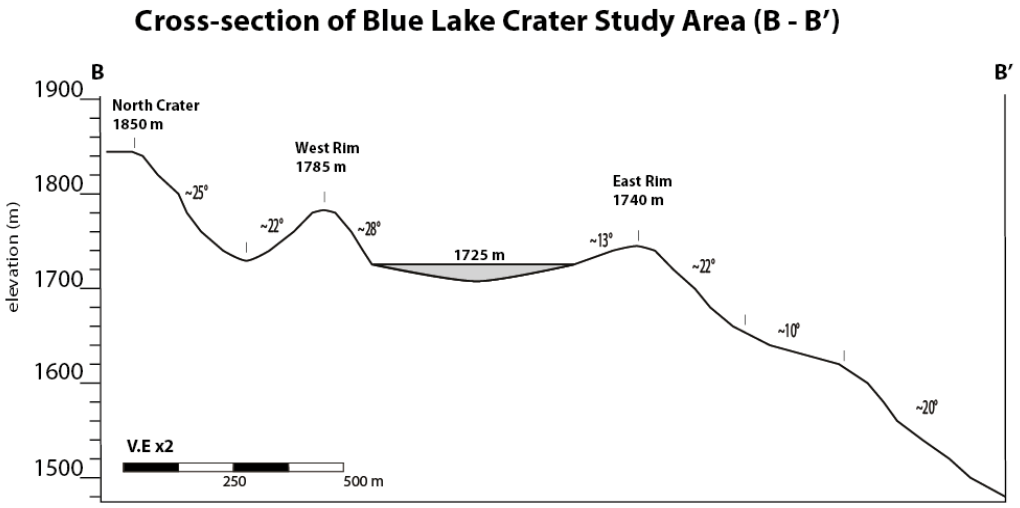

Figure 2.8. Cross section of BLC rim B-B'. The valley between North Crater (1850 m) and the western rim (1785 m) can be seen. The eastern rim (1740 m) drops away down the Mangahouhounui Valley.

2.5 Lithofacies of the Crater Rim

2.5.1 Intensely Welded Lithofacies

This facies consists of intensely agglutinated and welded, dense, massive, light to dark grey porphyritic andesite (Figure 2.9). Outcrops range in thickness from <2 to 8 m. The key feature of this facies is that it is generally coherent with no clasts or clast outlines visible. Rare small xenoliths occur and are typically 1-5 cm in size, light grey and angular. Irregular metre-scale (1-2 m) blocky jointing occurs in outcrop, with some sub-columnar jointing in thicker outcrops.

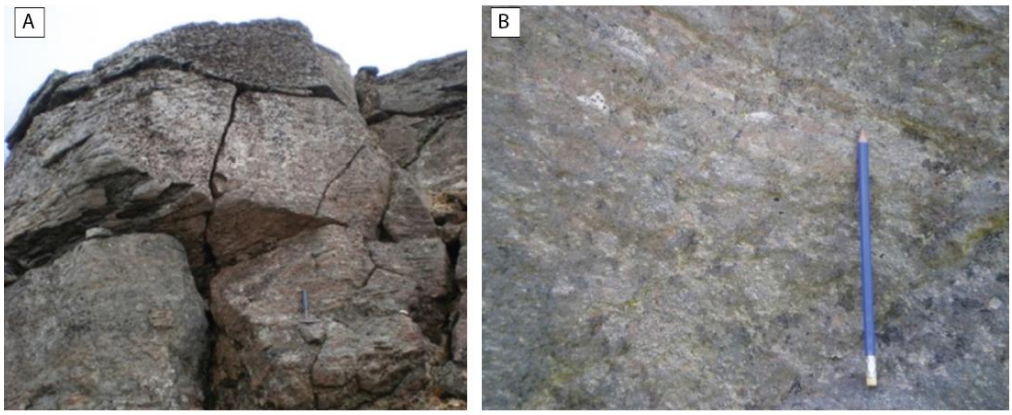

Figure 2.9. Intensely welded facies; (A) in outcrop; and (B) a close view of the internal features, highlighting the lack of clast outlines and homogenous appearance.

This facies is often platy in appearance, sometimes showing a very even-jointed, 5-30 cm size, brick-work-like pattern. Sometimes the unit is platy throughout its entire thickness (Figure 2.10). At other times this facies may have banding and ribbon-clasts which appear as grey, brown and/or yellow bands, often 2-20 mm thick (Figure 2.11). The banding can be horizontal or wavy with some deposits on the south rim showing very intricate patterns. The banding is laterally discontinuous with individual bands not lasting more than 5 m.

Figure 2.10. Platy-jointing within the intensely welded facies. Here the entire thickness is platy.

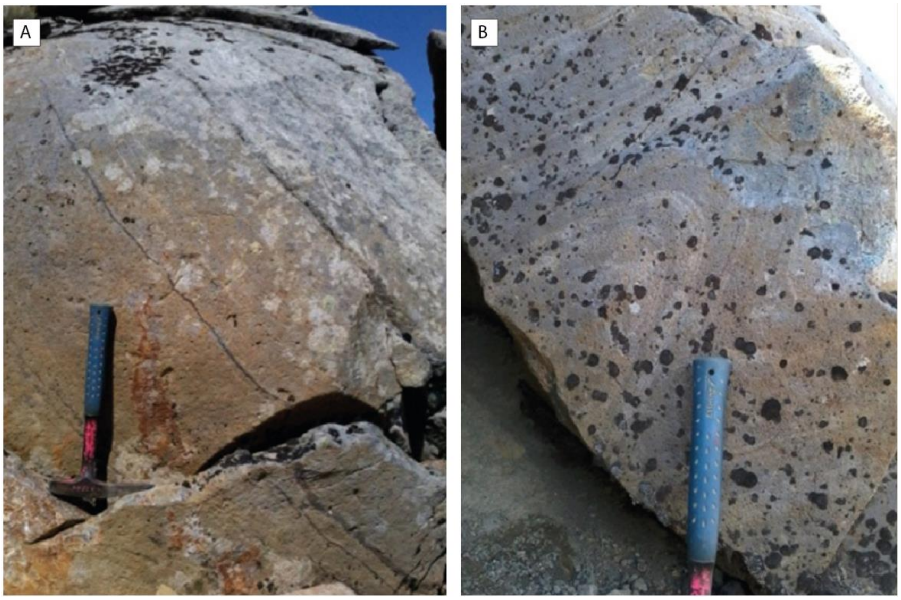

Figure 2.11. Variation of intensely welded facies showing thin ribbon-clasts. Bands display a range of colours. Some bands run parallel (A) others show intricate folding patterns (B).

The mode of origin for this facies is rapid spatter/still-hot-fluid particles accumulating by way of near-vent fire-fountaining undergoing post depositional movement and shearing of the still hot accumulate (Woolf and Sumner 2000; Sumner *et al.* 2005). The facies is interpreted to have involved processes including agglutination, coalescence, welding (Sumner *et al.* 2005). Banding and ribbon clasts are interpreted as hot fluid clasts that, after deposition, are stretched thin due to intense shear stress.

2.5.2 Strongly Welded Lithofacies

This facies consists of strongly agglutinated and welded, dense, massive, light to dark grey porphyritic andesite. This facies may be massive to weakly bedded, which is exaggerated by clast horizontality. This facies differs from the previous facies (intensely welded) via a few subtle textural differences (which indicate different eruption and emplacement dynamics). In the strongly welded facies clast outlines can be seen (Figure 2.12) and are typically feint, and always appear elongated and lens-shaped. They can be recognised by their different colour-tones to the massive body of the deposit. The facies contains pinkish, reddish and/or grey lensoidal clasts 2-10 cm thick and up to 1 m wide, with many fiamme-like smears at the clast boundaries. Flattened clasts and lamellae lie parallel to the underlying slope and indicate syn-depositional flow. This facies may occupy most of the thickness of a unit, or may occur as thin (0.1-1 m) layers within less intensely welded facies. Jointing in thick outcrops is typically blocky, 0.5-1 metre scale, with very crude sub-columnar joints. This facies can be platy, but the plates are less well-developed compared to intensely welded facies.

The mode of origin for this facies is rapid spatter/still-hot-fluid particles accumulating by way of near-vent fire-fountaining. Post depositional movement and shearing of the still hot accumulate occurs to a lesser degree than the intensely welded facies (Wolff and Sumner 2000; Sumner *et al.* 2005). Welding in this facies has not undergone near complete coalescence/cohesion, although smeared and lensoidal shaped clasts are still present (Wolff and Sumner 2000; Sumner *et al.* 2005).

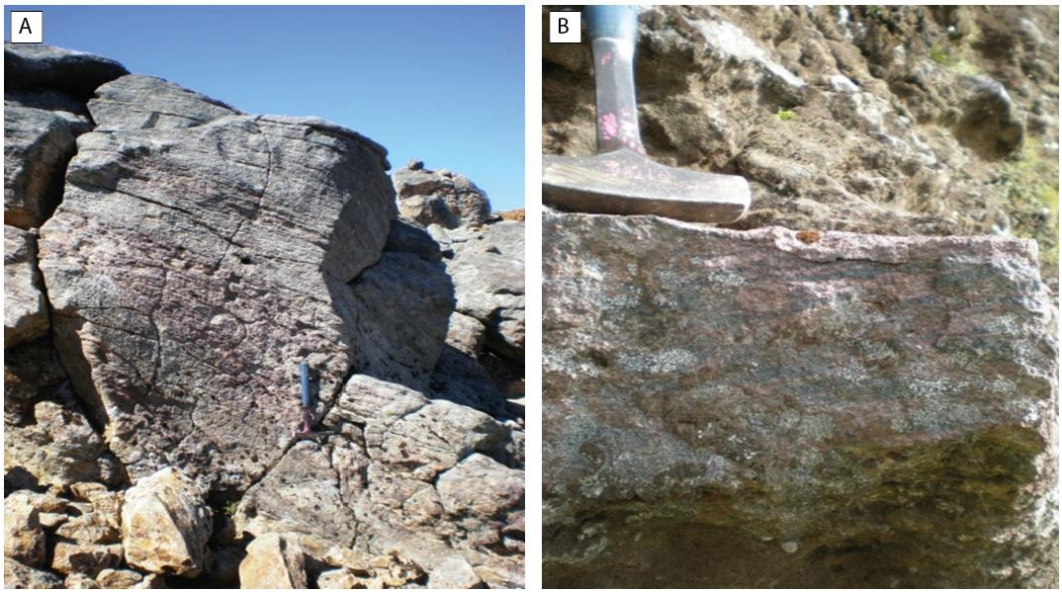

Figure 2.12. Strongly welded facies (A) in outcrop showing visible smeared clast outlines and fold structures; and (B) a thin layer of strongly welded facies within a scoria deposit with darker, grey lens-shaped clast outlines visible.

2.5.3 Moderately Welded Lithofacies

This facies consists of moderately agglutinated and welded grey porphyritic andesite. The facies is generally massive/structureless, although some crude bedding, and grading exists. It shows little evidence of coalescence as clast outlines are visible and range in size from lapilli to bombs and blocks; and are shaped from flattened spatter to brittle clasts (Figure 2.13). Spatter clasts are typically elongate, parallel cowpat bombs that are compacted together and lie parallel to the depositional surface. Brittle clasts are typically 5-20 cm in size, sub-rounded, and more scoriaceous. Dense bombs occur sparsely throughout this facies. They are grey to black, highly porphyritic and range in size from 1 to 30 cm.

The dominant post-depositional process for this facies is compactional welding in sections comprised dominantly of scoria clasts, and more a combination of coalescence, agglutination and welding in sections dominated by spatter clasts (Wolff and Sumner 2000; Sumner *et al.,* 2005). This facies formed as a consequence of pyroclastic fall from a high lava fountain, with some particles allowed time to cool before deposition. The deposit must have retained enough heat, however, to weld the deposit in-situ (Wolff and Sumner 2000; Sumner *et al.*,

2005). Post-depositional movement is limited although some fluid flow features occur. No remobilization of the entire facies thickness has occurred.

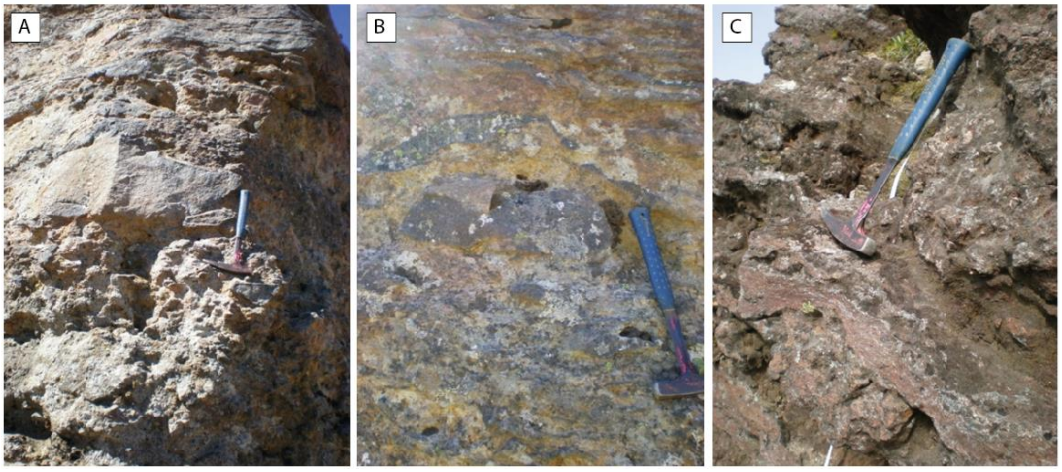

Figure 2.13. The variability of textures in moderately welded facies. (A) zones of brittle clasts in an agglutinate matrix. (B) A cow pat bomb draped around a rigid clast. (C) Thin layers of the facies within a predominantly poorly welded outcrop.

2.5.4 Non to Poorly Welded Lithofacies

This facies is comprised of non to poorly welded, massive to crudely bedded, bomb and lapilli spatter and scoria deposits (Figure 2.14). The facies ranges in thickness from 1-2 m to over 10 m and deposits are commonly poorly bedded. The dominant grain size ranges from coarse lapilli to bombs and blocks. Clast outlines are fully visible and dominated by intact brittle scoria clasts. Dense blocks and bombs range from 10 to 50 cm. The facies is either clast supported, or contains a matrix consisting of black/red coarse ash and lapilli. Fresh exposures of this facies are medium-dark grey, and where it is more weathered the rock has a rich red/orange hue. It is common for this facies to contain thin layers of more intensely welded facies (typically strongly to moderately welded). This facies varies over short distances and displays both normal and reverse grading.

The mode of origin for this facies is through the accumulation pyroclastic fall from a lava fountain, with particles allowed time to cool before deposition, while retaining enough heat to slightly weld in-situ (Wolff and Sumner 2000; Sumner *et al.* 2005). There is no evidence of any post depositional movement or flow. The

dominant process is likely compactional welding with very little to no coalescence or agglutination.

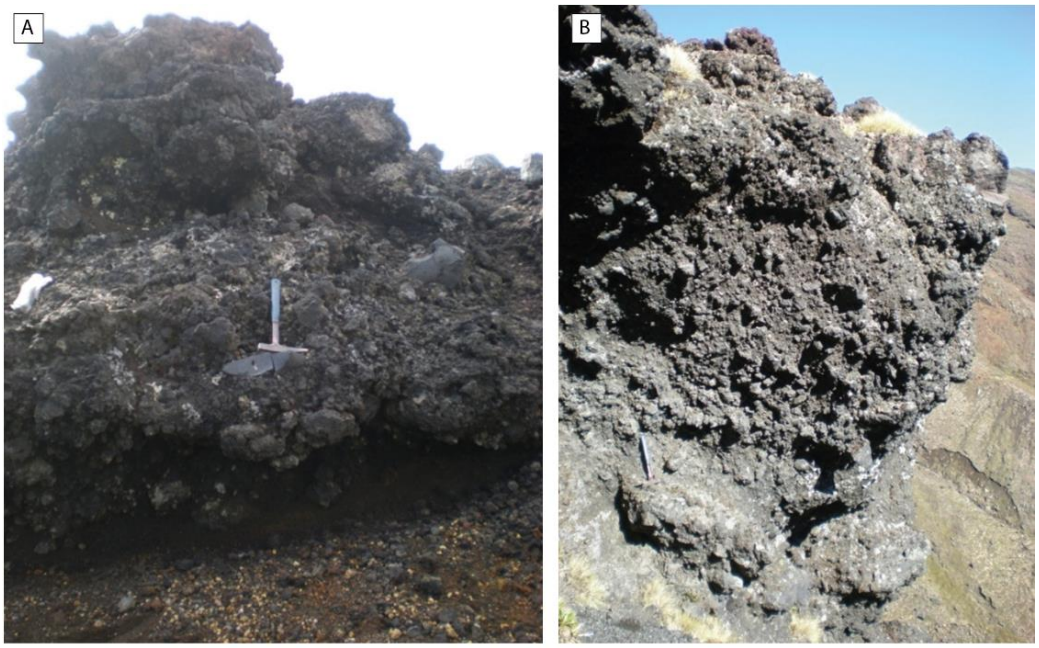

Figure 2.14. Non-poorly welded facies. (A) An outcrop comprised of poorly graded loose scoria and dense bombs (below hammer). (B) A massive non to poorly welded outcrop.

2.6 Lithofacies of the Blue Lake Crater Lava Flow

2.6.1 Autobreccia Lithofacies

The tops and bottoms of thick lava lobes are typically surrounded by an irregular zone (0.3 to 1 m thick) of light-dark grey, sub-angular to angular, moderately to highly vesicular, block sized clasts within a matrix of grey coarse lapilli and ash. Massive and poorly sorted, this facies grades upwards from the base of the flow into more coherent zone of blocky, highly jointed, less vesicular material (Figure 2.15). Occasionally there is inter-fingering of breccia clasts and dense lava at the flow front. The breccia at the top transitions downwards into coherent lava, however it is often obscured by vegetation and colluvium, or removed, and is typically less than 0.4 m thickness (Figure 2.15B).

A'a'-style autobreccia results from the viscous tearing of the cooling lava that forms scoriaceous rubble on the flow surface (Figure 2.16) (Cas and Wright 1987). Rubble layers result from cooled, spiny lava on top of, and along the steep front, of an advancing flow. The jagged flow front creeps forwards and steepens until small and large sections break off, and roll ahead of the flow. This repeated collapse of the flow front produces a rubbly layer over which the flow moves (Cas and Wright 1987; Kilburn 2000; Vergniolle and Mangan 2000).

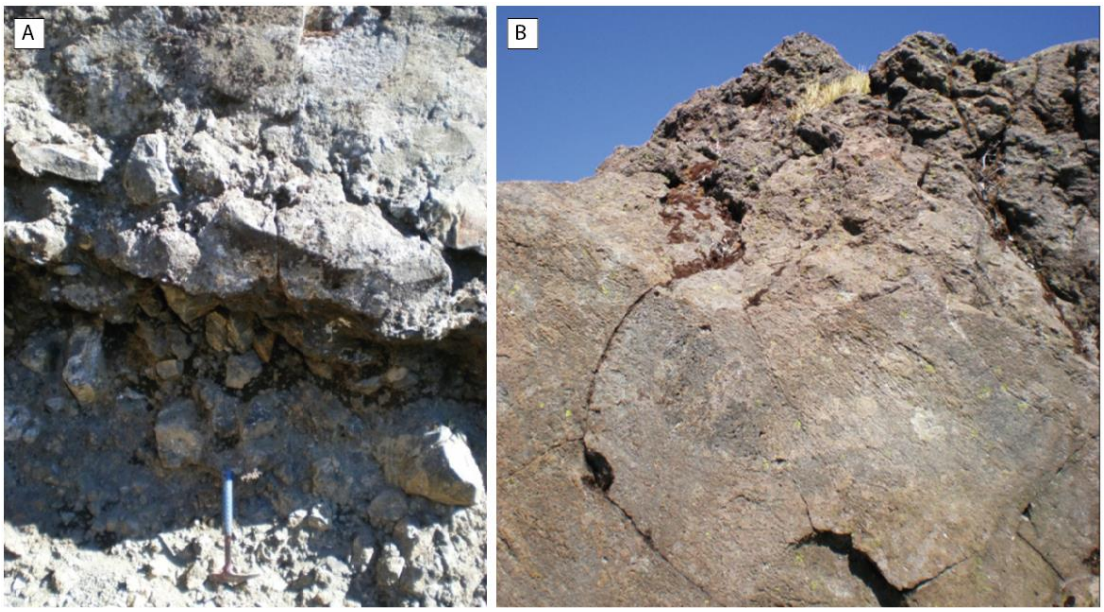

Figure 2.15. Autobrecciated lava facies at (A) the base of the flow and (B) the top of the flow.

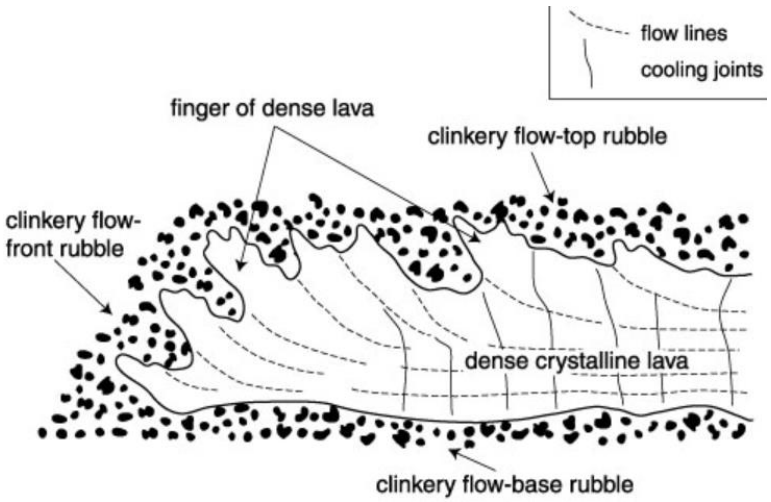

Figure 2.16. The main structural components of an A'a lava flow in vertical section. Adapted from Cas and Wright (1987).

2.6.2 Crystalline Lava Lithofacies

This facies consists of dense, massive, light to dark grey crystalline lava (Figure 2.17). Jointing is typically blocky, 0.3 - 1 m scale, with very crude sub-columnar joints in thick outcrops. Occasionally very feint clast outlines can be seen and appear elongated and lens-shaped. Rare xenoliths, typically 1-5 cm in size, can be seen in the rock face. In some locations the base of this facies has a zone of flow banding often 2-20 mm in thickness, with bands of ~1 cm in thickness. Banding can be horizontal, wavy or folded.

The likely mode of origin for the lava is from intense fire-fountaining, generating still hot fluid clasts that coalesce and remobilize down slope due to the intense heat. Crystalline lava forms in the core of the flow as it travels, and is not rapidly cooled, forming vertical cooling joints (Figure 2.16) (Cas and Wright 1987; Kilburn 2000; Vergniolle *et al.* 2004).

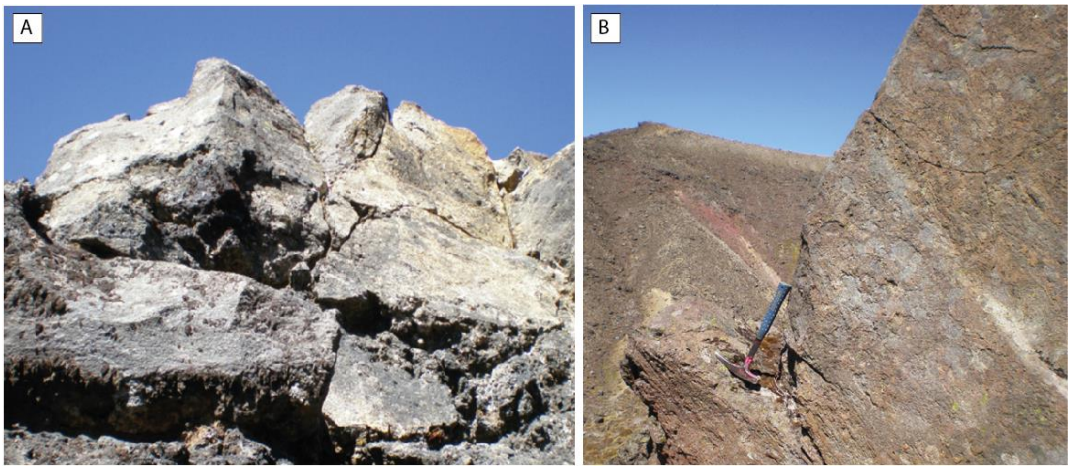

Figure 2.17. Crystalline lava facies. (A) Blocky jointing with vertical cooling and interfingering of autobreccia. (B) A zone of flow banding at the base of the facies (below hammer).

2.7 Stratigraphy of the Proximal Deposits of Blue Lake Crater

2.7.1 The Rotopaunga Succession

Dominating the northern rim of BLC is the volcanic massif, Rotopaunga. The massif rises 136 m above the lake and forms the northern inner-wall of BLC (Figure 2.7). The basal half of Rotopaunga is obscured by talus fans. It is

presumed that the bulk of the lower portion of Rotopaunga is comprised of old flank lavas and pyroclastic deposits from the Mangahouhounui Formation. The upper half of Rotopaunga is comprised of a succession of four thick, welded and agglutinated lava units, here named the Rotopaunga-Agglutinates (Rp-Ag), followed by three moderately to poorly welded scoria beds here-named the Rotopaunga Scorias (Rp-Sc).

2.7.1.1 The Rotopaunga Agglutinates (Rp-Ag)

The Rotopaunga Agglutinates consist of four agglutinated and welded, coherent, coalesced, andesite lava-like deposits. The units form thick, long exposures that drape over Rotopaunga to form an arc from W to E (Figure 2.18). Units range in thickness from 2-9 m and are thickest and best exposed in the middle of Rotopaunga (Figure 2.19). The units are much thinner where they sit on top of the rim exposed. The agglutinates occur at ~1795 m to ~1842 m a.s.l. The deposits range from intensely to moderately agglutinated facies and vary greatly over short distances between these facies. Complete units are typically platy jointed at the top, massive with sub-columnar jointing in the middle, with a basal ~ 1 m of lapilli to block sized loose, angular clasts. Units are numbered Rp-Ag1-4, beginning from the lowest stratigraphic unit. Due to the geometry of the deposits is most likely that the Rotopaunga Agglutinates are not sourced from BLC (this is discussed in Chapter 5).

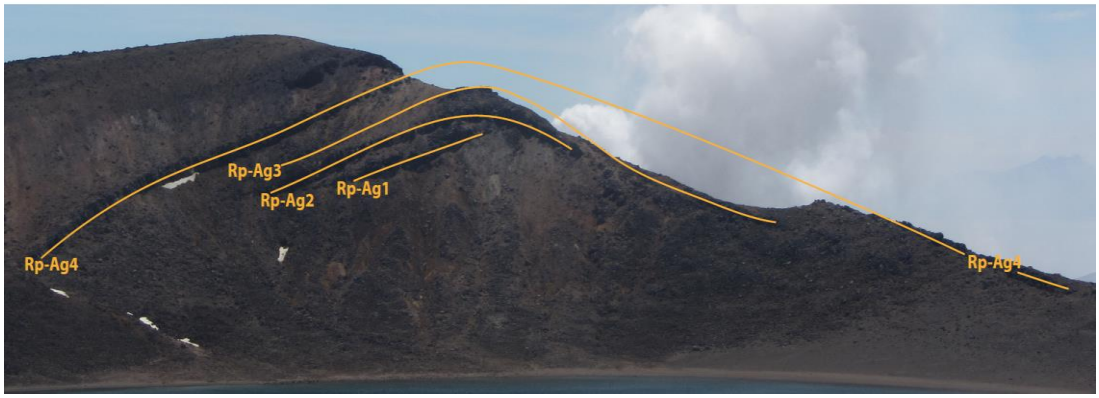

Figure 2.18. View of the northern BLC inner wall. Rotopaunga Agglutinate units Rp-Ag1, Rp-Ag2, Rp-Ag3, Rp-Ag4 are highlighted by yellow lines and their extent is traced across the gap in Rotopaunga.

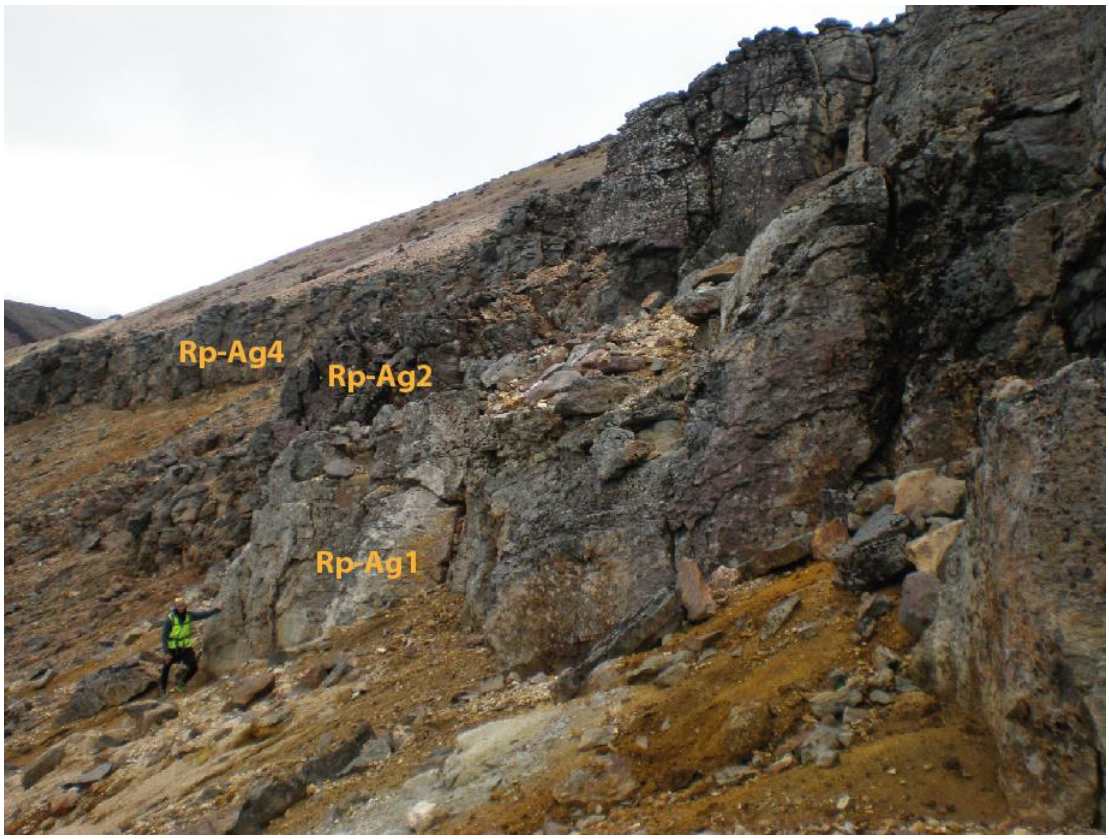

Figure 2.19. Rotopaunga Agglutinate units; Rp-Ag1, Rp-Ag2, and Rp-Ag4. Field assistant Jai Davies-Campbell for scale.

Rp-Ag1 (Unit 1)

Rp-Ag1 is exposed laterally for 80 m (Figure 2.18) and has a maximum thickness of 7.3 m at site 25 (Figure 2.20).The unit begins with 4 m of intensely to strongly welded, grey porphyritic facies with blocky to sub-columnar jointing. This transitions into 4-5 m of moderately welded facies with minor platy jointing. The unit becomes strongly to intensely welded in the upper 2.4 m. Contact between the top of Rp-Ag1 and the base of Rp-Ag2 is not visible. No basal exposure was observed and it is unknown what underlies this unit.

Rp-Ag2 (Unit 2)

Rp-Ag2 is exposed laterally for ~230 m and forms an impressive arc over Rotopaunga (Figure 2.18). It has a maximum thickness of 7.4m. The unit displays considerable variation over its lateral extent although it is generally more intensely and strongly welded on the western side of the BLC northern inner rim.

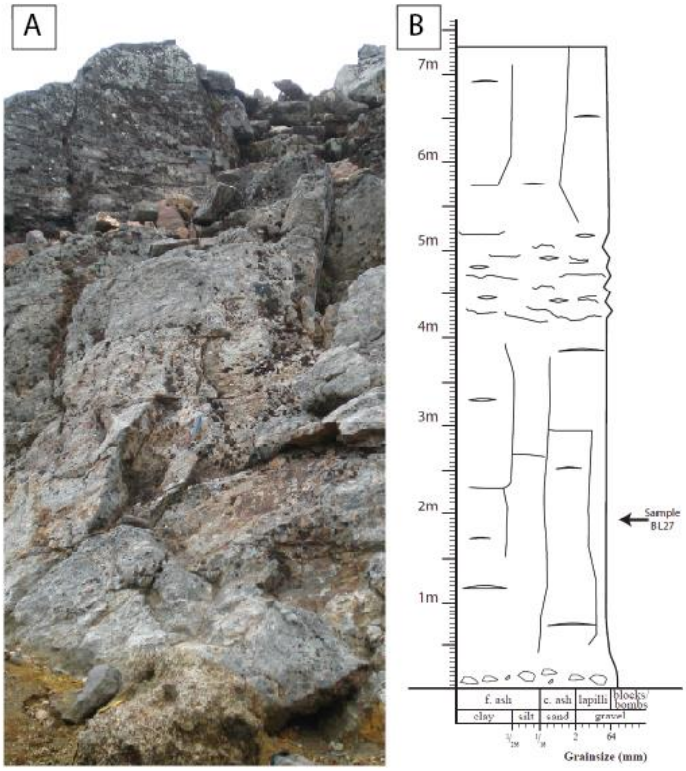

Figure 2.20. Exposure of Rp-Ag1 outcrop at Site 25. (A) Photograph. (B) Stratigraphic log. See text for description.

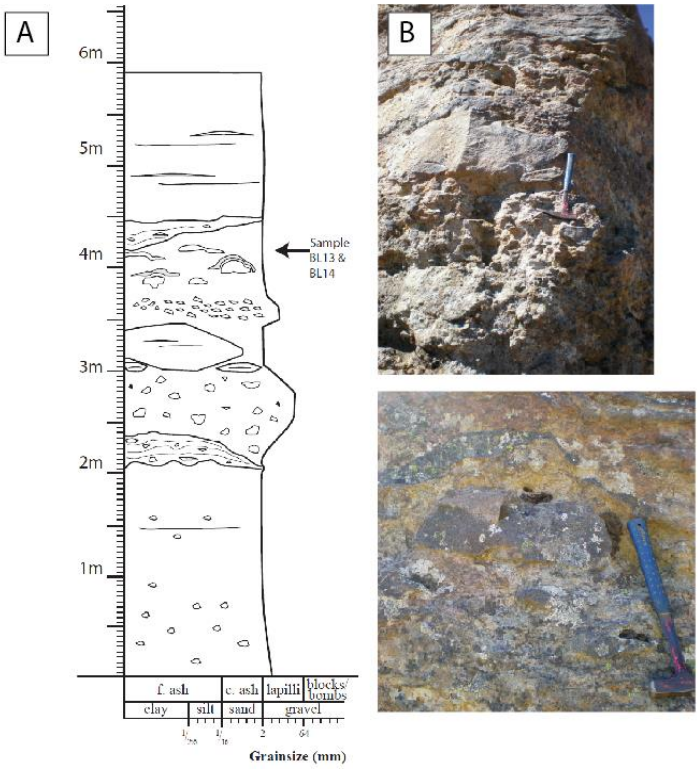

Figure 2.21. Rp-Ag2 at Site 13. (A) Stratigraphic log. (B) Rp-Ag2 in outcrop and a close up view showing an angular clast with a cow-pat bombs draping over it.

Site 13 describes a typical outcrop on the eastern side (Figure 2.21). The lower and upper 2 m of the unit is comprised of strongly-intensely welded material, while the middle 2 m consists of a complex inter-mixing of moderately welded spatter, with pockets of intensely and strongly welded facies interspersed throughout. Crude grading changes can be seen, with zones of fluid cow-pat bombs draping over angular clasts at ~4 m.

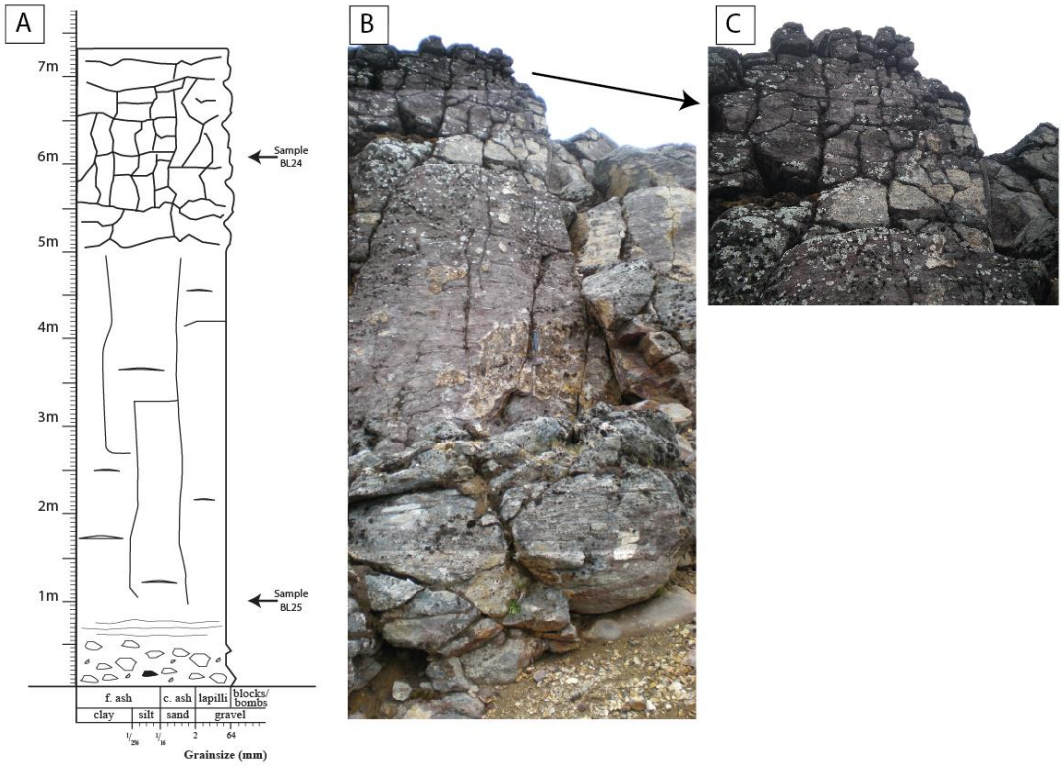

Figure 2.22. Rp-Ag2 at Site 24. Stratigraphic log (A), in outcrop (B), and (C). a close up view of the top of the unit showing brick-like platy jointing.

The west-dipping side of Rp-Ag2 is described at site 24 (Figure 2.22). The 7.3 m thick exposure is divided into three main sections. The lower 0.5 m is rarely exposed, but comprised of moderately welded, moderately sorted, blocky breccia that transitions into a thin layer (0.3 m) of ribbon-clasts above. The bulk of the outcrop consists of 5 m of strongly and intensely welded facies. The upper 2 m is comprised of very platy (almost brick-like) jointing, with the plates decreasing in size upwards. This outcrop is more akin to a lava flow than site 13, with minor auto brecciation at the base and a platy a'a' style flow surface with brick-like features at the top of the unit.

Rp-Ag3 (Unit 3)

Much of Rp-Ag3 has been removed by erosion (Figure 2.18). The unit only occurs sporadically with thin outcrops exposed on the eastern and western sides of Rotopaunga. These outcrops trace the outline of an arc through Rotopaunga and are interpreted as the same unit. The unit is comprised of intensely-moderately welded lithofacies and is up to 3 m thick, making it the thinnest of the Rotopaunga Agglutinates. No lower or upper contact is visible.

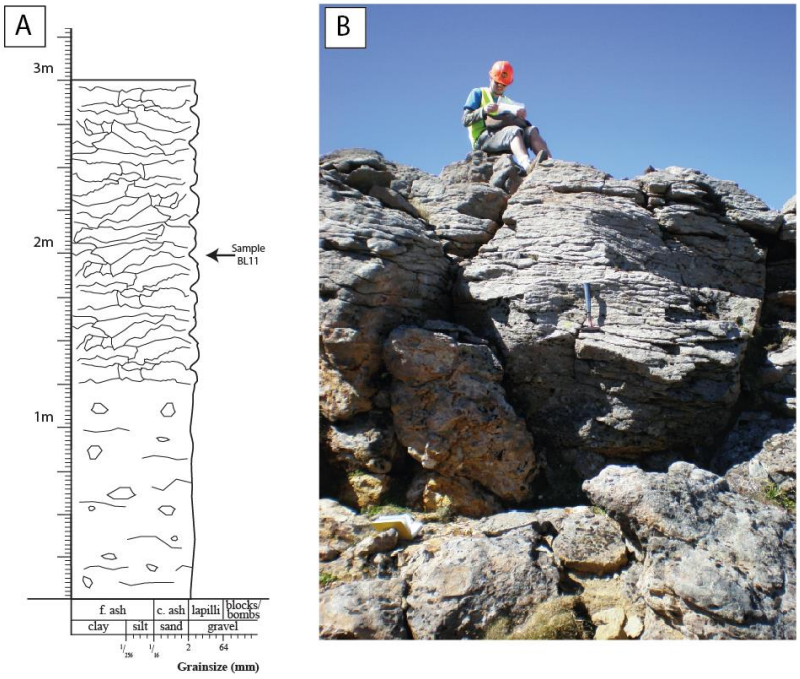

Figure 2.23. Rp-Ag3 at Site 11. Stratigraphic log (A), and in outcrop (B). Field assistant Mathew Norton for scale.

Descriptions of Rp-Ag3 on the eastern side are given at Sites 11 and 12. Site 11 consists of ~ 3 m of agglutinated rock (Figure 2.23). The lower 1.2 m of the exposure is dominated by strongly-moderately welded facies comprised of sub-rounded to sub-angular clasts within a more cohesive matrix. The upper 1.8 m of the outcrop is comprised of platy, intensely welded andesite. Jointing within the plates is roughly 10-20 cm in thickness and up to 50 cm horizontally. The plates dip in the same direction and angle as the slope, suggesting that the upper section of this unit flowed. At Site 12, Rp-Ag3 consists of 2 m of strongly welded facies with minor moderately welded facies occurring throughout the unit (Figure 2.24).

Flow banding in the outcrop is impressive, with complex folding seen in the middle of outcrop (at 1m).

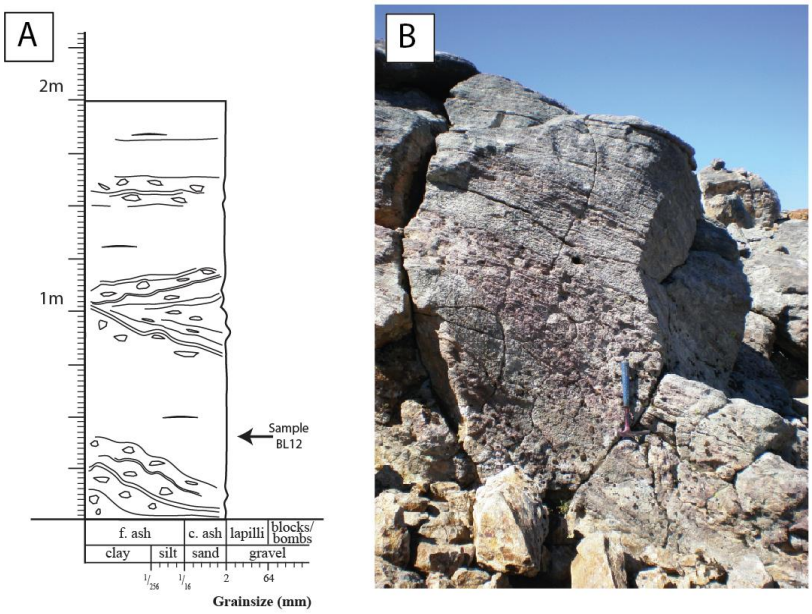

Figure 2.24. Rp-Ag3 at Site 12. Stratigraphic log (A) and the unit in outcrop (B).

The western side of Rp-Ag3 is described at Site 23, where 2.35 m thickness of strongly welded agglutinates outcrops laterally for 40 m (Figure 2.25). The rock displays many lensoidal clasts (Figure 2.26) distinguishable from the rest of the outcrop by subtle colour variations (red and black). These clasts range from 1-10 cm thick and 10 cm to 1 m long. A zone in the middle of the outcrop (1-1.3 m in stratigraphic log) shows an increase in smeared-out clasts.

Figure 2.25. Rp-Ag3 at Site 23.~40 m long exposure on the western side of BLC northern inner rim. Rp-Ag3 is laterally discontinuous and forms a wedge, ~2.4 m at its thickest that pinches out at both ends.

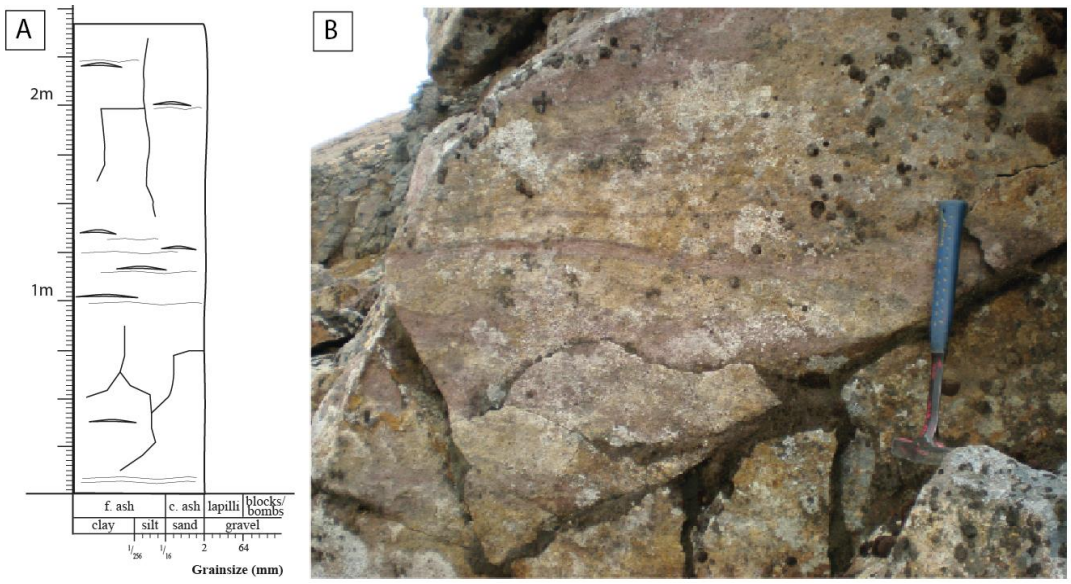

Figure 2.26. Stratigraphic log of Rp-Ag3 at Site 23 (A). Outcrop of Site 23 (B) showing lensoidal and ribbon clasts highlighted by their colour differences with the bulk of the deposit.

Rp-Ag4 (Unit 4)

Rp-Ag4 is the upper-most of the agglutinate deposits and possibly the largest. It forms a draping wall of sub-columnar, intensely-strongly welded light grey andesite through Rotopaunga that is interrupted in the central portion, leaving outcrops isolated on the eastern and western sides. The western exposure is ~270 m long and up to 9.5 m thick. On the eastern side the outcrop extends laterally ~190 m and is up to ~ 5.2 m thick. Rp-Ag4 is overlain by the Rotopaunga Scorias.

Three sites were described on the western side of Rp-Ag4 (Figure 2.29) Sites 3, 21 and 22. The base of the unit is comprised of loose material (Figure 2.27) the grain size of which is dominated by 4 mm (-6 phi) to -32 mm (-5 phi) clasts that collectivly make up 76% of the total weight (Figure 2.28). This loose material grades reversely with large clasts progressively becoming incorporated into the coherent middle of the unit. The lack of sharp bedding planes suggests that the unit is conformable and was deposited during the same event. The thick middle of the unit is comprised of massive, coherent intensely welded, sub-columnar andesite. The top 3-4 m of the unit is comprised of platy facies.

Two sites were described on the eastern side. At Site 10 the unit is comprised of 0.3 m moderately welded facies at the base transitioning into ~1.7 m of strongly

welded facies. Site 2 is comprised of 5.2 m thick outcrop of dominantly intensely welded facies and contains 1 to 2 m zones of platy joining (10-30 cm long and 5-20 cm high) at 1 m and forming the top if the outcrop.

Figure 2.27. Unit Rp-Ag4 showing ~1m of the unconsolidated basal material.

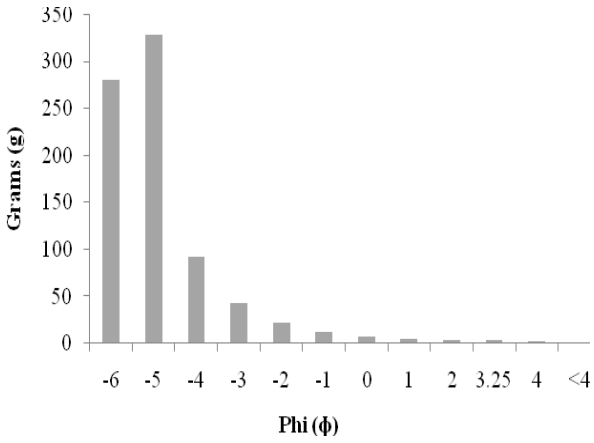

Figure 2.28. Grain size distribution by weight of sample BL23 from the unconsolidated basal material of Rp-Ag4 at Site 22.

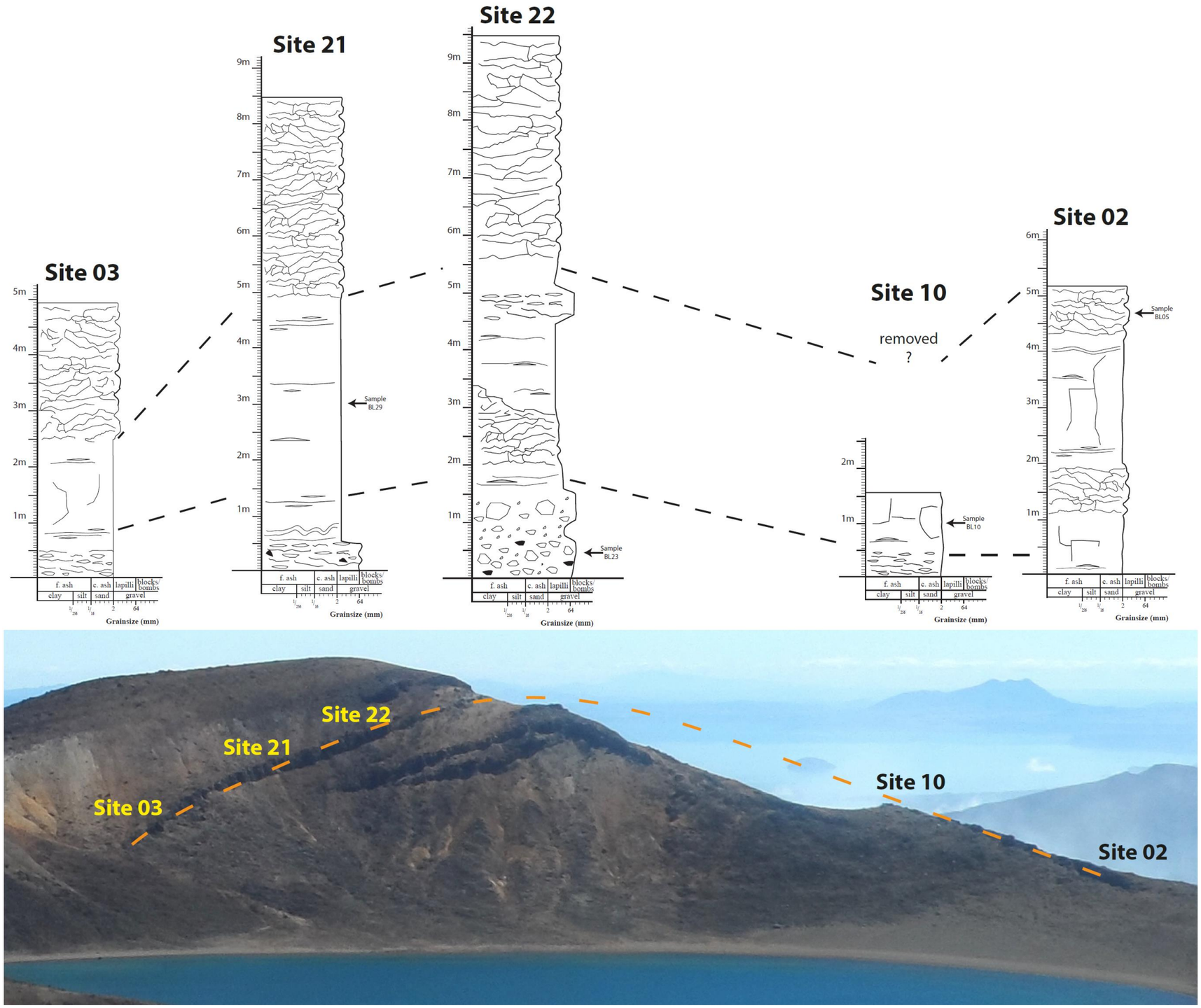

Figure 2.29. Northern BLC inner crater wall displaying stratigraphic logs of unit Rp-Ag4 and their correlation across the western and eastern portion of the unit.

2.7.1.2 The Rotopaunga Scorias (Rp-Sc)

The Rotopaunga Scorias are a succession of three scoria beds deposited on the slopes of Rotopaunga and the western rim of BLC (Figure 2.2). They occur stratigraphically above the Rotopauga Agglutinates and extend towards the Te Maari Craters, forming thin veneers. Units are numbered RpSc1-3, beginning with the lowest unit.

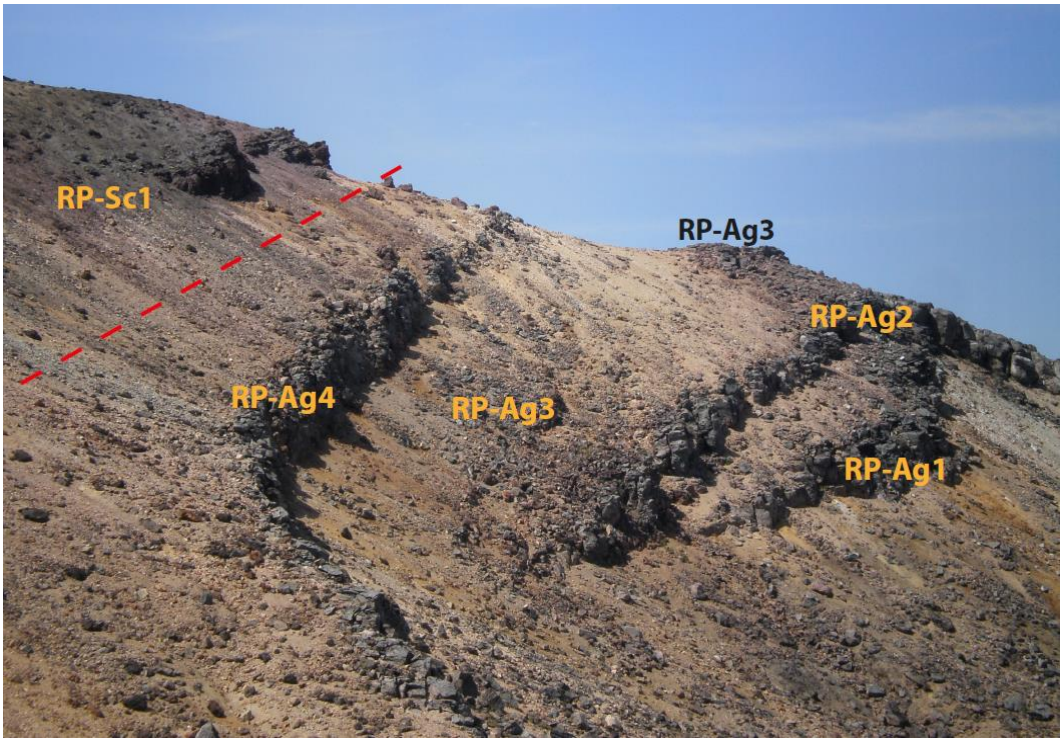

Figure 2.30. The top of the inner northern wall of BLC showing the four Rp-Ag units below Rp-Sc1 (divided by red dashed line).

Rp-Sc1 (Unit 1)

Rp-Sc1 occurs stratigraphically above Rp-Ag4 (Figure 2.30). A small outcrop remains within the inner rim at 1840 m a.s.l on Rotopaunga. This outcrop can be traced around the corner, making up the thick, welded, bedded, scoria deposits on the steep eastern bluffs of Rotopaunga. The bulk of the unit occurs on the eastern and western outer flanks of Rotopaunga (Figure 2.2).

Rp-Sc1 scoria beds form the impressive bluffs on the eastern flanks of Rotopaunga; they overlie Rotopaunga Agglutinates and pre-glacial cone lavas. These beds extend towards the Te Maari vents maintaining a thickness of more than 10 m (Figure 2.31). The scoria beds on the eastern bluffs were examined at Site 19, where more than 10 m of non-poorly welded spatter deposits are inter-layered with thin, moderately-strongly welded agglutinate beds (Figure 2.32). Poorly welded sections are comprised of angular scoria, spatter, and cow-pat bombs. The clasts are dominantly coarse lapilli to fine block grain size. Dense, angular, dark grey, glassy porphyritic clasts, 4-10 cm in size, occur sporadically. Lenses of moderately-strongly welded material are common; they extend up to tens of m laterally, and are typically 10-50 cm thick and comprised of cow-pat style fluid clasts and smeared clasts (Figure 2.33).

Figure 2.31. View from the peak of Rotopaunga looking north. The thick scoria beds of Rp-Sc1 extend towards the Te Maari Trig.

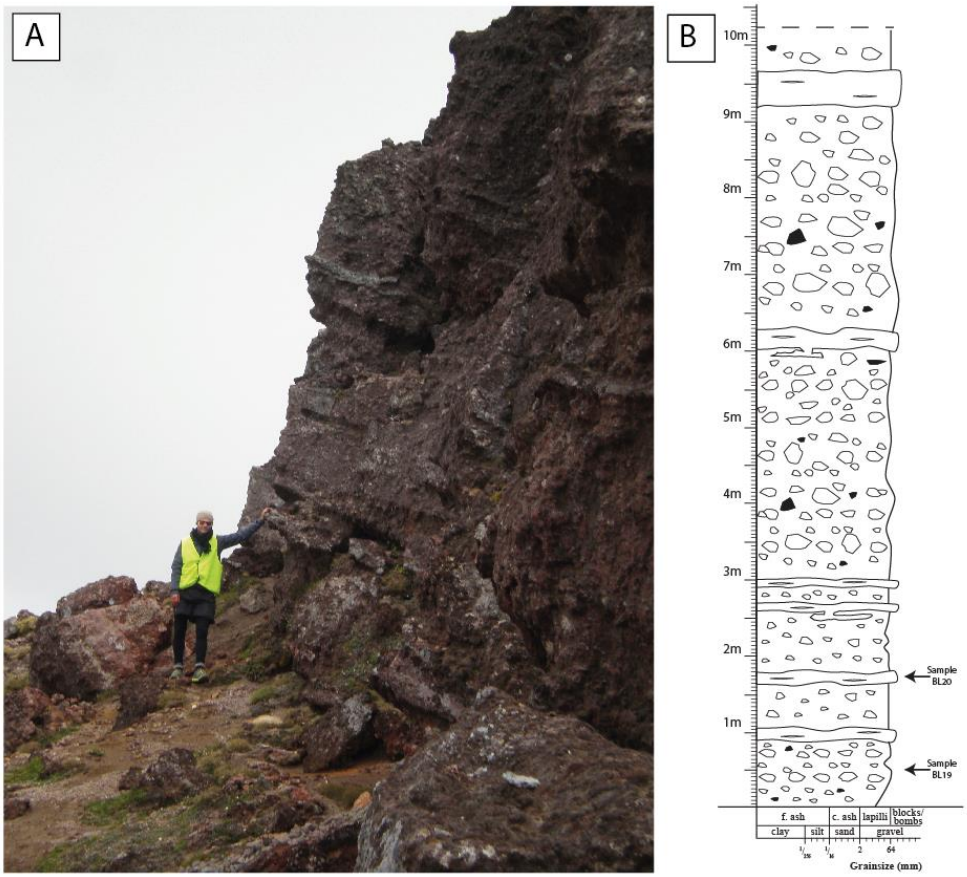

Figure 2.32. Rp-Ag1 at Site 19. (A) The deposit comprises more than 10 m of non to moderately welded scoria and interbedded zones of strongly welded facies. (B) Stratigraphic log of Site 19.

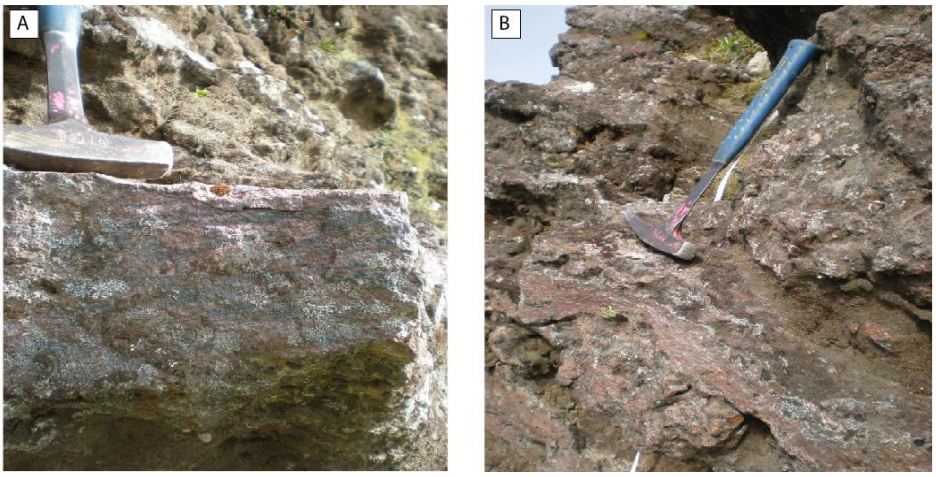

Figure 2.33. Moderately welded zones within unit Rp-Sc1. (A) Small lensiodal smears identifiable by their darker colouring. (B) Cow-pat bombs (below hammer head).

Rp-Sc1 occurs on the western flank of Rotopaunga as a 5 m veneer dipping steeply down-slope. Many small gullies have formed that cut through the unit (Figure 2.2). At Site 27 on the northern outer flanks of Rotopaunga the unit consists of an ~5 m thick bedded scoria bomb and block spatter and scoria bed (Figure 2.34). Several zones of moderately welded material are distributed through the deposit with varying thicknesses of 0.1-1 m. Large 0.3-0.5 m sized bread-crust bombs comprised of dense, dark, and highly porphyritic rock occur throughout the deposit, but are most concentrated at 1m. The grain size is dominated by loose scoria 32 mm (-5 phi) to 4 mm (-2 phi), making up 79 % of the total weight (Figure 2.35). At site 28, less than 50 m distance from Site 27, there is a noticeable absent of bedding, the unit shows little grading and very few strongly welded zones with the unit almost entirely comprised on non-poorly welded facies (Figure 2.36).

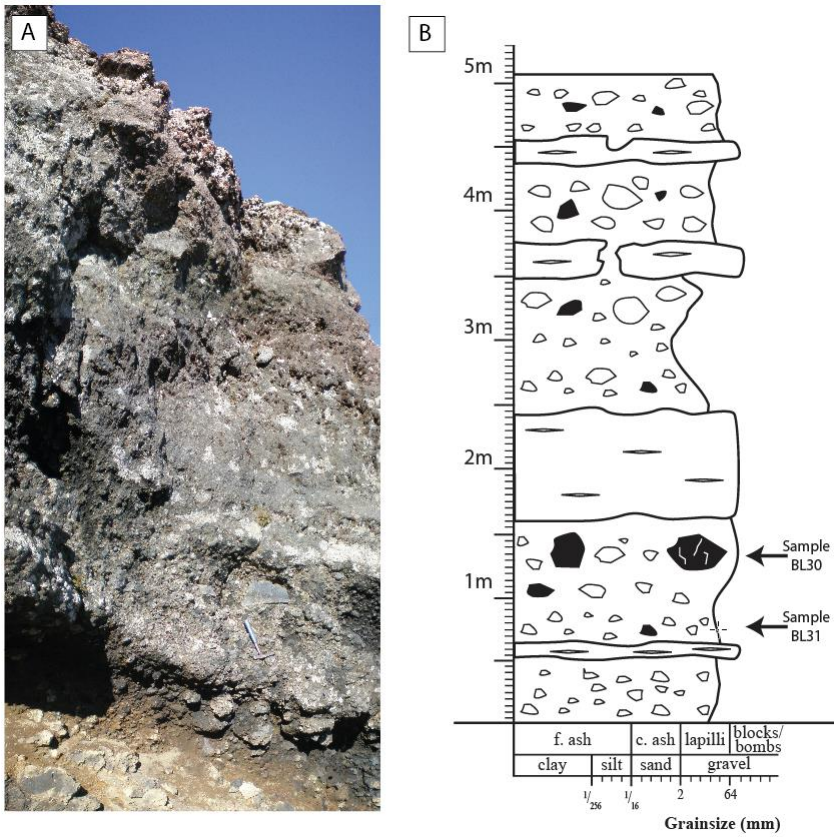

Figure 2.34. RpSc1 on the western flanks of Rotopaunga at Site 27. (A) In outcrop. (B) Stratigraphic log.

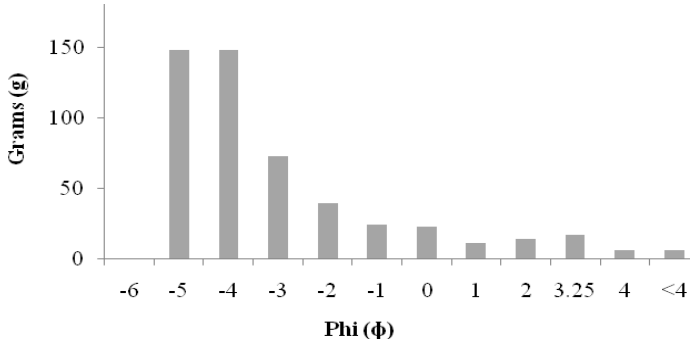

Figure 2.35. Grain size distribution of Rp-Sc1, sample BL31, Site 27

Figure 2.36. Rp-Sc1 at Site 28 on the western flanks of Rotopaunga.

A small outcrop of Rp-Sc1 sits on top of western BLC rim at Site 32 (Figure 2.1, Figure 2.2, and Figure 2.37). The 2.5m thin outcrop is similar to site 27 in that large bread-crust bombs are concentrated and largest at the base. The rest of the deposit is comprised of massive, poorly to moderately welded spatter bombs and blocks with strongly welded zones throughout. The deposit varies dramatically over the small exposure. The unit here overlies hydrothermally altered agglutinates (discussed in section 2.9).

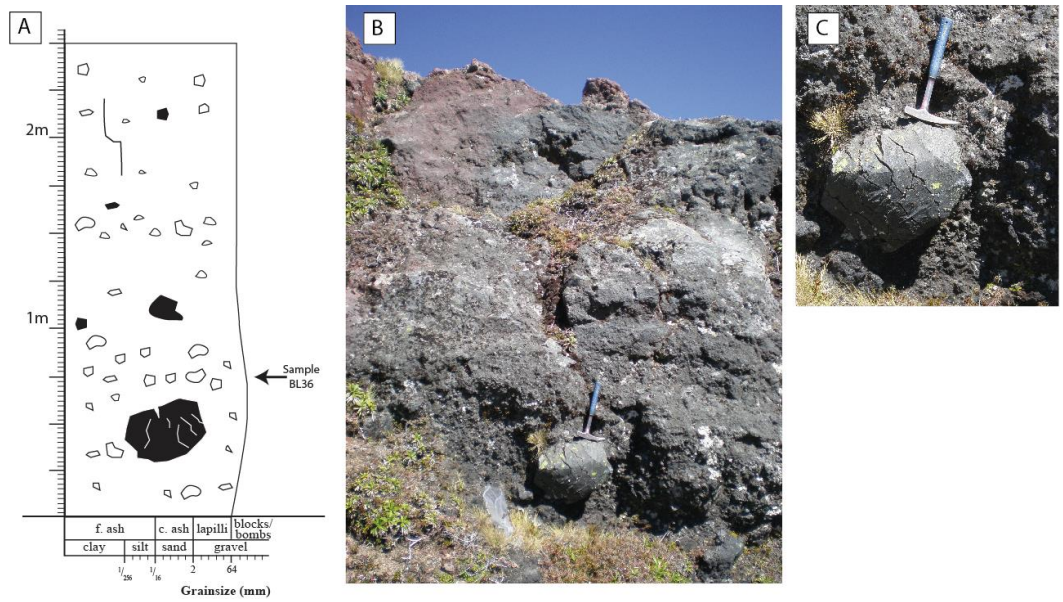

Figure 2.37. Rp-Sc1 at Site 32. (A) Stratigraphic log. (B) Site 32 in outcrop. (C) A close view of the 50 cm diameter dense bomb with breadcrust cooling joints.

Rp-Sc2 (Unit 2)

Rp-Sc2 occurs on the outer slopes of Rotopaunga and lies stratigraphically between Rp-Sc1 and Rp-Sc3 (Figure 2.38). Access to exposure of Rp-Sc2 was not possible during this study due to proximity to the Te Maari craters, and no outcrop of Rp-Sc2 was described.

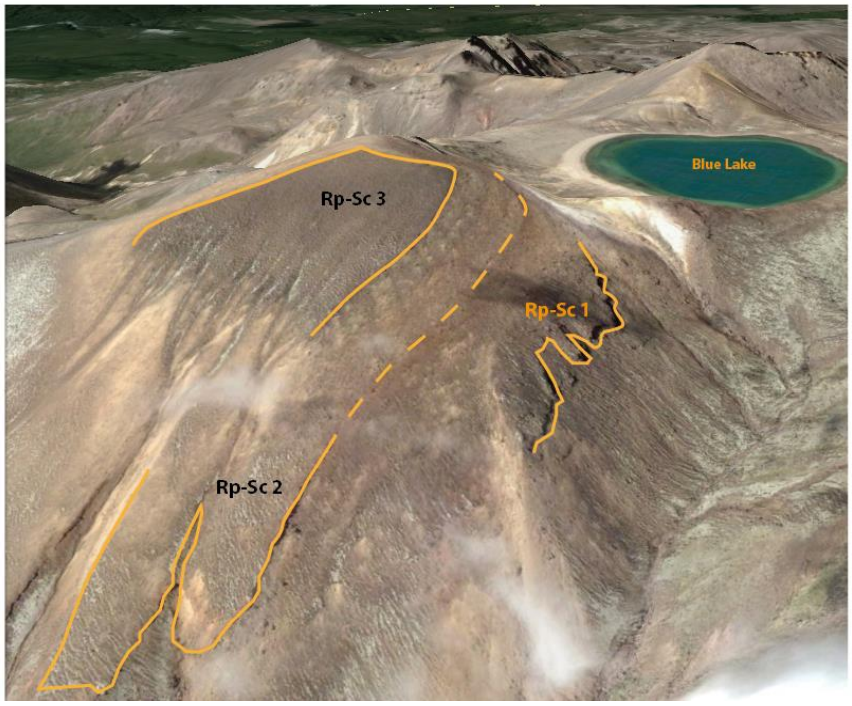

Figure 2.38. Digital Elevation Model (DEM) of the outer slopes of Rotopaunga showing units Rp-Sc1, Rp-Sc2 and Rp-Sc3 highlighted by yellow lines. Adapted from Google Earth.

Rp-Sc3 (Unit 3)

Rp-Sc3 forms a thin outcrop crowning the peak of Rotopaunga (Figure 2.2). The unit is thickest at elevation 1805 m a.s.l (2.2 m thick, Figure 2.39) and less than 1 m thick at the highest elevation of 1840 m (Figure 2.40). Site 4 describes the thickest section of the outcrop (Figure 2.39). Here the unit is comprised of non-poorly welded bomb and lapilli deposits with slight normal grading overall, and fluctuations in grading throughout. The unit contains inclusions of dense angular blocks and irregular scoriaceous bombs. The dense blocks are dark grey, glassy and highly porphyritic, and range in size from 10 to 30 cm, and are largest and most common ~0.5 m from the base. At Site 20, where there is less than1 m of outcrop (Figure 2.40), the deposit comprises of a massive, non-poorly welded, scoria lapilli and bomb deposit.

A small outcrop of scoria in the lower portion of the inner crater wall is described at Site 26, a small gully cutting (Figure 2.41). The unit is roughly 1.5 m thick and comprised of coarse laipilli to bomb-sized, dark grey, scoria. Overall the outcrop fines upward. Incorporated into the unit are zones of strongly welded material. Sample 28 taken from this site is dominated by 32 mm (-5 phi) clats. 64 mm (-6 phi) to 4 mm (-2 phi) makes up 87 % of the total weight (Figure 2.42).

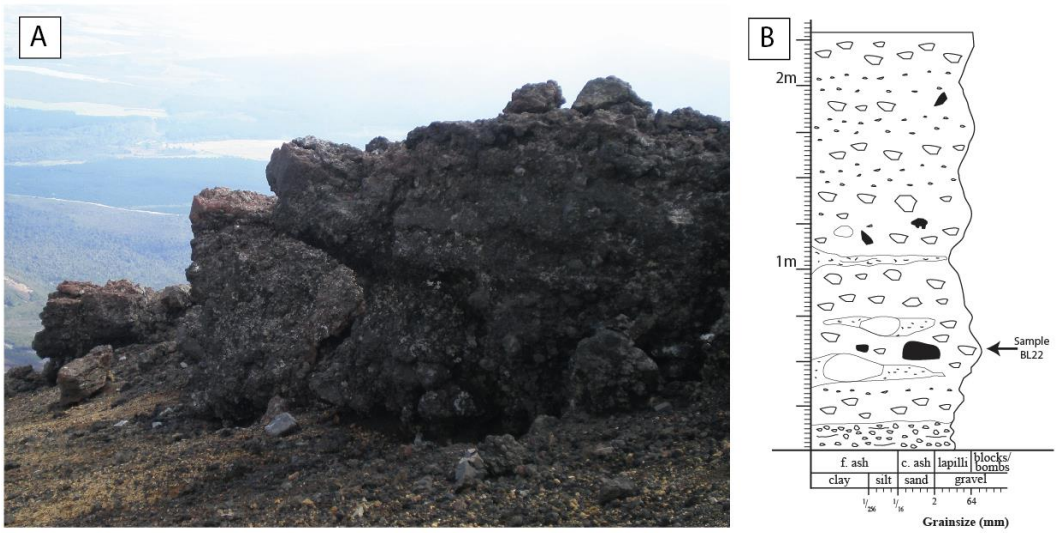

Figure 2.39. Rp-Sc3 in outcrop (A) looking northwest from the peak of Rotopaunga. (B) Stratigraphic log of RpSc1 at Site 4.

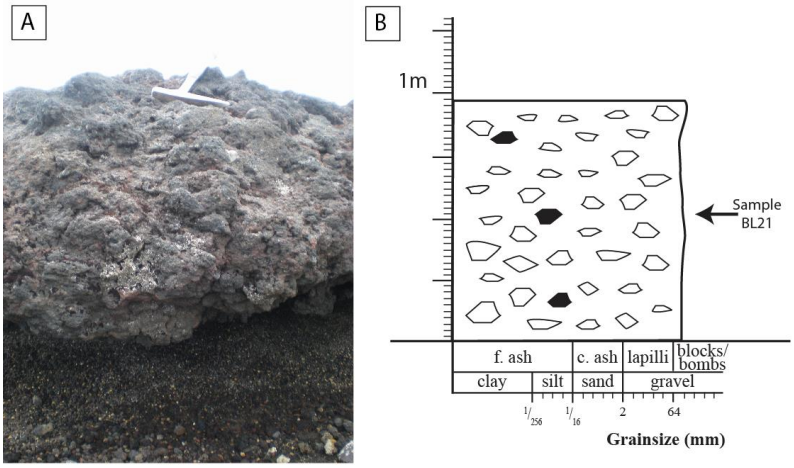

Figure 2.40. Rp-Sc3 at Site 20. In outcrop (A) and stratigraphic log (B).

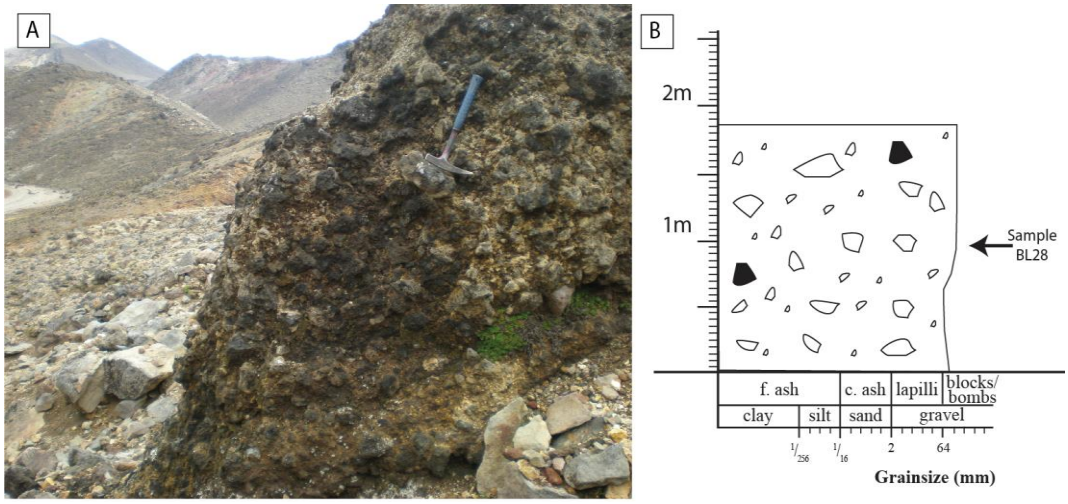

Figure 2.41. Rp-Sc3 at Site 26. In outcrop (A) and stratigraphic log (B).

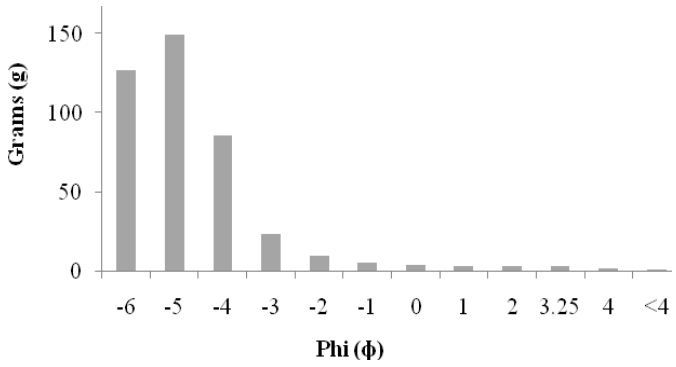

Figure 2.42. Grain size distribution of Rp-Sc3, sample BL28.

2.7.2 Deposits of the Western and Southern Rims

The deposits that mantle the western inner and outer crater rim of Blue Lake are poorly exposed, and are weathered with minor hydrothermal alteration. The outcrop is mostly limited to the very top of the crater rim (Figure 2.2). The inner slope is over steepened and most of the slope is littered with boulder-sized debris. It is difficult to determine which, if any, of these large boulders are *in situ*. Those determined to be *in-situ* occur as free-standing monoliths ~1-2 m high (Figure 2.43). Site 29 shows a typical monolith comprised of intensely to moderately welded, sometimes crudely bedded agglutinates. The lower 0.5 m of outcrop is comprised of a zone of horizontal smear clasts and ribbon clasts. This transitions into ~0.5 m of moderately welded facies that becomes more intensely welded towards the top. The outcrops at these sites are similar to that on the SW Rim and are likely correlative.

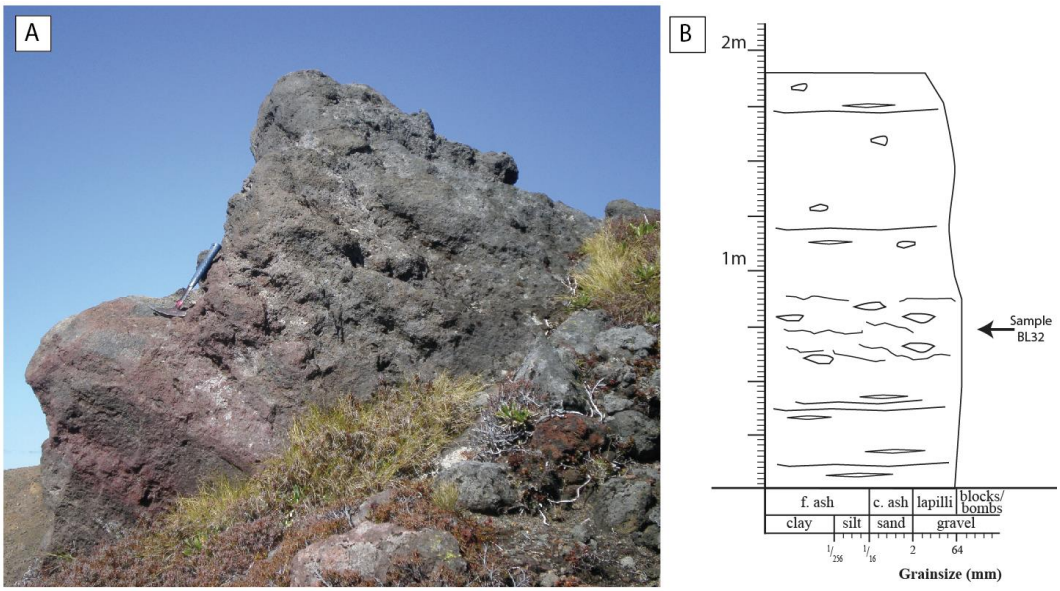

Figure 2.43. Outcrop of agglutinate monolith on the western rim at Site 29 (A). (B) Stratigraphic log of Site 29.

Further along the inner crater rim to the southwest there are several outcrops, each ~10-30 m in lateral extent that draper over the top and outer wall of the BLC rim. These outcrops over 7 m thick and all sit at about 1730 m a.s.l. These agglutinates differ laterally from west to south (Figure 2.44). Site 5 is comprised of 7.1 m of moderately welded, crudely bedded, lapilli and bomb and block deposit which grades vertically from coarse lapilli to bombs. Outcrops at sites 7 and 8 are

intensely-strongly welded blocky-jointed agglutinates with internal moderately welded zones. Site 8 displays very well developed flow banding and folding (Figure 2.45) indicating remobilization after deposition.

Agglutinates similar to those of the western and southwestern rims mantle the Central Crater peak directly south of BLC (Figure 2.46) and overlie the Mangahouhounui Formation. The agglutinates were described at sites 6 and 9 (Figure 2.1). I. Nairn (unpublished) interpreted these agglutinates as having been erupted from Blue Lake Crater prior to the Rotopaunga Scorias. They are, however, still post-glacial in age.

Site 6 is 1760 m a.s.l. The outcrop here wraps around the peak and dips down towards the Mangahouhounui Valley (Figure 2.47) and is weathered giving it a reddish-brown colour. The deposit is ~4 m thick and comprised of intensely-strongly welded agglutinate. A 0.2 m thick zone of tightly-packed ribbon clasts appears at the base of the unit (ribbons are 2-5 cm thick, and mostly horizontal). Above this the unit transitions into blocky jointed, strongly welded facies with feint 5-10 cm wide lensoidal smear clasts. The upper 1.5 m of the outcrop is comprised of intensely welded platy jointed facies.

Site 9 sits at 1830 m a.s.l on the eastern side of the Central Crater peak facing towards the Mangahouhounui Valle. The outcrop here is 4 m thick and comprised of intensely to moderately welded agglutinates (Figure 2.48). The outcrop begins with 0.6 m of moderately and strongly welded material, that transitions into a messy pocket of more scoriaceous intact clasts that is over-ridden by fluid clasts (0.6-1.2 m in Figure 2.48). The remainder of the unit, ~2.8 m thick, is dominated by sub-columnar jointed, intensely welded material with concentrations of thin, horizontal flow bands (1-2 cm thickness).

The deposits that mantle the west, southwest and southern rim of BLC are all of similar nature and display a similar range of facies characteristics. The deposits are correlative. and are here interpreted as the same unit and were deposited during the same eruptive period.

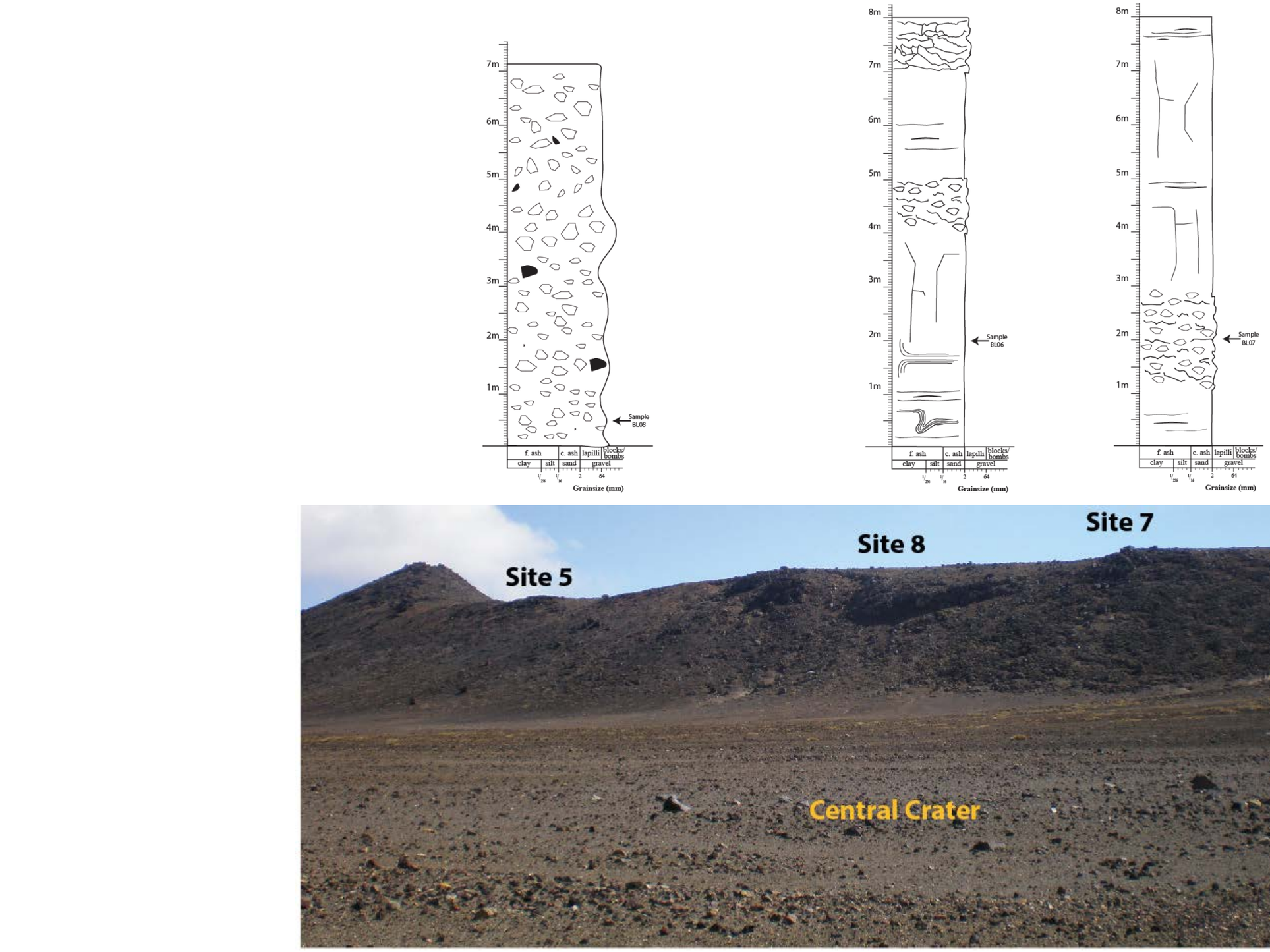

Figure 2.44. South western outer crater rim, showing site localities and paired stratigraphic logs.

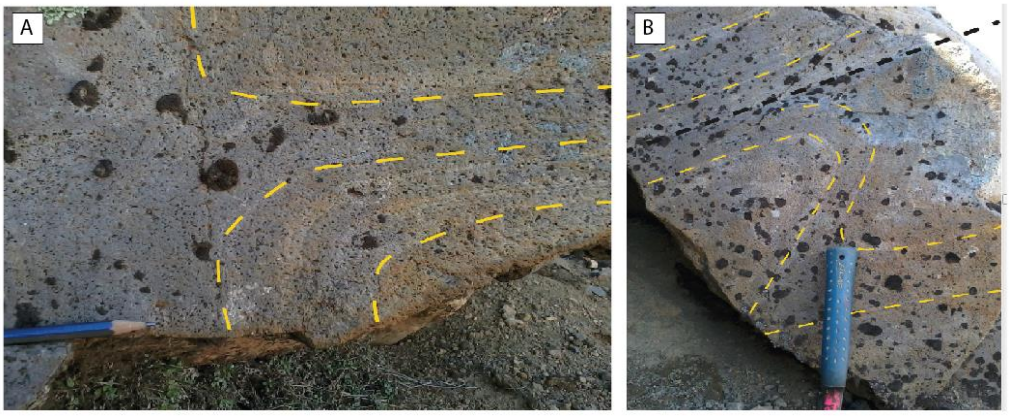

Figure 2.45. Flow banding textures at Site 8 displaying divergent flow paths (A) and horizontal and folded textures (B).

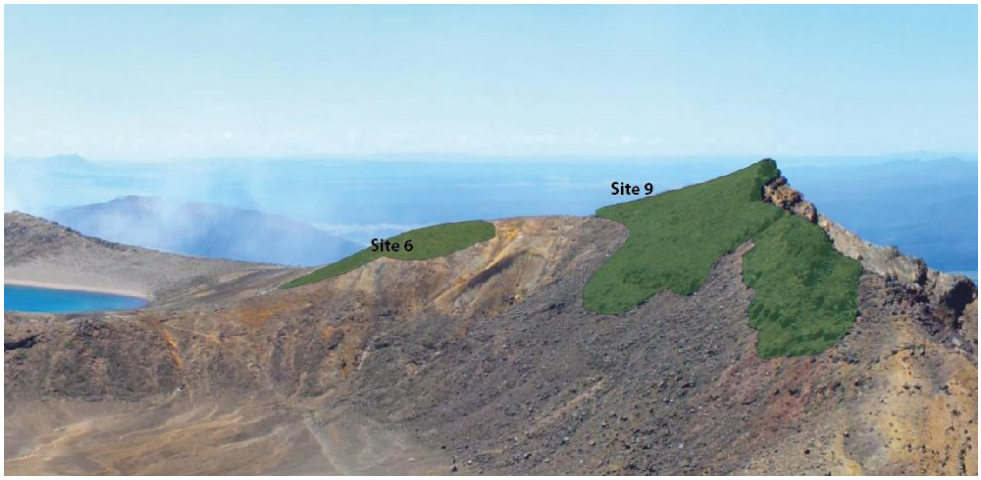

Figure 2.46. View of Central Crater peak from Red Crater. Mantling deposits are shaded green with site localities annotated.

Figure 2.47. Central Crater peak agglutinates sloping down the eastern rim of BLC near Site 6 (A). (B) Site 6 stratigraphic log.

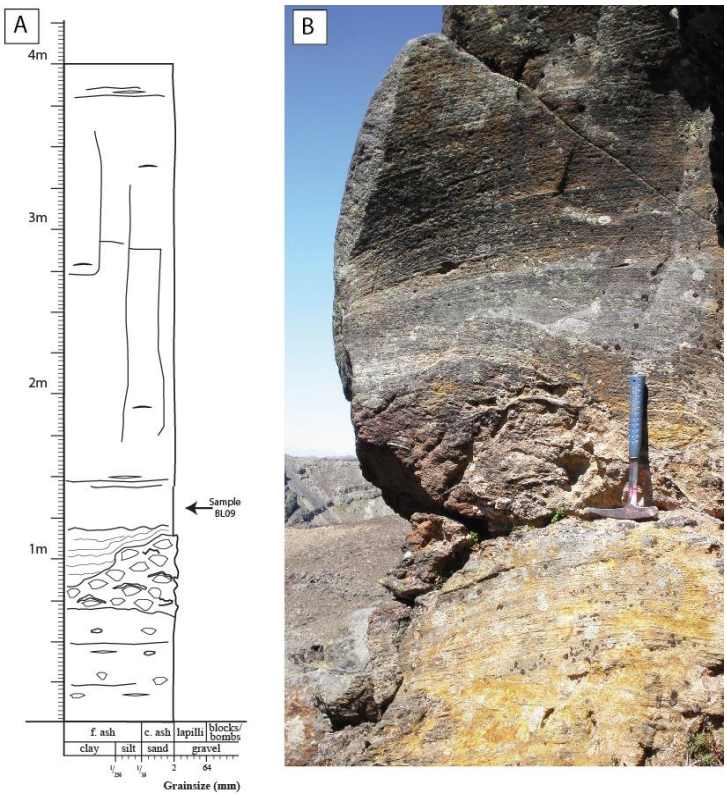

Figure 2.48. Crater rim agglutinates on the southern rim at Site 9. (A) Stratigraphic log and (B) in outcrop.

2.7.3 Deposits of the Mangahouhounui Valley and the Eastern Rim of Blue Lake Crater

The eastern rim of BLC is the lowest in elevation. The inner wall lacks outcrops and is buried by post-eruptive fill. On the crater's outer slopes and part way into the Mangahouhounui Valley is a lava flow consisting of four lobes. This lava flow is sourced from BLC however the volcanic deposits that it sits on top of are much older. The geology of the Mangahouhounui Formation, Pounamu Breccias and Tuffs, and Te Tatau Scorias are not a part of this study. Previous authors have described these units (Hobden *et al.* 1996; Nairn unpublished) and a brief overview of them is given below.

2.7.3.1 The Mangahouhounui Valley Succession

Mangahouhouni Formation

The Mangahouhounui Formation lavas form the northeast sector of the Tongariro complex, and extend north from the Oturere valley to the Tahurangi Stream

(Figure 2.2). They are deeply glacially eroded. K-Ar dates on the Mangahouhounui lavas near the Oturere valley range from -250 to 100 ka (Hobden *et al.* 1996). The formation is up to 300 m thick in the Mangahouhounui Valley, and appear to have been erupted from multiple vents in two main crater areas. 1) The major vent area is near the north wall of the western Oturere valley, and 2) a minor vent area in the head waters of the Mangahouhounui Stream (Nairn unpublished).

Pounamu Breccias and Tuffs

These deposits are tuffs, tuff breccias and brecciated lavas (Figure 2.2). They have been derived in part from landslides collapsed from adjacent higher areas. (Nairn, unpublished) presumed that they originated as proximal deposits in the core of the (old ~200 ka) Mangahouhounui cone, with later collapse into the glacially-eroded crater where hydrothermal alteration is ongoing.

Te Tatau Scorias

The TeTatau scorias and agglutinates are welded scoria fall deposits, agglutinates, and underlying tuffs (Figure 2.2).They overlie pumiceous lapilli and block fall units tentatively correlated with the widespread Rotoaira Lapilli tephra. They are presently interpreted as forming part of the complex sequence of Rotoaira eruptions (Nairn unpublished) and are thought to have erupted from the glacially eroded Te Tatau crater.

2.7.3.2 The Blue Lake Crater Lava Flow

The BLC lava flow travels down the Mangahouhounui Valley (Figure 2.2) where it overlies Pounamu breccias and tuffs. The ~4 m flow overlies the final Rotopaunga Agglutinate unit, Rp-Ag4, on the northern side of the eastern crater in which it overflows, and overlies crater rim mantling deposits on the southern side. The lava flow sits within the upper portions of the valley floor signifying that it is post-glacial in age. It extends ~700 m down the valley and has a width of 675 m at the widest point (Figure 2.2, Figure 2.49). The lava ranges in thickness from 2 to 4 m (Figure 2.50). The flow covers an area of ~100,000 m^2. This gives an estimated volume of the ~300,000 m^3, or 0.0003 km^3, assuming an average 3 m

thickness for the entirety of the flow. The width of the breach in the crater rim through which the lava flowed is 190 m. There are 7 lobes to the flow that range in size from the largest, the central lobe (450 m long and 162 m at its widest) to the smallest (250 m long and 30 m wide). The lobes to the north flow slightly less distance and are wider in lateral extent than the lobes in the south. The larger lobes (lobes 3 and 4 in particular) have small 2nd degree lobes. The largest travels ~40 m from the main lobe. The exact order of lobe emplacement is difficult to establish, although the largest central lobe (lobe 4 in Figure 2.49) was the last. Transverse pressure ridges radiate outwards and are up to 70 m in lateral extent and form 0.3-1 m steps down the flow. They are smaller and more tightly packed at the top of the flow, and are the largest and most pronounced in the lower middle portion of the flow, marking the point at which the underlying slope angle flattens out slightly.

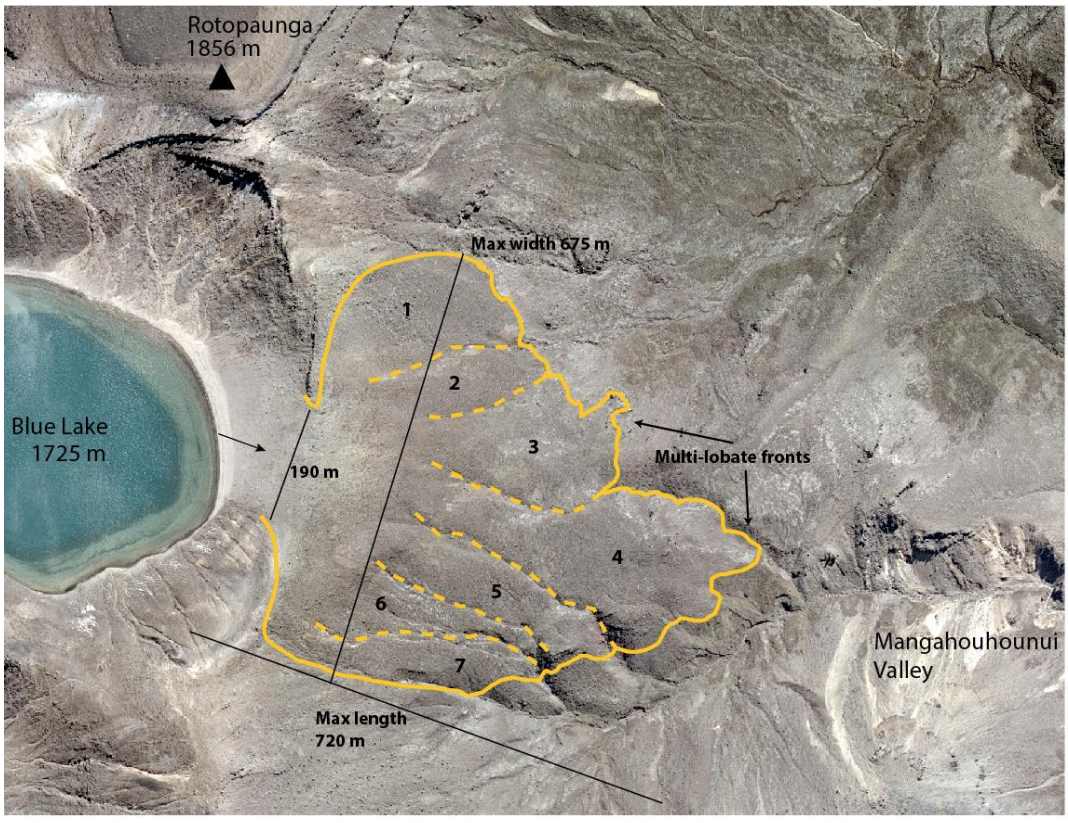

Figure 2.49. Aerial image of BLC lava flow giving the major dimensions of the flow. Lobes are labelled 1 to 7 from north to south.

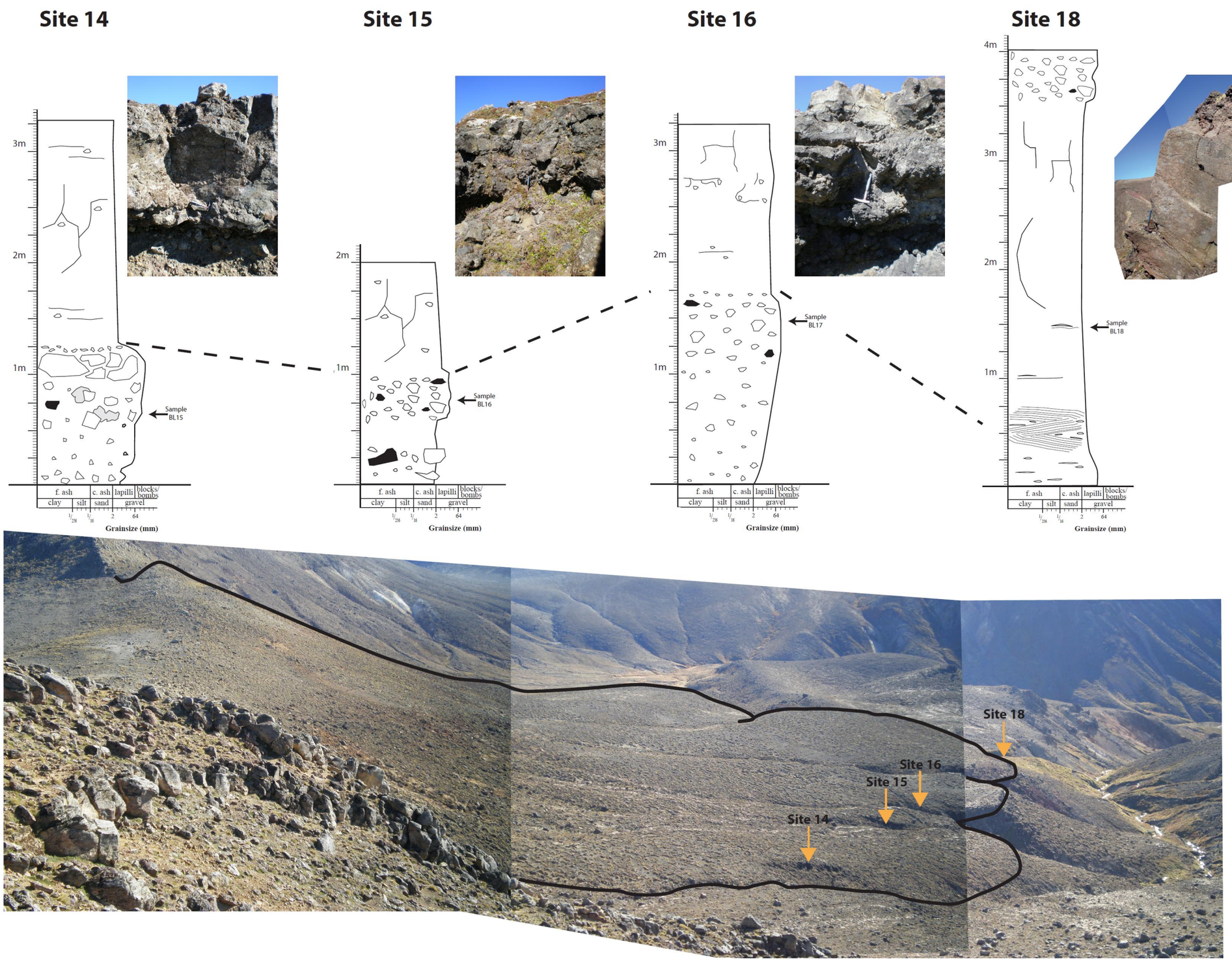

Figure 2.50. Lava flow showing site localities and stratigraphic logs. Dashed lines represent correlation of facies between outcrops

Deep channels that have been cut into the lobes providing good exposures of the flow and are described in stratigraphic logs at Sites 14,15,16, and 18 (Figure 2.50). The lava flow is comprised of three zones. The base of the flow is up to 1.5 m thick and comprised of block-sized breccia, dark grey in colour. The grain size of the basal breccia is dominantly made up of 64 mm (-6 phi) to 16 mm (-4 phi) (Figure 2.51) clasts, that collectively make up 74% of the total weight. The breccia in this zone coarsens upwards before transitioning into coherent, crystalline lava. The transition may be gradual (Site 15) or may be represented by a thin, ~5 cm layer of coarse angular lapilli (Sites 14 and 16). Alternatively, as in the case of Site 18, there may be a zone of flow-banding and folding (Figure 2.50). The middle zone of the flow is comprised of up to 2.5 m thickness of light-dark grey porphyritic, blocky jointed, dense lava. Jointing is typically 0.3-1 m. Occasional smeared clasts are incorporated randomly through the unit. The top zone, where preserved (Site 18), forms a 0.4 m in thick, spiny, rubbly a'a style flow surface comprised of similar angular and vesicular breccia as the base of the flow.

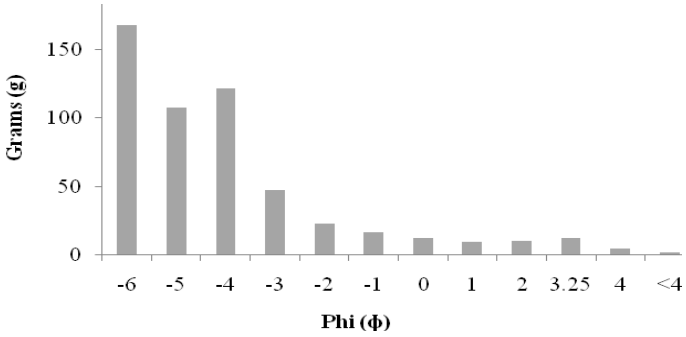

Figure 2.51. Grain size distribution of basal autobrecia (sample BL15, Site 14) of the BLC lava flow.

2.8 **Crater Fill**

Gullies have developed in the northern and eastern inner walls of BLC exposing fine grained volcaniclastic layers (Figure 2.52). The steep slopes of Rotopaunga are comprised mostly of scree and ash to fine block sized debris. Several gullies and fan systems have developed that feed this material down slope. A beach has formed around Blue Lake as a consequence of this influx of volcaniclastic

deposits. The top of Rotopaunga is comprised an assortment of loose, unconsolidated pyroclastic fall and ballistic deposits. Large, m-sized ballistic blocks were thrown onto Rotopaunga and the rim and lake of BLC during the 2012 Te Maari eruptions.

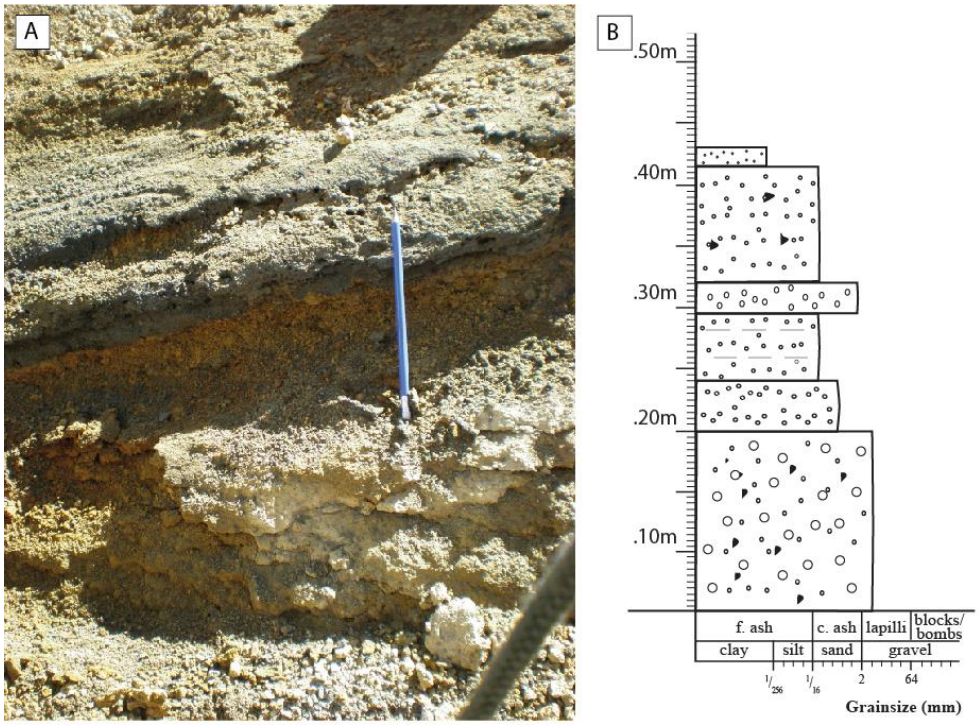

Figure 2.52. Gully cutting into the east of BLC at Site 1, in the centre is a small outcrop of volcaniclastic ash and lapilli (A). (B) Stratigraphic log of this exposure. The units are comprised of coarse ash and fine lapilli layers that are well sorted, and light orange to light-dark grey in colour. Discontinuous lamellae can be seen in the lapilli layer at 25-30 cm.

2.9 Zone of Hydrothermal Alteration

A zone of pronounced alteration occurs within the low saddle between the western rim of BLC and Rotopaunga (Figure 2.2). Steaming ground was witnessed by this author on one occasion during April 2013. The alteration zone is 200 m by 140 m, with an estimated area of 6500 m^2 (0.0065 km^2). Altered outcrops are exposed on the eastern side of the zone underlying Rp-Sc1 (Figure 2.53). Alteration appears mainly surfical, with colour changes from white at the top of the altered beds, going down into pink then red/orange at the base (Figure 2.54). Alteration has made it hard to describe the appearance of the deposit, although in outcrop it displays the characteristics of a bedded, welded agglutinate similar to those

exposed on the western and southern rims. Due to the degree of alteration, it is impossible to geochemically correlate the hydrothermally altered material with other units around BLC.

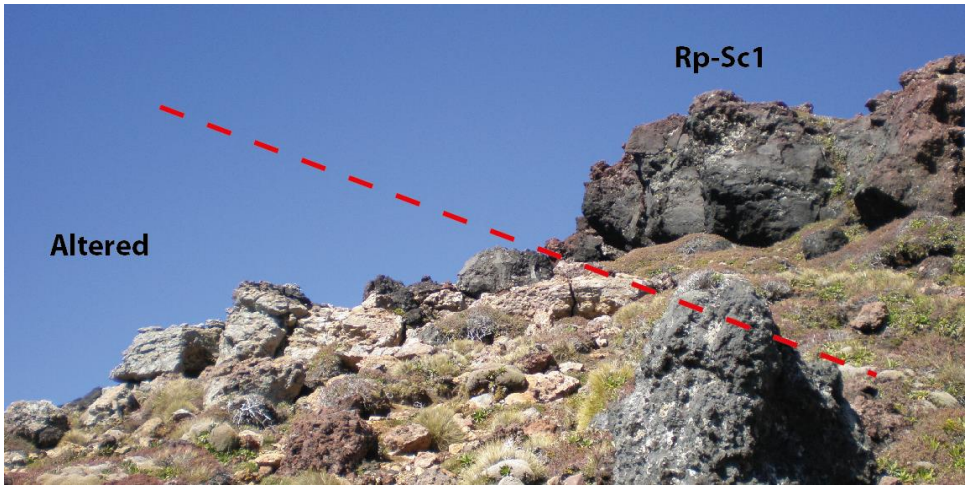

Figure 2.53. Exposure of altered agglutinates underlying Rp-Sc1. Notice pink orange and white coluration.

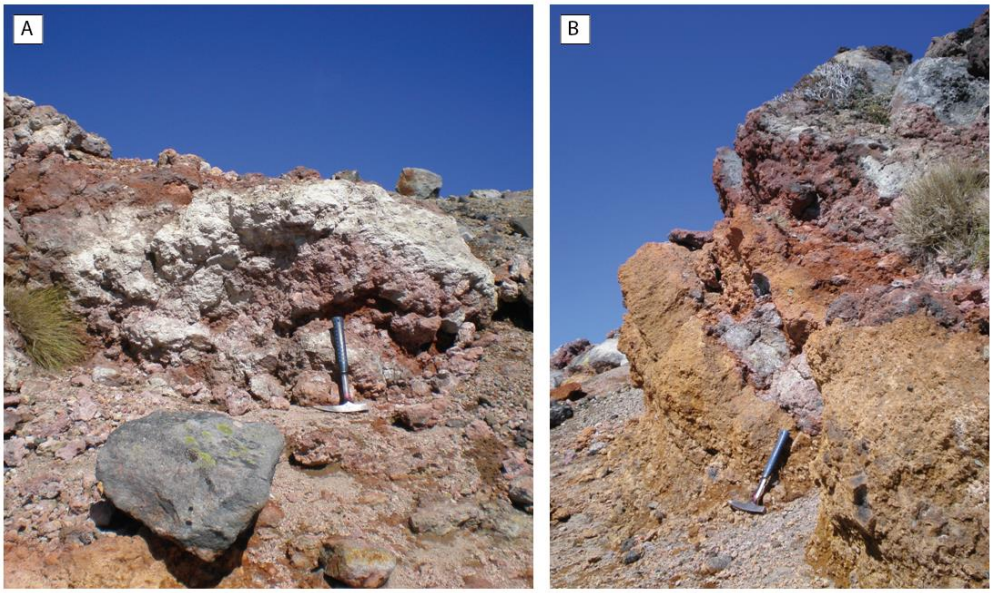

Figure 2.54. Outcrops of units within the hydrothermal alteration zone (A) and (B). A range of colours are displayed. The rock has broken down into sand and clay-sized loose material.

Chapter Three

Textural and Petrographic Characteristics

3.1 Introduction

This chapter details the petrographic and vesicularity studies that were carried out on representative samples of the proximal and vent-forming deposits of BLC..The main focus of this chapter is to describe the mineralogical and textural characteristics of rock thin sections; and quantative componentry by point counting of selected slides for modal abundances. Density and vesicularity studies were undertaken on scoria clasts from unconsolidated samples as well as a small selection of agglutinates and dense bombs. Figure 2.1 in Chapter 2 shows site localities and Appendix One matches sample numbers with site locations and their stratigraphic unit. Appendix Three gives a description of each thin section and Appendix Four gives raw vesicularity data.

Petrographic analysis was carried out on a combination of samples from the Rotopaunga Agglutinates, Rotopaunga Scorias, crater rim deposits and the BLC lava flow. 45 samples were cut and mounted on petrographic glass slides, the full methodology of which is described below. Samples are described in terms of their petrographic characteristics, including phenocryst and groundmass textures and assemblages, volcanic glass, vesicles and xenoliths. An Olympus BX51 microscope was used, implementing transmitted and reflected light at 2.5-50 times magnification. 14 samples were point counted to obtain modal abundances of rock components, with the count set at 300, and with a stage interval of 1 mm. Counted components include; plagioclase, orthopyroxene, clinopyroxene, Fe-Ti oxides, olivine, xenoliths, groundmass, and vesicles.

Figure 3.1. Images of the thin section making process at the sample preparation laboratory, University of Waikato.

3.2 Methodology

3.2.1 Thin Section Preparation

Forty five samples were made into thin sections and an additional 15 samples were surface-polished. The methodology for Thin section slide preparation is as follows:

i. Cut rock samples (hand sample or single clast) were cut into small ~3.5x2.5x2.5 cm blocks (Figure 3.1). The faces to be mounted were sanded and cleaned and left to dry on a hot plate overnight at 60 °C.
ii. Samples were surface-impregnated with Araldite K39 two-part resin using a ratio of 2 g resin to 1 g hardener. The samples were dried overnight at 60 °C.
iii. The sanded block faces were ground using a #600 polish powder on a frosted glass plate until the saw marks were removed. Samples were again dried overnight at 60 °C.
iv. Glass slides (4.5x2.7) cm were ground flat on one side until frosty with a diamond disco grinder (Struers Discoplan-TS).
v. The polished face of the samples were mounted onto the frosted glass slide with Hillquest thin section epoxy using a ratio of 0.7 g resin to 0.3 g hardener (this makes enough for four samples). Bubbles were removed from between the sample and the glass. The samples were cured overnight on a hot plate at 60-70 °C.
vi. The mounted blocks were trimmed down to ~1 mm thickness using the Struers Discoplan-TS. This was done in slow progression of ~10 µm. The remaining ~1 mm on the samples were trimmed further to ~30 µm.
vii. Samples were sealed with a glass cover slip using a small amount of petropoxy (ratio of 1 ml resin to 0.1 ml hardener for approx. ten slides) making sure that no bubbles remained between the cover slips and samples. The samples were then cured overnight on a hot plate at 70 °C.
viii. The excess petropoxy was cleaned from the samples using a blade. The samples were then labelled with small stickers.

3.2.2 Vesicularity Measurements

The methodology for determining vesicularity was adapted from Houghton *et al.* (1988) and Houghton and Wilson (1989). Full results are listed in Appendix Four.

i. Where possible, at least 10 juvenile clasts were collected between 4 and 10 cm in size.
ii. Samples were cleaned then dried in oven for several hours at ~60 °C.
iii. The balance and weighting stand was set up as shown in Figure 3.2.
iv. The balance was tiered and each sample was weighed dry (in the air).
v. 5x5 cm pieces of parafilm wax were cut out. These were weighed in water with the average being 0.03 g.
vi. Each clast was wrapped in parafilm sheets that were moulded into the surface irregularities and across large vesicles. More sheets were added as necessary to create an air-tight wrap around the samples. The number of sheets used was recorded.
vii. The samples were placed into the basket and lowered into the water with the basket not touching the sides or bottom of the container. A light tap was given to dislodge any small bubbles. The weight was then recorded.
viii. The basket was removed from the water, and the sample from the basket, which was then replaced with the next wrapped sample.

NOTE: any clasts that floated were ballasted with a lead sinker weighed in water. The D.R.E or dense rock equivalent value used is 2.6 g cm^{-3} typical of most andesites, taken from (Houghton *et al.*1988).

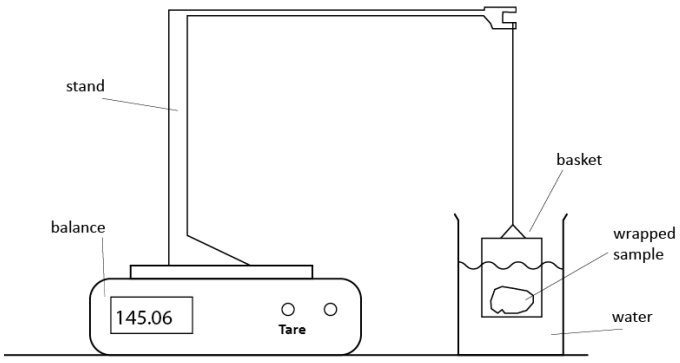

Figure 3.2. Diagram of apparatus used for determining vesicularity and density.

3.3 Introduction to the petrography of volcanic rocks of the TgVC

The volcanic rocks of the TgVC contain a mineral assemblage that is similar to that of typical calc-alkaline andesites and basaltic andesites (Ewart1982). They contain a typical phenocryst assemblage of:

Calcic Plagioclase + Augite + Orthopyroxene + Fe-Ti ± Olivine ± Hornblende

Hobden (1999) observed that the mineralogical variability between different volcano-stratigraphic units of Tongariro is generally quite subtle, and that the main distinction is often the degree of disequilibrium displayed. One distinguishing feature of more primitive magma compositions of the younger cones is the high proportion of olivine-bearing magmas, and the lack of hornblende-bearing lavas (Figure 3.3 and Figure 3.4) (Hobden 1997). The presence of orthopyroxene and lack of abundant olivine are often indicative of andesite.

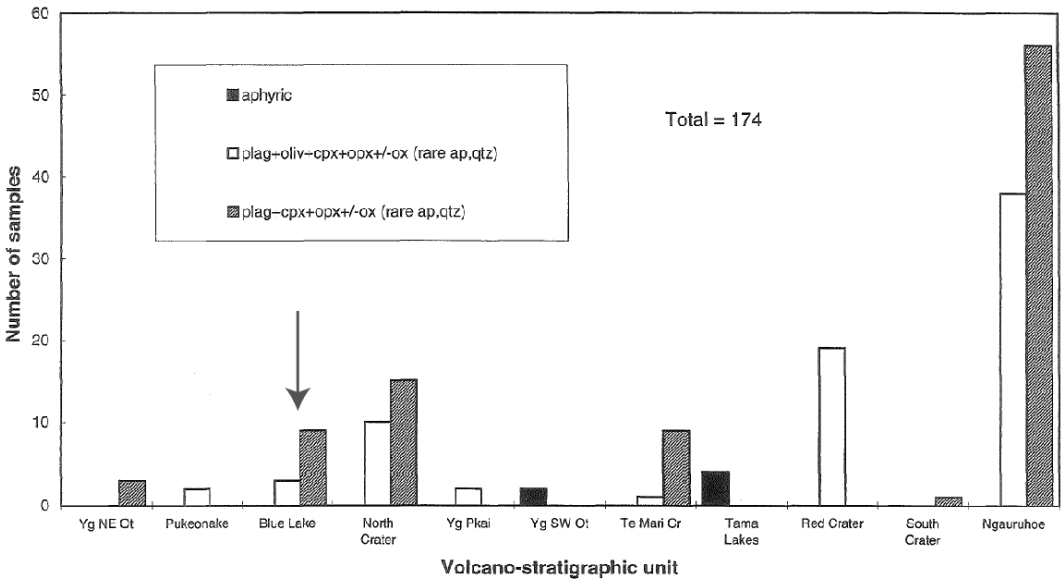

Figure 3.3. Samples from young eruptives of TgVC according to volcanic group from Hobden (1997). Samples of the deposits proximal to Blue Lake (arrow) contain no aphyric lavas and are primarily made up of plagioclase dominated two-pyroxene +/- Fe-Ti oxides. A minority of the samples contain olivine. Compare this to neighbouring North Crater which has a higher proportion of olivine bearing magmas, and the Te Maari Vents which have very little olivine bearing magmas. Adapted from Hobden (1997).

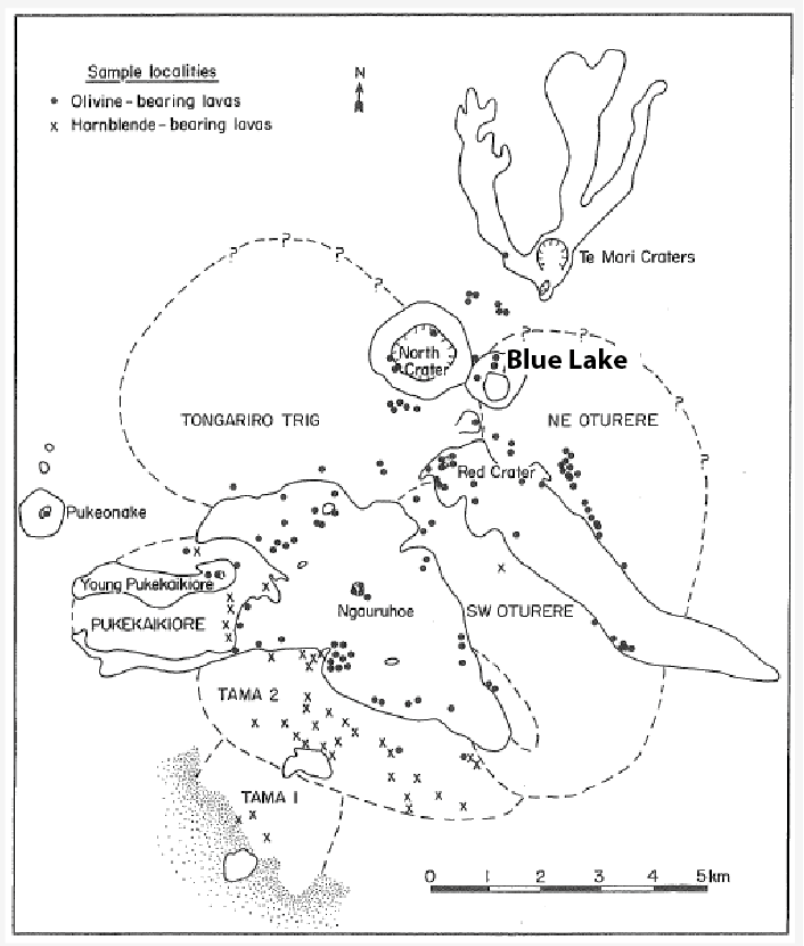

Figure 3.4. Spatial distribution of olivine (●) and hornblende (x) bearing lavas of the TgVC. Several localities around BLC and on Rotopaunga between BLC and the Te Maari Vents contain olivine. Adapted from Hobden (1997).

Hobden (1997) described the typical crystallisation sequence for a Tongariro andesite determined principally from textural relationships as;

Plagioclase → (Olivine) → Fe-Ti Oxides → Orthopyroxene → Clinopyroxene

Olivine (if present) crystallises early along with (or just after) plagioclase.

Evidence of Magma Mixing

Samples of the TgVC often display disequilibrium between phenocryst phases and groundmass, as well as the involvement of magma mixing processes. Evidence of magma mixing and mingling in TgVC rocks include; textural banding, sieve textures (indicating major resorption episodes during crystal growth) reverse and patchy zoning, disequilibrium mineral assemblages and disparate crystallisation temperatures. Sieve textures are concentrations of glass inclusions that often arranged in zones within the crystal. Their presence may indicate major

compositional breaks and/or reversals. Sieve textures are very common in plagioclase, sometimes with un-sieved material forming the rim (re-crystallised). Plagioclase also commonly displays strong oscillatory zoning, as well as both patchy and reverse zoning. Oscillatory zoning represents discontinuous repetitions of zones of normal (Ca core to Na rim) and reverse (Rim more Ca than core) zones within a single crystal (Nakagawa *et al.* 2002).These features are an indication that resorbtion of plagioclase back into the melt has occurred as a result of new magma being introduced. Clear, inclusion-free crystals are the exception rather than the rule. Hobden (1997) found that often there is no significant difference in composition between the sieved and unsieved crystal portions, or between coexisting sieved and unsieved plagioclase. In these cases, and in the absence of other criteria indicative of magma mixing, rapid decompression may be responsible for producing (particularly the coarse) sieve textures (Pearce *et al.* 1987; Nelson and Montana 1992). Tongariro plagioclase sieve textures are most likely the result of a combination of magma mixing and rapid decompression, although it is difficult to assess the relative contributions of the two processes.

3.4 Petrography

The most noticeable feature of deposits proximal to BLC is their moderately to strongly porphyritic nature, containing up to 40% phenocryst content (Table 3.1). The samples collected in this study contain a mineral assemblage typical of a two pyroxene-plagioclase system; dominated by plagioclase with lesser amounts of orthopyroxene and clinopyroxene and commonly containing Fe-Ti oxides. Tabular plagioclase phenocrysts may be flow-aligned, which contributes to mm-cm scale flow banding (rarely folded). The groundmass is either microcrystalline or glassy. 1-5 mm xenoliths are common. Many agglutinated deposits are weakly to moderately vesicular. Vesicles are typically 0.1-20 mm in diameter, spherical, ellipsoidal or irregular in shape with some visibly coalesced. Vesicles are sometimes stretched out and are aligned in a sub-parallel arrangement. In some scoria clasts the vesicularity is more than 60%. Scoria clasts show a variety of features; some contain moderately to highly vesicular cores with poorly vesicular outer crusts. Other clasts may have highly vesicular outer shells with a poorly to

incipiently vesicular core. Spatter attached on to chilled clasts is common. The samples in thin section generally show a fine-grained and hypocrystalline texture.

Glomeroporphyritic clots or aggregates of large crystals of the same size and mineralogy as phenocrysts are common in the samples (and in most andesites)(Gill 1981). They appear genetically related to the magma in which they occur, and are typically 0.5-4 mm in size (Figure 3.5, Figure 3.6B, Figure 3.8B and Figure 3.12) and are interpreted as phenocryst aggregates (that indicate a preference for heterogeneous nucleation during crystal growth).

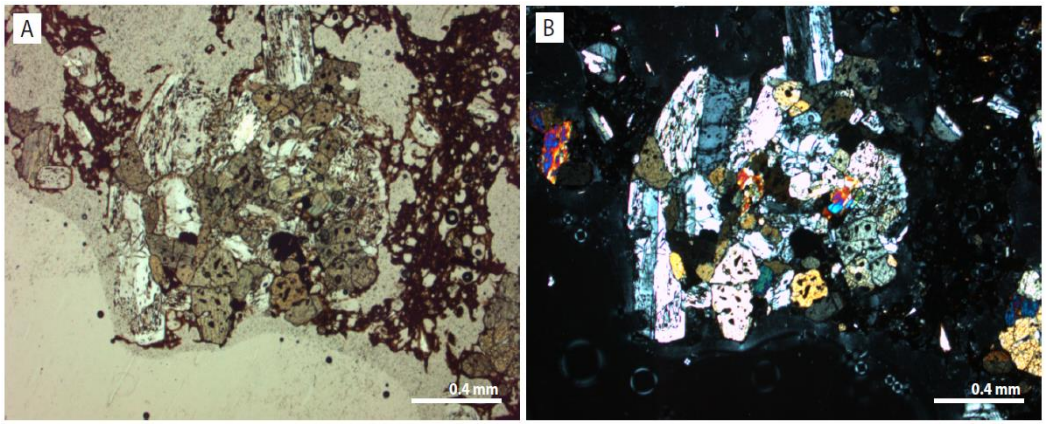

Figure 3.5. Photomicrographs of a glomeroporphyritic clot held in a framework of highly vesicular glassy groundmass. (A)Shows the image under ppl. (B) Shows the image under xpl. (sample BL36, Rp-Sc1).

3.4.1 Mineral Phases

Plagioclase

Plagioclase phenocrysts are ubiquitous and abundant within all deposits found proximal to BLC; with a modal abundance of 55-70% of total phenocryst composition, and 10-30% of the total bulk rock (Table 3.1). Crystals are typically subhedral and display a range of shapes including rectangular, lozenge and irregular (Figure 3.6A-F). The size of plagioclase crystals ranges from 10 µm to larger than 3mm. Crystals occur predominantly as discrete grains, however they also occur as part of glomeroporphyritic clots. Plagioclase is the major groundmass phase (microcrystalline and cryptocrystalline eu-anhedral) and often displays (sub-)trachytic flow textures. Plagioclase displays a wide range of textures, and the majority show some degree of disequilibrium including sieving, resorption and patchy zoning (Figure 3.6C).

Table 3.1. Point Counting Results of BLC eruptives. Included for comparison is Hobden (1997) point count on sample TG214.

			Bulk Composition								Phenocryst Composition				
Sample	Volc Strat Unit	Rock Type	G/M %	Lithics %	Vesicles %	Plag %	Opx %	Cpx %	Oliv %	Fe-Ti %	Phenocryst Total %	Plag %	Opx %	Cpx %	% of phenocrysts that occur as Glomeroclots
BL27	RpAg-1	Agl	56.67	1.67	1.00	24.67	9.00	5.67	-	1.33	40.67	62.71	22.88	14.41	22.13
BL14	RpAg-2	Agl	45.00	1.00	13.00	22.67	7.33	6.00	-	4.33	40.33	62.96	20.37	16.67	17.36
BL10	RpAg-4	Agl	57.67	-	7.67	19.67	6.67	5.33	-	3.00	34.67	62.11	21.05	16.84	44.23
BL19	RpSc-1	Scoria	30.67	1.33	43.00	15.67	4.33	3.67	-	1.33	25.00	66.20	18.31	15.49	18.67
BL30	RpSc-1	Dense	59.33	1.00	1.67	20.33	9.67	5.67	0.33	2.00	38.00	57.01	27.10	15.89	13.16
BL31	RpSc-1	Scoria	34.67	0.67	44.33	11.67	3.00	5.00	0.67	0.33	20.67	59.32	15.25	25.42	19.35
BL21	RpSc-3	Scoria	36.67	-	38.00	13.33	5.33	5.33	-	1.33	25.33	55.56	22.22	22.22	22.37
BL22	RpSc-3	Dense	50.33	-	0.33	28.67	7.67	12.33	-	0.67	49.33	58.90	15.75	25.34	33.78
BL06	SW rim	Agl	69.00	0.67	0.33	16.67	4.67	5.33	-	3.33	30.00	62.50	17.50	20.00	31.11
BL09	S rim	Agl	61.33	1.67	8.00	17.67	7.67	3.67	-	-	29.00	60.92	26.44	12.64	26.44
BL15	BLC lava	Brec.	27.67	2.67	45.67	15.33	5.33	2.67	-	0.67	24.00	65.71	22.86	11.43	6.94
BL16	BLC lava	Lava	61.00	0.67	4.00	22.00	5.00	5.00	-	2.33	34.33	68.75	15.63	15.63	15.53
BL17	BLC lava	Brec.	37.33		35.33	14.33	6.67	5.00	-	1.33	27.33	55.13	25.64	19.23	29.27
BL18	BLC lava	Lava	51.00	2.67	16.33	15.67	5.33	5.67	-	3.33	30.00	58.75	20.00	21.25	18.89
TG214[1]	RpAg	Agl	70.90	-	-	19.10	6.90	2.50	-	0.60	29.10	67.02	24.21	8.77	-

[1] *Hobden (1997) sample*

Sieve textures (glassy inclusions) appear in a variety of ways. Sieving may be most intense in the centre of the crystal, or within a concentric zone, or appear in patchy zones. Some crystals may be entirely replaced with sieving but contain thin, fresh rims. The range of sieve features in BLC plagioclase include:

i. Rounded, intensely-sieved resorbed cores surrounded by clear, euhedral mantles (Figure 3.6A).
ii. Un sieved cores (often only resorbed remnants) mantled by intermediate zones of glass inclusions that are then surrounded by a thin, clear, euhedral rims and often display patchy zoning Figure 3.6B and C.
iii. Only a relatively thin sieved core exists in an otherwise clear crystal, which may be euhedral or rounded and embayed.

Occasionally, plagioclase may contain inclusions of pyroxene and/or Fe-Ti oxides and/or glass (Figure 3.6E and F). Oscillatory zoning is also common (Figure 3.6A). It is not uncommon to find fresh crystals within the same sample as worn and highly sieved crystals, suggesting some form of magma mixing.

Orthopyroxene

Orthopyroxene is more commonly the dominant phase of the two pyroxenes in pre-and-syn-BLC deposits. It ranges in abundance from 3 to 9% of bulk rock composition and 15 to 27% of the phenocryst make up (Table 3.1). Orthopyroxene phenocrysts are typically smaller than the dominant plagioclase crystals and range in size from 0.2 to 2 mm. Phenocrysts are typically subhedral and display a range of morphologies including prismatic, tabular, lath and irregular (Figure 3.7A-F). Phenocrysts are often fractured or display coarse sieve textures and other disequilibrium features; some crystals are extensively corroded, resorbed and/or embayed (Figure 3.7A and B) and these gaps may be filled with inclusions of Fe-Ti oxides. The coarse sieve textures observed indicate resorption processes, and are suggestive of magma mixing, recharge or transport processes within the magma reservoir or conduit (Hobden 1997). Orthopyroxene often occurs in glomeroporphyritic clots along with other mineral phases (plagioclase, clinopyroxene and Fe-Ti oxides). In some of the samples, particularly samples from the Rotopaunga Scorias (Rp-Sc1 and Rp-Sc3),orthopyroxene crystals are sometimes surrounded by thin (up to 0.05 mm) overgrowths or reaction rims ofclinopyroxene (Figure 3,7E). Orthopyroxene also occur as the dominant

member of the mixed pyroxene rims observed around most olivine phenocrysts, and as inclusions within larger plagioclase phenocrysts. Othopyroxene crystals are typically homogeneous under the microscope, but microprobe analysis (discussed in Chapter 4 section 4.3.2) reveals many to be zoned.

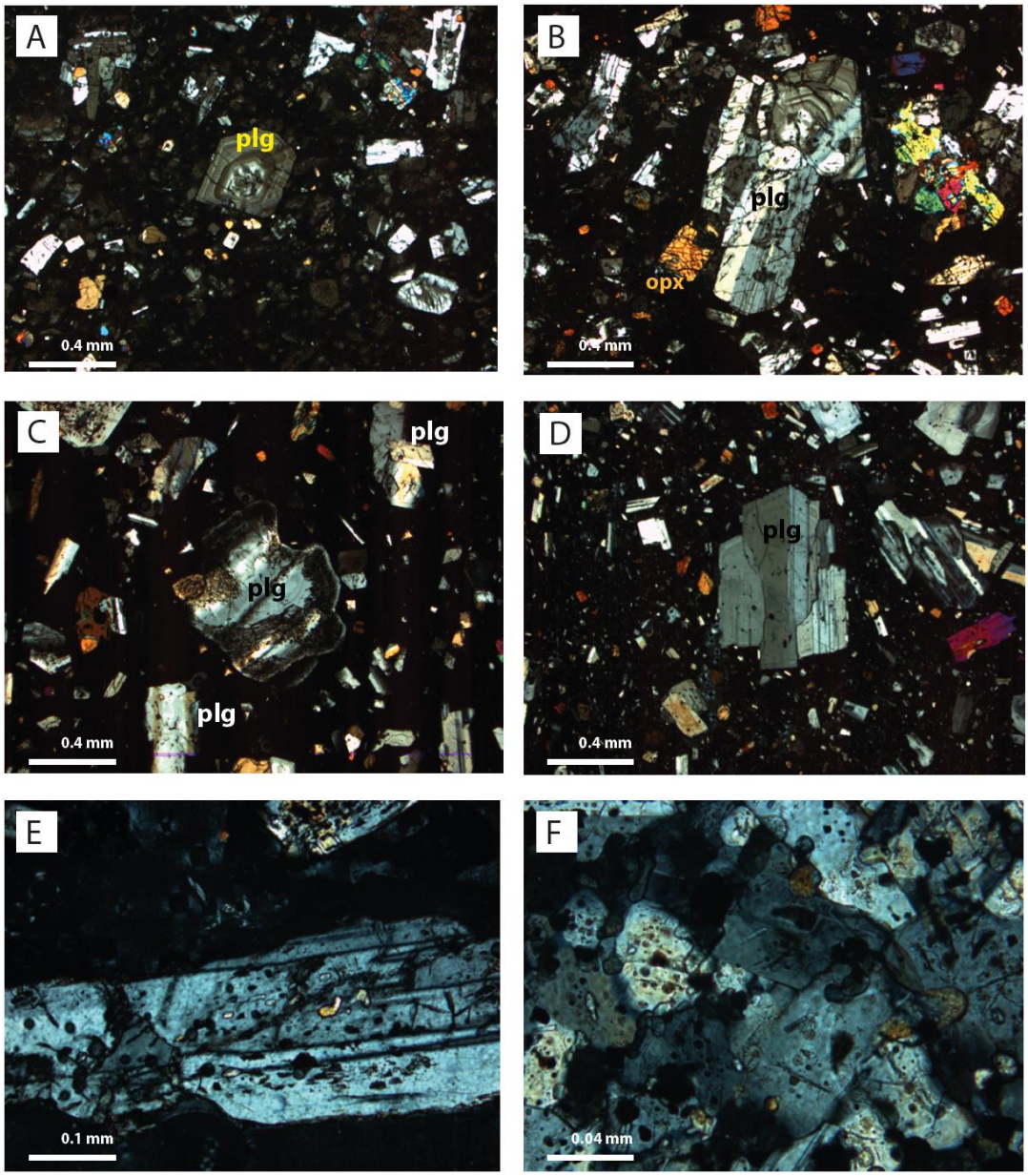

Figure 3.6. Photomicrographs of plagioclase within proximal deposits of BLC. (A) Strongly oscillatory zoned plagioclase with sieved core (sample BL24, Rp-Ag2). (B) Sub-glomerophorphyritic plagioclase cluster containing many glassy inclusions and minor patchy zoning. Oscillatory zoned plagioclase in the top portion of the cluster (sample BL30, Rp-Sc1). (C) Plagioclase with a thin, clear core and extremely patchy sieving in the middle of the crystal. The small euhedral plagioclase below contains glass and pyroxene inclusions (sample BL06, SW rim). (D) Large euhedral, mostly clear plagioclase with minor sieving and glassy inclusions. Faint oscillatory zoning is present in the outer portion of the crystal (sample BL16, BLC lava flow). (E) Pyroxene inclusions within a subhedral, sieved plagioclase (sample BL36, Rp-Sc1). (F) Pyroxenes, glassy inclusions and micro crystalline appetites formed within a plagioclase-dominant glomeroporphyritic clot (sample BL15, BLC lava flow).

Clinopyroxene

Clinopyroxene (augite) is, in the majority of samples, the subordinate pyroxene phase. It ranges in abundance from 3 to 12% total bulk rock composition and makes up 11 to 25% of the total phenocryst assemblage (Table 3.1). Clinopyroxene ranges in size from 0.1 to 2 mm. They are typically subhedral and displays a range of shapes including prismatic, tabular, lath and irregular (Figure 3.7A-F). A number of clinopyroxene crystals display twinning. They are generally fractured to varying degrees and/or display sieve textures, corrosion, resorbtion and/or embayment (Figure3.7A,B,C and F). These gaps may be filled with inclusions of Fe-Ti oxides. Clinopyroxene often occurs in glomeroporphyritic clots along with other mineral phases (plagioclase, orthopyroxene and Fe-Ti oxides). Clinopyroxenes frequently occur adjacent to orthopyroxene crystals and as reaction rims around orthopyroxene (Figure3.7E).

Fe-Ti Oxides

Fe-Ti oxides are a minor constituent of the samples analysed in this study, with modal abundances of <1 to 4%. Fe-Ti oxides occur as discrete crystals (Figure3.8A) as members of mixed plagioclase and pyroxene glomerocrysts (Figure 3.8B) within feldspathic xenoliths, or within the groundmass (Figure 3.8C). Fe-Ti oxides are typically euhedral and occur as sub-rounded cubic crystals (Figure 3.8A-C). Fe-Ti oxides range in size from <0.01 mm to 0.5 mm. In glomeroporphyritic clots they may be finer than other phenocrysts, or less commonly, the same size (Figure 3.8B). Under reflected light, titanomagnetite and ilmenite can be identified. Titanomagnetite is the most common, both as discrete euhedral to subhedral phenocrysts, and as small rounded grains within the groundmass. Hobden (1997) likewise found that the majority (90%) of Tongariro lavas contain Fe-Ti oxide minerals, principally magnetite, but also ilmenite as a minor phase.

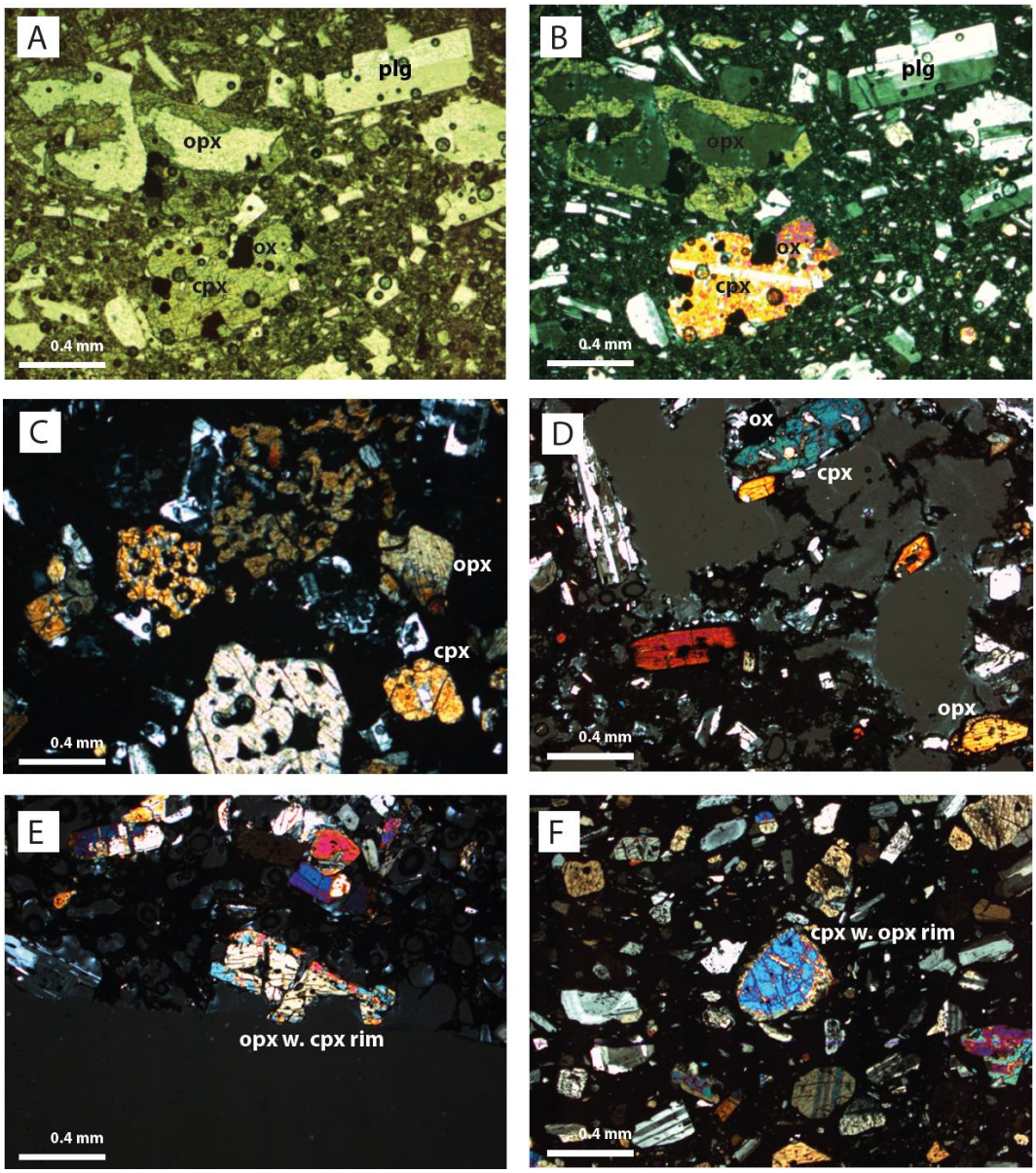

Figure 3.7. Photomicrographs of the variation of pyroxene phases within the deposits of BLC. (A & B) Severely damaged and embayed large, subhedral orthopyroxene and clinopyroxene phenocrysts. Fe-Ti oxides are infilling the embayments. The adjacent plagioclase appears more fresh. Twinning is visible in the lower clinopyroxene. (A) shows the view under ppl, (B) under xpl (sample BL16, BLC lava flow). (C) Large, intensely sieved orthopyroxene phenocrysts (sample BL27, Rp-Ag1). (D) Subhedral plagioclase and pyroxenes within highly vesicular, glassy groundmass. Notice the reaction rim formed on the orthopyroxene in the bottom right corner (sample BL19, Rp-Sc1). (E) Orthopyroxene with clinopyroxene reaction rim within a vesicular, glassy groundmass. A small glomeroporphyritic clot is present in top half of image (sample BL31, Rp-Sc1). (F) Clinopyroxene with an orthopyroxene reaction rim. Twinning can be seen within the clinopyroxene below the centre phenocryst (sample BL30, Rp-Sc1).

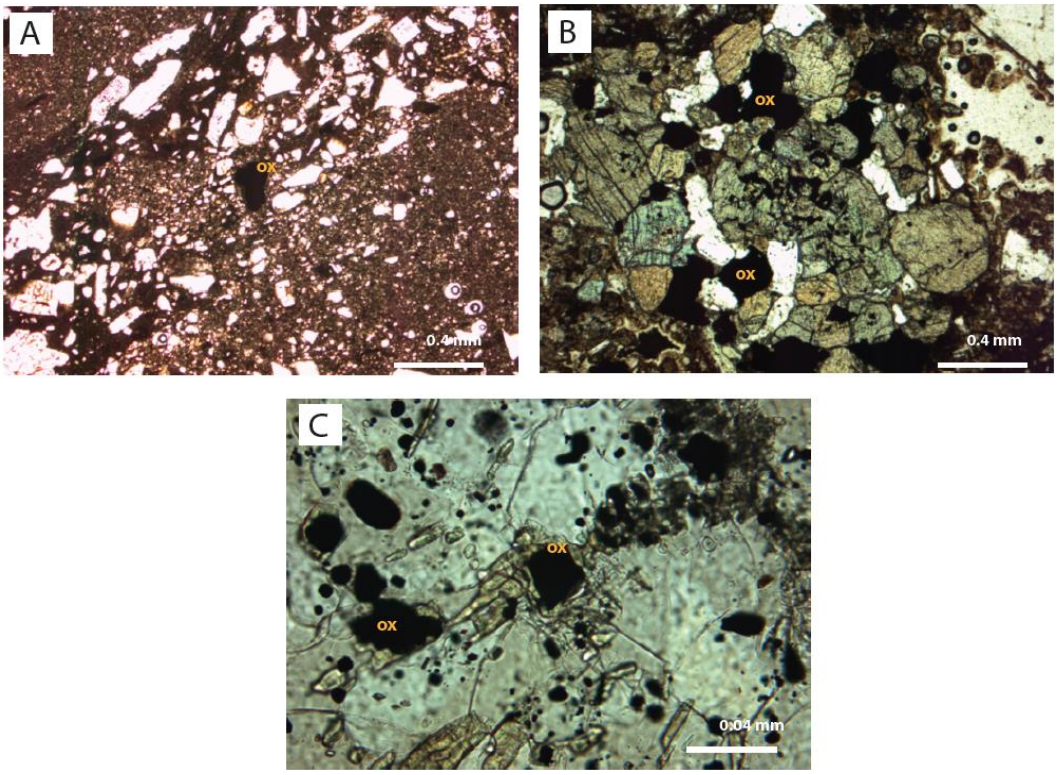

Figure 3.8. Photomicrographs of Fe-Ti oxides within the deposits of BLC.(A) 0.3 mm, angular, sub-cubic Fe-Ti oxide (likely titanomagnetite) within the banded groundmass of a dense bomb (sample BL30, Rp-Sc1). (B) Skeletal growths of Fe-Ti oxides within a large glomerocryst (sample BL29, Rp-Ag4). (C) A cluster of fine, angular, cubic Fe-Ti oxides along with very fine orthopyroxenemicrolites (sample BL15, BLC lava flow).

Olivine

Olivine was found as a very rare component of some Rotopaunga Scoria samples and some western rim deposits (Rp-Sc1-3: BL22, BL30, BL31, BL33 and BL36a; western rim: BL33, BL34, BL35 and BL35b). Olivine phenocrysts were found in loose scoria/spatter, as well as in dense bombs. When present, olivine occurs as sparsely populated, large (~0.5 to 3 mm) irregular, anhedral crystals (Figure 3.9A and B). All olivine crystals found have rims of fine-grained orthopyroxene, indicating disequilibrium with the enclosing magma. Some iddingsite was found in BL03, which is possibly formed as a consequence of olivine alteration (Figure 3.9C). Hobden (1997) suggested that some fine-grained pyroxenes within Tongariro deposits may actually be fine xenocrysts and originate from a deeper magma source, and that they represent olivine crystals that have completely reacted to pyroxene; an example of this may be Figure 3.7F.

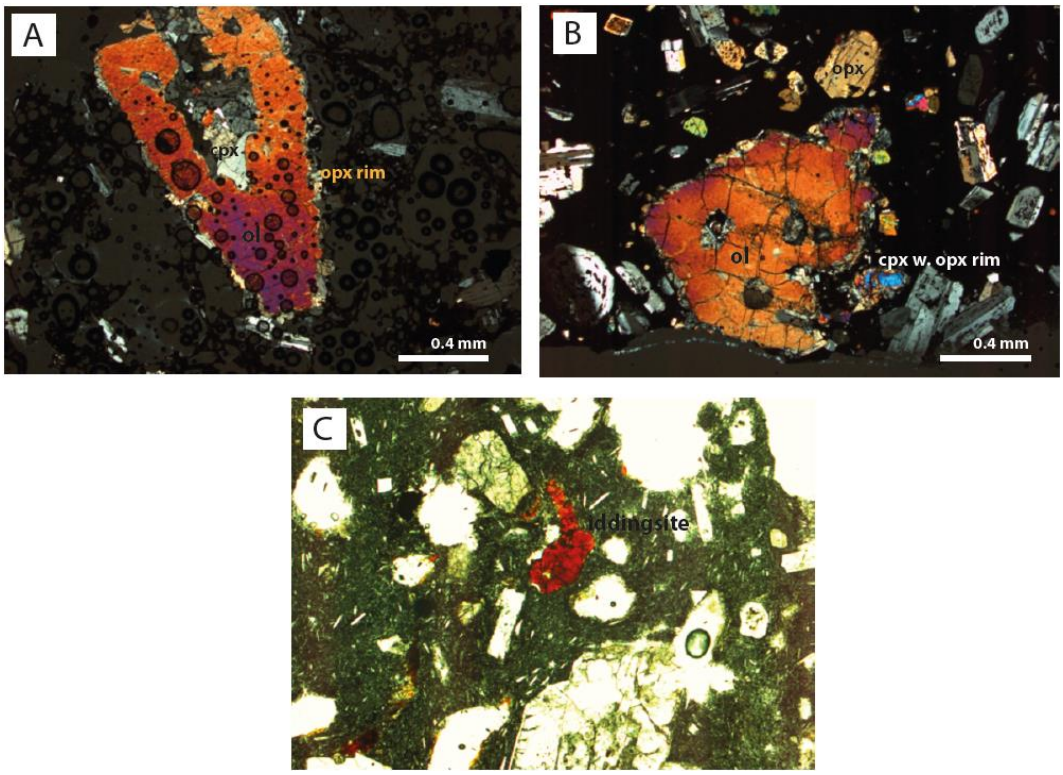

Figure 3.9. Photomicrographs of olivine in BLC deposits. (A) Large, anhedral phenocryst in a highly vesicular, glassy groundmass. The rim is surrounded by a thin ring of fine orthopyroxene (sample BL31, Rp-Sc1). (B) Olivine within in a glassy dense bomb. Rimmed by fine orthopyroxene. Holes in the crystal face are in-filled by pyroxenes and Fe-Ti oxides (sample BL22, Rp-Sc3). (C) Red iddingsite mineralisation has possibly replaced olivine (sample BL03, south rim.

Apatite

Euhedral-subhedral prismatic, elongate apatite was found on a small number of plagioclase crystals (Figure 3.6F) and occurs as a very minor phase. These apatites are microphenocrysts (generally <0.1 mm).

3.4.2 Groundmass

The samples display a range of groundmass types that range from 30 to 69% modal abundance of the bulk rock (Table 3.1). The groundmass is microcrystalline to cryptocrystalline (Figure 3.10) and many varieties are glass bearing or glass-rich giving rise to a dominantly hyalopilitic texture (Figure 3.11, Figure 3.12). Groundmass microlites are typically less than 0.1 mm and are dominated by euhedral to subhedral laths and tabular plagioclase; and lesser subhedral prismatic to anhedral pyroxene (mostly orthopyroxene) and anhedral granular Fe-Ti oxides. Microlites often show a sub-trachytic texture and a sub-

parallel alignment around phenocrysts. Sub-trachytic textures are common in the Rotopaunga Agglutinates and crater rim deposits. Trachytic textures are particularly prominent in the BLC lava flow. Aligned laths often swirl around the larger phenocrysts, which themselves may also be crudely aligned(Figure 3.10A). Dense glassy bombs display irregular bands and patches (1-5 mm thick) of microcrystalline and glassy textures (section 3.4.5).

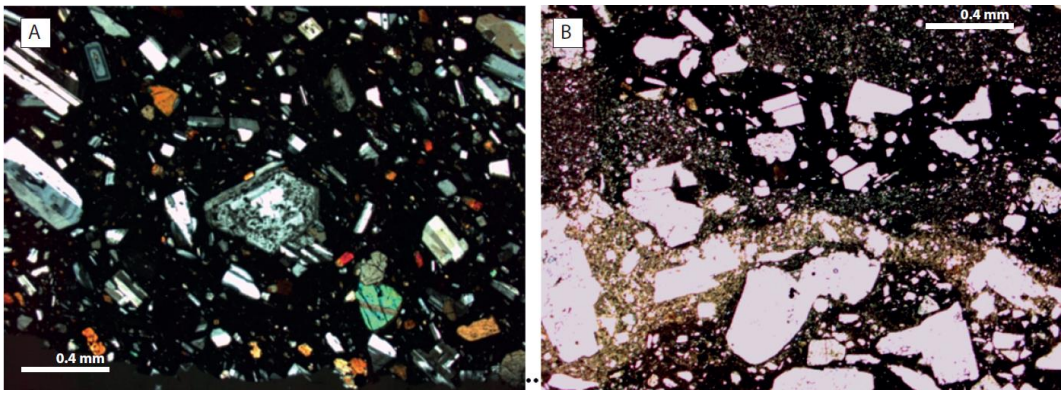

Figure 3.10. Photomicrographs of groundmass textures within the proximal deposits of BLC. (A) Shows sub-trachytic texture of phenocrysts and groundmass minerals. They are flow aligned and swirl slightly around the large sieved plagioclase in the centre of the image (sample BL16, BLC lava flow). (B) A typical texture found in dense bombs of the Rotopaunga Scorias (sample BL30, Rp-Sc1).

3.4.3 Glass

The majority of samples contain glass that occurs within, the groundmass as a minor constituent (Figure 3.11) as inclusions within phenocrysts (most commonly sieved plagioclase), and interstitially within glomeropophyritic clots. Glassy inclusions occur as small, indeterminate, pale to medium brown (often devitrified) patches interstitial to groundmass crystals. Unaltered glass was often observed as brown patches (up to 1 µm across) within the interstices of glomerophorphyritc clots. The groundmass of some scoria samples are near-completely holohaline and comprised of light to dark brown glass, with very few fine microcrystals interspersed throughout (Figure 3.12). This glassy groundmass is often in the early stages of devitrification (Figure 3.11A).

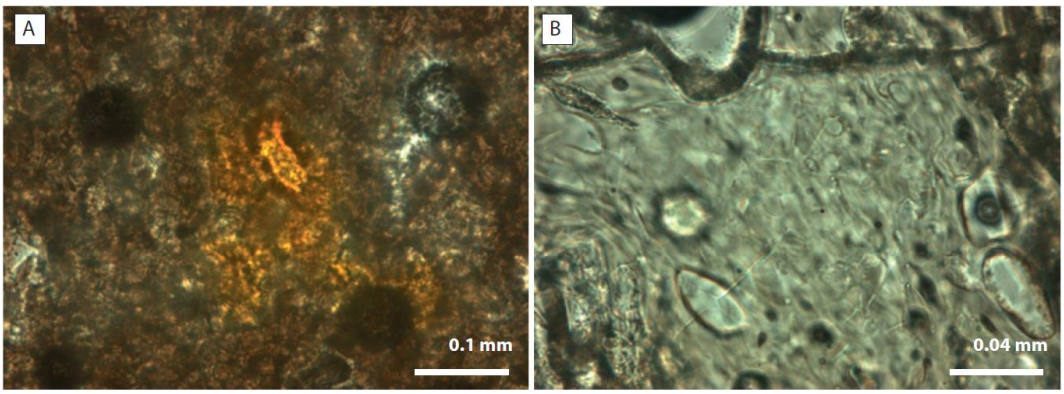

Figure 3.11. Photomicrographs of glass within deposits proximal to BLC. (A). Glass sphericles in multiple stages of devitrification (sample BL26, Rp-Ag1). (B) Microlites within the same glassy groundmass.

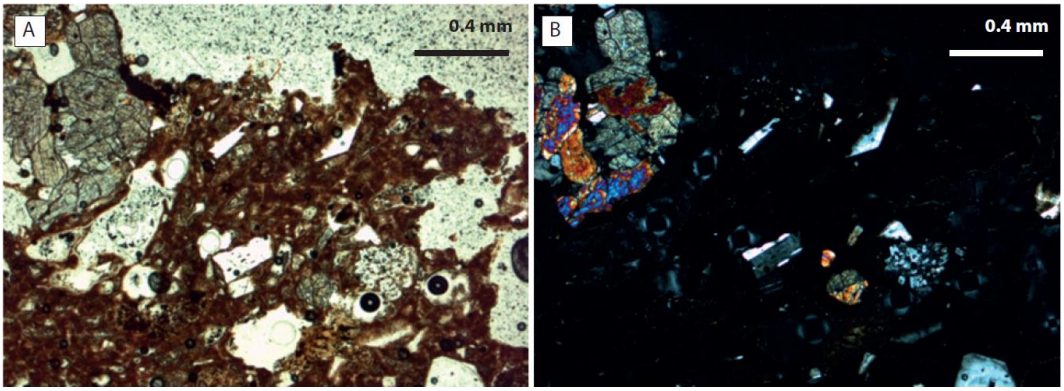

Figure 3.12. Photomicrographs of a near-holohaline groundmass typical of the highly vesicular clasts of the Rotopaunga Scoria units. (A) Shows a number of phenocrysts and one large glomerocryst within a devitrified groundmass (ppl) (B) Shows the same view under xpl. Notice the sparse nature of groundmass crystals. The few that are present are very angular and shard-like (sample BL28, Rp-Sc3).

3.4.4 Xenoliths

Xenoliths range from <1 to 5% abundance. They are typically subangular to subrounded and elongated in shape. Typical sizes range from 0.1 to 5 mm (Figure 3.13). Xenoliths are typically quartzo-feldspathic sedimentary rocks, which are fine grained, equigranular and contain quartz, plagioclase, fine pyroxene crystals and some Fe-Ti oxides. Some xenoliths show moderate-intense sieve textures, often more concentrated in the core (Figure 3.13). Some appear to have been dissolved around the edges, particularly smaller xenoliths (Figure 3.13A). The majority appear to be meta-sedimentary, as many of the grain contacts show triple junction points. The source of the quartzo-feldspatihic xenoliths is most likely to

be basement greywacke that the TgVC has evolved through, and been built on top of (Graham *et al.* 1988; Hobden 1997).

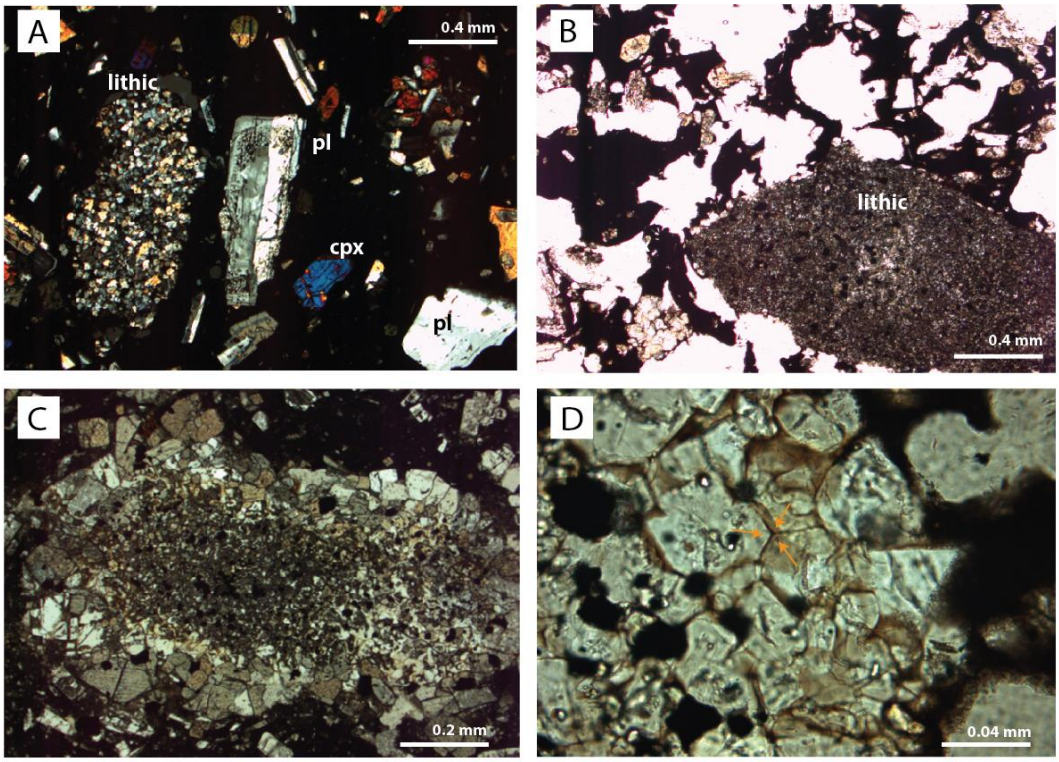

Figure 3.13. Photomicrographs of xenoliths within deposits of BLC. (A) A subrounded, elongate, fine grained, equigranular xenolith comprised of quartz, plagioclase and pyroxenes. The xenolith is adjacent to a sieved (right) and a clear (lower right) plagioclase (sample BL06, SW rim). (B) A large sub-rounded fine grained xenolith in a porphyritic highly vesicular glassy groundmass (sample BL32a, western rim). (C) A large subrounded and elongate xenolith. Crystals are equigranular but fine towards the core. The larger crystals around the rim may be re-growths. The xenolith displays severe sieving in the core that decreases outwards (sample BL27, Rp-Ag1). (D) Triple-point junctions between mineral phases in a xenolith (sample BL15, BLC lava flow).

3.4.5 Banded and Mingled Textures

Some of the dense bombs of the Rotopaunga Scorias, and the more coherent samples of the BLC lava flow contains what appear to be completely separate compositions of irregular banded and patchy zones (1-5 mm thick) of microcrystalline and glassy textures(Figure 3.14, Figure 15A-F). The bands are typically wavy, and pinch in and out, with some small arms branching off and inter-fingering with zones of other compositions. These textures are usually visible by eye, however in some of the samples the texture is only visible under microscope. Phenocrysts are sometimes confined to the banded zones, while

atother times they cross over the zones and appear more mixed, becoming homogenized. There are different groundmass and phenocryst modal sizes in the different bands, often with each zone in a different stage of devitrification. Occasionally the different zones are more blob-like, (e.g. Figure 3.15E).

Three petrographically distinct zones were identified in the Rp-Sc1 deposits:

i. Dark glassy groundmass, usually containing subhedral phenocrysts and finer shard-like micro-crystals (most visible in Figure 3.15A, C and D).
ii. Light to pale brown, less glassy groundmass containing many fine shards, and usually containing a moderate abundance of phenocrysts (visible in Figure 3.15A and C).
iii. A groundmass made entirely of fine shard-like crystals and devoid of phenocrysts. An appearance that suggests the magma was entirely disintegrated (Figure 3.15F).

Two zones were identified within the BLC lava:

i. Darker coloured, phenocryst-rich zones. Typically showing slightly greater devitrification (Figure 3.15B).
ii. Lighter coloured, phenocryst-poor zones comprised of fine shard-like groundmass constituents (Figure 3.15B).

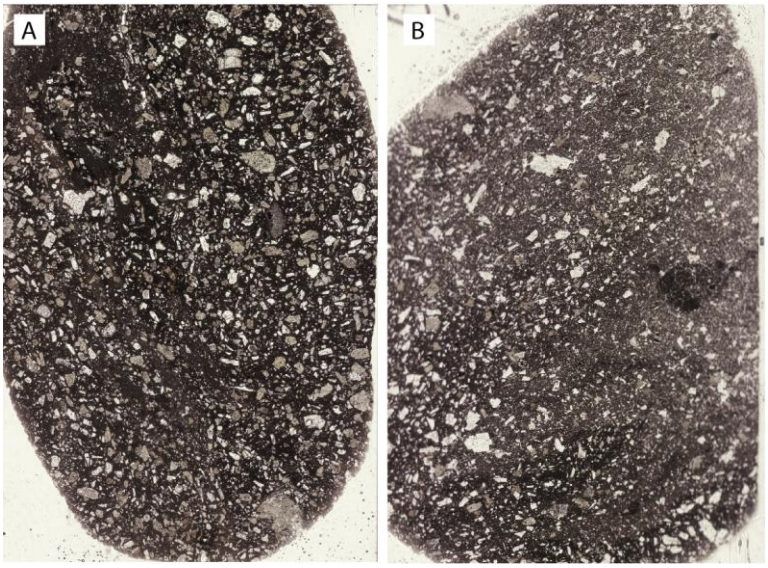

Figure 3.14. Scans of selected banded sample thin sections. (A) A dense bomb sample (BL30, Rp-Sc1). Thin streaks of fine-crystalline material within a dominantly phenocryst-rich glassy groundmass. (B) Streaked bands comprised of dark, phenocryst-rich zones and more fine-grained lighter-coloured zones (sample BL16, BLC lava flow).

Donaghue *et al.* (1995) described samples with visible streaking and banded zones, that occur in varying amounts, with sharp contacts between zones. Griffin (2007) examined dark and light glass banding on North Crater and found that within a single clast, the darker bands contained glass lower in SiO_2 and K_2O, and the lighter zones contained glass higher in SiO2 and K_2O. The importance of this texture, and the implications for magma and eruptive processes, is discussed in Chapter 5 section 5.7.

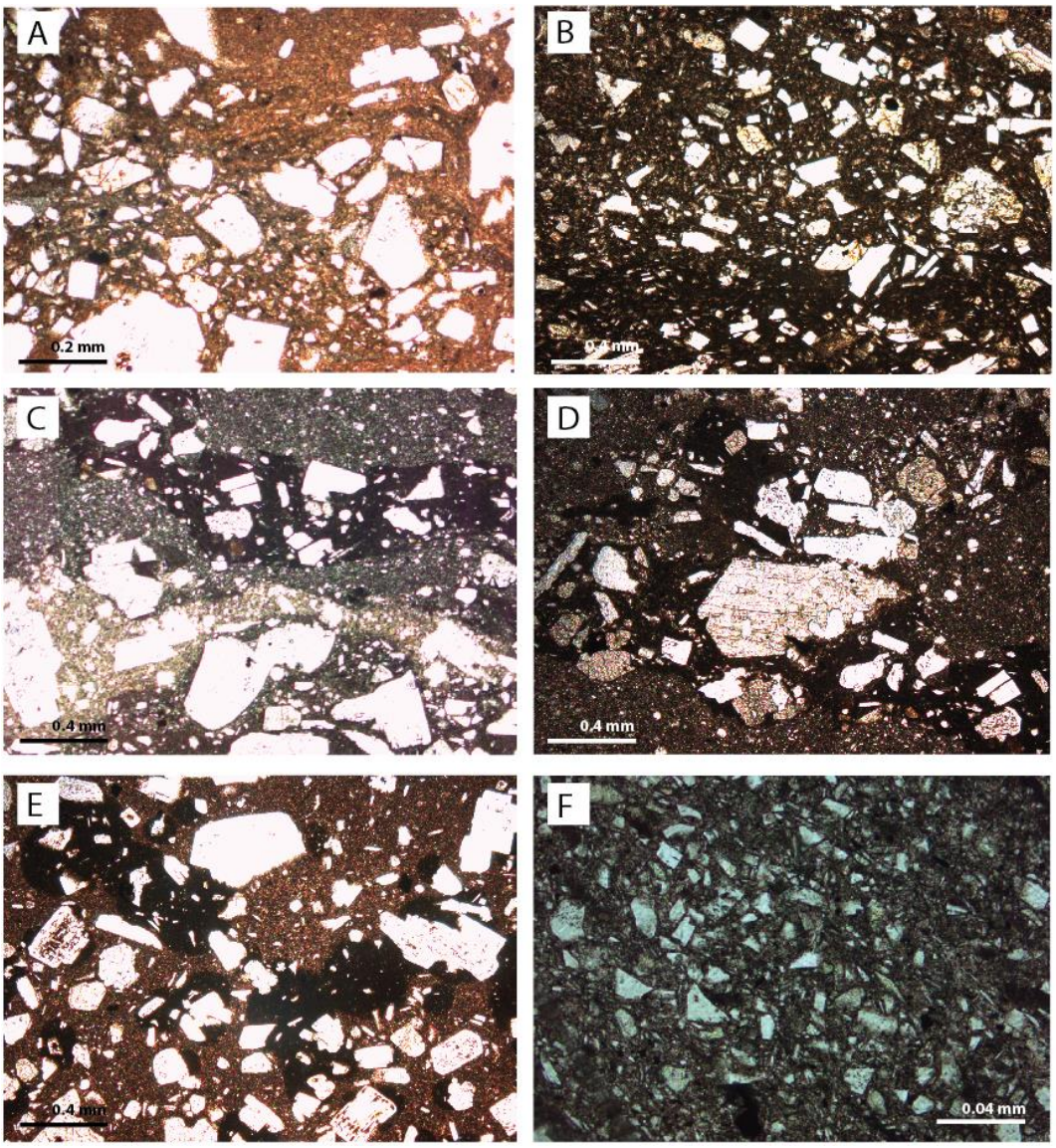

Figure 3.15. Photomicrographs of banded zones within selected samples of BLC proximal deposits. (A) Banding and intricate swirling of zones of differing crystallinity in a dense clast (sample BL19a, Rp-Sc1). (B) Thin banded zones of varying crystallinity and devitrification (sample BL16, BLC lava flow). (C) Very strongly defined banding of a dense breadcrust bomb (sample BL30, Rp-Sc1). (D) Further banding patterns from the previous sample (BL30). (E) Zoning can rarely appear blob-like (BL30). (F) Fine shard-dominated zones are comprised of disintegrated phenocrysts and contain shards of all of the major mineral phases (BL30).

3.5 Variation between Volcano Stratigraphic Units

This section discusses the variation in petrography across different volcano stratigraphic units of the BLC study area.

3.5.1 The Rotopaunga Agglutinates

The Rotopaunga Agglutinates (Rp-Ag1-4) are hypocrystalline to near holohaline, moderately porphyritic and glomeroporphyritic. They contain phenocryst assemblages typically over 30% (Table 3.1). The grain size is typically fine (less than 1 mm) although some phenocrysts and phorphyritic clots can be as large as 3 mm. Phenocrysts range from euhedral to anhedral. Plagioclase makes up ~62% of the total phenocryst assemblage (Table 3.1) with pyroxenes making up ~37%. Orthopyroxene is typically dominant over clinopyroxene (Rp-Ag4 is the exception, where clinopyroxene is dominant over orthopyroxene).The percentage of phenocrysts occurring as part of a glomerocryst range from 17.36 to 44.23%. Olivine is absent. Fe-Ti oxides range from 1.33% to 4.33%. Groundmass content ranges from 40 to 60%. Bulk rock textures are generally hyalopilitic, often with microlites displaying trachytic textures. Glass comprises up to 15% of the groundmass, with most glass in some stage of devitrification. Quartzo-feldspatihic xenoliths are a common feature, ranging in size from 0.5 mm to more than 5 mm and comprising ~1% of the bulk rock. The vesicularity of the Rotopaunga Agglutinates can be as great as 15% within intensely-strongly welded samples, and up to 30% in moderately welded samples. The breccia found at the base of the agglutinates was sampled for density and vesicularity measurements and the results are given in Table 3.2 below. Mean density is 1.24g cm^{-3}, and ranges from 0.71g cm^{-3} to 2.16 g cm^{-3}. Mean vesicularity is 52.26%, minimum 16.75% and maximum of 72.77%; this is typical of most scoria deposits.

Table 3.2. Density and vesicularity values of loose scoria and dense bombs of the Rotopaunga Scorias, unconsolidated basal material of the Rotopaunga Agglutinates, and autobreccia from the base of the BLC lava flow.

		Density (g cm^{-3})			Vesicularity (%)		
Unit	**Deposit Type**	**Min**	**Max**	**Mean**	**Min**	**Max**	**Mean**
Rotopaunga Scorias	Non-poorly welded Scoria	1.03	1.51	1.22	41.82	60.56	52.99
	Dense bombs	2.41	2.59	2.50	0.23	7.35	3.71
Rotopaunga Agglutinates	Base breccia	0.71	2.16	1.24	16.75	72.77	52.26
Lava Flow	Base Breccia	1.19	1.60	1.38	38.35	54.28	47.09

3.5.2 The Rotopaunga Scorias

The Rotopaunga scoria units are hypocrystalline, moderately porphyritic and glomeroporphyritic. They are dominated by fine grained phenocrysts which range in abundance from 20 to 25% in scoria clasts, and 38 to 49% in dense bombs (Table 3.1).Plagioclase makes up 57.0 to 66.2% of the total phenocryst composition and often displays moderate-intense sieve textures, and some patchy zoning (although clean, euhedral crystals are present). Pyroxene phenocrysts account for 33.8 to 44-4% of the total phenocryst assemblage, with orthopyroxene dominant over clinopyroxene. Olivine, when present, is rare (<1% modal) and occurs as large (up to 4 mm) phenocrysts with fine orthopyroxene reaction rims (Figure 3.7). Fe-Ti oxides range from 0.3 to 2% (Table 3.1).The percentage of phenocrysts occurring as part of a glomeroporphyritic clot is lower than the Rotopaunga Agglutinates, and ranges from 13.2 to 33.8%. Groundmass abundance ranges from 30 to 60% and are typically hyalopilitic to near holohaline in scoria samples (Figure 3.7D, Figure 3.12A). Glass is present with varying degrees of devitrification. The groundmass in dense bombs displays a banded texture of light and dark groundmass and differing crystal size ranges with some bands comprised entirely of shard-like material (Figure 3.15F). Xenoliths are quartzo-feldspathic and make up ~1 %. They range in size greatly and may be as large as 4 mm.

Vesicularity within the Rp-Sc units is variable (results in Table 3.2). Non-poorly welded clasts range in vesicularity from 40-60%, with a mean of 52.99%. Vesicles are rounded or elongate, and often coalesced. Dense bombs range in vesicularity from 7.35 to 0.23%. Bubbles are typically small and rounded.

3.5.3 Western and Southern Crater Rim Deposits

The agglutinates that mantle the western and southern rim of BLC are hypocrystalline, moderately porphyritic and glomeroporphyritic. The deposits are dominated by 30% fine grained phenocrysts, euhedral-anhedral in shape. Grain size is typically less than 1 mm although some phenocrysts and many glomerophorphyritic clots are larger. Plagioclase makes up ~60% of the total phenocryst assemblage (Table 3.1). Oscillatory zoning and sieve textures are common. Pyroxenes make up 37 to 39% of the phenocryst assemblage. Clinopyroxene is dominant over orthopyroxene in most samples. The percentage of phenocrysts occurring as part of a glomeroporphyritic clot is 26 to 31% (Table 3.2). Olivine was found in several samples on the western rim (BL33, BL34, BL35 and BL35b). Fe-Ti oxides range from <1% to 5%. Groundmass content ranges from 40 to 69% with textures that are generally hyalopilitic, often with microlites displaying subtrachytic textures. Some glass occurs in the groundmass, with most being in some stage of devitrification. Xenoliths are common and range in size from 0.4 mm to ~5 mm. Vesicularity can be 15% within intensely and strongly welded facies and greater than 30% in moderately welded facies.

3.5.4 The Blue Lake Crater Lava Flow

The BLC lava flow is hypocrystalline and porphyritic. The rock contains 0.3 to 2 mm euhedral-anhedral phenocrysts that make up 24 to 34% of total bulk rock (Table 3.1). Plagioclase makes up ~55 to 68% of the phenocryst assemblage. Orthopyroxene (5.3 to 6.6% bulk rock) is dominant over clinopyroxene (2.6 to 5.6%) in three of the four samples examined (Table 3.1). Oscillatory and patchy zoning are common in plagioclase, as are sieve textures of multiple severity. Fe-Ti oxides range from <1 % to 3.33% of bulk rock. The lava is less glomeroporphyritic than other units, with the percentage of phenocrysts as part of

a glomerocryst ranging from 6 to 29%. Xenoliths occur sporadically and range in size from 0.4 to 5 mm, with many containing triple-junction-point grain contacts.

The lava flow differs petrographically between the two facies types. The autobrecciated facies has less groundmass, 27 to 40% (Table 3.1) and is very glass-rich, with fine (less than 0.1mm) shard-like primary minerals. Phenocrysts make up 24 to 27% of the total bulk rock. The autobreccia facies is higher vesicularity, up to 54% (Table 3.2). The crystalline lava facies has much higher groundmass content 40 to 61% (Table 3.1) which is haliopilitic, feldsopheric and often (sub)trachytic (Figure 3.10A). This facies has a higher phenocryst composition, 30 to 34% and contains more Fe-Ti oxides (Table 3.1). The vesicularity of the internal component of the flow is much lower than the autobreccia, with values ranging from 5 to 10% of bulk rock.

3.6 Hydrothermal Alteration Zone

Five samples were obtained from the outcrop within the area of alteration. Phenocrysts are quite well preserved and the alteration minerals mainly replace groundmass (Figure 3.16). The groundmass is interstitial, with very fine grained cryptocrystalline, lath-like shards of clays and hydroxide minerals. This gives the samples a very mottled appearance. In places, primary groundmass minerals are preserved (with extinction angles etc) although most of the groundmass crystals are only psudomorphs of primary groundmass minerals. The groundmass is slowly becoming replaced by irregular domains of dark grey/black/brown areas which are intermingled with blebs of bright yellow/orange/brown, thinly layered, irregular secondary growths that form in patchy, vermiform (worm-like) networks.

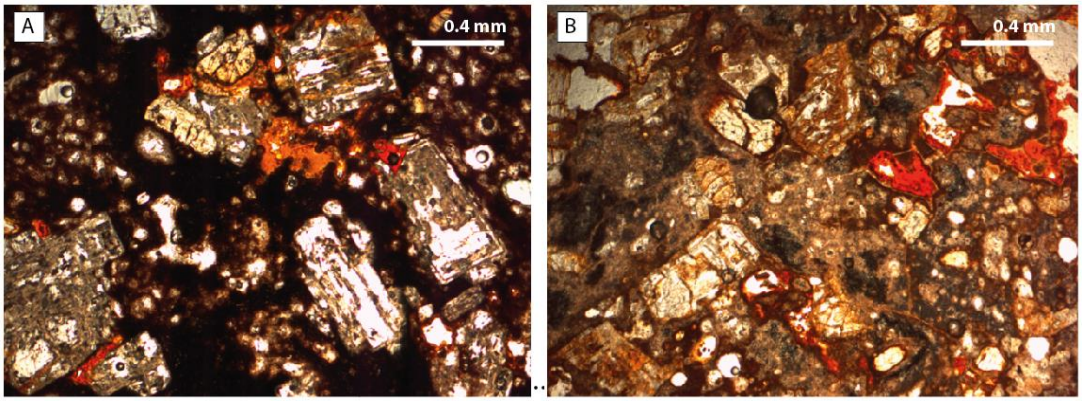

Figure 3.16. Photomicrographs of hydrothermally altered samples described in text. (A) SampleBLht2and (B) sample BLht5.

Chapter Four

Mineralogy and Geochemistry

4.1 Introduction

This chapter discusses the geochemical properties of the proximal and vent forming deposits of Blue Lake Crater. Selected samples have been analysed for phenocryst mineralogy and whole rock geochemistry in order to determine magma composition and understand magmatic processes. Six samples were examined for phenocryst compositions determined by electron microprobe analysis (EMPA). 36 samples were selected for whole rock geochemistry carried out by x-ray fluorescence (XRF) spectrometry. A complete set of electron microprobe results are included in Appendix Five. XRF results are presented in Appendix Six (major elements) and Appendix Seven (trace elements).

4.2 Methodology

4.2.1 Electron Microprobe Methodology

Polished thin sections of six selected samples from proximal and vent environments of BLC were prepared using the methods outlined in Chapter 3section 3.1. Samples intended for EMPA analysis did not receive a cover slip but were polished on a lap wheel using #800 polish paper and then fine alumina powder. These samples are; BL06 (SW rim), BL10 (Rp-Ag4), BL15 (BLC lava flow), BL19 (Rp-Sc1), BL27 (Rp-Ag1), and BL30 (Rp-Sc1). Samples were coated with carbon graphite before being analysed. The apparatus used was a JEOL-840M electron microprobe housed at Massey University in Palmerston North under the guidance of Professor Shane Cronin. All analyses were made using an electron gun with an accelerating voltage of 15 kV, an electron beam diameter of 3 µm with a run time of 120 seconds. Phenocrysts analysed include; plagioclase, orthopyroxene, clinopyroxene, olivine and Fe-Ti oxides. Ten elements were measured; SiO_2, TiO_2, Al_2O_3, FeO, MnO, MgO, CaO, Na_2O, K_2O, P_2O_5, SO_3; as well as Cl, Cr_2O_3 and NiO.

4.2.2 X-Ray Fluorescence Methodology

Major and trace elements for 36 samples were measured using a Spectro-Lab 2000 x-ray fluorescence apparatus at the University of Waikato. Ten major elements (SiO_2, TiO_2, Al_2O_3, Fe_2O_3, MnO, MgO, CaO, Na_2O, K_2O, P_2O_5) and 21 trace elements (S, Cl, V, Cr, Co, Ni, Cu, Zn, Ga, As, Rb, Sr, Y, Zr, Nb, Ba, La, Ce, Pb, Th, U) were measured. Small sections of rock cuttings were dried overnight at 80°C. Rock fragments from individual samples were then ground to fine powder in a tungsten carbide ring mill. Larger pieces were broken into small fragments with a heavy hammer while wrapped in paper to prevent contamination. Thorough cleaning and drying of the ring mill was necessary between each sample. Once powdered, samples were stored in labelled glass jars and dried overnight at 80°C prior to further preparation.

Fused Disks for Major Element Analysis

Fused glass discs were created using 0.35 g of each powdered whole rock sample, mixed in a dry platinum crucible with 2.5-2.55 g of flux (for andesites the flux used was 35 % Li-tetraborate/65 % Li-metaborate). Weights were recorded prior to heating. Samples were step-heated over a period of 45 minutes to 1040°C within a Broadway fusion furnace. After ~15 minutes at 1040°C the molten samples were quickly poured onto a heated (~250°C) graphite surface and pressed to produce glass discs. Samples, while ~200°C, were trimmed and labelled. The glass discs were cooled slowly overnight on a hotplate. Cross-contamination was a factor, and so special care was taken when measuring dry powders and cleaning tools and crucibles after each use.

Trace Elements

Trace elements were analysed using pressed powder pellets. Pellets were prepared by mixing 5g of powdered whole rock with ~15 drops of liquid PVA binder. The powder and PVA was mixed using a wooden tongue depressor until homogenous. The mix was poured into a small aluminium cup and compacted using a hydraulic press. The samples were then labelled and dried in an oven at 70°C overnight to evaporate the PVA binder before running the analysis.

Loss on Ignition

Loss on ignition (LOI) was determined for each sample by heating 2g of the powdered whole rock sample in a silica crucible at 1000°C for one hour. The samples were then cooled and weighed to ascertain the weight loss of the sample. Data is presented as a percentage.

4.3 Electron Microprobe Analysis

The results of electron microprobe analysis are discussed for each of the major phenocrysts present in proximal and vent forming deposits of BLC. Classification of mineral phases are determined, and cores and rims of selected phenocrysts are examined.

4.3.1 Plagioclase

Plagioclase feldspar is the most abundant mineral phase in the proximal and vent forming deposits of BLC. 46 probes of plagioclase phenocrysts were undertaken. A selection of representative data for plagioclase phenocryts is given inTable .Results are also plotted on an orthoclase-albite-anorthite ternary classification diagram after Rollingson(1993) (Figure 4.1). The plot reveals that BLC plagioclase is comprised of labradorite and bytownite, of which laboradorite is slightly dominant. The deposits range in anorthite composition from An_{58-84}. This falls within the range of plagioclase compositions across the TgVC, An_{45-90} (Hobden 1997) and is a higher range than in neighbouring North Crater eruptives, which range from An_{48-77}. (Griffin 2007).Ruapehu plagioclases range from An_{89-40} (Graham and Hackett 1987). Plagioclase has a significantly large variation in major oxide compositions. SiO_2 ranges from 47.36 to 57.04 wt. %; Al_2O_3 ranges from 25.92 to 31.98 wt. %; CaO ranges from 7.54 to 12.13 wt. % and Na_2O ranges from 2.34 to 5.31 wt. % (Appendix Five).

EMPA analyses of plagioclase cores and rims reveals that many of the crystals are geochemically zoned. Of the limited sample set analysed (Table 4.2) normal zoning is most common. Normal zoning consists of a Ca-rich core becoming progressively more Na-rich towards the rim (Sakuyama 1978, 1981; Nixon

1988a). Other crystals were revealed to be reverse-zoned, where Na-rich cores become progressively Ca-rich towards the rim (Sakuyama 1978, 1981; Nixon 1988a). Normal zoning is indicative of fractional crystallisation. Reverse zoning, along with sieve textures, is suggestive of magmas in disequilibrium, which indicates that the magma has undergone decompression or magma mixing and/or mingling (Sakuyama 1978, 1981; Nixon 1988a).

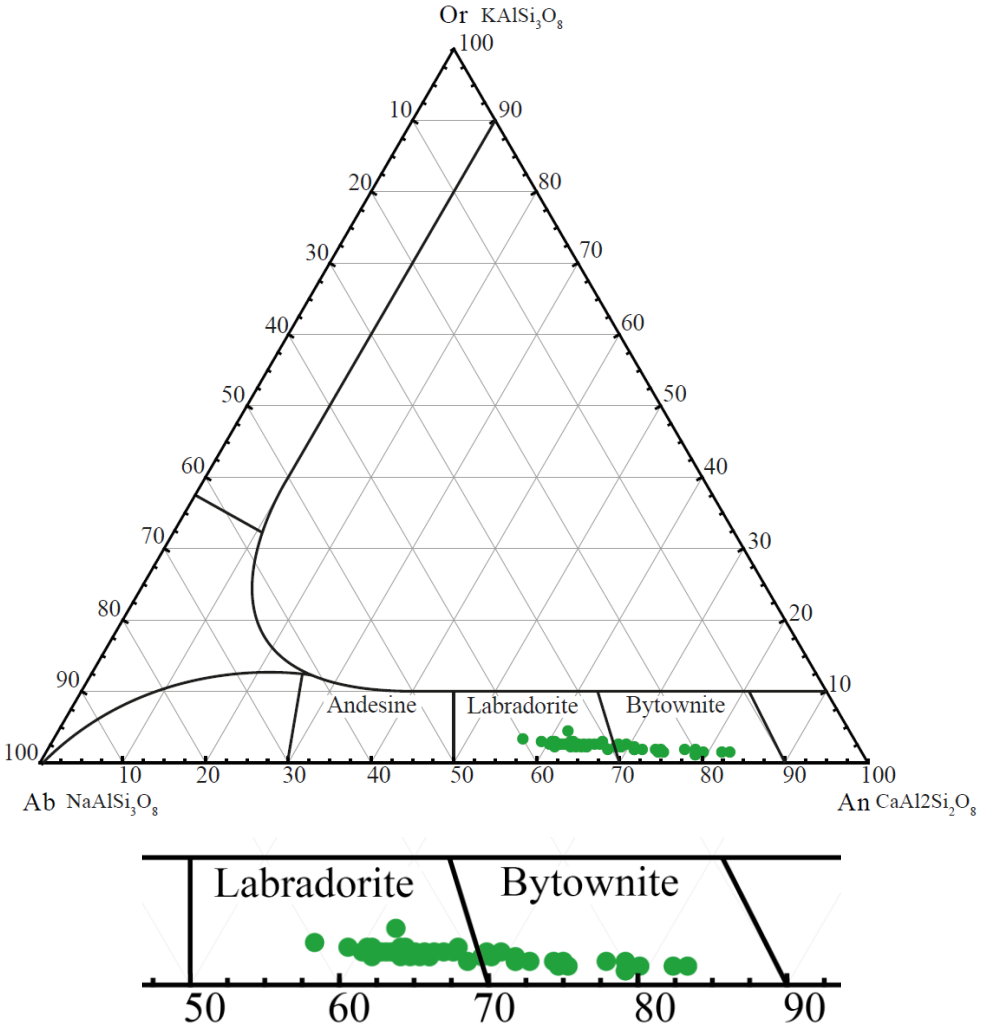

Figure 4.1. Orthoclase (Or)-albite (Ab)-anorthite (An) ternary diagram of plagioclase phenocrysts. After Rollingson (1993).

Table 4.1. Representative data from electron microprobe analysis of major mineral phases in BLC eruptives. A full set of results is given in Appendix Five.

	SiO2	TiO2	Al_2O3	FeO	MnO	MgO	CaO	Na_2O	K_2O	P_2O_5	SO_3	Cl	Cr_2O_3	NiO	Total
Plagioclase															
BL6-16	53.26	0	29.04	0.72	0	0	9.4	4.73	0.35	0.15	0	0	0.06	0.15	97.87
BL6-21	49.73	0.11	31.1	1.03	0	0	11.31	3.11	0.26	0	0	0	0.15	0.02	96.82
BL27-7	52.92	0.13	27.7	0.54	-0.04	0.07	8.39	5.01	0.29	0.07	-0.07	0.08	0.14	-0.1	95.14
Clinopyroxene															
BL10-9	51.04	0.46	1.46	13.55	0.37	13.37	14.09	-0.01	0.01	0.16	0	0.05	0.24	-0.11	94.69
BL10-20	51.62	0.46	1.25	13.71	0.29	12.93	14.64	0.31	0.08	0	-0.02	0	0.2	0.02	95.5
BL27-23	50.23	0.62	2.17	13.75	0.3	13.18	13.92	0.24	0.05	0.01	-0.04	-0.01	0	-0.02	94.41
Orthopyroxene															
BL6-18	52.49	0.33	0.89	22.53	0.66	21.76	1.09	0	0.05	0	0	0	0	0.05	99.85
BL19-16	49.69	0.23	0.72	27.73	0.51	17.91	0.98	0.12	0.05	-0.07	0.07	0.07	0.01	-0.04	97.98
BL27-12	52.86	0.3	0.94	17.32	0.3	24.66	1.27	-0.11	0.05	0.08	0.01	0.05	-0.02	0	97.72
Olivene															
BL31-22	38.95	-0.1	0.08	20.76	0.37	39.61	0.11	-0.11	0.04	0.06	-0.02	-0.01	-0.06	0.23	99.9
BL31-25	39.04	0.02	0.04	17.24	0.25	42.66	0.09	0.08	0.04	-0.14	-0.03	0.14	0.03	-0.01	99.45
BL31-27	37.73	-0.07	-0.02	23.8	0.44	36.75	0.1	-0.05	0.08	-0.17	0.02	0.07	0	0.1	98.77
Fe-Ti															
BL27-16	-0.01	47.1	0.16	49.87	0.49	1.66	0.03	-0.01	0.01	-0.03	0.16	0.05	0.19	-0.06	99.63
BL27-22	0.03	46.19	0.02	50.54	0.5	1.27	-0.06	-0.09	0.04	0.06	-0.07	0.03	0.04	-0.06	98.44
BL6-22	0.08	14.51	3.12	77	0.36	1.84	0	0	0	0	0	0.04	0.35	0	97.28
BL15-12	0.14	17.01	2.27	75.14	0.39	1.65	0.07	0.3	0	0.01	0.01	0.04	0.34	0.09	97.46

Table 4.2.Core and rims of plagioclase phenocrysts within BLC samples.

Plagioclase	CaO	Na_2O	Zonning
BL10-21 CORE	10.44	3.37	
BL10-22 RIM	8.71	4.67	Normal
BL15-25 CORE	10.97	3.56	
BL15-24 RIM	8.72	4.76	Normal
BL19-2 CORE	10.38	3.49	
BL19-3 RIM	8.76	4.43	Normal
BL19-10 CORE	9.01	4.21	
BL19-11 RIM	8.1	4.92	Normal
BL19-13 CORE	10.16	3.4	
BL19-14 RIM	10.88	2.8	Reverse
BL31-12 CORE	11.52	2.94	
BL31-13 RIM	12.13	2.34	Reverse
BL31-17 CORE	11.46	2.89	
BL31-18 RIM	9.03	4.51	Normal

4.3.2 Pyroxenes

The two pyroxene phases present in the proximal and vent forming deposits of BLC are orthopyroxene and clinopyroxene. They are plotted on a wollanstonite-enstatite-ferrosilite ternary classification scheme after Rollingson (1993) (Figure 4.2). Representative clinopyroxene and orthopyroxene compositions from Appendix Five are given in Table .

The clinopyroxene phase is augite. Augite ranges in SiO_2 from 50.23 to 51.75 wt. % and ranges in composition; Fe_{20-34} Mg_{31-41} Ca_{34-39}. They follow a trend of decreasing calcium (Wo) with increasing iron content (Fs) (Figure 4.2). The compositional range is higher in Fe than most units across the TgVC, which, after Hobden (1997) is Fe_{7-24} Mg_{35-52} Ca_{35-46}. Fe is also considerably higher in the analysed samples than in those of the neighbouring North Crater; Fe_{9-18} Mg_{41-50} Ca_{39-42} (Griffin 2007).

Orthopyroxene exists as clinoenstatite and clinoferrosilite, with clinoenstatite moderately dominant (Figure 4.2). SiO_2 in orthopyroxene ranges from 49.69 to 53.72 wt. %. Orthopyroxene ranges from En_{41} to En_{61} ($Fe_{29-61}Mg_{38-71}$ Ca_{0-4}). Orthopyroxenes show higher Fe, and lower Mg than the range of compositions

across the TgVC; Fe_{11-42} Mg_{55-86} Ca_{1-5} (Hobden 1997). Orthopyroxenes analysed in this study are more enstatite-rich and lower in calcium than North Crater orthopyroxene; En_{41-70} Fe_{26-47} Mg_{41-70} Ca_{3-8} (Griffin 2007).

Pyroxenes appear homogeneous under microscope, however microprobe analysis reveals many to be zoned. Two orthopyroxenes (
Table 4.3) were found to be normally zoned. Normal zoning consist of Mg- and Ca-rich cores that become Fe-rich towards the rim (Sakuyama 1978; Nixon, 1988a; Nakagawa *et al.* 2002). One clinopyroxene and three orthopyroxenes were found to be reverse zoned. Reverse zoning occurs when Fe-rich cores transition into Mg-rich rims (Nakagawa *et al.* 2002). Hobden (1997) noted that strong reverse zoning is common in young eruptives, particularly those from Red Crater, Pukeonake, and NE Oturere. Reverse zoning is likely related to magma mixing processes (Sakuyama 1981; Nixon 1988a;Feeley and Davidson 1994; Nakagawa *et al.* 2002).

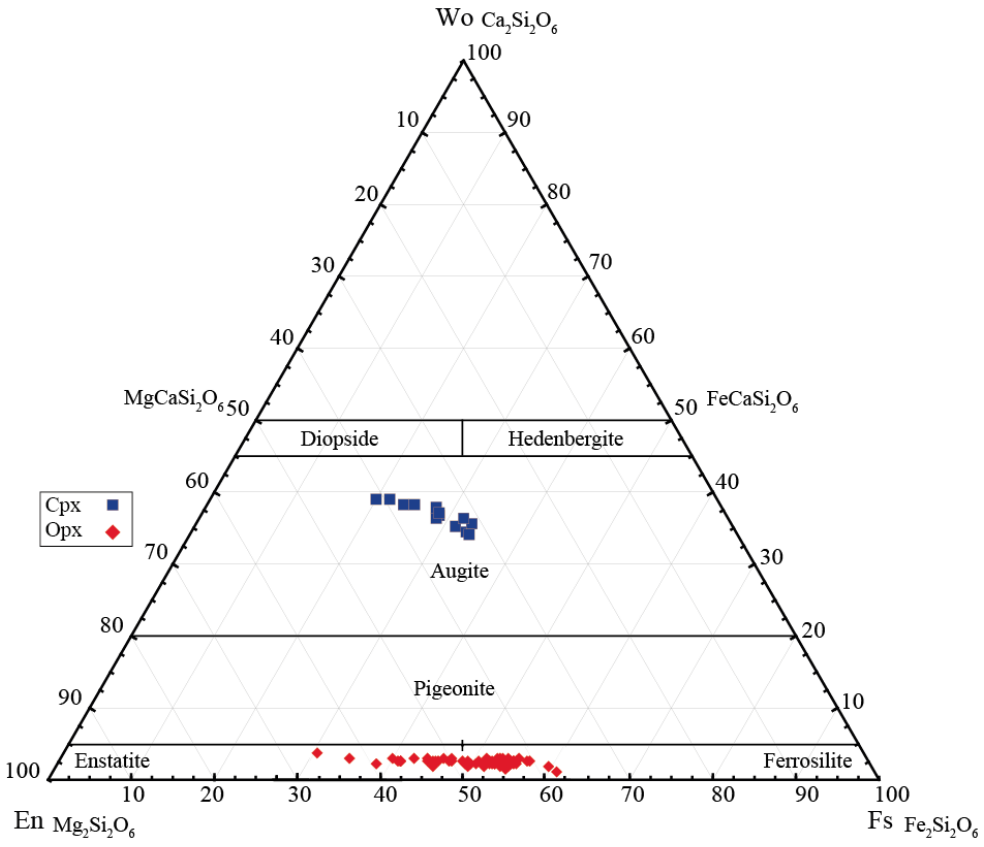

Figure 4.2. Wollanstonite (Wo)-enstatite (En)-ferrosilite (Fs) ternary diagram of pyroxene phenocrysts after Rollingson (1993).

Table 4.3. FeO and MgO concentrations in the Cores and Rims of augite and orthopyroxene phenocrysts.

Pyroxenes		FeO	MgO	Zonning	Mol % En variation
BL10-10	CORE	22.69	22.2		
BL10-12	RIM	25.77	19.37	Normal	2.83
BL15-2	CORE	29.14	18.07		
BL15-1	RIM	24.41	20.36	Reverse	2.29
BL15-9	CORE	24.49	20.08		
BL15-10	RIM	24.85	19.72	Normal	0.36
BL19-19	CORE	19.95	23.26		
BL19-20	RIM	16.81	25.9	Reverse	2.64
BL19-21	CORE	9.23	14.76		
BL19-22	RIM	8.22	15.08	Reverse	0.32
BL31-2	CORE	20.18	22.71		
BL31-3	RIM	18.65	23.89	Reverse	1.18

4.3.3 Olivine

Olivine is present as a minor (1-2 modal %) phenocryst phase in the proximal and vent forming deposits of BLC. It occurs in both Rotopaunga Scoria units as well as several samples of the western rim deposits. When present it occur as relatively large (0.5-4mm) phenocrysts that are often rimmed with granular orthopyroxene and/or clinopyroxene. Representative examples of olivine compositions are given in Table . Olivine compositions range from Fo_{61} to Fo_{73}, (Figure 4.3) which are relatively lower in Mg than neighbouring North Crater olivines Fo_{76} to Fo_{87} (Griffin 2007) and extend beyond the lower most Mg concentrations of olivines for the TgVC; Fo_{67} to Fo_{96} (Hobden 1997).

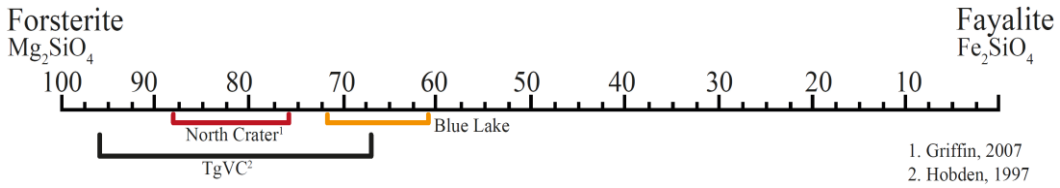

Figure 4.3. Classification diagram showing the range of olivine phenocrysts in Rp-Sc1 sample BL31. North Crater field from Griffin (2007).TgVC values from Hobden (1997).

A transect of an orthopyroxene-rimmed olivine phenocryst from sample BL30 is shown in Figure 4.4. The orthopyroxene rims are 100-500 µm thick. The rim becomes depleted in FeO from ~20 wt. % to 12-15 wt. % towards the olivine core,

while MgO increases from ~20 to 25 wt. %. This is reverse zoning. The olivine itself is also zoned from a high-Fe, low-Mg rim towards a low-Fe and high-Mg core. Inclusions of pyroxenes have been picked up by the transect, the largest measuring less than 50 µm (Figure 4.4)

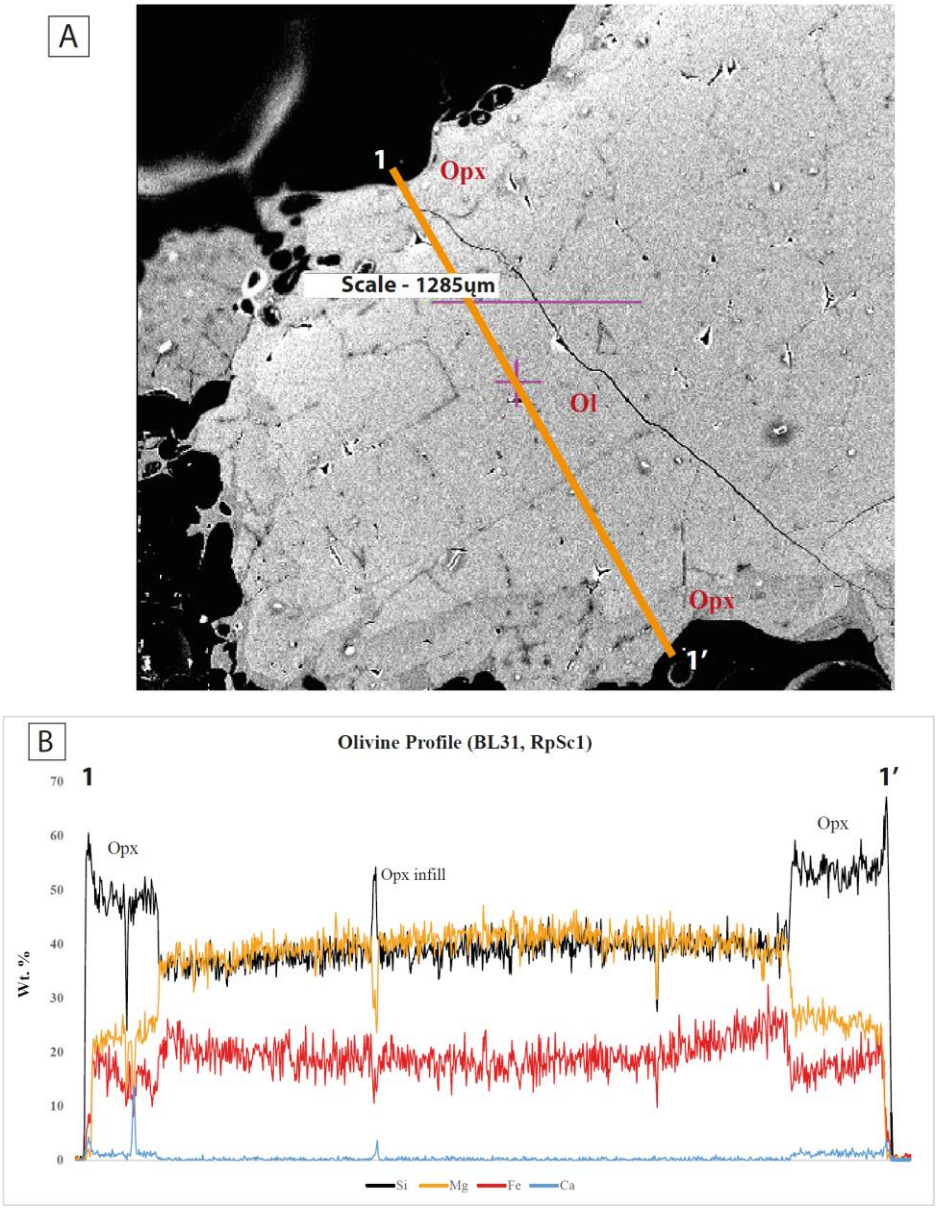

Figure 4.4. Profileof a pyroxene rimmed olivine phenocryst (BL31, Rp-Sc1). (A) Electron microprobe image of the olivine analysed. The thin horizontal purple line is the scale bar and measures 1285um. The thick orange line represents a line-scan transect across the phenocryst 1-1'. Slight shading differences reveals the rim of orthopyroxene that surrounds the crystal. (B) The compositional profile of the transect 1-1', measuring Si, Mg, Fe and Ca concentrations of the olivine phenocryst and orthopyroxene rims.

4.3.4 Fe-Ti Oxides

Twelve Fe-Ti oxides were analysed. Representative examples of compositions are given in Table . Eight of the crystals analysed were discovered to be titanomagnetite and four were ilmenite. Occasionally ilmenite and titanomagnetite occur adjacent to or in contact with, each other, indicating equilibrium (BL10-2 and -3; BL27-16 and -17). Titanomagnetite ranges in TiO_2 composition from 12.27 to 26.42 wt. % and FeO composition 61.11 to 79.6 wt. %. Ilmenite ranges in Ti O_2composition 46.19 to 51.26 wt. % and FeO composition 48.64 to 51.25 wt. %.

4.4 Whole Rock Geochemistry

XRF results are used to classify the deposits and to examine variation across volcano-stratigraphic units.

4.4.1 Rock Classification

The whole rock composition of BLC samples is displayed in a K_2O vs SiO_2 plot (Figure 4.5). The data are closely grouped within the medium-K range of the calc-alkaline series (after the classification scheme of Rollinson, 1993).The deposits are dominantly within the andesite field, with some samples within and near the boundary of the basaltic andesite field. There is a positive correlation of K_2O with increasing SiO_2. These findings lie well within the field of total TgVC eruptives and are consistent with those of Patterson and Graham (1988), Graham *et al*. (1995), and Hobden (1997). Graham *et al.* (1995) established that the most primitive compositions are those most recently erupted from Red Crater and Ngauruhoe. The most evolved compositions were produced during the middle part of Tongariro's eruptive history (e.g. the Tongariro Trig).

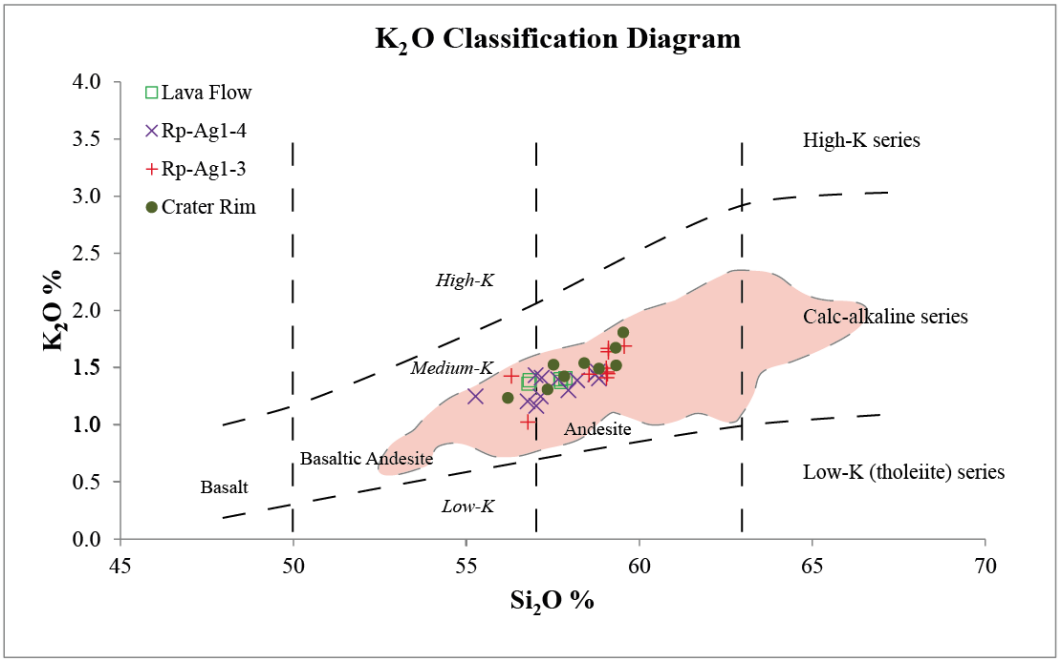

Figure 4.5. Whole rock K_2O vs SiO_2 classification diagram showing the composition of volcano stratigraphic units proximal to BLC. Alkali vs silica composition boundaries (vertical lines) after Rollinson (1993). The pink shaded region is the composition field of Tongariro after Hobden (1997). The data lies within the centre of this field, clustered within the basaltic andesite - andesite zone. Purple cross - Rotopaunga Agglutinates, RpAg-1-4; red cross - Rotopaunga Scorias 1&3, Rp-Sc1-3; green circle - crater rim deposits; green square - BLC lava flow.

4.4.2 Major Oxide Composition

Whole rock major oxide raw data are presented in Appendix Six. They are normalised to 100%. SiO_2 ranges from 55.26 to 59.55 wt. % which compare well to the reported SiO_2 ranges of 52.7 to 66.3 wt. % for TgVC eruptives (Graham *et al*. 1995). Other major elements are presented in Figure 4.6 plotted against SiO_2 on Harker diagrams. Most major elements generally show a narrow range in concentration. The data is often quite scattered and does not reveal many consistent compositional relationships. This is also the case with individual units as they also display no apparent relationships.

Concentrations of Na_2O vary from 2.20 to 2.80 wt %. Na_2O is generally incompatible with the fractionating mineral assemblage. The Na_2O Harker diagram shows no overall correlations with SiO_2 and a moderate amount of scatter occurs. K_2O shows a stronger positive correlation with SiO_2 (Figure 4.5), indicating that it behaves more incompatibly. The K_2O increase with increasing

SiO_2 is expected from fractional crystallisation involving the observed phenocryst phases (plagioclase, orthopyroxene, clinopyroxene, Fe-Ti oxides). K_2O ranges from 1.02 to 1.80 wt. %. CaO ranges from 4.62 to 7.32 wt. %. CaO does not show the negative correlation with SiO_2 that is expected with fractionation of plagioclase and clinopyroxene. The considerable scatter in many elements (e.g. Al_2O_3, Ti_2O and P_2O_5) suggest that processes other than closed-system fractional crystallisation was operating in the complex subvolcanic plumbing system. The scattered trend is also consistent with the samples being derived from multiple parent melts. This is compounded by the likelihood that the Rp-Ag units are from a different vent. The scatter evident on the plot of Al_2O_3 reflects the variable abundance of (mainly) plagioclase phenocrysts. Scatter on Ti_2O reflects varying magnetite and ilmenite abundances. No trend can be determined for FeO. No tends can be identified for MnO. MgO concentrations range from 2.83 % to 6.45 wt % and do not show the negative correlation between MgO and SiO_2 expected by fractionation of olivine and pyroxene. Some of the high SiO_2 samples also have high MgO contents. P_2O_5 contents range from 0.9 to 0.26 wt. %. Considerable scatter marks the P_2O_5 versus SiO_2 variation diagram. This is most likely representative of variable apatite fractionation and possibly some apatite accumulation. The different volcano stratigraphic units cannot be logically related by fractional crystallisation, suggesting that they represent different magma batches.

4.4.3 Trace Element Composition

Whole rock raw trace element raw data are presented in Appendix Seven. Trace element compositions are plotted on a multi-element diagram, normalised against primitive mantle (Figure 4.7). The volcanic units analysed display a strongly spiked pattern that is typical of subduction-zone arc magmas. The eruptives show enrichment of large ion lithophile elements (LILE) in particular Rb, and K, which are thought to be a consequence of enrichment of the mantle wedge by fluids released from the subducted slab (Tatsumi *et al.* 1986). The eruptives are moderately enriched in rare earth elements (REE) for example La and Ce. The eruptives are depleted in high field strength elements (HFSE) with Ta depletion and a pronounced Nb trough. These anomalies are also a characteristic feature of arc rocks

and have alternatively been explained by minor refractory phases in the source which retain these elements during partial melting, higher degrees of partial melting, or by derivation from an already depleted mantle wedge (Stolz *et al.* 1996). These trends, along with high Pb concentrations, are consistent with reported studies on other Tongariro and Ruapehu eruptives (Hobden 1997; Price *et al*. 2005).

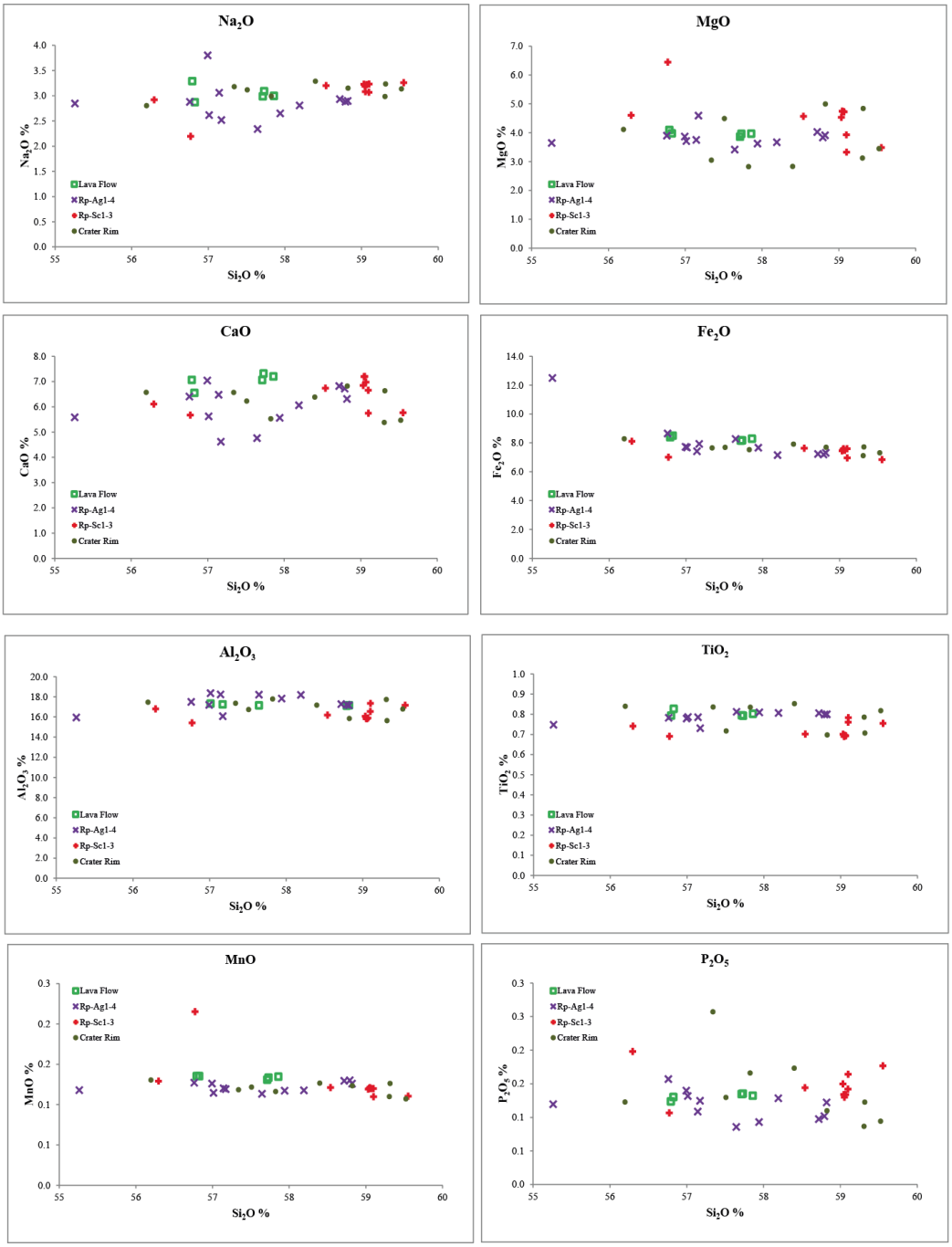

Figure 4.6. Harker variation diagrams of selected major oxides within BLC volcano-stratigraphic units; purple cross - Rotopaunga Agglutinates, Rp-Ag-1-4; red cross - Rotopaunga Scorias 1&3, Rp-Sc1-3; green circle - crater rim deposits; green square - BLC lava flow.

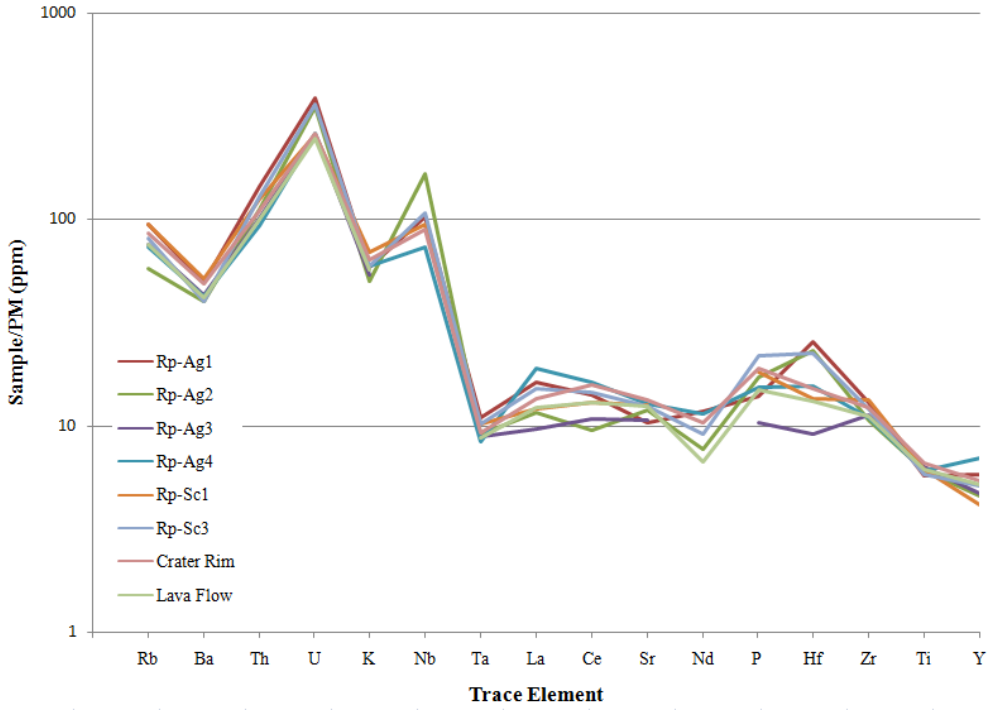

Figure 4.7. Multi-element diagram of selected samples ofdeposits proximal to BLC; Rp-Ag1 - BL26; Rp-Ag2 - BL25; Rp-Ag3 - BL12; Rp-Ag4 - BL05; Rp-Sc1 - BL19; Rp-Sc3 - BL21; Crater Rim; BL06; BLC lava flow - BL16. Trace elements are normalised against primitive mantle values of McDonough *et al.* (1992).

Harker variation diagrams for selected trace elements (Ba, Zr, Rb, Sr, La, Y, U, and Th) of selected samples are presented in Figure 4.8. The large-ion-lithophile elements, Rb and Ba display a slight increase with increasing SiO_2. Zr, Rb, Sr, Y, and Th have a narrower compositional range. No relationships or trends could be established. La and U are scattered and do not show a systematic relationship with SiO_2. As with major element compositions, the range of SiO2 wt. % compositions is too narrow to detect the general trends reported for TgVC magmas by Graham *et al*. (1995) and Hobden (1997). As with the major elements, there is no trend in trace element composition throughout the stratigraphic succession of BLC. Ni and Cr Harker diagrams display two groupings. In the case of Ni the majority of samples display ~6 to 16 ppm Ni while a second smaller grouping contains close to double this; ~28 to 35 ppm. With chromium the majority of samples contain ~20 to 50 ppm with the second grouping containing ~130 to 160 ppm. The same samples in each diagram have the raised Ni and Cr values and are deposits from Rp-Sc1, Rp-Sc3 and the western rim. These samples are olivine-bearing and the Ni and Cr enrichment reflects this.

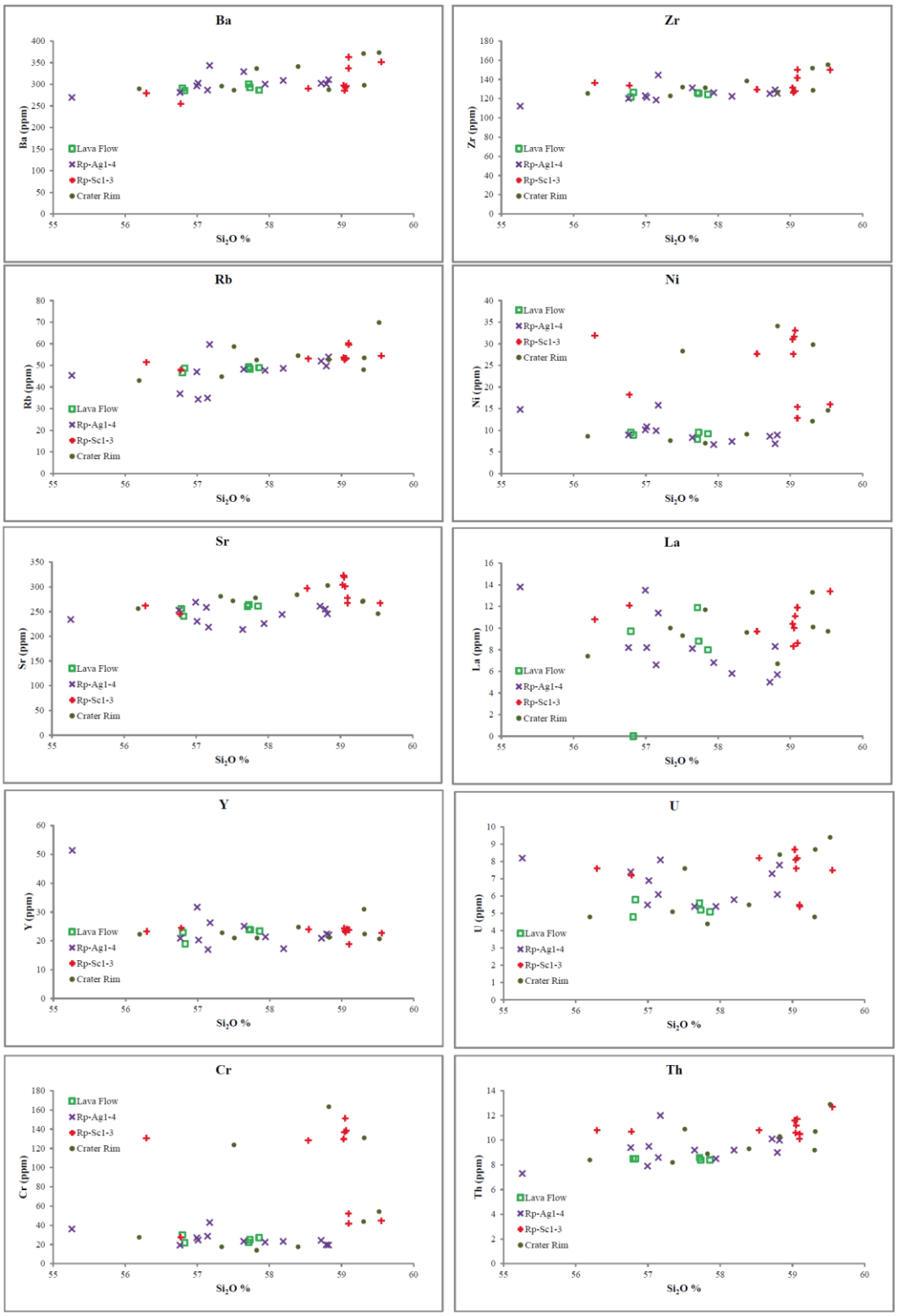

Figure 4.8. Harker variation diagrams of selected trace elements within BLC volcano-stratigraphic units; purple cross - Rotopaunga Agglutinates, Rp-Ag-1-4; red cross - Rotopaunga Scorias 1&3, Rp-Sc1-3; green circle - crater rim deposits; green square - BLC lava flow.

4.4.4 In Comparison with other Vents of the TgVC

The chemical composition of the products of BLC (excluding the Rotopaunga Agglutinates) do not differ markedly from the majority of Tongariro products (Figure 4.5). The deposits plot in a small coherent group near the middle of the Tongariro field and overlap with the fields of NE Oturere (values in Table 4.4), Tongariro Trig and SW Oturere (Graham *et al*. 1995; Hobden 1997). These older Tongariro magma compositions are echoed in the chemistry of younger eruptive units, suggesting some link in the type of magma available to the volcanic plumbing system over time, and in the processes operating on these magmas (Graham *et al*. 1995; Hobden 1997). Blue Lake Crater appears to be an extension of these older volcanic units, which interestingly, comprise a great deal of the other welded spatter deposits across Tongariro.

The young vents in the northern confines of the Tongariro complex; North Crater, Te Maari and BLC, share very similar geochemical values and have very similar compositional fields. North Crater and Te Maari eruptives display similar petrograpy, major oxide ranges and element ratios as BLC (Table 4.4). Te Maari and North Crater lavas contain moderate to low MgO and SiO_2 contents and similar Fe/Mg ratios to BLC suggesting that all three of these young northern vents are in some way linked. A common magma reservoir may be shared by these vents, with only minor chemical variations produced by slight differences in the type and degree of higher level differentiation processes experienced by the various magma batches erupted (Hobden 1997). A shared magmatic history between these young vents, or with the units of the Mangahouhounui Valley, would be consistent with their relatively close temporal and spatial associations. Red Crater data is included for comparison (Table 4.4). It is geochemistry different to that Blue Lake, North Crater and the Te Maari vents. It has a lower SiO_2 range and higher FeO, MgO and CaO ranges.

Table 4.4. A comparison of the major and trace element properties of BLC deposits with the neighbouring young Tongariro vents and the older NE Oturere volcanic ediface.

	Blue Lake Crater[1]	North Crater[2]	Te Maari Vents[2]	Red Crater[2]	NE Oturere[2]
SiO_2 wt %	56.2-59.6	56.3-60.10	57.5-60.2	53.0-61.1	55.4-62.2
FeO wt %	6.8-8.5	6.9-8.0	7.2-7.5	6.7-9.9	6.0-8.0
MgO wt %	2.8-6.5	3.3-5.3	3.1-4.4	3.8-7.7	3.5-7.1
CaO wt %	5.4-7.32	6.1-7.9	6.5-7.6	6.5-10.5	6.5-8.7
K_2O wt %	1.0-1.8	1.3-1.8	1.2-1.6	0.6-1.8	1.0-1.7
FeO/MgO	1.1-2.8	1.2-1.9	1.5-2.1	1.1-1.6	1.0-1.9
K/Rb	213-348	220.255	224-270	155-290	212-321
Rb/Sr	0.16-0.28	0.17-0.24	0.1-0.22	0.06-0.24	0.09-0.23
Rb/Zr	0.32-0.45	0.38-0.50	0.35-0.49	0.23-0.50	0.26-0.5

[1.] *This study excluding BL29.* [2.] *Hobden (1997)*

Chapter Five

Discussion

5.1 Introduction

BLC is a vent and pyroclastic rim crater in the northern section of the Tongariro complex in the TgVC. This chapter combines stratigraphic, petrological and geochemical observations to determine a number of processes related to BLC's origin and subsequent volcanic activity. This chapter also discusses the origin of the crater landform, eruption styles and depositional processes, magmatic processes, eruption triggers and magma ascent and vent dynamics of the eruptions that have formed the proximal deposits around BLC. The volcanic history of BLC is discussed, as are the hazards associated with BLC and any possible connection that BLC may have with the Te Maari craters and the northern section of Tongariro.

5.2 Origin of the Blue Lake Crater

The geomorphological expression of BLC is complicated by the presence of older landform features comprised of two topographic highs, two valley systems and a glacial cirque. The eruption that excavated the vent and built up the majority of the pyroclastic rim is difficult to identify. The only evidence for the eruption is the discontinuous crater rim and the depression that the lake has partially filled. The most well defined and best preserved part of the rim is to the SW (Figure 2.44). Here the rim sits on Central Crater where it rises ~40 m. Due to the presence of the lake it is difficult to establish if BLC is excavational, although it is assumed that it is. Volcanic craters are generally surrounded by vent-filling breccia comprised of disaggregated wall rock material from the vent, and coarse primary tephra, welded due to proximity (Vespermann and Schmincke 2000).No deposits comprised of vent-clearing breccia were found in the proximal areas of BLC, and there are no tephras that are positively attributed to BLC.

When compared to other excavational, wide-profile craters and lakes across Tongariro, BLC shares a number similarities and differences. The Tama Lakes

and craters are the most significant craters on Tongariro. There are six 20-50 m deep explosion craters, two of which are filled with water (Lower and Upper Tama Lakes) (Figure 5.1).The lakes are of comparable size to BLC. Upper Tama Lake has a diameter of ~800 m and is 10.5 m deep. Lower Tama Lake is ~600 m wide and 24 m deep (Michaelis 1981).The products of the Tama Lakes are basaltic andesite to dacite, 56.1-64.2 wt % SiO_2 in composition (Hobden 1997). Eruptions occurred during a period of intense volcanic activity on the complex at around 10 ka (Hobden 1997; Chizmar 2003).The products of the Tama craters are generally 2-6 m thick lava flows and domes. The styles of volcanism range from strombolian to phreatomagmatic to subplinianand there is evidence for at least one small volume ignimbrite-producing eruption (Hobden 1997; Chizmar 2003). The Tama craters are more steep sided than BLC and have not built up significant rim deposits. Explosive dome destruction probably occurred and may explain the origin of the craters (Hobden 1997).

The geomorphology of BLC is not typical of the products of fire-fountaining eruptions which usually build spatter and scoria cones. Examples of fire-fountaining cones on Tongariro include Red-Crater, North Crater and the 1954-1975 summit crater of Ngauruhoe. These vents have produced steep sided tephra cones, which are, in the case of red crater and Ngauruhoe, quite small and steep sided. BLC in comparison is wide and shallow with less steep walls.

It is probable that Blue Lake Crater was excavated by pheatomagmatic processes. Phreatic activity is common at composite cones when magma comes into contact with a crater lake, groundwater or hydrothermal system, or glacier/snow. Explosive steam eruptions, such as the 2012 eruptions at Te Maari, occur quite frequently and can be without any juvenile material (Vespermann and Schmincke 2000). BLC may have been formed when magma erupted through the hydrothermal system that resides beneath the sub-surface of Tongariro, or interacted with thick snow/ice accumulation on Central Crater.

Figure 5.1. The Tama Lakes and craters on the southern end of Tongariro.Adapted from Roscoe (undated).

The shape of BLC is very similar to a maar (Figure 5.2). Maars typically originate from an explosion caused by water coming into contact with hot magma (Valentine and Fisher 2000). The water may occur as shallow groundwater reservoirs or in standing bodies of water such as lakes. It is not uncommon that the satellite vent of a composite cone may interact with near-surface water forming a maar or tuff ring (Davidson and de Silva 2000). The interception of shallow water by ascending magma, however, is more likely to occur on the shallow slopes, lower reaches of the volcano, or on the ring plain rather than on the cone itself (Davidson and de Silva 2000). Maars are defined by a bowl-shaped crater that cuts 10 m to more than 500 m deep into the pre-eruption surface (Vespermann and Schmincke 2000). Maar crater-rim diameters average 0.7–0.8 km (very close to the size of BLC) and range from 0.2 to 3.0 km (Vespermann and Schmincke 2000). Rim deposits are commonly less than 50 m thick (again similar to BLC). Height/rim diameter ratios range between 0.13 and 0.05. BLC has ratios that ranges from 0.06 on the SW rim, to 0.11 on the western rim (1785 ma.s.l, Figure 2.8).

Maars are typically surrounded by low ramparts of well-bedded ejecta with beds dipping at 20-25° (again similar to BLC) that decrease rapidly in thickness away from the rim (Gutmann 1976; Valentine and Fisher 2000). They may consist of some 10 to 1000 single layers that are mainly emplaced by pyroclastic base surges and fallout. These are typically well-bedded and fine-grained deposits that contain xenolith compositions of up to 90 vol.% (Valentine and Fisher 2000). Phreatomagmatic tephra is almost always finer grained than magmatic tephra, and accretionary lapilli are common, indicating phreatomagmatic processes. Maars generally lack spatter and agglutinate deposits. The spatter and agglutinate facies sourced from BLC are exposed mantling the rim (e.g. Figure 2.44) and have been deposited after the initial rim-forming episode. Although the shape of BLC is very similar to that of a maar, sections through the BLC rim are not exposed, and the interpretation that BLC may be a summit-maar is based on geomorphology.

Figure 5.2. Elegante Crater maar in the El Pinacate volcanic field in Mexico. The crater is 1,400 meters from rim to rim and 140 meters deep. The rim in most places only rises about 50 m above the surrounding desert floor (Gutmann 1976). Image adapted from Rhoda and Burton (2010).

5.3 Rotopaunga Agglutinates (Rp-Ag)

The Rotopaunga Agglutinates are the lowest stratigraphic succession exposed in the inner rim of BLC. The group of four thick agglutinated lava-like deposits have a total thickness of ~27 m and occur stratigraphically below the Rotopaunga Scorias. They are characterized by a base, up to 1 m thick, of angular lapilli-bomb/block beds that transitions into a moderately to intensely welded facies interior up to 4 m thick. The tops the beds are comprised of platy jointed intensely welded lava up to 3 m thick. The Rotopaunga Agglutinates do not correlate with any deposits elsewhere on the rim. The agglutinates drape over a pre-existing topographic high in the centre of the northern inner crater wall, but they also continue beneath Rotopaunga peak and can be traced along the eastern bluffs of Rotopaunga towards the Te Maari Trig and importantly, they do not thin away from the vent. This geometrical distribution implies that the agglutinates were not derived from BLC, but instead make up part of the upper portion of the Mangahouhounui Valley succession that was erupted from part of an older volcanic edifice (Hobden 1996). They are presumably pre-glacial in age.

Although the source location of the Rp-Ag succession is unknown, they are still proximal to vent deposits that are indicative of intense fire-fountaining. These deposits must have formed sufficiently close to the erupting vent to remain hot enough to coalesce, agglutinate and re-mobilize (to varying degrees). A pre-existing vent near to the current location of Blue Lake must have been active; possibly somewhere within the Mangahouhounui Valley, or positioned at what is now Central Crater, or possibly underneath BLC. The Rotopaunga Agglutinates are petrologically and geochemically similar to the rest of the BLC proximal deposits, which highlights the difficulty in characterizing different volcanic units by geochemical methods in the TgCV, and in andesites in general.

5.4 Rotopaunga Scorias

The Rotopaunga Scoria beds are most likely sourced, at least in part, from BLC. They form a veneer on the outer northern slopes of the crater, with a small deposit on the western rim. They are unlikely to have originated from North Crater or Red

Crater as the deposits are not continuous between these vents. One potential problem in determining the origin of the scoria beds is that the lowest and thickest unit, Rp-Sc1, maintains a constant thickness across the eastern flank away from BLC towards the Te Maari Trig; almost 1 km away. This volume of material is unlikely have accumulated on one side of BLC without evidence of similar deposits elsewhere (e.g. Central Crater). This could mean that Rp-Sc1 is part of the Mangahouhounui Valley succession along with the Rotopaunga Agglutinates, and that it is not from BLC, or that the eastern exposure of Rp-Sc1 is not the same unit as the western exposure. However a small outcrop of Rp-Sc1 exists on the NW crater rim, indicating that it was deposited after the Blue Lake Crater-forming eruption. Geochemically the units of the west and east are very similar, and with all having SiO_2 concentrations of 59% wt %, the unit is the most uniform of any of the deposits. Another alternative is that the thick beds of Rp-Sc1 have been produced by multiple eruption sources contemporaneously. Multiple eruptions from different sources have been suggested by Nairn (unpublished) who proposed that the distribution of coarse clasts, and the lack of thinning of the lower beds towards Te Maari Trig, indicated that Rp-Sc1 may have been erupted from BLC and from another vent in the glaciated Te Tatau crater to east.

The upper units Rp-Sc2 and Rp-Sc3 do not have the same geometry as Rp-Sc1 and are more likely to be sourced from BLC. Rp-Sc3, and to a lesser extent Rp-Sc2, may have been deposited during the eruption sequence that produced the thin deposits that mantle the western to southern rim of BLC (discussed next section 5.5).

5.5 Crater Rim Deposits and the Blue Lake Crater Lava Flow

Sections through the western, southern or eastern rims are not exposed. Only the upper welded and agglutinated deposits that mantle the rim and outer slopes and Central Crater peak are exposed. The deposits do not appear to have constructed the ~40 m high rim, but rather form an incomplete ring of outcrops ranging in thickness from ~1 to 8 m, and in lateral extent from ~2 to over 20 m. The deposits vary from moderately to intensely welded facies, with the outcrops more welded and agglutinated on the south and eastern rims displaying strong banding and fluid

flow structures. The deposits are less agglutinated and become slightly crudely bedded on the western side. The rim deposits are most likely produced from similar Hawaiian to Strombolian fountaining and post-depositional processes as the Rotopaunga Agglutinates, although they do not correlate. The crater rim mantling deposits are instead likely associated with the lava flow, with the upper Rotopaunga Scoria units (Rp-Sc2, Rp-Sc3) accounting for the northern deposition of this material.

The lava flow is the best constrained unit associated with BLC and is almost certainly sourced from the vent. It is ~700 m long and ~600 m wide with a high aspect ratio. It is likely the youngest of all of the proximal BLC deposits. The ~4 m flow overlies the final Rotopaunga Agglutinate unit, Rp-Ag4, on the northern side of the eastern crater in which it overflows, and overlies crater rim mantling deposits on the southern side. The flow extends into the glaciated Mangahouhounui Valley but shows no signs of glacial shortening/thickening, this, and the preservation of surfical flow features (e.g. pressure ridges) indicate that it is post-glacial in age. There is a possibility that the production of the lava was effusive and extruded without significant cone forming deposits. For example, for the first 8,000 years of Red Crater's lifespan five large andesitic lava flows were erupted without construction of the cone (Bardsley 2004).

The structure of the lava indicates that it is an a'a style flow (Chapter 2 section 2.7.3.2). It overflowed the lowest point of the crater rim and travelled into the Mangahouhounui Valley before spreading at the change of slope onto the valley floor. The lava flow begins as a single flow then breaks into seven lobes in the middle of the flow path. The flow may have formed by multiple, individual flows or may have been one flow that divided at this point. The shape may be controlled by topography. The northern lobes are short and wide, almost equi-dimensional, and may be more clastogenic in origin with hot spatter deposits remobilizing on the steep slopes.

5.6 Magmatic Processes

5.6.1 Magma Chamber Processes

The petrographic and geochemical analyses undertaken in Chapters 3 and 4 provides insights into magma chamber processes. The TgVC is thought to be an open, complex plumbing system with andesite volcanism produced by complex processes involving fractional crystallisation, assimilation, mixing and mingling of multiple magma batches (Figure 5.3) (Graham and Hackett 1987; Hobden 1997; Nakagawa *et al.*2002; Price *et al.* 2005). This produces a range of magma types generally of medium explosivity (Wolhetz and Heiken 1992).

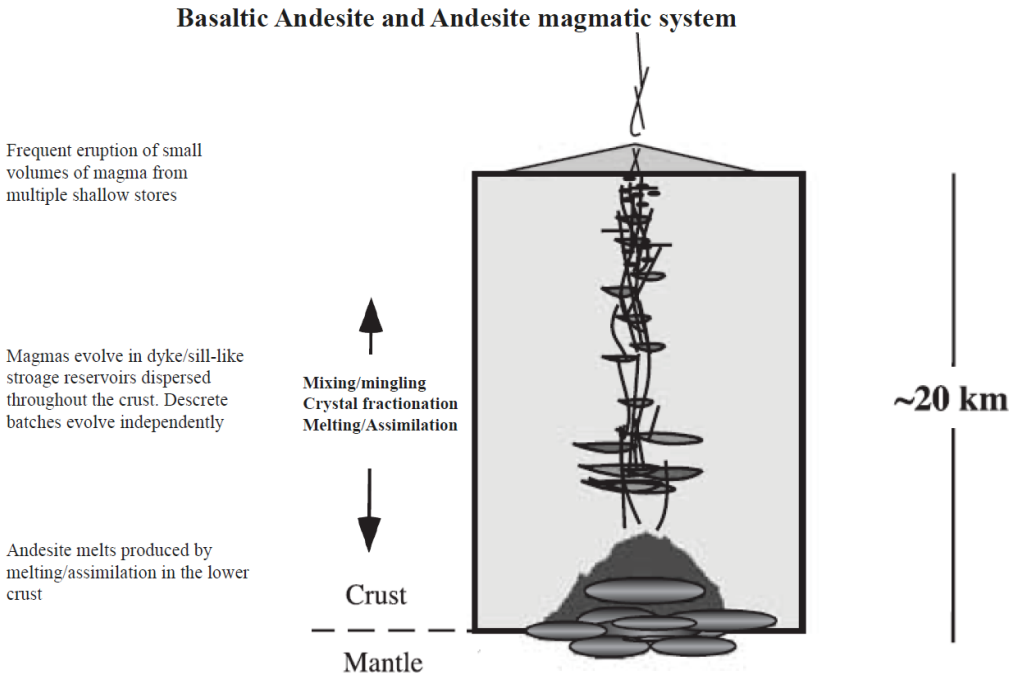

Figure 5.3. Diagram illustrating the development of andesite magma within the Taupo Volcanic Zone. The primary magmas are basaltic and originate from the mantle where they undergo fractional crystallisation, partial melting, mixing and mingling. The incorperation of crust results in basaltic andesite magma, and further fractionation produces basaltic andesites and andesites similar to those of the deposits proximal to BLC. Magma batches rise through the crust and temporarily reside in shallow reservoirs. Adapted from Price *et al.*(2005).

The deposits of the Rotopuanga Agglutinates; Rotopaunga Scorias; the crater rim deposits and the BLC lava flow are plagioclase-dominated porphyritic pyroxene andesites. The magmas erupted to produce these deposits ascended slowly and

stagnated at shallow depths in the crust (Figure 5.3). Geophysical studies of active composite cones has revealed the presence of shallow magma chambers that typically produce plagioclase-rich porphyritic magmas (Marti and Ernst 2005; Price *et al.* 2005). Andesite and basalt-andesite magmas at Tongariro crystallise at depths of 5-10 km (Nakagawa *et al.*, 1998). Xenoliths present in the majority of samples, indicate that crustal contamination/assimilation must also play some role.

Evidence for magma mixing and mingling in the Rotopaunga Agglutinates and BLC eruptives is strong as disequilibrium features are present in most of the deposits. Figure 5.4 illustrates a magma chamber under mixing conditions. Phenocrysts, particularly plagioclase and pyroxenes, commonlydisplay sieve textures, reaction rims,and reverse, patchy and oscillatory zoning (Sigurdsson *et al.* 1990; Nakegawa *et al.* 2002; Humphreys *et al.* 2006).Some dense bombs within the Rotopaunga Scorias, and several samples of the lava flow, show textures comprised of banded zones of different magma within the same clast. This is further evidence of magma mixing/mingling. Two separate zones were identified in the BLC lava flow (Chapter 3 section 3.4.5) and three zones were discovered in Rp-Sc1 dense bombs. Each zone is thought to represent a different magma batch, except for the zones of fragmented magma (Figure 3.15F) which are assumed to represent one or more of the other batches that have been disintegrated in the eruptive process. Samples that display thesebanded textures may provide a snap-shot of the final magma chamber where mixing is taking place immediately prior to eruption. To retain these textures, residence times after magma mixing must be relatively short.

Mixing and mingling further explains the geochemical variation (EMPA and XRF) within the deposits. Mixing/mingling of multiple magma batches may explain the wide range of compositions for plagioclase (SiO_2 varies up to 10 wt. %) and pyroxenes (FeO and MgO also vary by ~10 wt. %). Trends on Harker diagrams indicate that there are no systematic geochemical changes throughout the eruptive sequence. XRF bulk rock variation of samples from the same unit display a broad compositional range of SiO_2 with a generally narrow range for the other major oxides (Fe_2O, CaO, TiO_2, MnO, P_2O_5) and trace elements (Ba, Zr, Rb, Sr, Th). This suggests that magma chambers are emptied and refilled by new magma

batches (Nakegawa *et al*. 2002). The lack of geochemical trends through the stratigraphic sequence also indicates that there is no progression/evolution of magma through time which suggests multiple magma bodies, which are then mingled and erupted relatively quickly (Sigurdsson *et al.* 1990). Multiple small and semi-isolated magma batches may be feeding into, and mixing inside, a single chamber prior to eruption (Figure 5.3, Figure 5.4), however mixing and mingling inside the conduit may also be occurring.

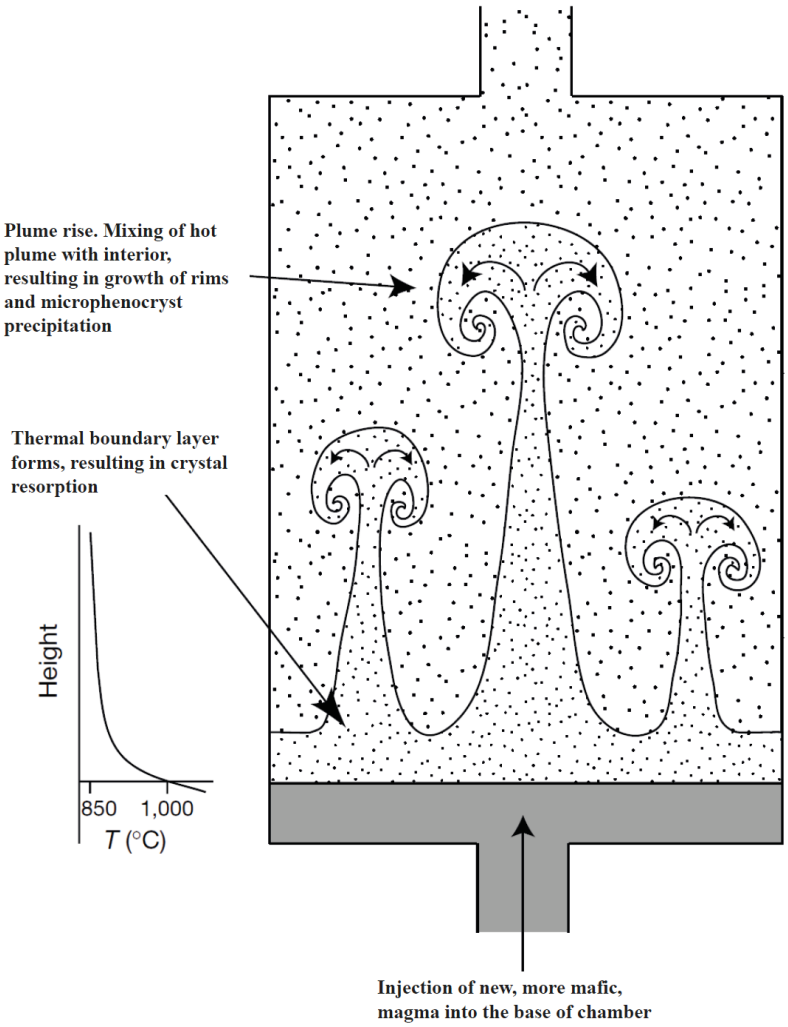

Figure 5.4. Thermal convectional mixing of a magma chamber with a hotter, less crystallised recharge magma. Adapted from Couch *et al.* (2001).

5.6.2 Eruption Triggers

The eruption triggers for the events that produced the Rotopaunga Agglutinates, Rotopaunga Scorias, the rim deposits and the BLC lava flow are most likely similar. It has been suggested by many authors (e.g. Sparks *et al.* 1977; Nakagawa *et al.* 2002) that the intrusion of a physically and chemically contrasting magma into the base of a magma body drastically alters the equilibrium, causing the magma at the base of the chamber to become super-heated. The super-heated magma then become less dense than the overlying magma which initiates vigorous magma convection along with vesiculation. The heating and vesiculation causes pressure to increase inside the chamber which results in fractures forming in the volcano and encasing rock. If the over-pressure in the shallow chamber grows to around 10 MPa it is sufficient to trigger an eruption (Tait *et al.* 1989; Woods and Cardoso 1997). The presence of olivine crystals with pyroxene reaction rims (or completely reacted to pyroxene) indicates the injection of a melt into a slightly contrasting magma chamber beneath BLC. In the case of multiple small magma batches such as Tongariro, the activity may affect the neighbouring chambers, causing them to become unstable and possibly feed into the erupting chamber via the plumbing system (Nakagawa *et al.* 1998). As the magma chamber convects, bubbles rise and become concentrated near the roof. Magma is tapped from this volatile-content-rich upper portion of the chamber which leads to explosive fire-fountaining (Tait *et al.* 1989; Woods and Cardoso 1997).

An alternative method of triggering an andesite-basaltic andesite eruption is that of the ‘second boiling’ of a dominant volatile phase (Woods and Cardoso 1997). This occurs when intermediate to silicic magma cools and crystallises which cause volatiles (water is the dominant in andesite magmas) to become increasingly concentrated in the residual melt. The melt eventually becomes saturated. Saturation triggers the exsolution of volatiles which causes a rise in the magma pressure and triggers an eruption (Nakagawa *et al.* 2002).

5.7 Eruption Styles and Depositional Processes

5.7.1 Hawaiian-and Strombolian-Style Eruptions

The deposits of both BLC and the pre-BLC Rotopaunga Agglutinates are comprised of non to intensely welded facies and all have been produced by mildly explosive Hawaiianto Strombolian fire-fountaining (Chapter 2 section 2.5). The key difference in eruption style is Hawaiian fire-fountains are continuous and Strombolian fountains occur as more intermittent magma bursts. Both Hawaiian and Strombolian fire-fountaining is associated with low degrees of bubble coalescence and high magma rates. The magma and gas rise as a homogenous, partially-coupled, two-phase flow (Head and Wilson 1989; Parfitt 2004). The deposits in this study are produced from andesitic and basaltic andesite magmas which do not typically erupt as fire-fountains. The andesitic magma must undergo relatively rapid magma ascent rates and low to moderate, partially decoupled gas content to allow the formation of fire-fountaining (Wolff and Sumner 2000). Factors such as high magmatic temperatures and low magmatic volatile contents, as well as vent geometry contributed to this eruptive style (Hobden 1997).

Fire-fountaining eruptions have built welded spatter deposits on North Crater, Tongariro Trig, the Oturere Valley and Ngauruhoe, and have produced significant lava flows (e.g. Ngauruhoe and Red Crater) (Gregg 1956; Nairn and Self 1978; Hobden 1997, 2002; Sanders 2010).The main controls on these deposits is the intensity of fire-fountaining, the accumulation rate of material and the temperature of clasts upon deposition. This determines the amount of agglutination, coalescence, compactional welding and post-depositional deformation.

Fire Fountain Processes

Fire-fountaining is the least violent style of explosive volcanism and dispersal is typically small. Fire-fountaining eruptions occur when magma in an open conduit or vent is torn apart by expanding gas and the fragments are propelled into the atmosphere (Wolff and Sumner 2000; Sumner *et al.* 2005). Magma is ejected as a low-pulsating ‘fire fountain’ or pillar-like jet of molten pyroclasts (spatter) and gas (Figure 5.5) (Vergniolle and Mangan 2000; Vergniolle *et al.* 2004; Marti and Ernst 2005). The degree of fragmentation is typically poor resulting in clasts

forming that are large; typically tens of centimetres. Magma-volume flux and volatile content controls fountain height, although vent dimensions and architecture are also contributing factors (Wolff and Sumner 2000).

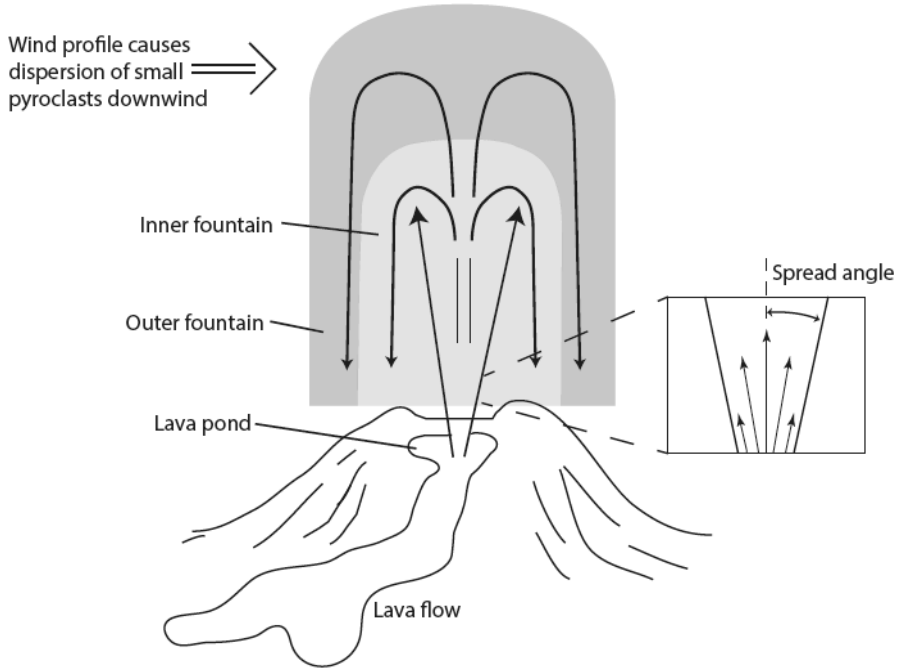

Figure 5.5. Diagram of the basic elements of a fire-fountain. The fountain consists of clasts following the general paths indicated by arrows. Widths of inner and outer fountains may vary. The length of the arrows in the inset indicate the velocity profile. Adapted from Head and Wilson (1989).

Strombolian fire-fountains differ from Hawaian in that they involve small scale bursts or discrete gas explosions. Sustained Hawaiian-style fire-fountains develop where magma rise speed is sufficient to prevent bubble accumulation near the surface of the erupting magma; otherwise Strombolian-style pulsing occurs. Strombolian eruptions usually involve higher viscosity magmas than Hawaiian, and may develop after a Hawaiian or Vulcanian eruption (Cas and Wright 1987; Parfitt *et al.* 1995; Vergniolle *et al.* 2004). Parfitt *et al.* (1995) looked into the transition between Hawaiian and Strombolian activity and concluded that the most important factor in determining eruption style was the speed of the magma ascent. In Strombolian eruptions, gas streams up the column at a greater rate than the magma, with small bubbles coalescing on the way. These bubbles coalesce further to produce what is known as a magma 'slug', with frothy magma in between these

slugs (Figure 5.6) (Parfitt *et al.* 1995; Vergniolle and Mangan 2000).When a slug of gas reaches the top of the magma column, or lava pond, it explodes. If many slugs occur rapidly then a continuous fire-fountain is produced. In this way, Hawaiian and Strombolian styles form a continuum and can transition into one another within a single eruptive episode.

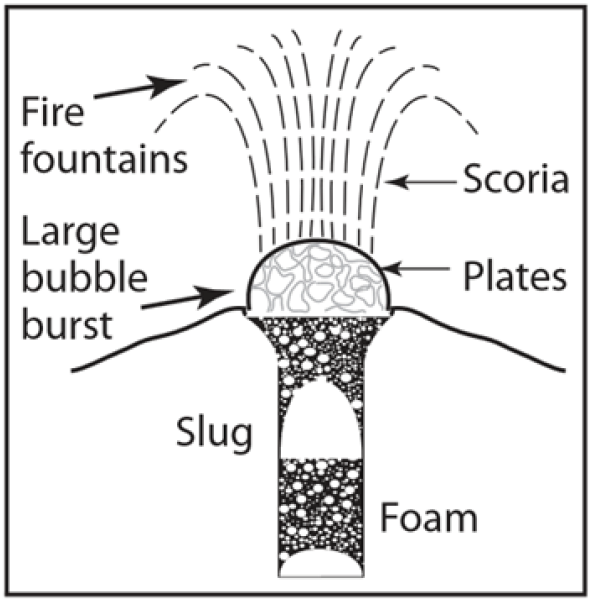

Figure 5.6. Model of a Strombolian eruption. Magma slugs form bubbles over the vent that explode periodically. Adapted from Ruth and Calder (2014).

Most basaltic fountains (exsolved magma gas contents of about 0.4% wt) do not exceed 500 m in height. Andesitic magma typically contains up to 6 wt % of exsolved gas which results in higher and more vigorous fountains, e.g. Izu-Oshima 1986, 1,600 m in height (Sumner 1998; Vergniolle *et al.* 2004). The structure of a fire fountain is determined by the velocity profile of the magma and the maximum spread angle (a narrow jet or broad spray) (Figure 5.5) (Parfitt 2004; Marti and Ernst 2005; Sumner *et al.* 2005). The overall fountain structure may be symmetrical or asymmetrical, and can be influenced by wind (significant wind velocity may bend the fountain over in one direction). Ejecta from fire-fountains usually fall close to the vent, with most forming a scoria cone comprised of coarse grained vesicular juvenile material (Cas and Wright 1987; Vergniolle and Mangan 2000; Vergniolle *et al.* 2004). Fire-fountaining from a single vent is commonly most vigorous at the start of an eruption and wanes thereafter. Factors such as lava

re-entrainment, shallow vent ponds and bubble coalescence can act to significantly reduce the height of a fountain, or even suppress a fountain completely (Parfitt *et al.* 1995).

Eruption temperatures are highest in the centre of the fountain (Figure 5.5) which consists of hot, incandescent fluid magma. Clasts agglutinate as they land or fall back close to the base of the fountain and coalesce, or become recycled in the vent. Hot fragments may also cool during flight when there is a higher fountain (Parfitt 2004; Marti and Ernst 2005). The outer portion is non-incandescent, less dense and comprised of lower temperature clasts (Figure 5.5) (Head and Wilson 1989). Accumulation of cold clasts produces brittle, non-welded scoria and spatter bombs deposited as solid tephra around the vent. Clasts may agglutinate and adhere only if they burst on landing to release their fluid interiors. This bursting process may be important in bonding together otherwise loose scoria (Sumner *et al.* 2005).The wind may strip, and rapidly chill fine particles and disperse ash downwind. Strombolian scoria is often of higher vesicularity than Hawaiian spatter. The deposits of Strombolian eruptions lack bedding or only display minor bedding, however pulsating eruptions often produce graded scoria deposits and may contain zones of more-welded material (Jaupart and Vergniolle 1988).

Post-and Syn-depositional Processes of Fire-Fountaining Eruptions

A number of post and syn-depositional processes play an important role in fire-fountaining eruptions. The processes apply to both Hawaiian-and Strombolian-style eruptions, which generally form a continuous range of deposits. As defined in Chapter 2 section 2.3, agglutination is the instantaneous syn-depositional adhesion and kinetic deformation of clasts, while welding is the post-depositional compaction of a hot pyroclastic deposit under its own weight (Wolff and Sumner 2000; Sumner *et al.* 2005). There is a continuum between agglutination and welding processes which reflects the varying eruption intensity and magmatic properties such as gas content, temperature and crystallinity (Sumner *et al.* 2005). The alternation in welding intensity exhibited by many spatter fall deposits can be correlated with rhythmic pulses of more or less intense fire-fountaining.Both welding and agglutination involve porosity loss, although spreading or splashing (e.g. from cow-pat bombs) is additionally involved in agglutination. The key

factor in influencing the degree of welding is the clast accumulation rate (Sumner *et al.* 2005). Welding is favoured if a clast at the surface of the accumulating deposit is buried before it can cool significantly, and if the density of falling hot clasts above the surface is great enough that radiative heat loss, both from the surface and the falling clasts, is minimized (Wolff and Sumner 2000; Sumner *et al.* 2005).

Fire-Fountains of the Pre-Blue Lake Crater Edifice (Rp-Ag)

Fire fountaining eruptions were occurring at the site of BLC before the crater was formed. The research for this thesis supports the findings of others (Healy 1963; Topping 1973; Hobden 1997) who concluded that the Rotopaunga Agglutinates were formed by vigorous fire-fountaining. All of the Rp-Ag units are dominated by intensely and strongly welded facies, with some 0.5-2 m thick zones of moderately welded facies included in the deposit. The deposits show adhesion and deformation of hot fluid clasts upon landing in the form of spatter bombs, cow-pat bombs and lensoidal clasts (Figure 2.21). Clast outlines are incipiently, partially or wholly retained; this is indicative of clasts originating from the hot internal parts of a fountain. The units contain (sub)vertical cooling joints and platy jointing indicating some form of post-depositional movement. Zones up to 1 m thick, that resemble flow banding, are the extreme flattening of clasts into a linear fabrics that occurs under intense welding (Figure 2.24). The changes in facies from intensely through to moderately welded, throughout the Rp-Ag units represent changes in eruption dynamics over time. The non-poorly welded scoria at the base of the units suggests that the first material deposited during the eruption of these units was cool. The Rp-Ag units are indicative of large, sustained and intense, probably Hawaiian-style, fire-fountaining.

Fire Fountaining Associated with Blue Lake Crater (Rp-Sc and the crater rim deposits).

Since the original crater-forming episode, BLC has produced a number of fire-fountaining deposits. The thick scoria beds of Rp-Sc1 were produced from the accumulation of scoria and spatter clasts, althoughthe unit has undergone considerably less agglutination and welding than the Rotopaunga Agglutinates, indicating that clasts were deposited much colder. The deposits of Rp-Sc1 are

comprised of a regular alternation of poorly to moderately-welded lapilli-bomb scoria zones up to 3 m thick, and sheet-like zones of intensely-strongly welded agglutinate up to 1 m thick. This is particularly pronounced in outcrops on the eastern bluffs of Rotopaunga (Figure 2.32). The intercalating of zones of intensely to strongly welded facies with the bulk of the deposit (scoria) indicates that the erupting fire-fountains pulsated, with the strongly-intensely welded zones representing surges in fire-fountaining energy. This is more typical of Strombolian-style eruptions than Hawaiian. The intensely-strongly welded zones thicken and become more sporadic towards the top of the unit, indicating that the pulsating became stronger, with longer intermittent periods over time. Some outcrops of Rp-Sc1 contain a concentration of large spatter clasts and breadcrust bombs at 1-2 m (Figure 2.34 and Figure 2.37); this likely represents a period of increased explosivity.

Rp-Sc3 is dominated by non to poorly welded bomb/block and lapilli scoria indicating again that the ejecta was cooled in-flight. The unit is much thinner than Rp-Sc1, but multiple grading changes within the deposit (from lapilli to large bombs/blocks) suggest that the erupting fire-fountain was pulsating (Figure 2.39). Like Rp-Sc1 there is a concentration of large breadcrust bombs in the lower 0.5-1 m of the unit, which suggests a period of increased explosively. Rp-Sc3 likely accumulated from the cool, outer portion of a slightly pulsating fire-fountain or the internal hot part of the fountain that was given time to cool in-flight. The height of Rotopaunga may prevent hot clasts accumulating, as the clasts that can be deposited on the topographic high must be ejected higher and therefore experience longer travel times.

The deposits that mantle the western and southern crater rim range in facies from non-poorly to intensely welded. The outcrops are up to 8 m thick and display a range of facies over quite short distances (Figure 2.44) with the deposits on the south and southwest rim generally more agglutinated and welded than those on the western rim. The depositsare interpreted as being deposited verynearto the vent from a mildly explosive, sustained, although asymmetrical, fire-fountain with hotter clasts deposited to the south/southwest. It is inferred that this fire-fountaining also produced the BLC lava flow (discussed next) and was possibly

contemporaneous with Rotopaunga Scoria unit Rp-Sc3. In that case, the fountain may have had a structure that concentrated hot spatter clasts towards the east and southwest (producing the lava and crater rim deposits) and cooler scoria deposits to the north (producing the Rp-Sc3).

5.7.2 The Blue Lake Crater Lava Flow

The BLC lava flow is an a'a lava. A'a lava flows are typically produced by basaltic andesite and andesite magmas. They produce long, thin flows with a widespread nature. Flows with high aspect ratios, such as the BLC lava, indicate relatively high viscosity and yield strength. The BLC lava ponds slightly at the base of the flow (where in places the development of extreme flow banding occurs) which further illustrates the high viscosity of basaltic-andesite to andesite lava flows. A'a flows can be emplaced within hours or days (Kilburn 2000).The surface of a'a flows consist of rubbly block-sized irregular clasts, often not welded to the flow. Rubbly surfaces occur when the surface of the lava flow is moving slower than the underlying lava due to different cooling rates (Kilburn and Lopes 1990; Kilburn and Guest 1993). Pressure ridges are formed when lava in the centre of the flow remains hotter than the margins, as the margins are exposed to the air and topography which increases their cooling rate. The faster moving underlying lava pulls the cooler crust along with it, while holding on to the outer margins of the flow creating ridges (Kilburn and Lopes 1990; Kilburn and Guest 1993).

The BLC lava flow may have been generated by fire-fountaining (in continuous or discrete bursts) or as a ponded lava lake that overflowed the eastern crater rim.

The BLC may have formed from the rapid accumulation of and re-mobilisation of spatter deposits produced from fire-fountaining. The high viscosities and yield strengths of intermediate and alkaline felsic ejecta generally favour the construction and preservation, of agglutinate piles. Clastogenic lavas are produced when a spatter pile becomes mobile as a result of either collapse/failure or from intense heat. Spatter cones/piles are quite sensitive to changes in accumulation rate, fountain width, and wind speed. Coherent pieces of spatter or welded scoria from the spatter pile may be carried away on the surface of the lava, especially

during a breaching episode, when large sectors of the cone/rim may be rafted out on the flowing lava (Head and Wilson 1989; Sumner 1998; Sumner *et al.* 2005). The BLC lava contains a few, isolated lensoidal and ribbon clasts, however it does not contain large portions of spatter/scoria cone-building deposits incorporated into the flow.

Another possible origin for the BLC lava flow is that it accumulated as ponded lava that then overflowed the crater rim. BLC is wide and shallow which favours the accumulation of spatter from fire-fountaining. The crater may have acted as a funnel to confine the inner fountain-fed lava to a vent pool, which then breached the eastern rim. Lava lakes typically form during weak (Hawaiian and Strombolian) explosive eruptions (Head and Wilson 1989; Parfitt and Wilson 1995). The Tongariro complex contains one well-preserved solidified lava lake in North Crater which is composed of andesitic lava (Griffin 2007). The andesitic magma that produced the lake must have had a very low initial gas content, and have been relatively hot for it to behave in such a fluidal manner. A relatively low magma discharge rate would have enabled decoupling of the magmatic volatiles from the magma, allowing gases to escape and the lava to accumulate within the crater (Griffin 2007). Disruption of the lava lake surface by the emerging gases may have caused periodic fire-fountaining, producing spatter deposits around the crater rim (the agglutinated crater rim deposits) and on top of Rotopaunga (which were cooled in-flight, producing scoria).

5.8 A Brief History of Activity at Blue Lake Crater

Pre-BLC Paleotopography

The landscape of northern Tongariro before the initiation of activity at BLC would have been significantly different to the present day topography. BLC is located at the junction point between several landforms. The Mangahouhounui Valley is pre-glacial and has probably not changed drastically. To the northwest of BLC, North Crater may not have been formed, leaving this flank sloping away from BLC. The peak of Rotopaunga, including the Rotopaunga Agglutinates, is interpreted as being older than BLC. Rotopaunga therefore would be lower in elevation. Central Crater is a glacial cirque and would have likely been a major

feature pre-BLC. It is likely that Central Crater was not flat, but rather a much more uneven terrain, and possibly a depression which has been filled-in and smoothed over after thousands of years of tephra accumulation (some of which may be sourced from BLC).

The Vent-Clearing Eruption and/or the Formation of the Crater Rim

It is very likely that a phreatic or phreatomagmatic eruption was involved in the clearing of the original vent that became BLC. Rising magma likely intersected the hydrothermal system under Tongariro, or snow or ice accumulation on Central Crater. This eruption formed the western-southern and eastern rim of BLC, with no rim formed on Rotopaunga due to geomorphology. It is unclear if more than one eruption of this style occurred. It also remains unclear if BLC filled with water after this period.

Activity from BLC after the Initial Vent Clearing Episode

Explosive eruptions that produced the Rotopaunga Scorias, the deposits that mantle the crater rim and the BLC lava flow, were initiated during this episode in the history of BLC. The eruptions were likely triggered by mixing of compositionally similar basaltic andesite to andesitic magmas from shallow and adjacent magma chambers. This period of activity most likely built up the Rotopaunga Scoria units, with apparently very little of these eruptionspreserved to the west, south or east of BLC. Central Crater may have been a sink for these deposits which have become subsequently obscured. Additionally, the younger cones of North Crater and Red Crater may have erupted through, or grown-over the top of, much of the western and southern deposits of BLC, obscuring them further. Rp-Sc1 may represent multiple vents active at the same time. The last of this sequence of eruptions may have produced Rp-Sc3, the rim-mantling deposits and the BLC lava flow.

Post Eruptive History

BLC may have been inactive for as long as 15,000 to 20,000 years. In this time new young vents have emerged, e.g. Ngauruhoe, Red Crater and the Te Maari craters. These vents have produced multiple tephra eruptions which have accumulated on the inner crater slopes of BLC. Colluvium and sedimentary

systems have eroded and re-worked these tephras, and alpine processes have degraded the shape of BLC and the surrounding landforms. Most of Rp-Sc3 is removed from the peak of Rotopaunga. With no drainage, the crater has filled with rainfall and snow melt to create the Blue Lake.

On the Timing of the Blue Lake

At some point in the history of BLC, it filled with water forming a lake. It is difficult to determine if the crater has filled with water more than once, or if the lake formed only since activity has ceased. Cronin *et al.* (1997) identified several lahars coming from the Mangahouhounui, Mangamate and Puketate rivers from the period of ~14-23 ka that most likely originated from the upper slopes of the Mangahouhounui Valley, of which BLC is the only standing water body. Almost all of the Holocene lahars of Tongariro have been linked to large-scale tephra eruptions (Donoghue *et al.* 1995). The dates of these lahars may serve as age constraints for activity at BLC. The timings of the lahars begin in the middle of the last glacial period in New Zealand; 28.8 ± 0.4 ka BP to c.18 ka and they end in a period of glacial-interglacial transition which lasted from c.18 ka to 11.88 ±0.18 cal. ka BP (Barrell *et al.* 2013).

5.9 Hazards Associated with Blue Lake Crater

Identifying the volcanic hazards associated with BLC is of particular importance as the Tongariro Alpine Crossing Track (TAC) one of New Zealand's 'Great Walks (attracting up to 700 walkers on busy days) is built on the SW rim. Potential hazards are based on past activity and eruption styles, both of BLC and of neighbouring young vents on TgVC. An eruption from BLC would most likely be of small scale; V.E.I of 1 to 3, and may occur without much warning.

An eruption through Blue Lake would likely cause a violent phreatomagmatic event. Magma may interact with hydrothermal water or steam under the surface where a vapour-dominated system exists under Tongariro, or with the lake or snow melt during winter. Active volcanic edifices that host a lake, present a high potential for hydrovolcanic eruptions that are typically far more destructive than an equivalent size eruption that lacks a lake (Delmelle and Bernard 2000). One of

the more dangerous aspects of these types of eruptions are pyroclastic base surges; turbulent density currents that flow outward from the base of a partially collapsing vertical eruption plume (Valentine and Fisher 2000). They characteristically have low particle concentration and are gas-rich (Valentine and Fisher 2000). Base surges may be dry (superheated steam as the fluid phase) or wet (condensing steam as fluid) (Waters and Fisher 1971) and range in transport and emplacement temperatures from cool to 200–300 °C (Vespermann and Schmincke 2000). Surges often run over topographic barriers and have been referred to as 'hot hurricanes' or 'blasts' (Valentine and Fisher 2000). They rarely have sufficient force to destroy buildings in their path, however, and are short lived compared with pyroclastic flows because of their lower momentum and density (Valentine and Fisher 2000). Low magnitude surgesare still highly dangerous to humans in the proximal area. The 1965 eruption at Taal volcano, Philippines, saw base surges tear trees from the ground and destroy houses, killing over 200 people (Waters and Fisher 1971; Valentine and Fisher 2000).

Pyroclastic flows have been produced by phreatic and magmatic eruptions at neighbouring North Crater and Te Maari (Griffin 2007; Pardo in-press). Andesite pyroclastic flows can extend several kilometres beyond their source at speeds of 10-100 m/s (Nakada 2000). A flow from BLC would probably be valley-confined and flow down the Mangahouhounui Valley or the valley to northwest (that intersects the TAC). A flow could also travel across Central Crater. Hot ash clouds/surges can decouple from the main flow and travel a further 6-8 km from the vent. Pyroclastic ash-cloud surges are capable of significant damage and may be the most dangerous aspect of low magnitude pyroclastic flows as their movement is not confined to valleys (Nakada 2000). Infrastructure at risk from pyroclastic flows include DoC tracks, roads, power networks, hydropower schemes, pastures and water ways.

If the water from BLC is ejected, or becomes used up,the eruption may progress to dry Hawaiian or Strombolian style. This would result in a fire-fountain, possibly in excess of 1000-1500 m height which would build spatter deposits in the proximal area. Stable scoria and spatter piles can undergo collapse days after deposition, resulting in remobilization of the material to form clastogenic lavas

that can travel several kilometres beyond their original site of deposition (Sumner 1998). Ballistics pose the largest risk of Hawaiian or Strombolian eruptions. Ballistics may travel up to 3-5 km from the vent. Hot bombs may cause fires in the surrounding areas of vegetation. The main danger from a fire-fountaining eruption is to the public users of the TAC.

Lahars from Tongariro have been attributed to a variety of generation mechanisms such as; flank collapse of hydrothermally altered and unstable portions of the cone/rim, phreatic and phreatomagmatic eruptions, sudden crater lake rim collapse and large volumes of tephra on snow-covered slopes later remobilized by heavy rain (Lecointre *et al.* 2004). Blue Lake contains an estimated 700,000 m^3 of water. It is possible that in the event of an eruption from BLC the lake water would be violently and rapidly ejected from the crater, causing a lahar. Almost all of the Holocene lahars of either Tongariro or Ruapehu have been linked to large-scale (0.2-0.9 km^3) tephra eruptions (Donoghue *et al.* 1995). There is a history of multiple lahars down the Tongariro River, and lahars sourced from the upper slopes of the Mangahouhounui Valley have occurred in the last 20,000 years (Cronin *et al.* 1997).

The areas of risk from lahar are the low-lying areas close to the Tongariro River. Of greatest risk is the town of Turangi, which is one of the most populated towns in the region and is built on top of old lahar surfaces. Another major hazard site is the small settlement of Rangipowhich the Mangahouhounui Stream cuts through (Figure 5.7)placing the Rangipo Reservoir, the Rangipo Prison and the Rangipo hydropower dam at risk. Lahars can deposit sediment across large areas of productive land, not only destroying crops but potentially resulting in a long term loss of production as a result of acidity and toxicity from low-pH crater lake waters (Cronin *et al.* 1997). State Highway 1 (one of New Zealand's most important roadways and the main north-south link through the North Island) is intersected by the major tributaries of the Mangahouhounui Valley via a number of bridges (Figure 5.7) which would likely suffer damage.

Another possible risk is that of failure of the eastern BLC rim or the hydrothermally altered zone in the northern rim of BLC. Acidic hydrothermal

water circulates within the host edifice, which alters and dissolves the rock.For example, over a 100-year period, dissolution at Poa´s and KawahIjen volcanoes has removed ~6 x 10^5 and 1.4 x 10^6 m^3 of rock, respectively (Delmelle and Bernard 2000). The process results in an increase in the permeability of flank aquifers over the lifetime of the hydrothermal system (hundreds to thousands of years) which eventually promotes crater rim collapse. Further geomechanical studies are required to accurately ascertain the long or short term risks of a breach in the Blue Lake Crater rim (Delmelle and Bernard 2000).

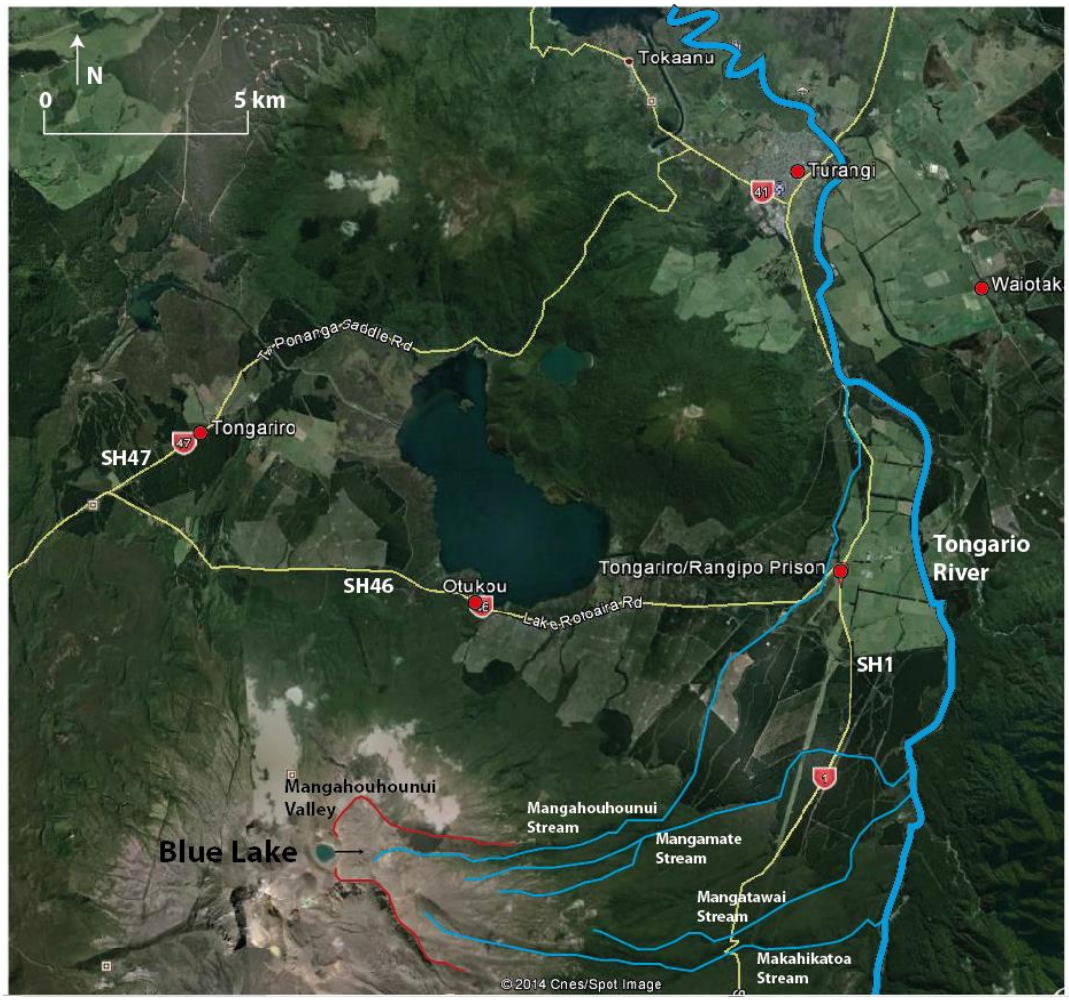

Figure 5.7. Lahar flow paths (in blue) of the major Mangahouhounui Valley streams. The Mangahouhouni, Mangamate, Mangatawai and Makahikatoa streams each cross State Highway 1 (SH1) before flowing into the Tongariro River towards the township of Turangi. The Mangahouhounui Stream intersects the small settlement of Rangipo before joining the Tongariro River. Adapted from Google Earth.

5.10 Links to the Te Maari Craters and the Young Northern TgVC Vents

The August and November 2012 eruptions of upper Te Maari crater were the first on Tongariro since 1975 (Nairn and Self 1978) and the first on the northern flanks of Tongariro since 1896 (Friedlander 1898). The re-activation of northern Tongariro has led to the re-examining of the other young vents that neighbour the Te Maari craters. The vents that occupy the northern confines of the volcano; North Crater, Te Maari craters and BLC share very similar magma geochemical compositions, age, origin and history. Similar Fe/Mg and trace element ratios suggest that all three of these young northern vents are related magmatically, although the configuration of the plumbing system is not known, or whether the same or different magma chambers were the source of the vents. The vents have erupted similar compositions of magma but display a variation of eruption styles, and the morphology of each vent is quite distinct.

It has been suggested that BLC may have erupted prior to North Crater (Kobayashi, pers communication in Griffin 2007). BLC is possibly the first of the young activity in the northern section of Tongariro; and Te Maari is the present day expression of this northern activity.

This author has witnessed steaming ground from the hydrothermal zone on the northern inner rim of BLC. The hydrothermal system below BLC is still active and manifests at the surface. BLC and Te Maari are possibly linked via the hydrothermal system that underlies them both. The TgVC contains several small geothermal areas at Ketatahi, Te Maari craters, Red Crater, Emerald Lakes and Ngauruhoe. Most of these surface manifestations are believed to be fed by the same underlying vapour-dominated system (with an area of 15-20 km^2) (Moore and Brock 1981; Hochstein 1985). The hydrothermal system formed from a combination of magmatic steam mixed with circulating meteoric water (Wilson 1960; Moore and Brock 1981; Hochstein 1985). Steaming ground (of temperatures above 70°C) was observed at the head of the Central Crater lava flow by Hobden (1997) which is the same elevation as the steaming ground beneath Red Crater. This is the result of an enhanced natural draught of steam

which presumably moves laterally beneath the valley floor Hochstein (1985). At the Te Maari craters, steaming ground covers an area of ~3000 m^2 (Hochstein 1985); the hydrothermally altered area at BLC covers ~6500 m^2.

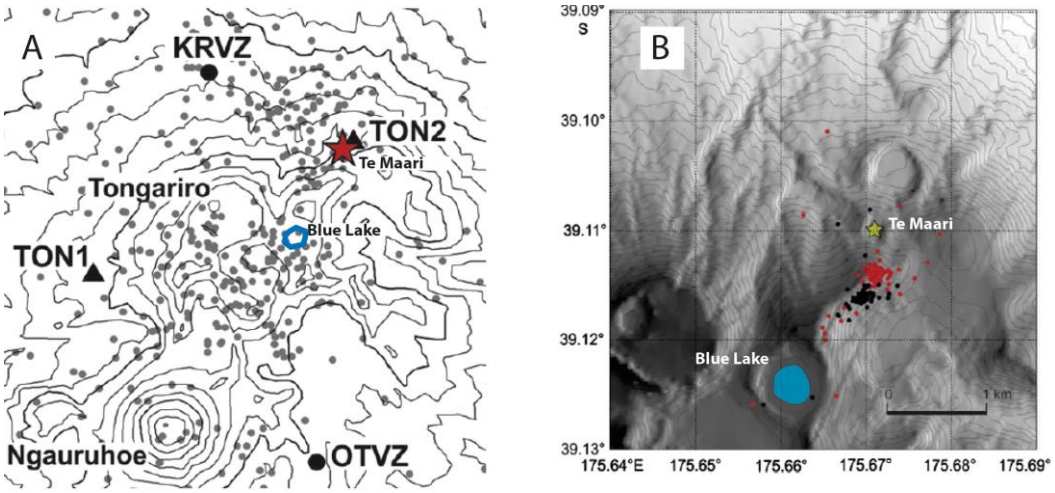

Figure 5.8. Seismic activity at the Tongariro complex. (A) Location map for the Tongariro massif. Circles show permanent seismic stations and triangles temporary stations. Epicentres of all shallow (depth ≤ 33 km) earthquakes (ML N 1.5) located from 1 Jan 1990 until 31 Dec 2011 are shown as grey dots. Blue Lake is represented by a blue circle and upper Te Maari by a red star. (B) Characteristics of the seismicity before the 6 August 2012 eruption of Te Maari 11 July to 6 August 2012 event. Black dots are locations derived from the 3-D TVZ velocity model, and red from the local area active source velocity model. Yellow star marks the Upper Te Maari crater. Adapted from Hurst et al. (in press).

Te Maari craters and BLC also appear to be linked in some way through seismic activity. Seismic studies of earthquakes from Tongariro during the period 1990 to 2011 (Figure 5.8A) shows that seismic activity below BLC has not abated. A relatively large cluster of earthquakes around BLC can be seen (Figure 5.8A). When the earthquakes from 11 July to 6 August 2012 that occurred in the weeks prior to the Te Maari eruptions are examined (Figure 5.8B) it can be seen that the majority of them lie between BLC and Te Maari; with some earthquakes situated around Blue Lake. While there is a common spatial distribution of seismic phenomenon between BLC and the Te Maari craters, this does not indicate a magmatic link between the two vents. The earthquakes suggest that magma movement occurred up to shallow depths under Tongariro, however they may also be caused by rock-breaking mechanisms caused by increasing gas pressure from underlying magma that may, or may not, be present in the seismic source region (Hurst *et al.*in press; Pardo *et al.* in press). Gas analyses suggest that magma was

present at shallow depths (Christenson *et al.* 2013)however geological studies of the 2012 eruptions seem to be inconclusive about whether or not magma was directly involved (Pardo *et al.* in press).

5.11 Conclusions

The geomorphological expression of BLC is complicated by the presence of older landform features. The eruption that excavated the vent, and built up the majority of the pyroclastic rim is difficult to identify and describe. The only evidence for the initial eruption is a discontinuous crater rim and the depression that the lake has partially filled. This is further complicated by the fact that the geomorphology of BLC is not typical of the type of landformproduced by fire-fountaining eruptions. It is therefore suggested thatBLC was excavated by pheatomagmatic processes, in which magma came into contact with the hydrothermal system below Tongariro, or withsnowor ice on the surface which created a maar.Sections through the BLC rim,however, are not exposed, and this interpretation that BLC may be a summit-maar is based on it's geomorphology.

The proximal-to-vent deposits of BLC, pre-or syn-BLC, have all been produced by explosive Hawaiian to Strombolian-style fire-fountaining. They display many features typical of this origin, along with a number of associated post and syn-depositional features. This Hawaiian to Strombolian fire-fountaining style oferuption was probably influenced by high magmatic temperatures, low magmatic volatile contents and wide flaring vent geometry.

The Rotopaunga Agglutinates are the lowest stratigraphic succession exposed in the inner rim of BLC. The group of four thick, agglutinated, lava-like deposits are not derived from BLC, but instead make up part of the upper portion of the Mangahouhounui Valley succession that was erupted from part of an older volcanic edifice. They are presumably pre-glacial in age. The Rotopaunga Scorias were produced predominantly from the accumulation ofcool spatter and scoria clasts ejected from more pulsating, Strombolian-style fire-fountains. The Rp-Sc units are most likely sourced, at least in part, from BLC. The deposits that mantle the rim and outer slopes do not appear to have constructed the ~40 m high rim of

BLC, but are interpreted as being deposited very-near-to-source from a sustained fire-fountaining eruption. The lava flow is the best constrained unit associated with BLC and is almost certainly sourced from the vent. The structure of the lava indicates that it is an a'a style flow.

The deposits of the Rotopuanga Agglutinates, the Rotopaunga Scorias, the crater rim deposits and the BLC lava flow are all plagioclase-dominated porphyritic pyroxene andesites. The lack of geochemical trends through the stratigraphic sequence indicates that there is no progression/evolution of magma through time. The common occurrence of disequilibrium features in thin section indicates magma mixing and mingling played a large role in the complex plumbing system below BLC. The magma of these units likely ascended slowly, and stagnated at shallow depths in the crust before receiving new injections ofcontrasting magma which are mingled and erupted relatively quickly.

The hazards associated with BLC include: phreatomagmatic pyroclastic density currents, fire-fountaining with ballistic bombs and blocks, and lahars caused either by a future eruption or from the failure of the BLC rim.

The northern vents of the TgVC (North Crater, Te Maari craters and BLC) are closely spaced and of a similar age and similar geochemical composition. BLC and Te Maari are likely to share a similar subsurface hydrothermal system and a spatial distribution of seismicity, although these alone do not imply a link in subsurface magma plumbing between the two vents.

Future work on BLC might includedetermining;the nature of the deposits that constructed the crater rim, how this style of andesite fire-fountaining is generated,glass compositions for the purposes ofcorrelating BLC deposits with ring-plain tephras, and the nature of the hydrothermal system that exists below BLC and permeates through the TgVC. Afinal, and potentially important study, would be to take a core of the lake, which most likely contains a high resolution record of the eruptive activity on the TgVC in the last 10-20 ka, and may provide some age constraints on the Blue Lake Crater.

Allen, L.R., 1948. Activity at Ngauruhoe, April- May 1948. *New Zealand Journal of Science and Technology B30*, 187-193.

Bardsley, C.J., Physical Volcanology of Red Crater, Tongariro. Unpublished Master of Science Thesis, University of Waikato, Hamilton, 2004.

Basher, R., Physical Volcanology and future risk from the Te Maari Craters, Tongariro. Unpublished Master of Science Thesis, University of Waikato, Hamilton, 2005.

Battey, M.H., 1949. The recent eruption of Ngauruhoe. *Records of the Auckland Institute and Museum, 3*, 387-395.

Cas, R.A.F., Wright, J.V., 1987. *Volcanic Successions: Modern and Ancient*. Allen & Unwin, London.

Cassidy, J., Ingham, M., Locke, C.A., Bibby, H., 2009. Subsurface structure across the axis of the Tongariro Volcanic Centre, New Zealand. *Journal of Volcanology and Geothermal Research, 179*, 233–240.

Chizmar, J.M., The nature and dynamics of explosive eruptions and associated crater formation at Tama Lakes, Tongariro Volcano. Unpublished Master of Science Thesis, University of Waikato, Hamilton, 2003.

Christenson, B.W., Britten, K.W., Mazot, A., Fitzgerald, J., 2013. The 2012 Eruption of Te Maari: Pre- and Post-eruption Gas Signatures from the Magmatic-Hydrothermal System. In: Te Maari day – a workshop to discuss scientific advances from the 2012 Te Maari eruption held at Council Office, Turangi 22 March 2013, Jolly, A.D. (Ed.), *GNS Science Miscellaneous Series.*

Christenson, B.W., Crump, M.E., 1994. Chemistry of springs and lakes in Tongariro National Park, 1989-1992. *New Zealand Volcanological Record no 21*, 98-99.

Cole, J.W., 1978. Andesites of the Tongariro Volcanic Centre, North Island, New Zealand. *Journal of Volcanology and Geothermal Research, 3* (1-2), 121–153.

Cole, J.W., Cashman, K.V, Rankin, P.C., 1983. Rare-earth element geochemistry and the origin of andesites and basalts of the Taupo Volcanic Zone, NZ. *Chemical Geology, 38*, 255-274.

Cole, J.W., Graham, I.J., Hackett, W.R., Houghton, B.F., 1986. Volcanology and petrology of the Quaternary composite volcanoes of Tongariro volcanic centre, Taupo volcanic zone. *Late Cenozoic Volcanism in New Zealand, Vol. 23*, 224–250.

Couch, S., Sparks, R.S.J., Carrol, M.R., 2001. Mineral disequilibrium in lavas expanded by convective self-mixing in open magma chambers. *Nature*, 411, 1037-1039.

Cronin S.J., Neall, V.E., Palmer, A.S., 1997. Lahar history and hazard of the Tongariro River, northeastern Tongariro Volcanic Centre, New Zealand. *New Zealand Journal of Geology and Geophysics*, *40*, 383-393.

Cronin, S.J., Neall, V.E., 1997. A late quaternary stratigraphic framework for the north eastern Ruapehu and eastern Tongariro ring plains, New Zealand. *New Zealand Journal of Geology and Geophysics*, *40* (2), 185–197.

Cronin, S.J., Wallace, R.C., Neall, V.E., 1996. Sourcing and identifying andesitic tephras using major oxide titanomagnetite and hornblende chemistry, Egmont volcano and Tongariro Volcanic Centre, New Zealand. *Bulletin of Volcanology*, *58*(1), 33–40.

Davidson, J., de Silva, S., Composite Volcanoes. In: *Encyclopaedia of Volcanoes*, H. Sigurdsson (Ed.). Academic Press, New York, 2000.

Deering, C.D., Cole, J.W., Vogel, T.A., 2008. A rhyolite compositional continuum governed by lower crustal source conditions in the Taupo Volcanic Zone, New Zealand. *Journal of Petrology, 49*, 2245-2276.

Delmelle, P., Bernard, A., Volcanic Lakes. In: *Encyclopaedia of Volcanoes*, H. Sigurdsson (Ed.). Academic Press, New York, 2000.

Dibble, R.R., Nairn, I.A., Neall, V.E., 1985. Volcanic hazards of the North Island, New Zealand – overview. *Journal of Geodynamics, 3,* 369-396.

Donoghue, S.L., Neall, V.E., Palmer, A.S., 1995. Stratigraphy and chronology of late Quaternary andesitic tephra deposits, Tongariro Volcanic Centre, New Zealand. *Journal of the Royal Society of New Zealand, 25:2,* 115-206.

Ewart, A., 1982. The mineralogy and petrology of Tertiary-Recent orogenic rocks with special reference to the andesite-basaltic compositional range. In: *Andesites: Orogenic andesites and related rocks,* R.S. Thorpe (Ed.). Chichester, Wiley.

Feeley, T.C., and Davidson, J.P., 1994. Petrology of calc-alkaline lavas at Volcan Ollague and the origin of compositional diversity at Central Andean stratovolcanoes. *Journal of Petrology 35,* 1295-1340.

Friedlander, B., 1898. Some notes on the Volcanoes of the Taupo District. *Transactions of the New Zealand Institute, 31,* 498-510.

Gill, J.B., 1981. *Orogenic andesites and plate tectonics.* Berlin, Springer-Verlag.

Google Inc., 2014. *Google Earth* (Version 7.1.2.2041). Mountain View, California.

Graham, I.J., Cole, J.W., Briggs, R.M., Gamble, J.A., Smith, I.E.M., 1995. Petrology and petrogenesis of volcanic rocks from Taupo Volcanic Zone: a review. *Journal of Volcanology and Geothermal Research, 68,* 59-87.

Graham, I.J., Grapes, R.H., Kifle, K., 1988. Buchitic metagreywacke xenoliths from Mount Ngauruhoe, Taupo Volcanic Zone, New Zealand. *Journal of Volcanology and Geothermal Research, 35,* 205-216.

Graham, I.J., Hackett, W.R., 1987. Petrology of calc-alkaline lavas from Ruapehu Volcano and related vents, Taupo Volcanic Zone, New Zealand. *Journal of Petrology 28,* 531-567.

Gregg, D.R., 1956. Eruption of Ngauruhoe 1954-1955. *New Zealand Journal of Science and Technology, B37,* 675-688.

Gregg, D.R., 1961a. The tectonic setting of the Tongariro Volcanoes, New Zealand. *Proceedings of the Ninth Pacific Science Congress,* 218-224.

Gregg, D.R., (1961b) Volcanoes of the Tongariro National Park. *A NZ Geological Survey Handbook,* 28:83.

Griffin, A.M., Products and processes of cone-building eruptions from North Crater, Tongariro. Unpublished Master of Science Thesis, University of Waikato, Hamilton, 2007.

Hagerty, M., Benites, R., 2003. Tornillos beneath Tongariro Volcano, New Zealand. *Journal of Volcanology and Geothermal Research*, *125* (1-2), 151–169.

Head, J.W., Wilson, L., 1989. Basaltic pyroclastic eruptions: Influence of gas-release patterns and volume fluxes on fountain structure, and the formation

of cinder cones, spatter cones, rootless flows, lava ponds and lava flows. *Journal of Volcanology and Geothermal Research 37***,** 261–271.

Healy, J., 1963. Welded pyroclastic rock at Tongariro. *New Zealand Journal of Geology and Geophysics, 6,* 712-713.

Hector, J.D., 1870. Eruption of the Volcano Tongariro, New Zealand. *Nature, 2,* 477-479.

Hill, H., 1891. Ruapehu and Ngauruhoe. *Transactions of the New Zealand Institut*e, 24, 603-625.

Hill, H., 1894. The volcanic outburst at Te Maari, Tongariro, in November, 1892. *Transactions of the New Zealand Institute, 26,* 388-392.

Hobden, B.J., Houghton, B.F., Davidson, J.P., Weaver, S.D., 1999. Small and Short-lived Magma Batches at Composite Volcanoes: Time Windows at Tongariro Volcano, New Zealand. *Journal of the Geological Society, 156,* 865–868.

Hobden, B.J., Houghton, B.F., Nairn, I.A., (2002). Growth of a young frequently active composite cone: Ngauruhoe volcano, New Zealand. *Bulletin of Volcanology, 64,* 392-409.

Hobden, B.J., Houghton, D.F., Lanphere, M.A., Nairn, I.A., 1996. Growth of the Tongariro volcanic complex: new evidence from K-Ar age determinations. *New Zealand Journal of Geology and Geophysics, 50,* 53-66.

Hobden, B.J., Modelling Magmatic trends in time and space: eruptive and magmatic history of Tongariro Volcanic Complex, New Zealand. Unpublished Ph.D. Thesis, University of Canterbury 1997.

Hochstein, M., 1985. Steaming Ground at Red Crater and in the Te Mari craters, Mount Tongariro, geothermal system (NZ). *Proceedings of the 7th NZ Geothermal Workshop,* 177-180.

Houghton, B.F., Wilson, C.J.N., 1989. A vesicularity index for pyroclastic deposits. *Bulletin of Volcanology, 51,* 451-462.

Houghton, B.F., Wilson, C.J.N., Smith, I.E.M., 1999. Shallow-seated controls on styles of explosive basaltic volcanism: a case study from New Zealand. *Journal of Volcanology and Geothermal Research, 91,* 97-120.

Humphreys, M.C.S., Blundy, J.D., Sparks, R.S.J., 2006. Magma evolution and open-system processes at Shiveluch Volcano: Insights from phenocryst zoning. *Journal of Petrography, 47*, 2303-2334.

Hurst, T., Jolly, A.D., Sherburn, S., in press. Precursory characteristics of the seismicity before the 6 August 2012 eruption of Tongariro volcano, North Island, New Zealand, *Journal of Volcanology and Geothermal Research*.

Jaupart, C., Magma ascent at shallow levels. In: *Encyclopaedia of Volcanoes*, H. Sigurdsson (Ed.). Academic Press, New York, 2000.

Kilburn, C.R.J., 2000. Lava flows and flow fields. In: *Encyclopaedia of Volcanoes*, H. Sigurdsson (Ed.). Academic Press, New York, 2000.

Kilburn, C.R.J., Lopes, R.M.C., 1991. General patterns of flow field growth: a'a and blocky lavas. *Journal of Geophysical Research, B, 96*, 719-732.

Krippner, J.B., Ngauruhoe inner crater volcanic processes of the 1954-1955 and 1974-1975 eruptions. Unpublished Master of Science Thesis, University of Waikato, Hamilton, 2009.

Lecointre, J., Hodgson, K., Neall, V., Cronin, S., 2004. Lahar-Triggering Mechanisms and Hazard at Ruapehu Volcano, New Zealand. *Natural Hazards 31,* 85–109.

Lecointre, J.A., Neall, V.E., Wallace, C.R., Prebble, W.M., 2002. The 55- to 60-ka Te Whaiau formation: A catastrophic, avalanche-induced, cohesive debris-flow deposit from Proto-Tongariro volcano, New Zealand. *Bulletin of Volcanology*, *63*(8), 509–525.

Lowe, D.J., Shane, P.A.R., Alloway, B.V., Newnham, R.M., 2008. Fingerprints and age models for widespread New Zealand tephra marker beds erupted since 30,000 years ago: a framework for NZ-INTIMATE. *Quaternary Science Reviews*, *27*(1-2), 95–126.

Malcolm, L., van Rossen, A., 1997. Ashes to ashes? *International water power and dam construction, February 1997,* 22-24.

Marti, J., Ernst, G., *Volcanoes and the Environment*. Cambridge University Press, Cambridge, 2005.

Matthews, W.H., 1967. A contribution to the geology of the Mount Tongariro massif, North island, New Zealand. *New Zealand Journal of Geology and Geophysics, 10,* 1027-1038.

McDonough, W.F., Sun, S.S., Ringwood, A.E., Jagoutz, E., Hofmann, A.W. 1992. Potassium, rubidium and cesium in the Earth and Moon and the evolution of the mantle of the earth. *Geochimica et Cosmochimica Acta, 56,* 1001-1012.

Michaelis, F.B., 1981. *The Lakes of Tongariro National Park.* Report to the National Parks and Reserves Authority.

Möebis, A., Cronin, S.J., Neall, V.E., Smith, I.E., 2011. Unravelling a complex volcanic history from fine-grained, intricate Holocene ash sequences at the Tongariro Volcanic Centre, New Zealand. *Quaternary International, 246* (1-2), 352–363.

Moore, P.R., Brock, S.L., 1981. A physical and chemical survey of Ketetahi Hot Springs, Mt Tongariro, NZ. *New Zealand Journal of Science, 24,* 161-177.

Nairn, I.A., Kobayashi, T., Nakagawa, M. 1998. The ~ 10 ka multiple vent pyroclastic eruption sequence at Tongariro Volcanic Centre, Taupo Volcanic Zone, New Zealand: Part 1. Eruptive processes during regional extension. *Journal of Volcanology and Geothermal Research, 86* (1-4), 19–44.

Nairn, I.A., Self, S., 1978. Explosive eruptions and pyroclastic avalanches from Ngauruhoe in February 1975. *Journal of Volcanology and Geothermal Research 3,* 39-60.

Nakada, S., Hazards from pyroclastic flows and surges. In: *Encyclopaedia of Volcanoes*, H. Sigurdsson (Ed.). Academic Press, New York, 2000.

Nakagawa, M., Nairn, I.A., Kobayashi, T., 1998. The ~ 10 ka multiple vent pyroclastic eruption sequence at Tongariro Volcanic Centre, Taupo Volcanic Zone, New Zealand: Part 2. Petrological insights into magma storage and transport during regional extension. *Journal of Volcanology and Geothermal Research, 86* (1-4), 45–65.

Nakagawa, M., Wada, K., Wood, C.P., 2002. Mixed magmas, mush chambers and eruption triggers: evidence from zoned clinopyroxene phenocrysts in andesite scoria from the 1995 eruptions of Ruapehu Volcano, New Zealand. *Journal of Petrology, 43,* 2279-2303.

Nelson, S.T., Montana, A., 1992. Sieve-textured plagioclase in volcanic rocks produced by rapid decompression. *American Mineralogist, 77,* 1242-1249.

Nixon, G.T., 1988a. Petrology of the younger andesites and dacites of Iztaccihuatl Volcano, Mexico: 1. Disequilibrium phenocryst assemblages as indicators of magma chamber processes. *Journal of Petrology 29*, 213-264.

Nixon, G.T., Pearce, T.H., 1987. Laser-inferometry study of oscillatory zoning in plagioclase: The record of magma mixing and phenocryst recycling in calc-alkaline magma chambers, Iztaccihuatl volcano, Mexico. *American Mineralogist, 72*, 1144-1162.

Pardo, N., Cronin, S.J., Németh, K., Brenna, M., Schipper, C., Breard I., White, E., James, D.L., Procter, J., Stewart, B., Agustín-Flores, J., Zernack, A., Kereszturi, G., Lube, G., Auer, A., Neall, V., Wallace, C., in press. Perils in distinguishing phreatic from phreatomagmatic ash; insights into the eruption mechanisms of the 6 August 2012 Mt. Tongariro eruption, New Zealand. *Journal of Volcanology and Geothermal Research.*

Parfitt, E.A., 2004. A discussion of the mechanisms of explosive basaltic eruptions. *Journal of Volcanology and Geothermal Research, 134*, 77-107.

Parfitt, E.A., Wilson, L., 1995. Explosive volcanic eruptions-IX. The transition between Hawaiian-style lava fountaining and Strombolian explosive activity. *Geophysics Journal International, 121***,** 226–232.

Parfitt, E.A., Wilson, L., 1999. A Plinian treatment of fallout from Hawaiian lava fountains. *Journal of Volcanology and Geothermal Research, 88*, 67-75.

Parfitt, E.A., Wilson, L., Neal, C.A., 1995. Factors influencing the height of Hawaiian lava fountains: implications for the use of fountain height as an indicator of magma gas content. *Bulletin of Volcanology*, *57*, 440-450.

Patterson, D.B., Graham, I.J., 1988. Petrogenesis of andesitic lavas from Mangatepopo Valley and Upper Tama Lake, Tongariro Volcanic Centre, New Zealand. *Journal of Volcanology and Geothermal Research, 35*,17-29.

Pearce, T.H., 1993. Recent work on oscillatory zoning in plagioclase. In: *Feldspars and their reactions*, I. Parsons (Ed.). Netherlands, Kluwer Academic Publishers.

Pearce, T.H., Russell, J.K. and Wolfson, I., 1987. Laser-interference and Nomarski interference imaging of zoning profiles in plagioclase phenocrysts from the May 18 1980 eruption of Mt St Helens, Washington. *American Mineralogist, 72*, 1131-1143.

Price, R.C., Gamble, J.A., Smith, I.E.M., Stewart, R.B., Eggins, S., Wright, I.C., 2005. An integrated model for the temporal evolution of andesites and rhyolites and crustal development in New Zealand's North Island. *Journal of Volcanology and Geothermal Research*, *140*, 1-24.

Rhoda, R., Burton, T., Geo-*Mexico; the geography and dynamics of modern Mexico.* Sombrero Books, Vancouver, 2010.

Rogan, W., Blake, S., 1994. Trace element zonation of phenocrysts from Ngauruhoe Volcano, New Zealand: constraints on magmatic processes. *Mineral Magazine, 58A*, 783-784.

Rollinson, H.R., 1993. *Using geochemical data: evaluation, presentation, interpretation.* Harlow, Longman.

Roscoe, R. (undated). *Blue Lake Crater, North Crater behind.* Photograph. Retrieved 10 January 2013 from, http://www.photovolcanica.com/VolcanoInfo/Tongariro/Tongariro.html.

Roscoe, R. (undated). *Tama Lake Craters with Ngauruhoe behind.* Retrieved 30 March 2014, from http://www.photovolcanica.com/VolcanoInfo/Tongariro/Tongariro.html.

Rowlands, D.P., White, R.S., Haines, A.J., 2005. Seismic tomography of the Tongariro Volcanic Centre, New Zealand. *Geophysical Journal International, 163*(3), 1180–1194.

Sable, J., Houghton, B.F., Del Carlo, P., Coltelli, M., 2006. Changing conditions of magma ascent and fragmentation during the Etna 122 BC basaltic Plinian eruption: evidence from clast microtextures. *Journal of Volcanology and Geothermal Research, 158*, 333-354.

Sakuyama, M., 1978. Petrographic evidence of magma mixing in Shirouma-Oike volcano, Japan. *Bulletin of Volcanology, 41*, 501-512.

Sakuyama, M., 1981. Petrological study of the Myoko and Kurohime volcanoes, Japan, Crystallization sequence and evidence for magma mixing. *Journal of Petrology, 22*, 553-583.

Sanders, F., Rheology and Flow Emplacement Processes of the 1954 Lavas, Mount Ngauruhoe. Unpublished Master of Science Thesis, University of Waikato, Hamilton, 2010.

Shane, P., Doyle, L.R., Nairn, I.A., 2008. Heterogeneous andesite-dacite ejecta in 26-16.6 ka pyroclastic deposits of Tongariro Volcano, New Zealand: The product of multiple magma-mixing events. *Bulletin of Volcanology, 70*(4), 517–536.

Sigurdsson, H., Carey, S., Palais, J.M., Devine, J., 1990. Pre-eruption compositional gradients and mixing of andesite and dacite magma erupted from Nevado del Ruiz Volcano, Columbia in 1985. *Journal of Volcanology and Geothermal Research, 41*, 127-151.

Sparks, R.S., Sigurdsson, H., Wilson, L., 1977. Magma mixing: a mechanism for triggering acid explosive eruptions. *Nature, 267*, 315-318.

Stolz, A.J., Jochum, K.P., Spettel, B., Hofmann, A.W., 1996. Fluid- and melt-related enrichment in the subarc mantle: evidence from Nb/Ta variations in island-arc basalts. *Geology, 24*,587-590.

Sumner, J.M., 1998. Formation of clastogenic lava flows during fissure eruption and scoria cone collapse: the 1986 eruption of Izu-Oshima volcano, eastern Japan. *Bulletin of Volcanology, 60*, 195– 212.

Sumner, J.M., Blake, S., Matela, R.J., Wolff, J.A., 2005. Spatter. *Journal of Volcanology and Geothermal Research 142,* 49– 65.

Sutton, A.N., Blake, S., Wilson, C.J.N., 1995. An outline geochemistry of rhyolite eruptives from Taupo volcanic centre, New Zealand. *Journal of Volcanology and Geothermal Research, 68*, 153– 175.

Szramek, L., Gardner, J.E., Larsen, J., 2006. Degassing and microlite crystallisation of basaltic andesite magma erupting at Arenal Volcano, Costa Rica. *Journal of Volcanology and Geothermal Research, 157*, 182-201.

Tait, S.R., Jaupart, C., Vergniolle, S., 1989. Pressure, gas content and eruption of a shallow, crystallising magma chamber. *Earth and Planetary Science Letters, 92*, 107-123.

Tatsumi, Y., Hamilton, D. L., Nesbitt, R.W., 1986. Chemical characteristics of fluid phase released from a subducted lithosphere and origin of arc magmas: evidence from high-pressure experiments and natural rocks. *Journal of Volcanology and Geothermal Research, 29*, 293-309.

Topping, W.W., 1973. Tephrostratigraphy and chronology of late Quaternary eruptives from the Tongariro volcanic centre, New Zealand. *New Zealand Journal of Geology and Geophysics, 16*, 397-423.

Topping, W.W., Some aspects of Quaternary history of Tongariro Volcanic Centre, Ph.D. Thesis, Victoria University, Wellington, 1974.

Turner, F.J., Verhoogen, J., *Igneous and metamorphic petrology*, McGraw-Hill, New York, 1960.

Vergniolle, S., Boichu, M., Caplan-Auerbach, J., 2004. Acoustic measurements of the 1999 basaltic eruption of Shishaldin Volcano, Alaska, 1. Origin of Strombolian activity. *Journal of Volcanology and Geothermal Research, 137*, 109-134.

Vergniolle, S., Mangan, M., Hawiian and Strombolian eruptions. In: *Encyclopaedia of Volcanoes*, H. Sigurdsson (Ed.). Academic Press, New York, 2000.

Vespermann, D., Schmincke, H., Scoria Cones and Tuff Rings. In: *Encyclopaedia of Volcanoes*, H. Sigurdsson (Ed.). Academic Press, New York, 2000.

Waters, A.C., Fisher, R. V., 1971. Base surges and their deposits: Capelinhos and Taal volcanoes. *Journal of Geophysical Research, 76***,** 5596–5614.

Wilson, C.J.N., Houghton, B.F., McWilliams, M.O., Lanphere, M.A., Weaver, S.D., Briggs, R.M., 1995. Volcanic and structural evolution of Taupo Volcanic Zone, New Zealand: a review. *Journal of Volcanology and Geothermal Research, 68*, 1–28.

Wilson, S.H., 1960. Physical and chemical investigation of Ketatahi Hot Springs. In: *The geology of Tongariro Subdivision.* D.R., Gregg (Ed.). *NZ Geological Survey Bulletin, 40*, 124-144.

Wolff, J.A., Sumner, J.M., 2000. Lava fountains and their products. In: *Encyclopaedia of Volcanoes*, H. Sigurdsson (Ed.). Academic Press, New York, 2000.

Wolhetz, K., Heiken, G., *Volcanology and Geothermal Energy*. University of California Press, Los Angeles, 1992.

Woods, A.W., Cardoso, S.S.S., 1997. Triggering basaltic volcanic eruptions by bubble melt seperation. *Nature, 385*, 518-520.

List of sample numbers, field site locations, GPS coordinates and analyses conducted.

Waikato No.	Sample No.	Site No.	Co-ordinates		Elevation (m a.s.l)	Sample Type	Unit/ Location	Thin Section	Point Count	Density and Vesicularity	XRD	EMPA	XRF
W14 0001	BL01	Site 1	S 39.07.641	E 175.39.745	-	Volcaniclastic ash/lapilli	Crater fill	-	-	-	-	-	-
W14 0002	BL02	Site 1			-	Volcaniclastic ash/lapilli	Crater fill	-	-	-	-	-	-
W14 0003	BL03	Site 6	S 39.07.244	E 175.39.653	-	Platy agl.	Central Crater peak	X	-	-	-	-	-
W14 0004	BL04	Site 6	S 39.07.112	E 175.39.676	-	Agl.	Central Crater peak	X	-	-	-	-	X
W14 0005	BL05	Site 2	S 39.07.513	E 175.39.416	-	Platy agl.	Rp-Ag4	X	-	-	-	-	X
W14 0006	BL06	Site 7	S 39.07.652	E 175.39.768	-	Agl.	SW Ag	X	X	-	-	X	X
W14 0007	BL07	Site 8	S 39.07.655	E 175.39.540	-	Platy agl.	SW Ag	X	-	-	-	-	X
W14 0008	BL08	Site 5	S 39.07.613	E 175.39.520	-	Agl.	SW Ag	X	-	-	-	-	X
W14 0009	BL09	Site 9	S 39.07.694	E 175.39.861	-	Agl.	Central Crater peak	X	X	-	-	-	X
W14 0010	BL10	Site 10	S 39.07.327	E 175.39.903	-	Agl.	Rp-Ag4	X	X	-	-	X	X
W14 0011	BL11	Site 11	S 39.07.313	E 175.39.868	-	Platy agl.	Rp-Ag4	X	-	-	-	-	X
W14 0012	BL12	Site 12	S 39.07.299	E 175.39.859	-	Agl.	Rp-Ag4	X	-	-	-	-	X
W14 0013	BL13	Site 13	S 39.07.286	E 175.39.849	-	Agl.	Rp-Ag2	X	-	-	-	-	X
W14 0014	BL14	Site 13	S 39.07.655	E 175.39.994	1652	Agl.	Rp-Ag2	X	X	-	-	-	X
W14 0015	BL15	Site 14	S 39.07.620	E 175.40.081	1639	Autobreccia	Lava flow	X	X	X	-	X	X
W14 0016	BL16	Site 15	S 39.07.614	E 175.40.140	1620	Lava	Lava flow	X	X	-	-	-	X
W14 0017	BL17	Site 16	S 39.07.644	E 175.40.217	1600	Lava	Lava flow	X	X	-	-	-	X
W14 0018	BL17a	Site 16				Dense block/bomb	Lava flow	-	-	-	-	-	X

W14 0019	BL18	Site 18	S 39.07.548	E 175.40.295	1593	Lava	Lava flow	X	X	-	-	-	X
W14 0020	BL19	Site 19	S 39.07.158	E 175.39.873	1821	Scoria	Rp-Sc1	X	X	X	-	X	X
W14 0021	BL19a	Site 19				Dense block/bomb	Rp-Sc1	X	-	X	-	-	X
W14 0022	BL20	Site 19	S 39.07.140	E 175.39.716	-	Scoria	Rp-Sc3	X	-	-	-	-	X
W14 0023	BL21	Site 20	S 39.07.214	E 175.39.732	1787	Scoria	Rp-Sc1	X	X	-	-	-	X
W14 0024	BL22	Site 4	-	-	-	Dense block/bomb	Rp-Sc3	X	X	-	-	-	X
W14 0025	BL23	Site 22	-	-	-	Basal breccia	Rp-Ag4	X	-	X	-	-	X
W14 0026	BL23a	Site 22	-	-	-	Basal breccia	Rp-Ag4	X	-	-	-	-	-
W14 0027	BL24	Site 24	S 39.07.234	E 175.39.783	1792	Platy agl.	Rp-Ag2	X	-	-	-	-	X
W14 0028	BL25	Site 24	S 39.07.245	E 175.39.793	-	Agl.	Rp-Ag2	X	-	-	-	-	X
W14 0029	BL26	Site 25	S 39.07.240	E 175.39.754	-	Basal breccia	Rp-Ag1	X	-	X	-	-	X
W14 0030	BL27	Site 25	S 39.07.008	E 175.39.531	1681	Agl.	Rp-Ag1	X	X	-	-	X	X
W14 0031	BL28	Site 26	S 39.07.077	E 175.39.533	1705	Scoria	Rp-Sc3	X	-	X	-	-	X
W14 0032	BL29	Site 21	S 39.07.414	E 175.39.393	1785	Agl.	Rp-Ag4	X	-	-	-	-	X
W14 0033	BL29a	Site 21				Dense block/bomb	Rp-Ag4	X	-	-	-	-	-
W14 0034	BL30	Site 27	S 39.07.356	E 175.39.388	-	Scoria	Rp-Sc1	X	X	X	-	-	X
W14 0035	BL31	Site 27	S 39.07.332	E 175.39.430	-	Agl.	Rp-Sc1	X	X	X	-	X	X
W14 0036	BL32	Site 29	S 39.07.332	E 175.39.520	1756	Agl.	Western rim	X	-	-	-	-	X
W14 0037	BL32a	Site 29			-	Dense block/bomb	Western rim	X	-	-	-	-	-
W14 0038	BL33	Site 30	S 39.07.239	E 175.39.585	-	Scoria	Western rim	X	-	-	-	-	-
W14 0039	BL34	Site 30	S 39.07.241	E 175.39.577	-	Scoria	Western rim	X	-	-	-	-	X
W14 0040	BL35	Site 31	S 39.07.239	E 175.39.551	-	Dense block/bomb	Western rim	X	-	-	-	-	X

W14 0041	BL35a	Site 31			-	Dense block/bomb	Western rim	X	-	X	-	-	X
W14 0042	BL36	Site 32	S 39.07.234	E 175.39.536	-	Scoria	Rp-Sc1	X	-	-	-	-	X
W14 0043	BL36a	Site 32			-	Dense block/bomb	Rp-Sc1	X	-	-	-	-	X
W14 0044	BLht01	Site 33	-	-	-	Altered	Hydrothermal Zone	X	-	-	X	-	-
W14 0045	BLht02	Site 34	-	-	-	Altered	Hydrothermal Zone	X	-	-	X	-	-
W14 0046	BLht03	Site 35	-	-	-	Altered	Hydrothermal Zone	X	-	-	X	-	-
W14 0047	BLht04	Site 35	-	-	-	Altered	Hydrothermal Zone	X	-	-	X	-	-
W14 0048	BLht05	Site 36	-	-	-	Altered	Hydrothermal Zone	X	-	-	X	-	-

Sample: BL15
Locality: Site 14
Unit: BLC lava flow

mm	phi	Weight (g)	Cumulative Weight (g)	Total %	Cumulative % finer
64	**-6**	167.84	167.84	31.27	68.73
32	**-5**	107.70	275.54	20.06	48.67
16	**-4**	121.68	397.22	22.67	26.00
8	**-3**	47.53	444.75	8.85	17.15
4	**-2**	23.07	467.82	4.30	12.85
2	**-1**	16.89	484.71	3.15	9.70
1	**0**	12.58	497.29	2.34	7.36
0.5	**1**	9.99	507.28	1.86	5.50
0.25	**2**	10.33	517.61	1.92	3.57
0.11	**3.25**	12.49	530.10	2.33	1.25
0.06	**4**	4.79	534.89	0.89	0.36
<0.06	**<4**	1.91	536.80	0.36	0.00

Sample: BL23
Locality: Site 22
Unit: Rp-Ag4

mm	phi	Weight (g)	Cumulative Weight (g)	Total %	Cumulative % finer
64	**-6**	279.38	279.38	35.20	64.80
32	**-5**	327.54	606.92	41.27	23.53
16	**-4**	91.44	698.36	11.52	12.01
8	**-3**	42.43	740.79	5.35	6.67
4	**-2**	21.00	761.79	2.65	4.02
2	**-1**	11.77	773.56	1.48	2.54
1	**0**	7.35	780.91	0.93	1.61
0.5	**1**	4.44	785.35	0.56	1.05
0.25	**2**	3.13	788.48	0.39	0.66
0.11	**3.25**	3.31	791.79	0.42	0.24
0.06	**4**	1.30	793.08	0.16	0.08
<0.06	**<4**	0.63	793.71	0.08	0.00

Sample: BL28
Locality: Site 26
Unit: Rp-Sc3

mm	phi	Weight (g)	Cumulative Weight (g)	Total %	Cumulative % finer
64	**-6**	126.63	126.63	30.57	69.43
32	**-5**	149.24	275.87	36.03	33.39
16	**-4**	85.65	361.52	20.68	12.71
8	**-3**	23.29	384.81	5.62	7.09
4	**-2**	9.29	394.10	2.24	4.85
2	**-1**	5.15	399.25	1.24	3.60
1	**0**	3.33	402.58	0.80	2.80
0.5	**1**	3.09	405.67	0.75	2.05
0.25	**2**	2.73	408.41	0.66	1.39
0.11	**3.25**	3.16	411.57	0.76	0.63
0.06	**4**	1.73	413.30	0.42	0.21
<0.06	**<4**	0.87	414.17	0.21	0.00

Sample: BL31
Locality: Site 27
Unit: Rp-Sc1

mm	phi	Weight (g)	Cumulative Weight (g)	Total %	Cumulative % finer
64	**-6**	0.00	0.00	0.00	100.00
32	**-5**	147.81	147.81	28.88	71.12
16	**-4**	147.68	295.49	28.86	42.26
8	**-3**	72.82	368.31	14.23	28.04
4	**-2**	39.95	408.26	7.81	20.23
2	**-1**	24.52	432.78	4.79	15.44
1	**0**	23.16	455.94	4.53	10.91
0.5	**1**	11.59	467.53	2.26	8.65
0.25	**2**	14.38	481.91	2.81	5.84
0.11	**3.25**	17.07	498.98	3.33	2.51
0.06	**4**	6.29	505.27	1.23	1.28
<0.06	**<4**	6.53	511.80	1.28	0.00

The mineral abbreviations used here are:

plg = plagioclase
ol = olivine
cpx = clinopyroxene
opx = orthopyroxene
ox = Fe-Ti oxides (magnetite and ilmenite)
Grain size measurements are given for the maximum crystal dimension

Sample #	Unit	Phenocrysts Present	Phenocrysts (%)	Size and Shape of Phenocrysts	Vesicles (%)	Xenoliths (%)	Groundmass (%)
BL03	Central Crater Peak	Pl>Cpx>Opx>Ox	65>17>13>5	fine sub-an	30		40; hyalopilitic
BL04	Central Crater Peak	Pl>Cpx>Opx>Ol>Ox	70>10>10>5>5	course-med sub	30 rounded coalesed		50; felsophyric, trachytic (minor), minor glass
BL05	Rp-Ag4	Pl>Cpx>Opx>Ox	65>15>15>5	med-fine sub	5		60; felsophyric, minor gass
BL06	SW agglutinates	Pl>Cpx>Opx>Ox	70>12>12>6	course-med sub		>1 qtz/feld	65; felsophyric, trachytic
BL07	SW agglutinates	Pl>Cpx>Opx>Ox	80>10>7>3	(med)-fine sub	5 rounded		55; felsophyric, hyalopilitic with minor devit
BL08	SW agglutinates	Pl>Opx>Cpx>Ox	70>15>10>5	fine sub	20-30		50; hyalopilitic, devitrified
BL09	Central Crater Peak	Pl>Opx>Cpx>Ox	60>20>15>5	med-fine sub-an	15	1 fine qtz/feld equigranular	60; hyalopilitic, devitrified
BL10	Rp-Ag4	Pl>Opx>Cpx>Ox	65>15>15>5	course-med eu-sub	10-15	2 fine qtz/feld equigranular	60; hyalopilitic, intersertal w. pyrx

BL11	Rp-Ag3	Pl>Opx>Cpx>Ox	60>18>18>4	med eu-an	<5		50; vitrophyrc
BL12	Rp-Ag3	Pl>Opx>Cpx>Ox	50>30>15>5	med eu-sub	<5	5 qtz/feld	30-40; feldspathic, vitrophyric
BL13	Rp-Ag2	Pl>Opx>Cpx>Ox	60>22>10>2	fine sub-an	15-20		50-60; hyalopilitic
BL14	Rp-Ag2	Pl>Opx>Cpx>Ox	60>19>19>2	med-fine sub	30 minor coalesed	5 fine qtz/feld equigranula r	40-50; trachytic, minor glass, intersertal
BL15	Lava Flow	Pl>Opx>Cpx>Ox	65>16>14>5	med-fine sub	40	5 one 2 mm qtz/feld	30-40; hyalopilitic, minor devit
BL16	Lava Flow	Pl>Opx>Cpx>Ox	70>14>14>4	fine sub-an	5	<5 qtz/feld	50-60; trachytic,some glass with minor devit
BL17	Lava Flow	Pl>Opx>Cpx>Ox	65>18>12>5	med sub	45		40; feldsophric, hyalopilitic,
BL18	Lava Flow	Pl>Cpx>Opx>Ox	65>18>12>5	fine sub-an	10	<5	60; trachytic, hyalopilitic
BL19	Rp-Sc1	Pl>Opx>Cpx>Ox	45>25>25>5	course-med eu-sub	60		30-40; hyalopilitic
BL19a	Rp-Sc1	Pl>Opx>Cpx>Ox	45>25>25>5	course-med eu-sub		5 qtz/feld cluster	30; halyopilitic, minor trachytic
BL20	Rp-Sc1	Pl>Opx>Cpx>Ox	55>20>20>5	sub	50-60	5 fine qtz/feld w. sieve texture	30-40; hyalopilitic
BL21	Rp-Sc3	Pl>Opx>Cpx>Ox	50>23>23>4	course-med sub	50-60	5 fine grained	30-40; hyalopilitic devitrified
BL22	Rp-Sc3	Pl>Opx>Cpx>Ol>Ox	55>20>15>5>5	course-med sub	<5		40; feldsopheric, hyalopilitic w. minor devit

BL23	RP-Ag4	Pl>Opx>Cpx>Ox	60>20>15>5	med-fine sub		5 large qtz/feld	trachytic, intersertal w. pyrox, minor glass
BL23a	RP-Ag4	Pl>Opx>Cpx>Ox	60>20>15>5	fine sub	40-50	<5 fine grained, rounded	hyalopilitic, devitrified
BL24	Rp-Ag2	Pl>Opx>Cpx>Ox	50>25>20>5	course-med eu-sub		1 small qtz/feld	40-50; minor trachytic, minor glass w. devit
BL25	Rp-Ag2	Pl>Opx>Cpx>Ox	50>25>24>1	med sub-an		1 small, rounded (~1 mm)	40; trachytic, quite glassy w. devit
BL26	Rp-Ag1	Pl>Opx>Cpx>Ox	65>20>10>5	med eu-sub	10		40 feldsopheric, hyalopilitic w. devit
BL27	Rp-Ag1	Pl>Opx>Cpx>Ox	60>25>20>5	med eu-an	<5	5 qtz/feld	45; minor trachytic, microcrystaline glassy and devit, some pyrx
BL28	Rp-Sc3	Pl>Opx>Cpx>Ox	65>25>15>5	med eu-sub	40 rounded and coalesed, up to 7 mm	<1 one v. small qtz/feld lithic	50; hyalopilitic
BL29	Rp-Ag4	Pl>Opx>Cpx>Ox	65>18>12>5	med sub-an	1-5	5 qtz/feld	60-70; hyalopilitic, pl and pyrx
BL30	Rp-Sc1	Pl>Opx>Cpx>Ol>Ox	50>20>20>5>5	sub-an		3 one 5 mm qtz/feld	30; hyalopilitic, fine and shard-like microlites
BL31	Rp-Sc1	Pl>Cpx>Opx>Ol>Ox	55>20>15>10	course-med sub	40-50		40; hyalopilitic, devitrified
BL32	Western Rim	Pl>Opx>Cpx>Ox	60>20>16>4	med sub	20-30 rounded, elongate		40; hyalopilitic, devitrified

BL32a	Western Rim	Pl>Cpx>Opx>Ox	50>25>20>5	course-med sub	20-25	4 qtz/feld	40; hyalopilitic, devitrified
BL33	Western Rim	Pl>Cpx>Opx>Op>Ox	55>20>20>4>1	med sub	30	4 qtz/feld	30; hyalopilitic, devitrified
BL34	Western Rim	Pl>Cpx>Opx>Ox>Ol	60>24>21>4>1	course-med eu-sub		1	55; hyalopilitic
BL35	Western Rim	Pl>Cpx>Opx>Ox>Ol	56>21>16>5>2	course sub-an	20-25	5 4 mm, fine grained qtz/feld	40; hyalopilitic
BL35a	Western Rim	Pl>Opx>Cpx>Ox>Ol	55>16>15>5>4	fine-med Sub-an (shards)			40; hyalopilitic
BL36	Rp-Sc1	Pl>Cpx>Opx>Ox	60>25>15>5	(course)-med sub	30-40 rounded, coalesed, bi- modal size		40; hyalopilitic, devitrified
BL36a	Rp-Sc1	Pl>Opx>Cpx>Ol>Ox	60>19>18>8>5	med sub-an (shrads)		2 qtz/feld	40-50; hyalopilitic

Sample: BL15
Locality: Site 14
Unit: BLC lava flow

Sample	Clast No.	Dry	Wet	Wax	Ballast Weight	Density	Vesicularity (%)
BL15	1	60.69	19.54	3		1.48	43.15
	2	45.48	11.94	2		1.36	47.75
	3	9.49	2.43	2		1.36	47.86
	4	10.05	2.34	1		1.31	49.67
	5	8.90	1.98	1		1.29	50.32
	6	4.88	0.75	1		1.19	54.28
	7	6.00	1.88	1		1.47	43.58
	8	7.71	2.87	1		1.60	38.35
	9	5.03	1.13	1		1.30	50.01
	10	3.95	1.11	1		1.41	45.93

Mean	1.38	47.09
Std Dev	0.12	4.52
Min	1.19	38.35
Max	1.60	54.28

Sample: BL19
Locality: Site 19
Unit: Rp-Sc1

Sample	Clast No.	Dry	Wet	Wax	Ballast Weight	Density	Vesicularity (%)
BL19	1	42.73	7.76	2		1.22	52.92
	2	12.34	1.24	1		1.11	57.13

Mean	1.17	55.02
Std Dev	0.08	2.97
Min	1.11	52.92
Max	1.22	57.13

Sample: BL19a
Locality: Site 19
Unit: Rp-Sc1

Sample	Clast No.	Dry	Wet	Wax	Ballast Weight	Density	Vesicularity (%)
BL19a	1	51.44	30.93	2		2.52	3.25
	2	11.29	6.66	1		2.45	5.60
	3	7.01	4.07	1		2.41	7.35

Mean	2.46	5.40
Std Dev	0.05	2.05
Min	2.41	3.25
Max	2.52	7.35

Sample: BL23
Locality: Site 22
Unit: Rp-Ag4

Sample	Clast No.	Dry	Wet	Wax	Ballast Weight	Density	Vesicularity (%)
BL23	1	56.12	25.79	2		1.85	28.69
	2	23.78	9.67	1		1.69	35.04
	3	10.36	1.82	1		1.22	53.18
	4	13.36	3.43	1		1.35	48.10
	5	8.24	1.86	1		1.30	50.09
	6	11.32	6.06	1		2.16	16.75
	7	4.34	1.01	1		1.32	49.42
	8	4.96	1.44	1		1.42	45.34
	9	5.42	1.26	1		1.31	49.53
	10	5.26	0.88	1		1.21	53.49

Mean	1.48	42.96
Std Dev	0.32	12.18
Min	1.21	16.75
Max	2.16	53.49

Sample: BL26
Locality: Site 25
Unit: Rp-Ag1

Sample	Clast No.	Dry	Wet	Wax	Ballast Weight	Density	Vesicularity (%)
BL26	1	14.55	33.35	1	34.67	0.92	64.67
	2	10.30	32.21	1	34.67	0.81	68.88
	3	10.80	34.51	2	34.67	0.99	61.89
	4	6.11	36.43	1	34.67	1.41	45.60
	5	2.88	35.03	1	34.67	1.15	55.78
	6	1.15	34.70	1	34.67	1.04	59.97
	7	1.52	34.32	1	34.67	0.82	68.48
	8	2.09	34.89	1	34.67	1.13	56.67
	9	2.16	34.68	1	34.67	1.02	60.81
	10	0.97	34.24	1	34.67	0.71	72.77

Mean	1.00	61.55
Std Dev	0.20	7.83
Min	0.71	45.60
Max	1.41	72.77

Sample: BL28
Locality: Site 26
Unit: Rp-Sc3

Sample	Clast No.	Dry	Wet	Wax	Ballast Weight	Density	Vesicularity (%)
BL28	1	39.74	13.41	2		1.51	41.82
	2	17.41	3.41	2		1.25	51.96
	3	13.19	2.39	2		1.23	52.76
	4	14.93	35.79	2	34.67	1.09	58.24
	5	14.91	8.52	1		2.34	9.83
	6	7.80	0.45	1		1.07	59.02
	7	3.99	0.56	1		1.17	54.86
	8	3.22	0.57	1		1.23	52.73
	9	5.72	37.85	1	34.67	2.28	12.35
	10	2.42	34.70	1	34.67	1.03	60.56

Mean	1.42	45.41
Std Dev	0.49	18.83
Min	1.03	9.83
Max	2.34	60.56

Sample: BL30
Locality: Site 27
Unit: Rp-Sc1

Sample	Clast No.	Dry	Wet	Wax	Ballast Weight	Density	Vesicularity (%)
BL30	1	106.91	64.35	3		2.52	3.18
	2	130.77	80.27	3		2.59	0.23
	3	87.35	52.78	2		2.53	2.66

Mean	2.55	2.02
Std Dev	0.04	1.58
Min	2.52	0.23
Max	2.59	3.18

Sample: BL31
Locality: Site 27
Unit: Rp-Sc1

Sample	Clast No.	Dry	Wet	Wax	Ballast Weight	Density	Vesicularity (%)
BL31	1	17.32	36.57	2	34.67	1.13	56.63
	2	30.78	9.87	2		1.48	43.22
	3	13.88	3.63	1		1.36	47.76
	4	6.60	0.36	1		1.06	59.12
	5	11.32	1.75	2		1.19	54.22
	6	10.82	1.10	2		1.12	56.92
	7	9.27	2.12	1		1.30	49.92

8	5.70	0.52	1	1.11	57.43
9	7.60	2.53	1	1.51	42.00
10	4.82	0.70	1	1.18	54.67

Mean	1.24	52.19
Std Dev	0.16	6.12
Min	1.06	42.00
Max	1.51	59.12

Sample: BL32a
Locality: Site 29
Unit: Western rim

Sample	Clast No.	Dry	Wet	Wax	Ballast Weight	Density	Vesicularity (%)
BL32a	1	21.15	42.70	2	34.67	1.62	37.71
	2	21.66	42.44	2	34.67	1.57	39.76
	3	13.84	39.78	2	34.67	1.60	38.60
	4	15.98	39.63	2	34.67	1.46	43.92
	5	15.69	40.45	2	34.67	1.59	38.73

Mean	1.57	39.75
Std Dev	0.06	2.44
Min	1.46	37.71
Max	1.62	43.92

Values are in wt. %

Plagioclase	SiO_2	TiO_2	Al_2O_3	FeO	MnO	MgO	CaO	Na_2O	K_2O	P_2O_5	SO_3	Cl	Cr_2O_3	NiO	Total
BL6-6	52.79	0.18	25.92	3.27	0.08	2.11	9.19	3.7	0.34	0.15	0.04	0.03	0	0	97.8
BL6-9	57.04	0.06	29.58	0.55	0	0	10.23	4.69	0.43	0	0	0	0.06	0	102.64
BL6-14	53.49	0	28.36	0.36	0	0	8.7	4.84	0.61	0	0	0.05	0	0	96.4
BL6-16	53.26	0	29.04	0.72	0	0	9.4	4.73	0.35	0.15	0	0	0.06	0.15	97.87
BL6-21	49.73	0.11	31.1	1.03	0	0	11.31	3.11	0.26	0	0	0	0.15	0.02	96.82
BL10-1	51.26	0	29.54	0.54	0.03	0.11	9.89	3.82	0.28	0.06	0.11	0.02	0.07	0.01	95.74
BL10-4	50.62	0	29.75	0.76	-0.03	0.07	10.11	3.68	0.24	-0.02	-0.02	0	0	0.06	95.23
BL10-7	53.74	0.15	28.01	0.59	0.07	0.11	8.28	4.73	0.36	0.2	-0.02	0.02	-0.03	0.16	96.38
BL10-14	53.33	-0.02	28.2	0.56	0.06	0.08	8.5	4.67	0.32	-0.07	-0.05	-0.03	0.12	0.02	95.71
BL10-19	53.15	0	28.2	0.63	0.05	-0.03	8.8	4.63	0.35	0.09	-0.02	0.01	-0.06	-0.07	95.72
BL10-21	50.28	0.14	30.29	0.7	0.01	0.18	10.44	3.37	0.22	-0.04	-0.01	0.03	0.1	0.27	95.97
BL10-22	53	0.05	28.02	0.59	0.01	0.21	8.71	4.67	0.32	0.11	0.05	0.04	-0.05	-0.02	95.72
BL10-24	51.29	0.04	29.25	0.69	-0.09	0.26	9.54	3.99	0.29	0.16	0.07	0.07	-0.06	0.03	95.52
BL10-25	53.02	0.05	27.87	0.56	-0.01	0.01	8.45	4.93	0.37	-0.03	-0.07	0	0.04	0.13	95.33
BL10-26	54.4	0.08	27.68	0.63	0.02	0.22	8.2	4.9	0.38	0	0.01	-0.04	0.1	0.21	96.76
BL15-7	52.64	0.04	29.44	0.66	0.02	0	9.65	4.37	0.29	0.25	0.05	0.03	0.12	0.07	97.62
BL15-19	52.9	0	28.16	0.48	0	0.07	8.88	4.79	0.4	0	0	0	0.13	0	95.81
BL15-20	52.64	0.14	28.11	0.69	0	0	9.1	4.36	0.38	0	0	0.02	0	0.02	95.47
BL15-22	53.04	0.06	28.4	0.32	0	0.07	8.87	4.65	0.32	0.06	0	0.03	0.17	0	95.99
BL15-23	53.15	0.05	28.44	0.61	0	0.01	9.04	4.6	0.36	0.06	0.04	0.01	0	0.02	96.39
BL15-24	53.35	0.03	28.34	0.46	0	0.04	8.72	4.76	0.4	0.1	0	0.07	0	0	96.27
BL15-25	49.84	0.11	30.48	0.45	0	0	10.97	3.56	0.28	0	0.14	0.01	0.19	0	96.03
BL19-2	49.93	0.05	30.12	0.48	0.04	0.17	10.38	3.49	0.26	0.15	-0.01	0.01	0.03	0.13	95.24
BL19-3	52.15	-0.05	28.17	0.41	0.12	0	8.76	4.43	0.29	0.09	0	0.02	0.1	-0.12	94.37

BL19-9	47.66	0.05	31.56	0.64	-0.01	-0.02	11.56	2.41	0.21	0	-0.06	0.01	0.1	-0.09	94
BL19-10	51.94	0.06	28.38	0.63	-0.06	0.05	9.01	4.21	0.34	0.1	0.13	0.03	0.1	0.18	95.1
BL19-11	53.48	0.01	27.69	0.35	0.15	0.04	8.1	4.92	0.42	0.06	-0.03	0.04	0.05	0.12	95.4
BL19-12	54.2	0.09	27.57	0.54	-0.01	0.04	8.01	5.17	0.42	0.11	-0.02	0.07	0.01	0.13	96.32
BL19-13	49.81	0.14	30.05	0.59	-0.02	0.04	10.16	3.4	0.21	-0.01	-0.03	0.04	0.17	0.12	94.65
BL19-14	48.63	0.01	30.95	0.67	-0.09	0.1	10.88	2.8	0.18	0.1	-0.02	0.05	0	0.06	94.31
BL19-17	51.06	0	29.37	0.58	-0.02	0.14	9.7	3.72	0.28	0.13	-0.02	0	-0.02	-0.01	94.89
BL19-23	53.58	0.08	26.58	0.25	-0.03	-0.03	7.54	5.31	0.44	0.05	0.01	0.01	0.01	0.12	93.92
BL27-1	52.8	0.01	27.76	0.59	-0.02	0	8.12	4.79	0.36	-0.08	0.06	0.02	0.07	0.07	94.55
BL27-2	53.04	-0.02	27.38	0.61	0.04	0.12	8.15	4.81	0.33	0.12	-0.1	0.04	0.02	-0.15	94.39
BL27-6	50.99	0.07	28.55	0.61	-0.02	0.13	9.36	3.91	0.34	0.08	-0.12	0.04	0.21	0.12	94.26
BL27-7	52.92	0.13	27.7	0.54	-0.04	0.07	8.39	5.01	0.29	0.07	-0.07	0.08	0.14	-0.1	95.14
BL27-9	50.69	0.01	29.06	0.63	0.13	0.07	9.62	3.69	0.32	0.07	0.13	0.09	-0.06	-0.04	94.41
BL27-18	51.13	0.01	29.15	0.47	-0.05	0.13	9.47	3.92	0.29	0.16	-0.01	0.07	0.08	-0.04	94.8
BL27-19	53.29	0.16	27.48	0.56	-0.02	0.08	8.14	5.05	0.35	0.13	0	0.03	-0.01	0.11	95.35
BL31-5	51.46	0	29.06	0.68	0	0	9.91	4.27	0.35	0	0.03	0.06	0	0.09	95.92
BL31-12	48.67	0.06	31.12	0.64	0.01	0	11.52	2.94	0.19	0.28	0.1	0.04	0.07	0	95.63
BL31-13	47.36	0	31.98	0.69	0	0	12.13	2.34	0.24	0	0	0.01	0.07	0	94.8
BL31-14	48.72	0	31.29	0.52	0.09	0	11.57	2.77	0.22	0.05	0	0.03	0.14	0	95.4
BL31-17	48.55	0	31.23	0.65	0	0	11.46	2.89	0.28	0	0.03	0.02	0	0	95.14
BL31-18	53.22	0.02	28.36	0.54	0	0.1	9.03	4.51	0.38	0	0	0.02	0.03	0	96.21
BL31-20	54.17	0	27.64	0.59	0	0	8.42	4.76	0.34	0.18	0	0	0.07	0.13	96.31
Clinopyroxene															
BL10-9	51.04	0.46	1.46	13.55	0.37	13.37	14.09	-0.01	0.01	0.16	0	0.05	0.24	-0.11	94.69
BL10-15	51.75	0.39	1.44	11.56	0.41	13.85	14.82	0.11	0.14	0.25	0.06	0.04	-0.02	-0.23	94.57
BL10-17	51.36	0.45	1.4	12.66	0.31	13.53	14.35	0.3	0.07	0.07	0	0.03	0.23	-0.03	94.73
BL10-18	51.53	0.41	1.8	11.22	0.24	13.99	15.31	0.25	0.06	-0.05	0.06	0.05	0.1	-0.19	94.76

BL10-20	51.62	0.46	1.25	13.71	0.29	12.93	14.64	0.31	0.08	0	-0.02	0	0.2	0.02	95.5
BL15-17	50.84	0.51	1.25	13.09	0.46	13.18	15.06	0.25	0.17	0.19	0.05	0.09	0.12	0	95.25
BL15-18	50.5	0.58	2.43	11.67	0.24	14.41	14.9	0.26	0.11	0.19	0	0.02	0.05	0	95.37
BL19-7	50.67	0.44	2.38	9.78	0.17	14.41	14.91	-0.04	0.14	0.23	-0.08	0	0.25	0.15	93.42
BL19-18	51.3	0.67	3.04	7.6	0.26	15.6	14.9	0.17	0.12	0.14	0.12	0.08	0.38	0.03	94.4
BL19-21	50.73	0.66	2.75	9.23	0.2	14.76	14.84	0.06	0.03	0.1	0.04	0.03	0.29	-0.06	93.66
BL19-22	50.33	0.64	3.6	8.22	0.09	15.08	14.97	0.05	0.09	0.28	0.01	0.08	0.36	0.06	93.86
BL27-23	50.23	0.62	2.17	13.75	0.3	13.18	13.92	0.24	0.05	0.01	-0.04	-0.01	0	-0.02	94.41
BL27-25	50.65	0.39	1.5	11.48	0.25	13.75	14.94	0.22	0.08	0.41	0.08	0.08	0.12	0.14	94.1
Orthopyroxene															
BL6-17	52.56	0.02	0.1	25.43	0.76	20.6	0.76	0	0.02	0.01	0	0	0.01	0.08	100.33
BL6-18	52.49	0.33	0.89	22.53	0.66	21.76	1.09	0	0.05	0	0	0	0	0.05	99.85
BL6-19	51.94	0.35	0.84	23.52	0.6	20.91	1.32	0	0.08	0.26	0.05	0	0	0.18	100.04
BL6-20	51.96	0.2	0.57	24.46	0.67	20.24	1.27	0	0	0.11	0	0	0.19	0	99.66
BL6-23	51.68	0.14	0.75	23.56	0.74	20.7	1.27	0	0.1	0.18	0	0	0.01	0.14	99.28
BL6-24	51.95	0.25	0.52	24.25	0.63	20.86	1.16	0	0.14	0.1	0	0	0.01	0.1	99.96
BL6-25	52.46	0.28	1.77	19.86	0.51	23.75	1.26	0	0.06	0.12	0.02	0	0.11	0	100.2
BL6-26	52.4	0.27	1.75	20.26	0.5	23.58	1.23	0	0.12	0.13	0.1	0.01	0	0	100.35
BL6-27	51.45	0.2	0.85	24.25	0.58	20.16	1.23	0	0.01	0.07	0.11	0.05	0	0	98.96
BL6-28	50.87	0.2	0.81	24.24	0.64	20.05	1.36	0	0.06	0	0	0	0	0	98.22
BL6-29	52.87	0.11	0.54	23.56	0.66	21.24	0.93	0	0.07	0.1	0	0.03	0.09	0	100.19
BL6-30	52.71	0.31	1.88	19.53	0.48	23.3	1.33	0	0.08	0.31	0	0.02	0.09	0	100.06
BL10-5	52.11	0.27	0.81	25.91	0.6	19.78	1.08	-0.03	0.01	0.08	-0.03	0.03	0.04	-0.1	100.56
BL10-8	51.95	0.32	1.12	25.72	0.65	20.14	1.14	0.25	0.08	-0.01	0.04	-0.01	0.1	0.07	101.55
BL10-10	52.92	0.32	1.16	22.69	0.61	22.2	0.92	0	0.09	0.05	0	-0.01	0.01	0.01	100.98
BL10-12	51.65	0.3	1.19	25.77	0.6	19.37	1.33	0.05	0.04	0.04	-0.05	-0.04	-0.02	0.01	100.23
BL10-13	51.87	0.25	1.05	23.62	0.69	21.22	1.11	-0.04	0.09	0.08	0	0.01	0.05	0.21	100.22

BL10-16	51.59	0.26	0.62	25.69	0.61	19.56	1.3	-0.02	0.11	-0.04	-0.05	0.04	0.12	0.08	99.88
BL10-23	52.66	0.34	0.88	24.93	0.64	21.05	1.04	0.23	0.09	-0.05	0.06	0.01	0.13	-0.19	101.83
BL10-27	52.36	0.29	0.89	24.32	0.49	20.83	1.14	0.04	0.09	-0.01	-0.04	0.08	0.09	-0.05	100.5
BL15-1	51.71	0.3	0.58	24.41	0.89	20.36	1.36	0	0.09	0.42	0	0	0	0	100.11
BL15-2	50.78	0.09	0.72	29.14	0.66	18.07	0.47	0	0.06	0.15	0	0	0.07	0	100.2
BL15-3	52.56	0.18	2.65	14.65	0.26	26.42	1.29	0	0.06	0	0	0.02	0.13	0	98.22
BL15-4	51.17	0.31	1.15	25.16	0.59	19.47	1.3	0	0.01	0.08	0	0.02	0.09	0.06	99.43
BL15-5	51.46	0.21	0.78	25.74	0.63	19.86	1.33	0	0.1	0.16	0	0	0.02	0.16	100.45
BL15-6	51.25	0.37	0.79	26.34	0.64	18.86	1.26	0	0.09	0.01	0	0.03	0	0	99.64
BL15-8	52.49	0.3	0.92	20.24	0.57	23.21	1.27	0.03	0.1	0.06	0	0	0.01	0.14	99.32
BL15-9	51.54	0.19	0.91	24.49	0.63	20.08	1.25	0	0.04	0.11	0	0	0	0	99.23
BL15-10	51.47	0.33	0.66	24.85	0.73	19.72	1.35	0	0.1	0.17	0	0	0	0.05	99.45
BL15-11	51.62	0.18	0.64	26.47	0.76	18.75	1.26	0	0.05	0.17	0	0	0.08	0	99.97
BL15-13	51.42	0.28	1.15	24.6	0.57	20.15	1.08	0	0.01	0	0.08	0.03	0.03	0.01	99.4
BL15-14	51.92	0.34	1.22	20.57	0.44	22.7	1.4	0.13	0.1	0.09	0	0.03	0.06	0	99.02
BL15-15	51.97	0.14	1.12	24.2	0.62	20.63	1.12	0	0.08	0.14	0.04	0.03	0	0	100.08
BL19-1	52.16	0.19	0.89	22.73	0.5	20.94	1.21	-0.02	0.1	0.07	0	0	0.07	0.02	98.86
BL19-5	51.59	0.27	1.24	23.41	0.58	20.36	1.18	0.16	0.1	0	0.05	0.05	0.13	0.11	99.23
BL19-6	52.3	0.07	1.07	23.2	0.52	20.94	1.12	-0.01	0.06	-0.09	0.01	0.02	-0.03	-0.02	99.15
BL19-15	52.04	0.16	1.09	23.93	0.58	20.79	1	0.08	0.1	-0.05	-0.07	0	0.04	0.07	99.76
BL19-16	49.69	0.23	0.72	27.73	0.51	17.91	0.98	0.12	0.05	-0.07	0.07	0.07	0.01	-0.04	97.98
BL19-19	51.81	0.37	2.57	19.95	0.47	23.26	0.92	0.08	0.05	0.12	0.08	0.05	0.06	-0.03	99.76
BL19-20	52.67	0.26	2.51	16.81	0.46	25.9	1	-0.04	0.06	-0.04	-0.02	0.02	-0.03	-0.02	99.53
BL27-3	51.17	0.33	0.74	24.26	0.76	19.79	1.39	0	0.06	0.01	-0.05	0.04	0.06	-0.08	98.47
BL27-4	50.87	0.21	0.94	25.21	0.62	19.48	1.13	0.01	0.07	0.11	-0.05	0.02	-0.01	-0.03	98.6
BL27-8	51.03	0.21	1.11	24.08	0.65	19.65	1.19	-0.02	0.09	0.12	0.04	0.05	-0.03	-0.05	98.12
BL27-10	50.75	0.23	0.82	25.07	0.58	19.63	1.26	-0.05	0.07	0.06	0.07	0.03	-0.03	0.17	98.65

BL27-12	52.86	0.3	0.94	17.32	0.3	24.66	1.27	-0.11	0.05	0.08	0.01	0.05	-0.02	0	97.72
BL27-14	51.31	0.33	0.8	25.07	0.71	19.45	1.3	-0.03	0.08	0	0.09	0.07	0.06	-0.01	99.24
BL27-15	53.72	0.1	1.53	12.65	0.19	27.55	1.54	0.16	0.09	0.01	0.02	0	0.15	-0.01	97.71
BL27-20	51.93	0.27	0.88	22.2	0.7	21.89	0.98	-0.02	0.1	-0.02	-0.07	0.05	0.04	0.04	98.97
BL27-21	51.61	0.14	0.74	25.23	0.69	20.03	0.95	-0.06	0.08	0.12	-0.02	0.06	0.03	0.04	99.64
BL27-26	51.49	0.11	0.82	24.49	0.62	20.25	0.95	0.06	0.05	0.04	-0.06	0.06	0.06	0.21	99.15
BL27-27	51.48	0.12	0.81	25.21	0.72	19.8	1.03	0.17	0.04	0.08	0.13	0.08	0.08	-0.07	99.67
BL27-28	52.15	0.18	0.86	22.84	0.66	21.34	0.95	0	0.05	0.13	0.02	0.01	-0.02	-0.03	99.15
BL31-1	51.97	0.37	0.94	20.97	0.53	22.34	1.27	0	0.04	0	0	0.03	0.07	0	98.54
BL31-2	52.21	0.37	1.18	20.18	0.37	22.71	1.25	0	0.01	0.1	0	0.05	0.11	0	98.54
BL31-3	52.39	0.38	1.33	18.65	0.35	23.89	1.35	0.01	0.02	0.16	0	0	0.05	0	98.58
BL31-4	52.08	0.11	0.92	21.25	0.49	22.43	1.39	0	0.12	0.11	0.01	0.04	0	0	98.95
BL31-6	51.72	0.2	0.99	21.68	0.58	21.73	1.26	0	0.1	0.08	0.13	0.04	0	0	98.52
BL31-8	52.12	0.32	0.88	21.29	0.63	22.57	1.2	0.11	0.07	0	0	0	0	0	99.2
BL31-11	52.93	0.17	0.74	18	0.34	24.66	1.25	0	0.04	0	0	0.08	0	0	98.22
BL31-16	51.45	0.3	0.81	23.48	0.73	20.61	1.28	0	0.06	0.16	0	0.05	0.15	0.28	99.36
BL31-19	52.04	0.05	1.07	22.19	0.58	21.47	1.18	0	0.03	0	0.1	0.05	0.07	0.2	99.04
BL31-23	52.26	0.23	2.06	17.87	0.49	24.55	1.15	0.06	0.08	0.02	-0.03	0.04	0.1	-0.01	98.87
BL31-28	52.42	0.34	1.73	17.75	0.33	24.35	1.17	-0.04	0.08	0.15	0.01	0.02	0.13	-0.09	98.36
BL31-29	52.51	0.18	1.48	18.01	0.47	24.97	1.11	-0.04	0.13	0.09	0.02	0.01	-0.01	-0.07	98.86
Olivine															
BL31-22	38.95	-0.1	0.08	20.76	0.37	39.61	0.11	-0.11	0.04	0.06	-0.02	-0.01	-0.06	0.23	99.9
BL31-24	38.79	0.03	0.07	19.36	0.26	40.19	0.13	0.01	0.05	0.08	-0.01	0	-0.03	0.09	99.02
BL31-25	39.04	0.02	0.04	17.24	0.25	42.66	0.09	0.08	0.04	-0.14	-0.03	0.14	0.03	-0.01	99.45
BL31-26	39.24	0.11	0.09	17.4	0.24	42.17	0.07	0	0.08	-0.01	-0.02	0.05	0.05	-0.01	99.45
BL31-27	37.73	-0.07	-0.02	23.8	0.44	36.75	0.1	-0.05	0.08	-0.17	0.02	0.07	0	0.1	98.77
Fe-Ti Oxides															

BL6-13	0.04	51.26	0.15	48.64	0.81	2.14	0.03	0	0.06	0	0.02	0	0.04	0	103.19
BL6-22	0.08	14.51	3.12	77	0.36	1.84	0	0	0	0	0	0.04	0.35	0	97.28
BL10-2	-0.02	46.51	0.18	51.25	0.64	1.34	0.02	0.18	0.05	0.14	0.01	-0.01	0.1	0.11	100.52
BL10-3	-0.01	16.04	2.32	75.63	0.42	1.69	0	-0.03	0.01	-0.08	-0.04	-0.01	0.27	0.16	96.37
BL10-6	1.48	26.42	2.75	61.11	0.52	1.47	0.05	0.06	0.01	0.16	-0.01	-0.02	0.3	-0.05	94.25
BL15-12	0.14	17.01	2.27	75.14	0.39	1.65	0.07	0.3	0	0.01	0.01	0.04	0.34	0.09	97.46
BL19-4	0.03	14.63	1.82	71.53	0.57	1.31	0.11	0.15	0.07	0	0.08	0.04	0.76	0.14	91.23
BL27-16	-0.01	47.1	0.16	49.87	0.49	1.66	0.03	-0.01	0.01	-0.03	0.16	0.05	0.19	-0.06	99.63
BL27-17	0.01	12.27	1.54	79.6	0.47	0.74	-0.01	0.29	-0.02	0.04	-0.05	0.06	0.36	-0.1	95.19
BL27-22	0.03	46.19	0.02	50.54	0.5	1.27	-0.06	-0.09	0.04	0.06	-0.07	0.03	0.04	-0.06	98.44
BL27-24	0.19	14.18	1.73	77.03	0.42	1.13	-0.01	0.34	0.08	0.11	0	0.02	0.32	0.24	95.78
BL31-9	0	12.85	3.16	74.86	0.27	2.7	0	0.17	0.04	0	0.12	0	1.23	0	95.4

Element (%)	BL4	BL 5	BL 6	BL 7	BL 8	BL 9	BL 10	BL 11	BL 12	BL 13
Na_2O	3.01	3.77	3.30	3.16	2.94	2.77	3.03	2.79	2.64	2.35
MgO	2.85	3.84	2.84	3.03	3.08	4.06	3.71	3.65	3.60	3.43
Al_2O_3	17.91	17.05	17.26	17.27	17.48	17.23	18.06	18.10	17.74	18.26
SiO_2	58.24	56.50	58.66	57.02	58.47	55.43	56.57	57.90	57.65	57.81
P_2O_5	0.17	0.14	0.17	0.26	0.09	0.12	0.11	0.13	0.09	0.09
K_2O	1.43	1.42	1.54	1.30	1.65	1.22	1.23	1.38	1.29	1.40
CaO	5.57	6.98	6.41	6.53	5.31	6.48	6.41	6.03	5.54	4.77
TiO_2	0.84	0.77	0.86	0.83	0.77	0.83	0.78	0.80	0.81	0.81
MnO	0.12	0.13	0.13	0.12	0.11	0.13	0.12	0.12	0.12	0.11
Fe_2O_3	7.58	7.66	7.95	7.61	7.01	8.17	7.34	7.12	7.63	8.29
LOI	3.01	0.89	1.32	2.32	1.69	2.21	1.64	1.48	2.40	2.97
Total	97.72	98.24	99.13	97.13	96.90	96.42	97.36	98.01	97.10	97.32

Element (%)	BL 14	BL 15	BL 16	BL 17	BL 17a	BL 18	BL19	BL 19a	BL20	BL21
Na_2O	2.89	3.00	3.05	3.26	2.95	2.85	3.20	3.04	3.22	2.89
MgO	3.84	3.88	3.91	4.06	3.91	3.95	3.29	3.89	3.44	4.56
Al_2O_3	17.24	17.30	16.93	17.01	16.87	17.18	17.15	16.41	16.97	16.64
SiO_2	58.86	57.92	56.95	56.34	57.01	56.37	58.43	58.58	58.86	55.73
P_2O_5	0.10	0.14	0.13	0.12	0.13	0.13	0.16	0.14	0.17	0.20
K_2O	1.46	1.40	1.35	1.34	1.38	1.37	1.65	1.62	1.67	1.41
CaO	6.73	7.08	7.22	7.01	7.10	6.49	5.69	6.60	5.70	6.05
TiO_2	0.80	0.80	0.78	0.79	0.79	0.82	0.77	0.75	0.75	0.73
MnO	0.13	0.13	0.13	0.13	0.13	0.13	0.11	0.12	0.11	0.13
Fe_2O_3	7.20	8.19	8.06	8.32	8.16	8.43	6.88	7.53	6.76	8.03
LOI	0.87	0.53	0.14	0.81	0.10	1.47	1.55	0.44	1.19	2.63
Total	99.25	99.82	98.51	98.39	98.44	97.73	97.32	98.69	97.65	96.37

Element (%)	BL 22	BL 23	BL 24	BL 25	BL 26	BL 27	BL 28	BL 29	BL 30	BL 31
Na_2O	3.09	2.94	2.63	2.88	2.53	2.90	2.18	2.87	3.24	3.25
MgO	4.75	4.04	3.73	3.90	4.61	3.91	6.40	3.67	4.75	4.56
Al_2O_3	15.86	17.32	18.42	17.48	16.14	17.14	15.30	16.06	16.01	16.16
SiO_2	59.22	58.87	57.21	56.71	57.41	58.80	56.36	55.64	59.44	59.35
P_2O_5	0.13	0.10	0.13	0.16	0.13	0.12	0.11	0.12	0.13	0.15
K_2O	1.46	1.44	1.17	1.20	1.41	1.40	1.01	1.25	1.45	1.50
CaO	7.22	6.84	5.64	6.40	4.64	6.31	5.63	5.62	7.02	6.88
TiO_2	0.70	0.81	0.79	0.78	0.73	0.80	0.69	0.75	0.70	0.70
MnO	0.12	0.13	0.11	0.13	0.12	0.13	0.21	0.12	0.12	0.12
Fe_2O_3	7.62	7.25	7.71	8.65	7.96	7.31	6.96	12.58	7.53	7.49
LOI	0.11	0.53	2.81	1.63	4.74	1.15	4.43	2.00	0.24	0.38
Total	100.17	99.73	97.53	98.28	95.68	98.81	94.84	98.69	100.40	100.16

Element (%)	BL 32	BL 34	BL 35	BL 35a	BL 36	BL36a
Na_2O	3.16	3.14	3.12	3.24	3.18	3.18
MgO	3.47	4.98	4.49	4.85	4.54	4.73
Al_2O_3	16.90	15.80	16.72	15.66	16.08	15.79
SiO_2	59.91	58.66	57.48	59.37	58.15	58.83
P_2O_5	0.09	0.11	0.13	0.12	0.14	0.13
K_2O	1.82	1.48	1.52	1.52	1.43	1.40
CaO	5.51	6.80	6.23	6.64	6.69	7.17
TiO_2	0.82	0.70	0.72	0.71	0.70	0.69
MnO	0.11	0.12	0.12	0.13	0.12	0.12
Fe_2O_3	7.36	7.67	7.68	7.73	7.58	7.51
LOI	1.51	0.25	1.74	0.14	0.73	0.08
Total	99.15	99.48	98.20	99.95	98.61	99.56

Element (%)	BL4	BL 5	BL 6	BL 7	BL 8	BL 9	BL 10	BL 11	BL 12	BL 13	BL 14	BL 15
S	5934	117	2033	16820	542	1342	313	542	3112	645	323	159
Cl	413	343	456	118	85	239	166	114	42	72	348	466
V	218	215	219	222	157	222	205	174	206	185	215	207
Cr	14	27	18	18	44	28	29	23	22	23	19.7	22
Co	38	50	45	57	43	43	39	21	32	33	51	74
Ni	7	10.1	9.1	7.6	12.1	8.6	9.9	7.4	6.7	8.3	6.9	7.9
Cu	35	12.6	12.9	8.5	20	4.6	6.8	9.7	36	17.9	11.3	11.6
Zn	80	82	89	101	64	78	85	73	76	82	81	83
Ga	19.1	18	19.7	19.6	19.2	18.9	18.4	19.3	18.6	18.8	18.8	19.1
Rb	53	47	55	45	48	43	35	49	48	48	50	49
Sr	278	269	284	281	270	256	259	244	226	214	255	261
Y	21	32	25	23	31	22	17	17.3	21	25	22	24
Zr	131	123	138	123	152	125	119	123	126	131	129	126
Nb	6.3	6	6.6	6.3	7.5	6.1	5.9	6.3	6.3	6.5	6	6.4
Mo	1.9	1.6	1.9	1.8	1.6	1.8	1.5	1.7	1.8	1.5	1.7	1.9
Ba	336	296	341	296	371	290	287	309	300	329	300	301
La	11.7	13.5	9.6	10	13.3	7.4	6.6	5.8	6.8	8.1	8.3	11.9
Ce	25	30	29	25	36	21	12.4	15.8	19.7	15.7	19.4	26
Nd	16.4	15.7	14.3	15.1	20	15.8	< 10	< 10	< 10	< 10	< 10	< 10
Hf	5.1	4.8	4.7	4.1	5.4	5.1	3.8	4	2.8	4.4	4.5	3.2
Ta	5.7	3	3.7	2.9	4.6	3.8	< 2.7	< 2.7	< 3.6	3.4	3.5	< 3.3
W	114	145	366	198	99	122	209	71	82	76	268	557
Pb	9.6	8.3	10.4	8.3	9	6.6	6.3	6.7	8.2	9.6	9.3	9.6
Th	8.9	7.9	9.3	8.2	9.2	8.4	8.6	9.2	8.5	9.2	9	8.6
U	4.4	5.5	5.5	5.1	4.8	4.8	6.1	5.8	5.4	5.4	6.1	5.6

Element (%)	BL 16	BL 17	BL 17a	BL 18	BL19	BL 19a	BL20	BL21	BL 22	BL 23	BL 24	BL 25
S	87	216	112	1479	481	228	305	992	138	2569	445	393
Cl	273	118	473	581	40	557	96	441	535	47	224	71
V	206	212	209	222	110	165	138	175	171	190	203	197
Cr	25	30	27	22	42	52	45	131	151	24	25	19
Co	44	48	64	47	39	49	59	56	66	48	35	51
Ni	9.5	9.5	9.2	8.9	15.4	12.8	16	32	32	8.6	10.8	8.9
Cu	6.8	12.8	11.2	8.9	19.9	13.9	22	51	27	17.5	18.6	8.6
Zn	82	86	83	81	77	81	86	81	78	97	160	94
Ga	18.5	19.2	18.9	19.4	19.8	18.9	18.6	18.5	18.1	19.7	19.1	18.3
Rb	48	47	49	49	60	60	54	52	53	52	34	37
Sr	264	256	261	241	267	278	267	262	320	261	230	253
Y	24	23	23	19	18.8	24	23	23	23	21	20	21
Zr	126	122	125	127	150	142	150	136	128	125	121	120
Nb	6.3	6	6.1	6.1	7.3	6.9	7.9	7.3	6.9	6.9	6.4	6.5
Mo	2	1.7	1.8	1.9	1.4	2.1	2	2.3	2.1	1.8	1.9	2
Ba	293	291	286	285	363	337	351	280	293	302	303	281
La	8.8	9.7	8	< 4.9	8.6	11.9	13.4	10.8	10	5	8.2	8.2
Ce	24	22	23	12.5	24	28	28	27	24	12.8	18.2	17.6
Nd	9.2	10.1	10.8	< 10	< 10	13	10.6	12.4	< 10	< 10	11	10.6
Hf	4.1	4.8	3.4	4	4.2	6.1	7.7	7	5.7	5	6.9	7.2
Ta	< 2.9	< 3.2	< 3.1	< 3.0	3.9	< 3.2	6.5	4.4	< 3.8	3.5	< 3.1	6.8
W	326	386	389	254	185	420	270	377	411	252	84	140
Pb	8.2	9.2	9.4	8.2	9.8	11.9	23	10.4	11.2	8.5	9.8	9.4
Th	8.4	8.5	8.4	8.5	10.5	10.1	12.7	10.8	11.2	10.1	9.5	9.4
U	5.2	4.8	5.1	5.8	5.4	5.5	7.5	7.6	7.6	7.3	6.9	7.4

Element (%)	BL 26	BL 27	BL 28	BL 29	BL 30	BL 31	BL 32	BL 34	BL 35	BL 35a	BL 36	BL36a
S	779	1482	1206	797	149	253	724	188	873	212	331	106
Cl	578	40	430	106	455	648	103	240	180	24	691	500
V	149	184	128	229	166	168	167	201	149	195	171	170
Cr	43	19	28	36	139	130	54	163	124	131	128	137
Co	56	56	37	43	60	65	49	58	49	56	72	58
Ni	15.8	8.9	18.2	14.8	33.1	31	14.6	34	28	30	28	28
Cu	10	19	9.9	16.5	29	31	42	16.5	26	18.2	24	22
Zn	146	108	75	168	76	76	73	74	78	80	80	76
Ga	17.8	20	17.1	17.2	17.9	18.8	19.3	17.5	17.8	18.2	19.4	18.4
Rb	60	54	48	45	53	54	70	53	59	54	53	53
Sr	219	246	245	234	301	304	246	303	272	272	297	323
Y	26	22	25	51	24	24	21	21	21	22	24	23
Zr	145	126	134	112	128	131	155	127	132	129	130	126
Nb	7.8	6.6	7.3	6.1	7.4	7.5	8.3	7	7.1	6.9	7	7.1
Mo	1.9	1.9	1.6	1.9	2.6	2.3	2.2	2.1	2.2	2.3	2.3	2
Ba	343	311	255	270	296	297	373	287	286	298	290	285
La	11.4	5.7	12.1	13.8	11.1	10.4	9.7	6.7	9.3	10.1	9.7	8.3
Ce	26	15	27	37	25	25	24	18.3	23	24	25	24
Nd	15.9	< 10	11.8	21	15.6	9.9	< 10	< 10	< 10	< 10	9.3	12.9
Hf	7.9	6.3	7.2	7.5	8.4	6.8	6.6	7.9	6.8	5.2	4.6	6.5
Ta	4.2	5.1	3.9	4.3	4.7	< 4.0	< 3.8	5.5	6.8	< 3.5	< 3.9	4.8
W	142	303	108	93	344	567	202	262	214	372	657	310
Pb	15.2	11.2	10.8	9.2	9.8	10.6	12.5	9.4	9.3	8.5	10	10
Th	12	10	10.7	7.3	11.7	11.6	12.9	10.3	10.9	10.7	10.8	10.6
U	8.1	7.8	7.2	8.2	8.2	8.7	9.4	8.4	7.6	8.7	8.2	8.1